May 2020

Development and Application of Effective Stochastic Potential Method for Investigating Temperature-dependent Electronic Properties of Nanomaterials

Jeremy Scher
Syracuse University

Abstract

Temperature plays an incredibly important role in determining what values a quantum mechanical property of a chemical system can assume. The mechanism by which temperature and the other features of a chemical system's environment effects observable properties is through their effect on the population of thermally-accessible structures. As temperature changes, the population of these thermally-accessible structures shifts, and correspondingly so do the distributions of quantum mechanical properties. Prediction, calculation, and analysis of these distributions are fundamental to the study of statistical mechanics, and are integral to understanding what role the chemical environment has on any quantum mechanical property that may be of interest. One of the largest ongoing challenges concerning the determination of quantum mechanical distributions is the need for 10^5 to 10^6 conformational samples from the population of structures in order to obtain accurate and reliable distributions of properties. For large chemical systems consisting of many electrons, performing ab-initio calculations on such a large number of structures is computationally infeasible using traditional quantum chemistry methods. This problem is even further exacerbated when distributions of excited electronic state properties such as electronic spectra are desired, due to the increased computational cost of ab-initio excited-state techniques.

To overcome this computational barrier, I have developed the Effective Stochastic Potential (ESP) method which addresses the challenge of conformational sampling. The ESP method is a first-principles technique which uses random matrix theory to treat noisy chemical environments of a system stochastically. In doing so, the computational cost of performing conformational sampling on the system can be drastically reduced. The accuracy of the ESP method has been confirmed by benchmarking against calculations of both ground and excited-state properties of H_2O. I have applied the ESP method on various systems, including semiconductor nanoparticles to efficiently obtain temperature-dependent distributions of HOMO-LUMO gap energies, excitation energies, and exciton binding energies comprised of a million samples. For many of the systems studied, calculation of these distributions using traditional first-principle methods would be infeasible. Using the ESP method, it has been calculated that the distributions of excitation energies of PbS and CdSe nanoparticles have a pronounced red-shift as the temperature of the system increases. It has also been found that the excitation energy distributions in PbS nanoparticles exhibit sub-Gaussian characteristics at physically-relevant temperatures. These results highlight the ability of the ESP method to uncover unique temperature-dependent features of quantum mechanical distributions that may otherwise be impossible to obtain.

Development and Application of Effective Stochastic Potential Method for Investigating Temperature-dependent Electronic Properties of Nanomaterials

Jeremy A. Scher

B.S. Binghamton University, State University of New York, 2012

Dissertation

Submitted in partial fulfillment of the requirements for

the Degree of Doctor of Philosophy in Chemistry.

Syracuse University

May 2020

Acknowledgements

First and foremost, I would like to thank my advisor and mentor, Dr. Ari Chakraborty. His academic and professional guidance over the course of my graduate studies has been indispensable. Ari has always been eager and willing to provide his insight into the nature of complex problems associated with doing computational and theoretical research. He has always made himself available when I needed him. I would not be the scientist that I am today without his help, and I am tremendously grateful for all the assistance he has given to me. I would also like to thank the other members of my PhD committee, Dr. Joseph Chaiken, Dr. Timothy Korter, Dr. John Franck, Dr. Lisa Manning, and Dr. Weiwei Zheng for having interest in my work and for taking time out of their busy schedules to help me through the PhD defense process.

Thank you to my fellow lab-mates over the years: Dr. Jennifer Elward, Dr. Christopher Blanton, Dr. Michael Bayne, Dr. Benjamin Ellis, Peter McLaughlin, and Nicole Spanedda. I owe the completion of my degree in large part to your friendship, your advice, and your share of the coffee club funds. You made many of the hardest moments of day-to-day research more bearable. I also thank the undergraduate and high school research students I have supervised during my time at Syracuse University: Eric Harris, Jackson Hernandez, Jasmine Johnson, Sheng Li, Chengpei Liu, Nathan Mascari, and Kameron Shrum. Thank you all for your kindness and patience while I learned how to become an effective mentor myself.

Many thanks to the entire Syracuse University Chemistry Department office staff for your help with all of the logistical issues that needed tending to during my time at Syracuse. Special thanks to Jodi Randall for helping me through an embarrassing number of bureaucratic knots that I managed to get myself into throughout my graduate studies. Thank you also to Larne Pekowsky and Eric Sedore of the Syracuse University Research Computing Team, for providing all of your help with running calculations and submitting jobs on OrangeGrid. Your expertise greatly simplified the work-flow of a number of my projects.

Last but certainly not least I would like to thank my family and friends. To my mom and dad, Madeleine and Michael, I can't thank you enough for all the love and support you have provided me over the years. I could not ask for better parents. Thank you to my sister Sarah, for your empathy during hard times, and for being the push I needed to move out of that terrible apartment. Finally, to my significant other, Lili Karam, thank you for your unwavering companionship. I simply don't know where I would be today without you. For all that you do for me, I count myself among the luckiest of people.

Contents

Acknowledgements iv

Contents v

List of Tables x

List of Figures xi

1 Scope: The Structure-Property Relationship in Quantum Chemistry 1

1.1 The Role of Structure in Quantum Chemistry . . . 1

1.2 The Effect of Temperature and Chemical Environment on Structure . . . 3

1.3 The Importance of Performing Sufficient Conformational Sampling . . . 5

2 Background: Probability Theory and Statistical Mechanics 8

2.1 Statistical Distributions . . . 8

2.1.1 Random Variables . . . 8

2.1.2 Probability Distribution Functions . . . 8

2.1.3 Normal Distributions . . . 10

2.1.4 Expectation Values . . . 11

2.2 Statistical Metrics . . . 11

2.2.1 Central Moments . . . 11

2.2.2 Standard Scores . . . 12

2.2.3 Skewness and Kurtosis . . . 12

2.3 Sampling . . . 13

2.4 Temperature and Boltzmann Statistics . . . 14

3 The Effect of Random Noise in Structure on Electronic Properties 17

3.1 Introduction . . . 17
3.2 Theoretical and Computational Details . . . 19
3.2.1 System Details and Setup . . . 19
3.2.2 Electronic Structure Calculation Details . . . 19
3.3 Results and Discussion . . . 20
3.3.1 Population Distributions of Electronic Properties as a Function of Random Noise . . . 20
3.3.2 Fluctuation in CIS Oscillator Strengths in H_2O . . . 21
3.3.3 Determining Effective Temperature of Noise from Distribution of Ground State Energy . . . 23
3.3.4 Connection of Fluctuation in Nuclear Repulsion Energy to Electronic Properties . . . 25
3.4 Conclusions . . . 27

4 The Effective Stochastic Potential Method 29
4.1 Introduction . . . 29
4.1.1 The Effect of Temperature and Solvent on Semiconductor Nanoparticles . . . 29
4.1.2 Using Random Matrix Theory to Solve Chemical Problems . . . 30
4.1.3 Conceptual Picture of the Effective Stochastic Potential . . . 32
4.2 Theory . . . 33
4.2.1 System Setup and Definitions . . . 33
4.2.2 Definition of Deformation Potential . . . 34
4.2.3 Conceptual Construction of Effective Stochastic Potential . . . 35
4.3 Computational Details . . . 37
4.3.1 Canonical Ensemble Sampling Using Monte Carlo and Molecular Dynamics . . . 37
4.3.2 1-Particle Basis for Representing the Deformation Potential . . . 38
4.3.3 Stochastic Sampling Using Gaussian Random Matrices . . . 39
4.4 Results and Discussion . . . 40
4.4.1 Statistical Distribution of HOMO-LUMO Gap of H_2O at 300 K . . . 40
4.4.2 HOMO-LUMO Gap of $Cd_{20}Se_{19}$ in water at 300K . . . 43
4.5 Conclusions . . . 45

5 Using Effective Stochastic Potentials to Calculate Temperature-dependent Distributions of Excited-state Properties 46
5.1 Introduction . . . 46
5.2 Theory . . . 47
5.2.1 Construction of the Stochastic Fock Matrix . . . 47

5.2.2 Derivation of the ESP-CIS Method . . . 48
5.2.3 Connection to Linear Response Time Dependent Hartree Fock and Density Functional Theory 48
5.3 Computational Details . . . 50
5.3.1 Generation of a Boltzmann-like Sample Population . . . 50
5.3.2 Computational Setails of the ESP-CIS Method . . . 50
5.3.3 System-specific Computational Details . . . 52
5.4 Results . . . 52
5.4.1 ESP-CIS Benchmark Calculations on H_2O at 300K . . . 52
5.4.2 Excited-state Properties of PbS Nanoparticles . . . 52
5.4.3 Excited-state Properties of Energetic Material TKX-50 . . . 56
5.4.4 Excited-state Properties of (**R**)-**1** TADF Organic Molecule . . . 58
5.4.5 Excited-state Properties of PROTAC MD-224 . . . 62
5.4.6 Excited-state Properties of SERCA Activator CDN1163 . . . 65
5.5 Conclusions . . . 68

6 The Effect of Isovolumetric Transformation on the Optoelectronic Properties of Semiconducting Nanoparticles 70

6.1 Introduction . . . 70
6.1.1 The Computational Challenge of Investigating Optoelectronic Properties of Semiconductor Nanoparticles . . . 70
6.1.2 Size-tunability of Semiconductor Nanoparticles . . . 72
6.1.3 Shape-tunability of Semiconductor Nanoparticles . . . 72
6.1.4 Isovolumetric Transformation on Semiconductor Nanoparticles . . . 72
6.2 Theory . . . 74
6.2.1 Treatment of Electron-hole Correlation . . . 74
6.3 Computational Details . . . 76
6.4 Results . . . 77
6.4.1 Effect of Shape and Size on Exciton Binding Energy . . . 77
6.4.2 Effect of Shape on Electron-hole Recombination Probability . . . 79
6.5 Conclusions . . . 87

7 Investigating Optoelectronic Properties of Perovskite Nanoparticles 89

7.1 Introduction . . . 89
7.1.1 Cesium Lead Halide Nanoparticles . . . 89

7.1.2 Optoelectronic Properties of $CsPbX_3$ Nanoparticles . . . 89
7.1.3 Applications of $CsPbX_3$ Nanoparticles . . . 90
7.1.4 Calculation of $CsPbX_3$ Nanoparticle Optoelectronic Properties . . . 90
7.2 Computational Details . . . 91
7.2.1 System Setup and Parameters . . . 91
7.2.2 Mathematical Description of Optoelectronic Properties of Interest . . . 92
7.3 Results and Discussion . . . 92
7.3.1 Effect of Dot Size on Electron-hole Separation Distance . . . 92
7.3.2 Effect of Dot Size on Exciton Binding Energy . . . 93
7.3.3 Effect of Dot Size on Electron Hole Recombination . . . 94
7.3.4 Effect of Electron-hole Separation Distance on Exciton Binding Energy and Electron-hole Recombination . . . 94
7.3.5 Comparison of Trends to Bulk $CsPbX_3$ Exciton Properties . . . 95
7.4 Conclusions . . . 96

8 Temperature-dependent Exciton Binding Energies of CdSe Nanoparticles 98
8.1 Introduction . . . 98
8.1.1 Thermal and Solvent Effects on Optical Properties of Semiconductor Nanoparticles . . . 98
8.1.2 Integration of the ESP and eh-XCHF Methods . . . 100
8.2 Theory . . . 100
8.2.1 Generation of Stochastic Electron-hole States . . . 100
8.2.2 Calculation of Temperature-Dependent Exciton Binding Energies . . . 101
8.3 Computational Details . . . 102
8.3.1 System Details . . . 102
8.3.2 Canonical Ensemble Sampling Using Monte Carlo and Molecular Dynamics . . . 102
8.3.3 eh-XCHF Geminal Parameters and Exciton Binding Energy Approximations . . . 103
8.3.4 Flowchart: Calculation of Exciton Binding Energy . . . 104
8.4 Results and Discussion . . . 105
8.4.1 Temperature-Dependent Mean HOMO-LUMO Gaps for $Cd_{20}Se_{19}$ . . . 105
8.4.2 Distribution of Exciton Binding Energies of $Cd_{20}Se_{19}$ at 300K and 350K . . . 105
8.5 Conclusions . . . 107

9 Conclusions and Future Work 109

Bibliography **111**

List of Tables

4.1 Absolute means (μ) and standard deviations (σ) of HOMO-LUMO gap energy in atomic units, and ratios of μ and σ HOMO-LUMO gap energy distributions between Hartree Fock (cc-pVDZ basis) and ESP method for 10,000 sampling points. Calculated Hartree-Fock values for μ and σ were 0.545523 hartrees and 0.004557 hartrees, respectively. Water geometries were generated from a Monte Carlo procedure. . . 42

4.2 Mean HOMO-LUMO gap energy (in eV) of gas-phase water molecules calculated using the ESP method for an increasingly larger set of deformation potentials, N_{def}. 43

4.3 Comparison of $Cd_{20}Se_{19}$ HOMO-LUMO gap energies (eV) calculated by ESP and Hartree Fock method (LANL2DZ basis). 44

5.1 Mean (μ) and standard deviation (σ) of the $S_0 \rightarrow S_1$ vertical excitation energies (in eV) of H_2O (6-31G basis) calculated using CIS and ESP-CIS ($N_{\text{sample}} = 10^4$) at 300K. 52

5.2 First eight central moments (in eV) of the HOMO-LUMO gap distributions in TKX-50 at 250 K, 300 K, 350 K, 400 K, and 450 K ($N_{\text{sample}} = 10^6$). 59

5.3 First eight central moments (in eV) of the HOMO-LUMO gap distributions in TADF (**R**)-**1** at 275 K, 300 K, 325 K, 350 K, and 375 K ($N_{\text{sample}} = 10^6$). 61

5.4 First eight central moments (in eV) of the HOMO-LUMO gap distributions in CDN1163 at 280 K, 290 K, 300 K, 310 K, and 320 K ($N_{\text{sample}} = 10^6$). 67

6.1 **Approximate chemical formula of CdSe, CdS, CdTe, and PbS nanoparticle systems in this study**. All volumes are in nm^3. 76

6.2 **System parameters used to calculate properties of nanoparticles. [250, 251]** ε is the dielectric screening constant of the material, m_e is the effective mass of the electron, m_h is the effective mass of the hole, and m_0 is the mass of a free electron. η is the composite material parameter that depends on ε and the reduced mass of the electron-hole pair. 76

7.1 **System parameters used to calculate properties of NPs. ε is the dielectric constant of the material, m_e is the effective mass of the electron, m_h is the effective mass of the hole, and m_0 is the mass of a free electron.** . . . 91

7.2 **Exciton Bohr radii of the three different perovskite systems, and their respective exciton Rydberg energies. Calculated exciton binding energies for $D = 5$ nm spherical NPs are included for comparison.** 96

8.1 Comparison of $Cd_{20}Se_{19}$ optical properties calculated by ESP and Hartree Fock method (cc-pVDZ basis). 106

List of Figures

1.1 (a) Three different allotropes of carbon: diamond, graphene, and amorphous [1]. (b) A simplified depiction of bromomethane reacting with hydroxide anion to form methanol. (c) Conformation energy as a function of dihedral angle in butane [2]. . . . 1

1.2 Simplified diagram of the functional dependence of molecular orbitals on the effective electron-electron interaction. . . . 3

1.3 Graphical depiction of how a distribution of structures corresponds to a distribution of quantum mechanical properties. . . . 5

1.4 Random normal distributions ($\mu = 0.0$, $\sigma = 1.0$) with (a) 10^2, (b) 10^3, (c) 10^4, and (d) 10^6 sampling points. 6

1.5 Overview of the process for obtaining the temperature-dependent distribution of a quantum mechanical property of interest. . . . 6

2.1 **Left:** Probability distribution function and **Right:** the corresponding cumulative distribution function. . . . 9

2.2 Normal distributions with different means and standard deviations. . . . 10

2.3 Comparison of Boltzmann population distributions at 200K and 400K. . . . 15

3.1 Representation of how random noise in the nuclear coordinates of a molecule correspond to a probability distribution of quantum mechanical properties (in this case, total ground state energy). As the magnitude of the random noise increases, the form of the probability distribution changes. . . . 17

3.2 H_2O population distributions at difference noise levels for **Top Left**: Total ground-state energy, **Top Right**: Nuclear repulsion energy, **Bottom Left**: MP2 correlation energy, and **Bottom Right**: HOMO-LUMO gap energy. All energies in hartrees. 21
3.3 NH_3 population distributions at difference noise levels for **Top Left**: Total ground-state energy, **Top Right**: Nuclear repulsion energy, **Bottom Left**: MP2 correlation energy, and **Bottom Right**: HOMO-LUMO gap energy. All energies in hartrees. 22
3.4 CH_4 population distributions at difference noise levels for **Top Left**: Total ground-state energy, **Top Right**: Nuclear repulsion energy, **Bottom Left**: MP2 correlation energy, and **Bottom Right**: HOMO-LUMO gap energy. All energies in hartrees. 23
3.5 Benzene population distributions at difference noise levels for **Top Left**: Total ground-state energy, **Top Right**: Nuclear repulsion energy, **Bottom Left**: MP2 correlation energy, and **Bottom Right**: HOMO-LUMO gap energy. All energies in hartrees. 24
3.6 C_{60} population distributions at difference noise levels for **Top Left**: Total ground-state energy, **Top Right**: Nuclear repulsion energy, **Bottom Left**: MP2 correlation energy, and **Bottom Right**: HOMO-LUMO gap energy. All energies in hartrees. 25
3.7 Population distribution of the first ten CIS oscillator strengths (a.u.) for 1,000 deformed H_2O structures at $\eta = 0.1$ bohr. Numbered arrows indicate which CIS root the distribution correspond to. 26
3.8 Effective temperatures for H_2O at $\eta = 0.1, 0.05, 0.075$, and 0.1 bohr calculated by fitting total energy population distributions to Boltzmann distributions. 27
3.9 Scatter plots of how the standard deviations (relative to the standard deviation of the nuclear repulsion energies for the same noise level) of each calculated distribution change with increasing noise. Data shown for H_2O, NH_3, CH_4, benzene, and C_{60}. 28

4.1 Conceptual diagram of how the Effective Stochastic Potential method corresponds to the chemical environment of a system at a given temperature. 32
4.2 Comparison of HOMO-LUMO gap energy Z-scores of a single gas-phase water molecule between Hartree Fock (cc-pVDZ basis) and ESP method. 42
4.3 HOMO-LUMO gap Z-scores for a $Cd_{20}Se_{19}$ quantum dot at $T = 300$K. 44

5.1 Example of histogrammed total ground state energies (in units of K) relative to the minimum energy structure for a sample population of 1,000 structures of H_2O at 300K. 51
5.2 Example of how solvent can effect the ensemble of thermally-accessible structures at a given temperature. 51

5.3 Benchmark comparisons of probability distributions of the $S_0 \rightarrow S_1$ vertical excitation energies of H_2O (6-31G basis) calculated using CIS and ESP-CIS ($N_{\text{sample}} = 10^4$), at 300K. Dashed line correspond to the excitation energy of the energy-minimum H_2O structure. 53
5.4 Probability distributions and cumulative distributions for the lowest ESP-CIS excitation energies (in eV) of Pb_4S_4, $Pb_{28}S_{28}$, and $Pb_{43}S_{43}$ at 200 K, 250 K, 300 K, 350 K, and 400 K ($N_{\text{sample}} = 10^6$). Vertical dashed lines indicate the respective lowest CIS excitation energies of the energy-minimized reference systems. . . 53
5.5 Effect of temperature on (a) mean and modes, (b) standard deviations (σ), and (c) ranges (all in eV) of excitation energies for Pb_4S_4, $Pb_{28}S_{28}$, and $Pb_{43}S_{43}$ NPs from 200 K to 400 K using 10^6 ESP-CIS samples using the LANL2DZ-ECP basis set and effective core potentials. 54
5.6 (a) Skewness and (b) Kurtosis of ESP-CIS excitation energies (in eV) of Pb_4S_4, $Pb_{28}S_{28}$, and $Pb_{43}S_{43}$ at 200 K, 250 K, 300 K, 350 K, and 400 K calculated with ESP-CIS ($N_{\text{sample}} = 10^6$) using the LANL2DZ-ECP basis set and effective core potentials. 55
5.7 Comparison of timing data in days (left y-axis, log-scale) and seconds (right y-axis, log scale) for Pb_4S_4, $Pb_{28}S_{28}$, and $Pb_{43}S_{43}$ NPs using CIS vs. ESP-CIS. Timing shown is for ($N_{\text{sample}} = 10^6$) ESP-CIS calculations, and an approximate projection of the timing for ($N_{\text{sample}} = 10^6$) CIS calculations using the LANL2DZ-ECP basis set and effective core potentials. 55
5.8 A comparison of excitation energy (eV) distributions obtained for $Pb_{43}S_{43}$ at 300 K using ESP-CIS with (a) $N_{\text{sample}} = 10^2$, (b) $N_{\text{sample}} = 10^3$, (c) $N_{\text{sample}} = 10^4$, and (d) $N_{\text{sample}} = 10^6$. 56
5.9 Solid-state structure of TKX-50 at 100K. 57
5.10 Probability distributions and cumulative distributions for the ESP HOMO-LUMO gaps (in eV) of TKX-50 at 250 K, 300 K, 350 K, 400 K, and 450 K ($N_{\text{sample}} = 10^6$). Vertical dashed lines indicate the respective HOMO-LUMO gap of the energy-minimized reference system. 58
5.11 Mean ESP HOMO-LUMO gap energies (in eV) in TKX-50 at 250 K, 300 K, 350 K, 400 K, and 450 K. Error bars correspond to one standard deviation from the mean. 58
5.12 Probability distributions for the first 15 ESP-CIS excitation energies (in eV) of TKX-50 at 250 K, 300 K, 350 K, 400 K, and 450 K ($N_{\text{sample}} = 10^6$). 59
5.13 Schematic depiction of a general reverse-intersystem crossing process. 60
5.14 Structure of the (**R**)-**1** CPL-TADF emitter. The chiral perturbing unit is in the highlighted box. Molecule modeled in Avogadro [150]. 60
5.15 Probability distributions and cumulative distributions for the ESP HOMO-LUMO gaps (in eV) of TADF (**R**)-**1** at 275 K, 300 K, 325 K, 350 K, and 375 K ($N_{\text{sample}} = 10^6$). Vertical dashed lines indicate the respective HOMO-LUMO gap of the energy-minimized reference system. 61

5.16 Mean ESP HOMO-LUMO gap energies (in eV) in TADF (**R**)-**1** at 275 K, 300 K, 325 K, 350 K, and 375 K. Error bars correspond to one standard deviation from the mean. 62
5.17 Probability distributions for the first 15 ESP-CIS excitation energies (in eV) of TADF **R**)-**1** at 275 K, 300 K, 325 K, 350 K, and 375 K ($N_{\text{sample}} = 10^6$). 63
5.18 **Left**: MI-1061 molecule bound to MDM2 protein. **Right**: PROTAC MD-224 molecule. 64
5.19 Probability distributions and cumulative distributions for the ESP HOMO-LUMO gaps (in eV) of MD-224 at 280 K, 290 K, 300 K, 310 K, and 320 K ($N_{\text{sample}} = 10^6$). Vertical dashed lines indicate the respective HOMO-LUMO gap of the energy-minimized reference system. 64
5.20 Probability distributions for the first three ESP-CIS excitation energies (in eV) of MD-224 at 280 K, 290 K, 300 K, 310 K, and 320 K ($N_{\text{sample}} = 10^6$). Vertical lines correspond to theline spectra of the minimum energy reference structure. 65
5.21 **Left**: SERCA protein in the Ca^{2+}/ATP bound state. **Right**: CDN1163 molecule. 66
5.22 Probability distributions and cumulative distributions for the ESP HOMO-LUMO gaps (in eV) of CDN1163 at 280 K, 290 K, 300 K, 310 K, and 320 K ($N_{\text{sample}} = 10^6$). Vertical dashed lines indicate the respective HOMO-LUMO gap of the energy-minimized reference system. 67
5.23 Mean ESP HOMO-LUMO gap energies (in eV) in CDN1163 at 280 K, 290 K, 300 K, 310 K, and 320 K. Error bars correspond to one standard deviation from the mean. 68
5.24 Probability distributions for the first 10 ESP-CIS excitation energies (in eV) of CDN1163 at 280 K, 290 K, 300 K, 310 K, and 320 K ($N_{\text{sample}} = 10^6$). Vertical lines correspond to theline spectra of the minimum energy reference structure. 69

6.1 Pictorial diagram of the difference between how electronic excitation is represented in the many-electron picture and in the electron-hole picture. 71
6.2 Graphical representation of the difference between two real electrons interacting and a quasi-electron interaction with a quasi-hole. 71
6.3 A representative ellipsoid showing the A, B, and C semi-axes. The nanoparticles in this investigation are ellipsoids with semi-axis lengths constructed so that there are three sets of differently shaped NPs of equal volume. Nanorods are constructed to have length equal to eight times their diameter, and nanodisks are constructed to have diameter equal to eight times their thickness. 73
6.4 Exciton binding energies (in meV) of CdSe, CdS, CdTe, and PbS nanoparticle spheres, disks, and rods. Experimental results for CdSe nanospheres provided for comparison. Dashed lines correspond to the exciton Rydberg energy (in meV) for each material. 77

6.5 Material parameter η vs. exciton binding energy. Data points are grouped into four sets, each corresponding to the labeled material type with volumes of $V = 524$ nm^3. 78
6.6 Electron hole recombination probabilities of CdSe, CdS, CdTe, and PbS nanoparticle spheres, disks, and rods. P_{eh} is presented relative to a referenced P^0_{eh} with $P^0_{\text{eh}} = 2.9945 \times 10^{-18}$). 79
6.7 Material parameter η vs. electron-hole recombination probability. Data points are grouped into four sets, each corresponding to the labelled material type with volumes of $V = 524$ nm^3. P_{eh} is presented relative to a referenced P^0_{eh} with $P^0_{\text{eh}} = 2.9945 \times 10^{-18}$). 80
6.8 Electron-hole separation distance of CdSe, CdS, CdTe, and PbS nanoparticle spheres, disks, and rods. The separation distance increases as both nanoparticle size and anisotropy increases. Dashed lines correspond to the exciton Bohr radius (in nm) for each material. 81
6.9 The entire set of calculated results for each nanoparticle studied. Spheres, disks, and rods were studied at volumes of 524, 1437, and 4189 nm^3. CdSe, CdS, CdTe, and PbS nanoparticles were investigated at these morphologies, and exciton binding energy (E_{EB}), electron hole recombination probability (P_{eh}), and electron hole separation distance ($\langle r_{\text{eh}} \rangle$) were all calculated using eh-XCHF. P_{eh} is presented relative to probabilty $P^0_{\text{eh}} = 2.9945 \times 10^{-18}$. 82
6.10 **Top**: Nanoparticle volume V vs. $A(V)_{\text{RMSD}}$ for both $A = E_{\text{EB}}$ (left) and $A = P_{\text{eh}}$ (right). **Bottom**: Nanoparticle material type M vs. $A(M)_{\text{RMSD}}$ for both $A = E_{\text{EB}}$ (left) and $A = P_{\text{eh}}$ (right). 82
6.11 Exciton binding energy vs. recombination probability in CdSe, CdS, CdTe, and PbS nanoparticles. Data includes nanoparticles of all shapes, sizes, and compositions investigated. 83
6.12 Surface plot (a) and contour plot (b) of CdSe nanoparticle A and B semi axis lengths vs. exciton binding energy. Representative ellipsoids are placed over the surface plot for reference. 84
6.13 Surface plot (a) and contour plot (b) of nanoparticle A and B semi-axis lengths vs. electron-hole separation distance. 85
6.14 Surface plot (a) and contour plot (b) of nanoparticle A and B semi axis lengths vs. relative electron-hole recombination probability. 86
6.15 Exciton binding energy vs. recombination probability for 900 ellipsoidal isovolumetric CdSe nanoparticles. 86
6.16 Exciton binding energy vs. $\langle r_{\text{eh}} \rangle^{-1}$ in CdSe ellipsoids. The linear relationship between exciton binding energy and $\langle r_{\text{eh}} \rangle^{-1}$ is readily apparent. The red line is a linear fit with the form $f(x) = 321$ meV(x), and has a correlation coefficient [255] $R^2 = 0.9997$, max deviation = 2.140, average signed deviation = 0.03909, average unsigned deviation = 0.4510. 87

7.1 Electron hole separation distance vs. NP radius for $CsPbCl_3$ ($y = 0.5145x, R^2 = 0.9675$), $CsPbBr_3$ ($y = 0.5263x, R^2 = 0.9797$), and $CsPbI_3$ NPs ($y = 0.5195x, R^2 = 0.9763$). 93

7.2 Exciton binding energy vs. NP radius for $CsPbCl_3$ ($y = 12.284x^{-5.713}, R^2 = 0.993$), $CsPbBr_3$ ($y = 14.522x^{-6.004}, R^2 = 0.9973$), and $CsPbI_3$ ($y = 97.187x^{-6.938}, R^2 = 0.992$) NPs. 94

7.3 Electron hole recombination probability vs. NP radius for $CsPbCl_3$ ($y = 798.48x^{-0.949}, R^2 = 0.9907$), $CsPbBr_3$ ($y = 666.89x^{-0.98}, R^2 = 0.9955$), and $CsPbI_3$ ($y = 466.33x^{-0.884}, R^2 = 0.9786$) NPs. 95

7.4 Exciton binding energy vs. inverse electron hole separation distance for $CsPbCl_3$ ($y = 444.1x, R^2 = 0.9962$), $CsPbBr_3$ ($y = 363.53x, R^2 = 0.9985$), and $CsPbI_3$ ($y = 286.26x, R^2 = 0.9454$) NPs. 96

7.5 Electron hole recombination probability vs. inverse electron hole separation distance for $CsPbCl_3$ ($y = 0.3388x^{5.9377}, R^2 = 0.9926$), $CsPbBr_3$ ($y = 0.3575x^{6.128}, R^2 = 0.9957$), and $CsPbI_3$ ($y = 2.16x^{7.710}, R^2 = 0.9752$) NPs. 97

8.1 Flowchart of exciton binding energy calculation. 104

8.2 HOMO-LUMO gap energy scaling of $Cd_{20}Se_{19}$ quantum dot ($m = -0.0068, R^2 = 0.745$) with respect to temperature. Temperature scaling results of $Cd_{33}Se_{33}$ as calculated by Prezdo and coworkers for comparison ($m = -0.25$, $R^2 = 0.966$). 106

8.3 HOMO-LUMO gap Z-scores for a $Cd_{20}Se_{19}$ quantum dot at $T = 300$K. 107

8.4 Exciton binding energy Z-scores for a $Cd_{20}Se_{19}$ quantum dot at $T = 300$K. 108

8.5 Exciton binding energy (in eV) distributions of a thermalized $Cd_{20}Se_{19}$ QD calculated using ESP method at T=300K. 108

Chapter 1

Scope: The Structure-Property Relationship in Quantum Chemistry

The Role of Structure in Quantum Chemistry

Chemical structure is foundational to the entire field of chemistry. Structure informs much of how we understand and conceptualize the properties of materials and how they react. The importance of chemical structure is so broad, it can be seen in areas of chemistry such as conformational isomers, crystal polymorphs, and transition-state theory.

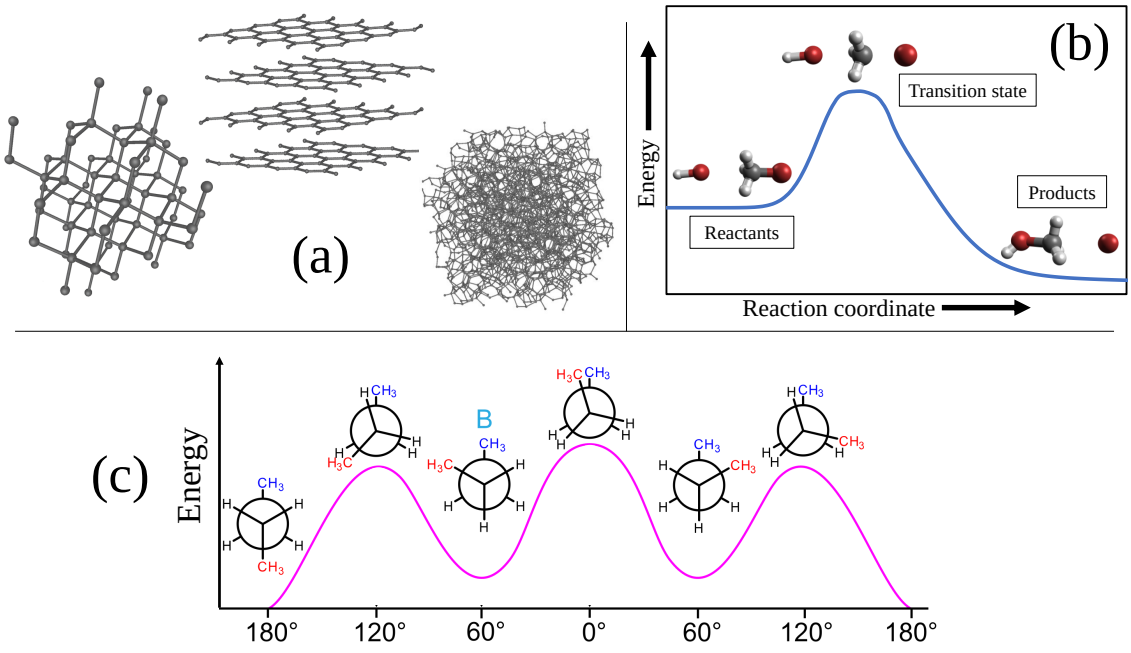

Figure 1.1: (a) Three different allotropes of carbon: diamond, graphene, and amorphous [1]. (b) A simplified depiction of bromomethane reacting with hydroxide anion to form methanol. (c) Conformation energy as a function of dihedral angle in butane [2].

Figure 1.1 shows a few of these examples in more detail. In panel (a) three different allotropes of elemental carbon are shown (diamond, graphene, and amorphous/coal). Changing how the carbon atoms are arranged with respect to one another results in materials with vastly different physical and chemical properties. In panel (b), a simple

representation of the energetics of bromomethane reacting with hydroxide anion to form methanol is shown. The reaction coordinate is an abstraction of the relative positions of all the atoms during the course of the reaction, and the existence of a transition state as pictured can have a significant impact on the reaction kinetics. Finally, in panel (c), the conformation energy as a function of dihedral angle in butane is plotted. The proximity of the atoms to one another has a large effect on which conformations are energetically favorable.

The relationship between structure and property is immediately apparent in quantum chemistry through the electronic Schrödinger Equation (Equation 1.1):

$$H_{\text{elec}}\Phi_{\text{elec}} = E_{\text{elec}}\Phi_{\text{elec}} \tag{1.1}$$

where H_{elec} is the electronic Hamiltonian and Φ_{elec} is the electronic wave function. Under the Born-Oppenheimer approximation, Φ_{elec} has only a parametric dependence on the coordinates of all nuclei in the system, $\mathbf{R}$ (Equation 1.2):

$$\Phi_{\text{elec}} = \Phi_{\text{elec}}\left(\{\mathbf{r}\};\{\mathbf{R}\}\right). \tag{1.2}$$

However, the positions of the nuclei still have a major role in the electronic properties of the system. To demonstrate this, consider a general many-electron system, which typically requires an effective one-electron Hamiltonian as a starting point, as in the Hartree-Fock (HF) approximation or in density functional theory (DFT). Such an effective one-election Hamiltonian $h(\mathbf{r})$ has the form seen in Equation 1.3:

$$h(\mathbf{r}) = \frac{-\hbar^2}{2m}\nabla^2 + v_{\text{ext}}(\mathbf{r}) + v_{\text{eff}}(\mathbf{r}), \tag{1.3}$$

where $\frac{-\hbar^2}{2m}\nabla^2$ is the kinetic energy of the electron, $v_{\text{ext}}(\mathbf{r})$ is the interaction of the electron with the external potential field, and $v_{\text{eff}}(\mathbf{r})$ is the effective interaction with all other electrons in the system. The problem of generating the molecular orbitals of the system then reduces to solving the pseudo-eigenvalue equation in Equation 1.4

$$h_i\chi_i = \varepsilon_i\chi_i, \tag{1.4}$$

where h_i is the effective one-electron Hamiltonian for an arbitrary electron i, χ_i is the molecular orbital of that electron, and ε_i is the energy of that molecular orbital. This pseudo-eigenvalue problem can be solved through a mean-field approximation, also known as a self-consistent field (SCF) procedure, in which each electron interacts with the average field of all other remaining electrons [3]. The SCF procedure can be summarized as the process of first defining a

guess Hamiltonian (Equation 1.5):

$$\mathbf{h}^{\text{core/Hückel}}[\mathbf{R}], \tag{1.5}$$

then diagonalizing to calculate guess molecular orbitals (Equation 1.6):

$$\mathbf{h}^{\text{core/Hückel}}\chi_i = \varepsilon_i\chi_i[\mathbf{R}]. \tag{1.6}$$

The electron density of the resulting guess orbitals in Equation 1.6 can be used to construct a guess for the effective electron-electron (e-e) interaction potential. In this way, the self-consistent determination of the effective e-e interaction potential makes it a functional of the nuclear coordinates, as shown in Figure 1.2. The key point to this

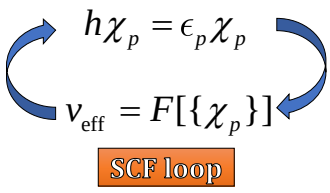

Figure 1.2: Simplified diagram of the functional dependence of molecular orbitals on the effective electron-electron interaction.

discussion is that the nuclear coordinates of a chemical system and its environment have a profound effect on the system's observable electronic properties.

The Effect of Temperature and Chemical Environment on Structure

The connection between a system's structure and its chemical environment is one of the central concepts in chemical thermodynamics. Specifically, in the case of a canonical ensemble, the population of various chemical structures ($\mathbf{R}$) depends on the temperature of the system, as given by Boltzmann statistics [4]. Consequently, all of the quantum mechanical (QM) properties (X) of a chemical system at thermal equilibrium are determined not by its singular minimum-energy structure, but by an ensemble of conformations which are mapped by the electronic Schrödinger equation (Equation 1.1).

Generation, evaluation, and analysis of the statistical distribution of QM properties is crucial for the description and prediction of temperature-dependent phenomena. For example, atomic motion due to temperature and solvent interaction is one of the primary sources of spectral line broadening in electronic spectra [5, 6, 7]. In computational studies of spectra, this temperature effect is often approximated as a post-processing step by fitting the 0K line spectrum to a temperature-dependent Lorentzian or Gaussian function [8]. However, this approach is completely empirical,

and is often a poor representation of the true finite-temperature spectra for many chemical systems. [9, 10, 11].

Specific examples of the relationship between temperature, structure, and property in chemistry are as broad as there are molecules to investigate. One example where the computational cost of treating this temperature-structure connection is especially demanding is in the area of crystal structure prediction (CSP). The arrangement of organic molecules in a lattice can have a significant impact on the properties of the crystal. In the pharmaceutical industry, different crystal polymorphs can exhibit very different solubilities and, correspondingly, bioavailabilities [12, 13, 14]. In CSP, the free energies of various configurations of a crystal lattice are calculated and ranked in order to identify likely polymorphs at the temperature of interest [15]. The computational challenges of performing CSP for pharmaceutical applications are multifaceted [14, 13, 16]. In summary, these include:

1. The huge search space of potentially viable crystal structures,
2. Wide varieties of intermolecular forces at play that must be properly treated,
3. Small energy differences between possible polymorphs, and
4. Molecular conformations which depend strongly on how electron correlation is treated.

Calculation of free energies in CSP involves accounting for the thermal expansion that the lattice undergoes at finite temperature. This thermal expansion of pharmaceutical crystals is a result of changes to various intermolecular forces, such as hydrogen and halogen bonding, $\pi - \pi$ stacking, van der Waals forces, and covalent bonding [17]. Since the interactions between organic molecules are relatively weak, the structure of a given crystal can expand significantly between 0 K and room temperature, leading to significant thermal effects. The lattice-energy minimum found at higher temperatures is often substantially different from the ones found at lower temperatures [18], resulting in major shifts to the ensemble of structures. Various approaches for treating the effect of temperature in CSP have been employed, including semi-empirical incorporation of thermal pressures or quasi-harmonic approximations in the model [19, 20]. However, thermal expansion of the lattice is often neglected entirely, and static lattice energies are ranked instead of the temperature-dependent free energies for CSP.

A number of computational methods exist for treating the effects of temperature on QM properties. Ab-initio molecular dynamics (AIMD) is one such first-principles technique, in which the structure of the system is able to change over time due to interaction with a thermostat and solvent [21]. Mixed quantum-classical dynamics (MQCD) is another technique for treating chemical dynamics in which an equilibrium trajectory of the system is obtained from classical mechanics, and QM calculations are performed on structures sampled from the trajectory [22]. The classical trajectory allows for simulation of longer time scales on larger systems than AIMD. However, regardless of how the dynamics of the system is treated, neither is able to overcome the computational barrier of performing the necessary sampling of structures at thermal equilibrium.

The Importance of Performing Sufficient Conformational Sampling

The procedure to obtain distributions of QM properties from an ensemble of structures appears at first glance to be simple from Figure 1.3: sample from the distribution of thermally-accessible structures and solve the electronic Schrödinger equation for each one to get the distributions of properties of interest.

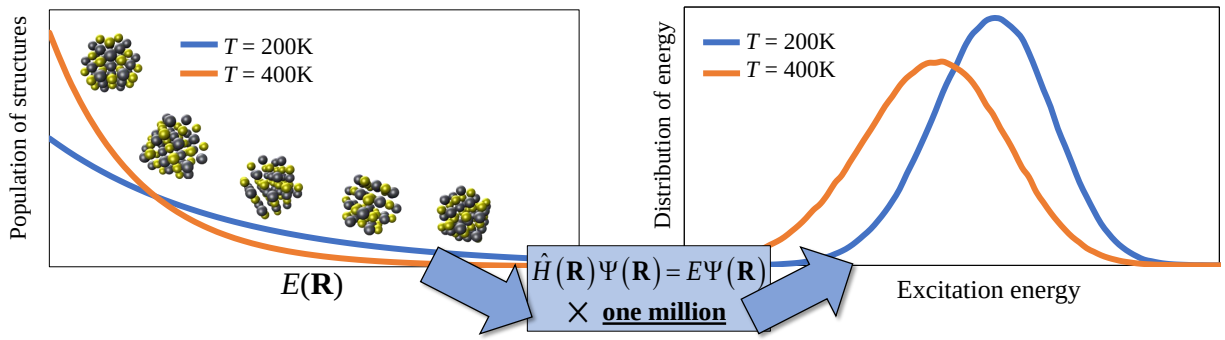

Figure 1.3: Graphical depiction of how a distribution of structures corresponds to a distribution of quantum mechanical properties.

Immediately, however, a computational hurdle is reached for nearly all chemical systems of interest; in order to obtain accurate distributions of QM properties, sampling must be performed on the order of 10^5 - 10^6 conformations [23, 24]. For nearly any chemical system, it is computationally infeasible to solve the Schrödinger equation such a large number of times.

This requirement of sampling so many times is not a characteristic that is unique to quantum mechanics or physical systems in general. In Figure 1.4, a random normal variable with a mean of 0.0 and standard deviation of 1.0 has been sampled an increasing number of times, starting from one hundred all the way up to one million. Here, the value of the random variable is on the x-axes, and the probability of obtaining that value of the variable is on the y-axes. It can be seen that, for smaller values of N_{sample}, the sampled distributions look nothing like what the true population of the normal distribution should look like. It is not until $N_{\text{sample}} = 10^6$ in panel (d) of **??** that the distribution begins to look indistinguishable from a normal distribution with $\mu = 0.0$ and $\sigma = 1.0$.

In order to make reliable and quantitatively accurate predictions about the temperature and solvent-dependent excited state properties of chemical systems, the following computational conditions should be satisfied: (1) The chemical structures being sampled correspond to the ab-initio equilibrium trajectory, (2) the population of sampled conformations are a good representation of the entire configuration space of the equilibrium system, and (3) the excited electronic states of the population are treated from first principles. The difficulty in satisfying all three of these conditions is the tremendous computational cost incurred. In order to be confident of obtaining ensemble-averaged properties to within chemical accuracy ($\approx$ 0.003 eV [3]), sampling must be performed on the order of at least 10^5 thermally-accessible structures [23, 24].

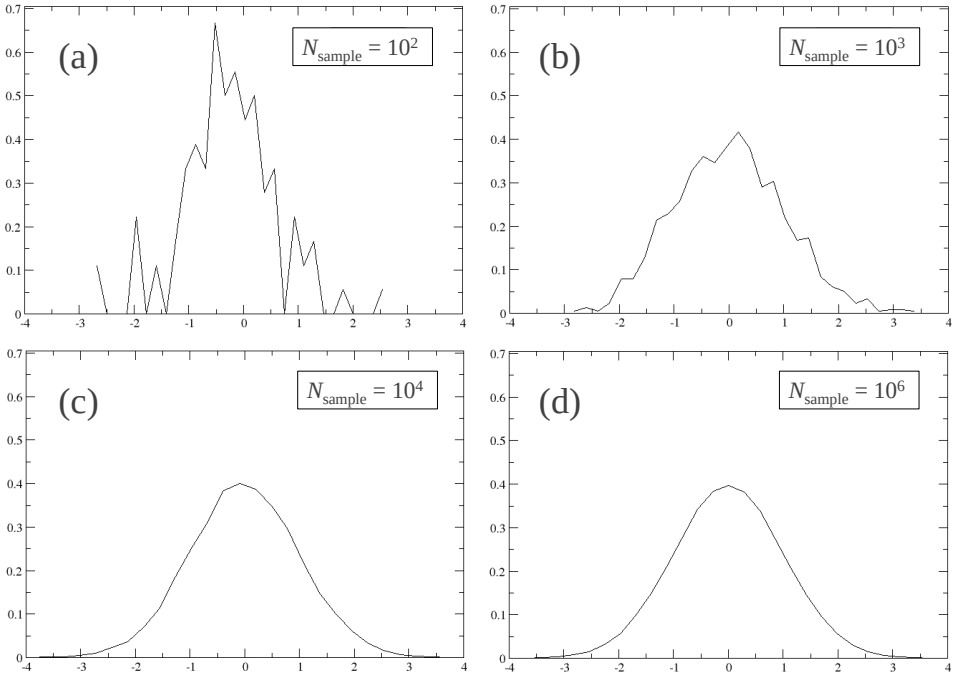

Figure 1.4: Random normal distributions ($\mu = 0.0$, $\sigma = 1.0$) with (a) 10^2, (b) 10^3, (c) 10^4, and (d) 10^6 sampling points.

While semi-empirical excited-state methods such time dependent density functional tight binding (TD-DFTB) [25] can be used in conjunction with AIMD or MCQD methods to perform the necessary conformational sampling over thermally-accessible structures, the QM results for the population are no longer obtained from first-principles.

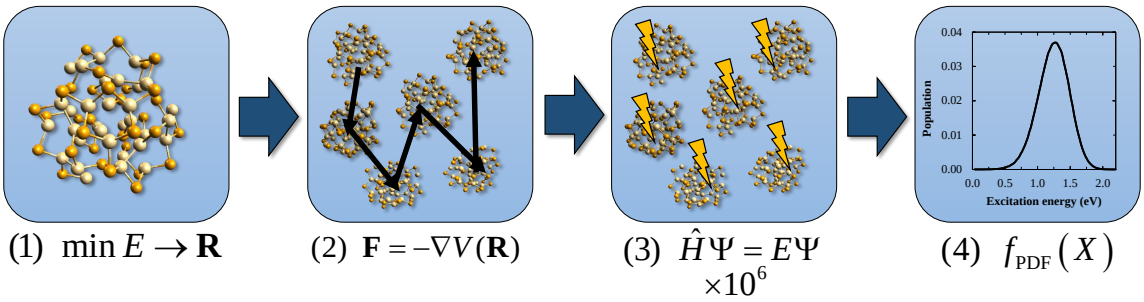

Figure 1.5: Overview of the process for obtaining the temperature-dependent distribution of a quantum mechanical property of interest.

Figure 1.5 shows the general process of how a temperature-dependent distribution of a QM property of interest can be obtained (in this case, excitation energy). In step one, an energy-minimum structure is obtained from a geometry optimization. In step two, a dynamics simulation at the temperature of interest is performed, generating hundreds of thousands of ensemble structures. This can be done using classical MD or AIMD. In the third step, structures from that trajectory are sampled to perform ab-initio QM calculations on. This must be done 10^5 to 10^6 times in order

to reliably and accurately resolve the distribution. In the last step, the data is collected and analyzed to generate the probability distribution of excitation energies.

In this work, I have developed a method, called the Effective Stochastic Potential (ESP) for alleviating the computational cost of the third step in the process outlined in Figure 1.5. The chapters that follow introduce methods for overcoming these challenges related to sampling and treating the effect of structure on chemical systems. In Chapter 2, a mathematical overview of the necessary probability theory and statistical mechanics for the method is presented. Chapter 3 provides insight into the effect of random noise in nuclear coordinates on electronic properties. In Chapter 4 I introduce the details of the ESP which has been developed for addressing the challenge of conformational sampling. In Chapter 5 I introduce an extension of the ESP method to treat electronically excited state properties. Chapter 6 is an investigation of isovolumetric deformation of semiconductor nanoparticles using the electron-hole explicitly correlated Hartree-Fock (eh-XCHF) method. Chapter 7 is an investigation of cesium lead halide nanoparticles using the electron-hole explicitly correlated Hartree-Fock (eh-XCHF) method. Chapter 8 discusses how the ESP and eh-XCHF method can be integrated to investigate temperature-dependent exciton properties in nanoparticles. Finally, Chapter 9 contains some concluding remarks on these studies, and proposes some fruitful directions this work can be progressed in the future.

Chapter 2

Background: Probability Theory and Statistical Mechanics

Statistical Distributions

Random Variables

Quantum mechanics is fundamentally a statistical theory, and particles behaving quantum mechanically, by their very nature, exhibit random behavior. For this reason, it will be beneficial to briefly cover some concepts from probability theory concerning randomness and distributions of random variables.

In probability and statistics, a random (or stochastic) variable can be described as a variable whose values depend on random outcomes [26]. Random variables are defined on some probability space, which describes the probability of the variable assuming any given value. Generating all of the possible probabilities that a random variable X can assume yields the probability distribution of X. A probability distribution function (PDF) is a mathematical representation of the relative probabilities of all the possible outcomes of a random variable.

Probability Distribution Functions

A continuous probability distribution (one which corresponds to a real random variable and that is differentiable everywhere) can be described by a PDF. While the probability that a random variable can assumes any specific value is exactly zero, a PDF can give the relative probabilities in which the random variable may exist [26]. If x in a continuous random variable, then it has a probability density function $f(x)$ which gives the probability for falling between an interval $[a,b]$ by the integral Equation 2.1

$$\mathrm{P}\left[a \leq X \leq b\right] = \int_a^b f(x)dx. \tag{2.1}$$

From this relationship, we find that the PDF for x has the property given in Equation 2.2

$$\int_{-\infty}^{\infty} f(x)dx = 1, \tag{2.2}$$

which is equivalent to the statement that a random variable x always has *some* real value.

A cumulative distribution function (CDF) is a function that gives the probability that a random variable x can take a value less than or equal to some number. Equivalently, it returns the area under the curve for a corresponding probability density function from $-\infty$ to some value x. An example of how the CDF relates to a corresponding PDF is shown in Figure 2.1. The CDF of a continuous random variable X can be expressed as (Equation 2.3)

$$F_X(x) = \mathrm{P}[X \leq x]. \tag{2.3}$$

Integrating a PDF f from $-\infty$ to a gives the probability that a random variable x is less than or equal to a, or

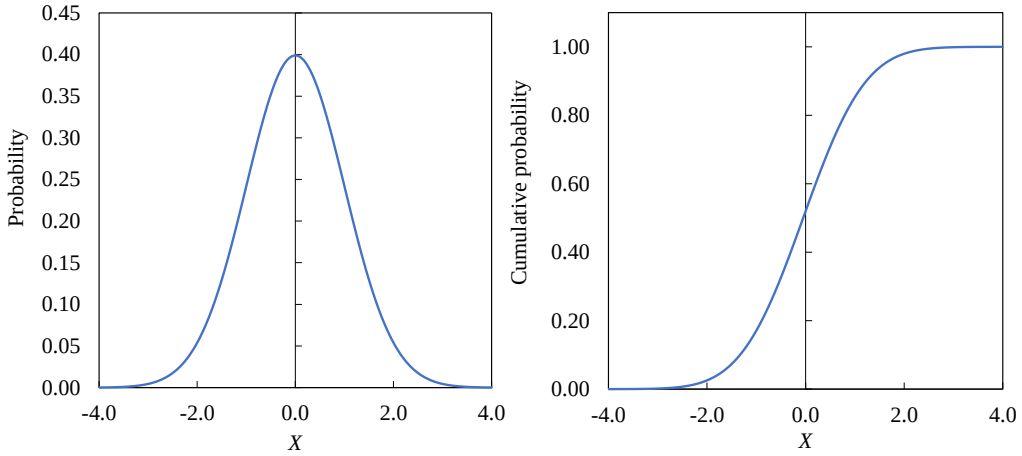

Figure 2.1: **Left:** Probability distribution function and **Right:** the corresponding cumulative distribution function.

equivalently, gives the value of the corresponding CDF F_X as shown in Equation 2.4:

$$F_X(a) = \int_{-\infty}^{a} f(x)dx. \tag{2.4}$$

For continuous CDFs, the PDF is equal to the derivative of the CDF (Equation 2.5:

$$\frac{d}{dx}F(x) = f(x). \tag{2.5}$$

Normal Distributions

The normal distribution is a commonly encountered continuous probability distribution. Measured physical quantities which are the sum of many independent processes often have normal, or approximately normal distributions [26]. The normal distribution is useful because of the central limit theorem, which states that the average values obtained from samples of random variables that are independently drawn from the same PDF become normally distributed when the number of samples drawn tends towards infinity. The PDF of the normal distribution has the form shown in

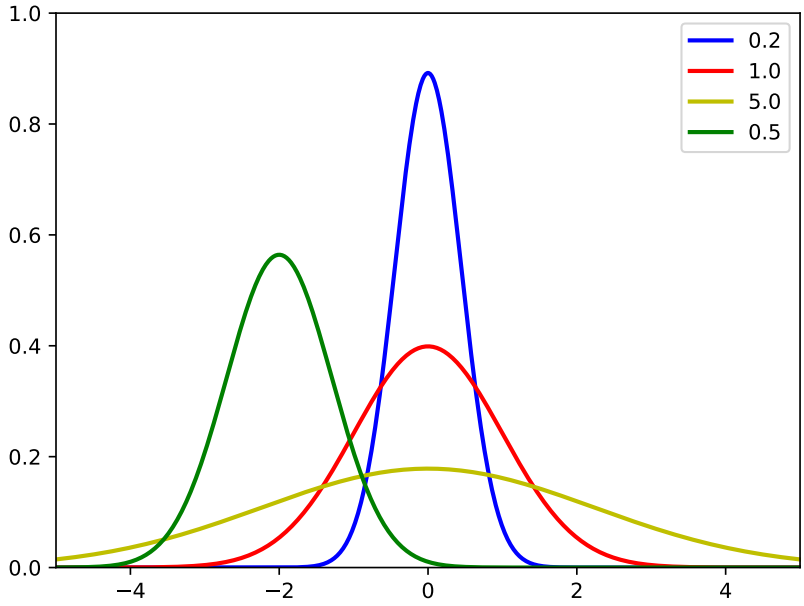

Figure 2.2: Normal distributions with different means and standard deviations.

Equation 2.6

$$f(x \mid \mu, \sigma^2) = \frac{1}{\sqrt{2\pi\sigma^2}} e^{-\frac{(x-\mu)^2}{2\sigma^2}}, \tag{2.6}$$

where μ is the mean and σ is the standard deviation of the PDF corresponding to the random normal variable. Various normal distributions with different values of μ and σ are shown in Figure 2.2. Random variables which are normally distributed can be represented by the notation given in Equation 2.7

$$X \sim \mathcal{N}\left(\mu, \sigma^2\right), \tag{2.7}$$

where μ and σ correspond to the PDF of X. The random normal distribution is convenient to use when applicable because of this known analytical form.

Expectation Values

The expectation value (also known as the expected value, mean, or first moment) of a random variable is a key element of its probability distribution [26]. A random variable's expectation value represents the average of a large number of independently sampled drawings of the random variable. If a random variable x is given ,and its distribution corresponds to a PDF f, then the expectation value can be calculated as the integral given in Equation 2.8:

$$\mathrm{E}[X] = \int_{-\infty}^{\infty} x\, f(x) dx. \tag{2.8}$$

In other words, each possible value the random variable can assume is multiplied by its probability of occurring, and the resulting products are summed to produce the expectation value. For a data set, the expectation value is equivalent to the arithmetic mean, or the central value of a discrete set of numbers. More specifically, it the sum of the values divided by the number of values. The arithmetic mean of a set of numbers x_1, x_2, ..., x_n is can be denoted by $\bar{x}\bar{x}$. If the data set is based on a series of observations obtained by sampling from a statistical population, the arithmetic mean is called the sample mean (denoted $\bar{x}\bar{x}$) to distinguish it from the mean of the underlying distribution, which is the population mean (denoted $\mu\mu$ or $\mu_x\mu_x$).

The population mean is a measure of the central tendency either of either a probability distribution or of the random variable characterized by that distribution. In the case of a discrete PDF of a random variable X, the population mean is equal to the sum over every possible value weighted by the probability of that value as computed in Equation 2.9:

$$\mu = \sum_{i=1}^{N} x_i p_i. \tag{2.9}$$

For a finite population, the population mean of a property is equal to the arithmetic mean of the given property while considering every member of the population. The sample can differ significantly from the population mean for small samples. The law of large numbers dictates that the larger the size of the sample, the more likely it is that the sample mean will be close to the population mean [26].

Statistical Metrics

Central Moments

In probability and statistics, a moment is a measure of a distribution's shape. A *central* moment is a moment of a probability distribution of a random variable about the random variable's mean. Central moments are the expected value

of a specified integer power of the deviation of the random variable from the mean [26] as shown in Equation 2.10

$$\mu_n = \mathrm{E}\left[(X - \mathrm{E}[X])^n\right] = \int_{-\infty}^{+\infty} (x-\mu)^n f(x). \tag{2.10}$$

The central moments form one set of values by which the properties of a PDF can be characterized. For example, central moments can be used to measure the asymmetry or the heaviness of the tails of a PDF. Central moments are used in preference to ordinary moments, computed in terms of deviations from the mean instead of from zero, because the higher-order central moments relate only to the spread and shape of the distribution, rather than also to its location.

Standard Scores

The standard score (or Z-score) is the signed fractional number of standard deviations by which the value of an observation or data point is above the mean value of what is being observed or measured [26]. This means that observed values above the mean of a data set have positive Z-scores, while values below the mean have negative Z-scores. Z-scores are useful metrics of distributions and observations of random variables, because they are dimensionless quantities. They are calculated by subtracting the population mean from an individual raw score and then dividing the difference by the population standard deviation, as shown in Equation 2.11

$$z = \frac{x - \mu}{\sigma}. \tag{2.11}$$

When the population mean and the population standard deviation are unknown, the Z-score may be calculated using instead the sample mean and sample standard deviation as estimates of the population values. In these cases, the z-score is calculated as in Equation 2.12

$$z = \frac{x - \bar{x}}{S}, \tag{2.12}$$

where $\bar{x}$ is the mean of the sample and S is the standard deviation of the sample.

Skewness and Kurtosis

Skewness is a measure of the asymmetry of the probability distribution of a random variable about its mean [26]. The skewness value can be positive or negative, or undefined. Mathematically, skewness is defined as in Equation 2.13,

$$\gamma_1 = \mathrm{E}\left[\left(\frac{X-\mu}{\sigma}\right)^3\right] = \frac{\mu_3}{\sigma^3} = \frac{\mathrm{E}\left[(X-\mu)^3\right]}{\left(\mathrm{E}\left[(X-\mu)^2\right]\right)^{3/2}} = \frac{\kappa_3}{\kappa_2^{3/2}}. \tag{2.13}$$

For a unimodal distribution (a distribution with one distinct peak or mode), negative skew commonly indicates that the tail of the distribution is on the left side of the distribution, and a positive skew indicates that the tail is on the right. For example, a skewness of zero means that the tails on both sides of the mean balance out overall. This is the case for a symmetric distribution, and can also be true for an asymmetric distribution where one tail is long and thin, and the other is short but fat.

Kurtosis is a measure of the "tailedness" of the probability distribution of a real-valued random variable [26], and is mathematically defined in Equation 2.14,

$$\text{Kurt}[X] = \text{E}\left[\left(\frac{X-\mu}{\sigma}\right)^4\right] = \frac{\text{E}[(X-\mu)^4]}{(\text{E}[(X-\mu)^2])^2} = \frac{\mu_4}{\sigma^4}. \tag{2.14}$$

Similar to skewness, the kurtosis of a distribution describes the shape of a probability distribution and, just as for skewness, there are different ways of quantifying it for a theoretical distribution and corresponding ways of estimating it from a sample from a population. The Kurtosis of a normal distribution is exactly 3. Distributions with a kurtosis less than 3 have fewer outliers than the normal distribution does.

Sampling

A random sample is a subset of data points chosen from a larger set, called a population [4]. Each data point is chosen randomly, with some probability of being chosen which is specific to the population at any stage during the sampling process. Sampling is performed on a statistical population in order to estimate characteristics of the whole population. Data points are drawn from a sample, rather than the entire population, when the entire population is too large to feasibly measure a characteristic of interest from the entire set. Monte Carlo methods or simulations are a class of computational algorithms that utilize random sampling to obtain numerical results [4]. The underlying motivation of Monte Carlo methods is to use randomness to solve problems that may be deterministic in principle. They are often used in physical and mathematical problems and are most useful when it is difficult or impossible to use other approaches.

The standard deviation of a random variable or probability distribution is the square root of its variance, the second-order central moment of a sample [4], and is given by Equation 2.15:

$$s = \sqrt{\frac{1}{N-1}\sum_{i=1}^{N}(x_i-\bar{x})^2}. \tag{2.15}$$

Standard deviation is a measure of how spread out the data of a sample is. A useful property of the standard deviation is that, unlike the variance, it has the same units as the data being sampled from. For this reason, in addition to expressing the spread of a sample, the standard deviation is commonly used to measure confidence in statistical

results. This derivation of the standard deviation is often called the "standard error" of the estimate or "standard error of the mean" when referring to a mean [4].

The sample distribution of means of a population is generated by repeatedly sampling and calculating mean values. This forms a distribution of different means, and this distribution has its own mean and variance. The relationship between the standard error and the standard deviation is such that, for a given sample size, the standard error is equal to the standard deviation divided by the square root of the sample size (the number of times sampled). This means that the standard error of the mean is a measure of the dispersion of sample means around the population mean, mathematically shown in Equation 2.16,

$$\sigma_{\bar{x}} = \frac{\sigma}{\sqrt{N}} \approx \frac{s}{\sqrt{N}}. \tag{2.16}$$

Temperature and Boltzmann Statistics

A partition function describes the statistical properties of a system in thermodynamic equilibrium. Partition functions are functions of the thermodynamic state variables, such as temperature and volume. The partition function is dimensionless, scalar quantity [4]. Each partition function is constructed to represent a particular statistical ensemble, meaning they are specific to a given set of state variables.

A canonical ensemble is one in which the number of particles N, the volume V, and the temperature T are all fixed. For this reason, the canonical ensemble is also known as an NVT ensemble. For a canonical ensemble that is classical and discrete, the partition function can be written as (Equation 2.17)

$$Q = \sum_i e^{-\beta E_i}, \tag{2.17}$$

where $\beta = \frac{1}{k_B T}$, k_B is the Boltzmann constant, and T is the temperature. The principle thermodynamic variable of the canonical ensemble is the temperature of the system, which determines the probability distribution of states that the ensemble can exist in.

Each microstate of the canonical ensemble has a probability of existing given by Equation 2.18:

$$P_i = \frac{1}{Q} e^{\frac{E_i}{kT}}. \tag{2.18}$$

The Boltzmann distribution is a probability distribution corresponding to a canonical ensemble. It gives the probability of a certain state as a function of that state's energy and temperature of the system to which the distribution is applied,

and it is the distribution that maximizes the entropy of the system. The partition function can be calculated if we know the energies of the states accessible to the system of interest. It is given by Equation 2.19

$$P_i = \frac{1}{Q} e^{\frac{E_i}{kT}}, \tag{2.19}$$

where p_i is the probability of state i, ε_i is the energy of state i, k the Boltzmann constant, T the temperature of the system and M is the number of all states accessible to the system of interest. The canonical partition function Q can be calculated as the sum over all possible Boltzmann probabilities P_i (Equation 2.20),

$$Q = \sum_{i=1}^{M} e^{-\varepsilon_i/kT}. \tag{2.20}$$

The probabilities of all accessible states must add up to 1, and so the partition functions serves as a kind of normalization for each individual probability. The Boltzmann distribution shows that states with lower energy will always have a higher probability of being occupied than the states with higher energy. It can also give the quantitative relationship between the probabilities of any two states being occupied. The ratio of probabilities for states i and j is given as (Equation 2.21

$$\frac{p_i}{p_j} = e^{(\varepsilon_j - \varepsilon_i)/kT} \frac{p_i}{p_j} = e^{(\varepsilon_j - \varepsilon_i)/kT}, \tag{2.21}$$

where p_i is the probability of state i, p_j the probability of state j, and ε_i and ε_j are the energies of states i and j, respectively.

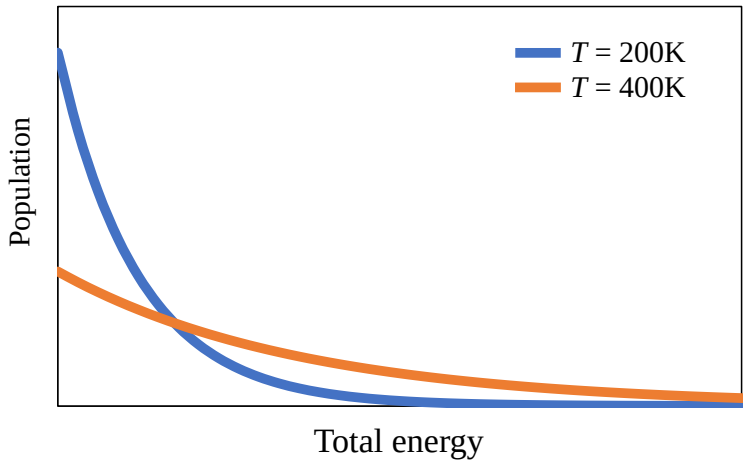

Figure 2.3: Comparison of Boltzmann population distributions at 200K and 400K.

The Boltzmann distribution is often used to describe the distribution of particles, such as atoms or molecules, over energy states accessible to them at a given temperature. The effect that temperature has on the Boltzmann population

of states of a given energy are graphically shown in Figure 2.3.

Chapter 3

The Effect of Random Noise in Structure on Electronic Properties

Introduction

The previous two chapters have highlighted the effects that temperature can have on chemical structure; temperature and solvent are both responsible for the noise in the chemical environment. This noise in turn is responsible for the distribution of chemical structures that can exist in that environment, and the corresponding distributions of QM properties of those structures. This is the nature of the fundamental connection between temperature, random noise, and the statistical ensemble of a chemical system, and a graphical representation of this phenomenon is pictured in Figure 3.1. For this reason, it would be incredibly convenient if there was a method to approximately relate the

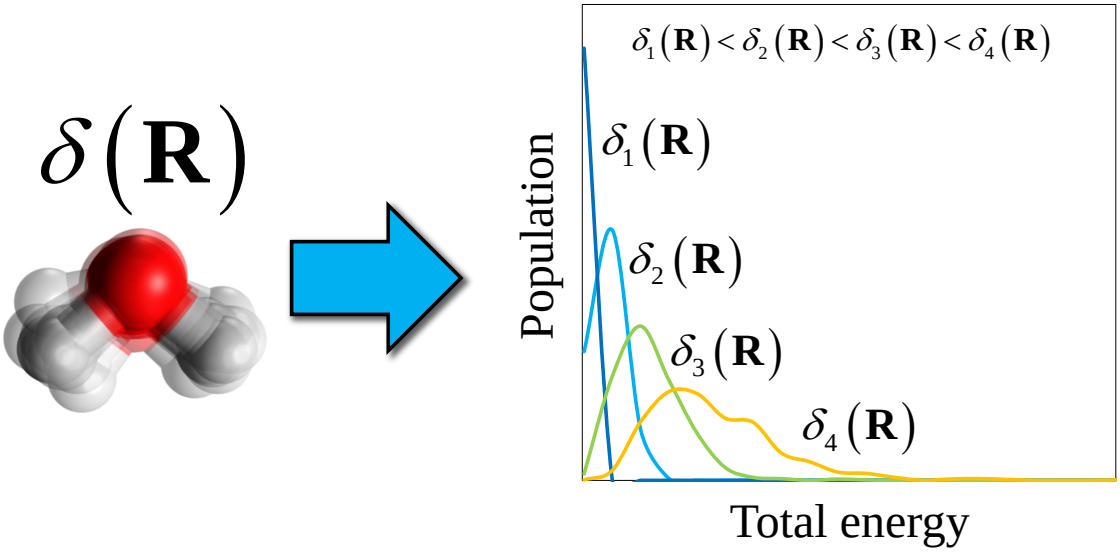

Figure 3.1: Representation of how random noise in the nuclear coordinates of a molecule correspond to a probability distribution of quantum mechanical properties (in this case, total ground state energy). As the magnitude of the random noise increases, the form of the probability distribution changes.

distribution of structures directly to the distribution of QM properties we are interested in. For example, the bottleneck

of the Effective Stochastic Potential (ESP) method detailed in the next chapter is performing QM calculations on a sample population of structures in order to obtain a suitable basis for constructing the ESP. If an approximate ESP could be constructed without having to perform any QM calculations, the computational speed-up of the already highly-efficient method would be considerable.

From probability theory, we know that a PDF of one random variable X can be written in terms of a PDF of a different random variable Y if Y can be written as a function of X, as in Equation 3.1

$$\rho_Y(y_0) = \int_{-\infty}^{+\infty} dx \rho_X(x) \delta[g(x) - y_0]. \tag{3.1}$$

$\delta[g(x) - y_0]$ is the Dirac delta function [26]. For functions of variables, the Dirac delta function has the form [26] in Equation 3.2:

$$\delta[g(x) - y_0] = \sum_i \frac{\delta(x - x_i)}{|g'(x_i)|}. \tag{3.2}$$

Substituting this form of the Dirac delta function into Equation 3.1, we arrive at Equation 3.3:

$$\rho_Y(y_0) = \sum_i \frac{\rho_X(x_i)}{|g'(x_i)|}. \tag{3.3}$$

The implications of this relationship with respect to the challenge of predicting temperature effects on electronic properties are profound. Equation 3.3 can allow us to predict what the distribution of an electronic property is at a certain temperature if we can write that property as a function of a known random variable. For example, we can run a molecular dynamics simulation at some temperature and randomly sample structures from the equilibrium trajectory to obtain a distribution of classical nuclear-nuclear repulsion energies. If we know a function that can transform the nuclear-nuclear repulsion energy to the total electronic energy with reasonable accuracy, from that PDF we can generate a PDF of total electronic energies. This computational route would be must faster than performing the QM calculation directly, since calculating the classical nuclear-nuclear repulsion energy is so computationally inexpensive.

In the following investigation, in order to try and determine an underlying first-principle connection to structural noise and distribution of electronic properties, I have calculated the distributions of a number of electronic properties for multiple molecules as a function of systematically increasing deformation in the nuclear coordinates of those molecules. What follows is an overview of how these deformed structures were obtained, an analysis of the distributions calculated for each molecule, and a discussion of what insight can be gathered from these results.

Theoretical and Computational Details

System Details and Setup

In this investigation, we wanted to calculate the effects of systematic noise in nuclear coordinates on H_2O, NH_3, CH_4, benzene, and C_{60} (fullerene). Starting with the minimum energy structure of each system (obtained from NIST Computational Chemistry Comparison and Benchmark Database [27]), Gaussian random noise was applied to the x, y, and z coordinates of each atom in the system, with the exception of the first three atoms in the system. For each molecule, the first atom was fixed in space, and noise was applied only along one and two dimensions of the second and third atoms, respectively. In this way, translational and rotational motion of the molecules due to the random noise could be removed. The noise added to each nuclear coordincate was normally-distributed, such that the deformed coordinates have the form shown in Equation 3.4

$$x = x_0 + \mathcal{N}(0.0, \eta), \tag{3.4}$$

where x is one of the three spatial coordinates, and $\mathcal{N}$ is a random normal variable, with $\mu = 0.0$ and σ is equal to a parameter η. In this way, each coordinate is a random variable with an analytically-expressible form. For example, the total nuclear-nuclear repulsion term of the molecular Hamiltonian has the form (Equation 3.5)

$$V_{\mathrm{N-N}} = \sum_{A,B>A}^{M} \frac{Z_A Z_B}{\mathbf{R}_A - \mathbf{R}_B}, \tag{3.5}$$

which, under the Born-Oppenheimer approximation, can be calculated analytically. Therefore, the nuclear repulsion term for a single pair of nuclei is a random variable that is a function of the random normal noise shown in Equation 3.6

$$Y = \frac{1}{\sqrt{(A+X)^2 + B}} \tag{3.6}$$

where X in this case is the random normal variable $\mathcal{N}(0.0, \eta)$, and A and B are constants corresponding to the other spatial dimensions of the nuclei.

Electronic Structure Calculation Details

We looked at the effects of systematic noise in the nuclear coordinates on the distributions of electronic properties at η values of 0.001, 0.01, 0.025, 0.05, 0.075, and 0.1 bohr. This noise was systematically applied in order to generate 1,000 deformed structures of each molecule at all six values of η. For the H_2O, NH_3, CH_4, and benzene systems, ground-state second order MllerPlesset perturbation theory (MP2) [28] calculations were performed on each deformed

structure using cc-pVDZ basis functions. We have chosen to use MP2 due to its analytical form of the correction to the ground state energy as given in Equation 3.7:

$$E_0^{(2)} = -\frac{1}{4}\sum_{ab}^{N_{\text{vir}}}\sum_{ij}^{N_{\text{occ}}}\frac{\left|\langle ab|r_{12}^{-1}|ij\rangle\right|^2}{\varepsilon_a+\varepsilon_b-\varepsilon_i-\varepsilon_j}. \tag{3.7}$$

Because of the large number of electrons in the C_{60} system compared to the other systems being investigated, we have used the Resolution-of-Identity (RI-MP2) method [29] with RIMP2-VDZ auxiliary basis functions [30]. The RI-MP2 method replaces four-center two electron integrals with linear combinations of three-center integrals, making the electronic structure calculations scale much better with system size.

All electronic structure calculations were performed using the Q-Chem software package [31]. The properties of interest in this study were total ground state electronic energy, nuclear-nuclear repulsion energy, MP2/RI-MP2 correlation energy, and HOMO-LUMO gap energy. To generate PDFs of each property, the calculated values were then histogrammed.

Results and Discussion

Population Distributions of Electronic Properties as a Function of Random Noise

Figures 3.2–3.6 show the PDFs of all properties of interest for the applied magnitudes of random noise in the nuclear coordinates. From these figures, we have confirmation that all systems are within the small-deformation regime. 100% of the total ground state electronic energies all fall into the smallest bin for $\eta = 0.001$ and $\eta = 0.01$ for all systems under investigation. This is important because as the random noise increases further and further, it becomes less and less applicable to physical stochastic interactions due to thermal and solvent effects. As the magnitude of the random noise η that is applied to the nuclear coordinates increases, both the standard deviation σ and range of all distributions also increases. While the σ values of these distributions tend to be larger for molecules with a higher number of nuclear degrees of freedom, it is not universally true. For example, focusing only on the 10-electron systems (H_2O, NH_3, and CH_4), we see that as the nuclear degrees of freedom increase, σ values for the total energy and HOMO-LUMO gap distributions increases at the same η value. However, this trend does not hold for the nuclear-nuclear repulsion energy and MP2 correlation energy distributions, where we find that, for the same value of η, σ values for CH_4 are less than those for NH_3.

One of the great insights we gain from these results is that it is not just the shape and spread of these distributions that is changing as η increases. First, it can be seen that as η increases, the correlation energy distributions red-shift for all molecules. Since more negative correlation energy implies a greater contribution to the total electronic energy, this informs us that on average, it is even more important to accurately treat electron-electron correlation for deformed

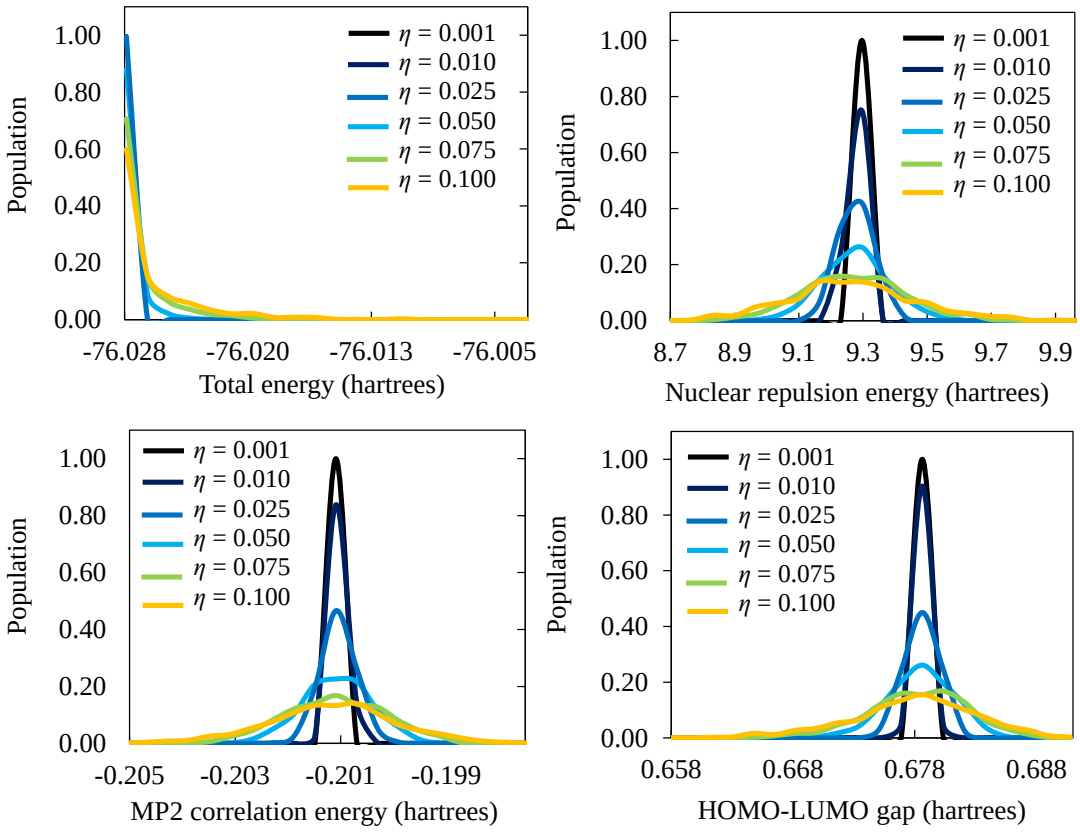

Figure 3.2: H_2O population distributions at difference noise levels for **Top Left**: Total ground-state energy, **Top Right**: Nuclear repulsion energy, **Bottom Left**: MP2 correlation energy, and **Bottom Right**: HOMO-LUMO gap energy. All energies in hartrees.

structures than for their corresponding minimum-energy structure.

Second, we find that as η increases, the HOMO-LUMO gap distributions also red-shift. While this trend is true for each molecule studied, this red-shifting is especially prominent in the cases of CH_4, benzene, and C_{60}. In the case of C_{60}, the mean of the HOMO-LUMO gap distribution shifts nearly 1 eV from $\eta = 0.001$ to $\eta = 0.1$. We can conclude from this trend that on average, a random deformation of a minimum-energy structure tends to result in a narrowing of the HOMO-LUMO gap, making low-lying excitations more energetically favorable in these conformations.

Fluctuation in CIS Oscillator Strengths in H_2O

Oscillator strength is a measure of how strongly a particular electronic transition interacts with an external potential inducing the interaction, such as an incoming photon of light. Accurate determination of oscillator strength is important for predicting how strongly a particular electronic excitation will couple to that incoming photon. In atomic units,

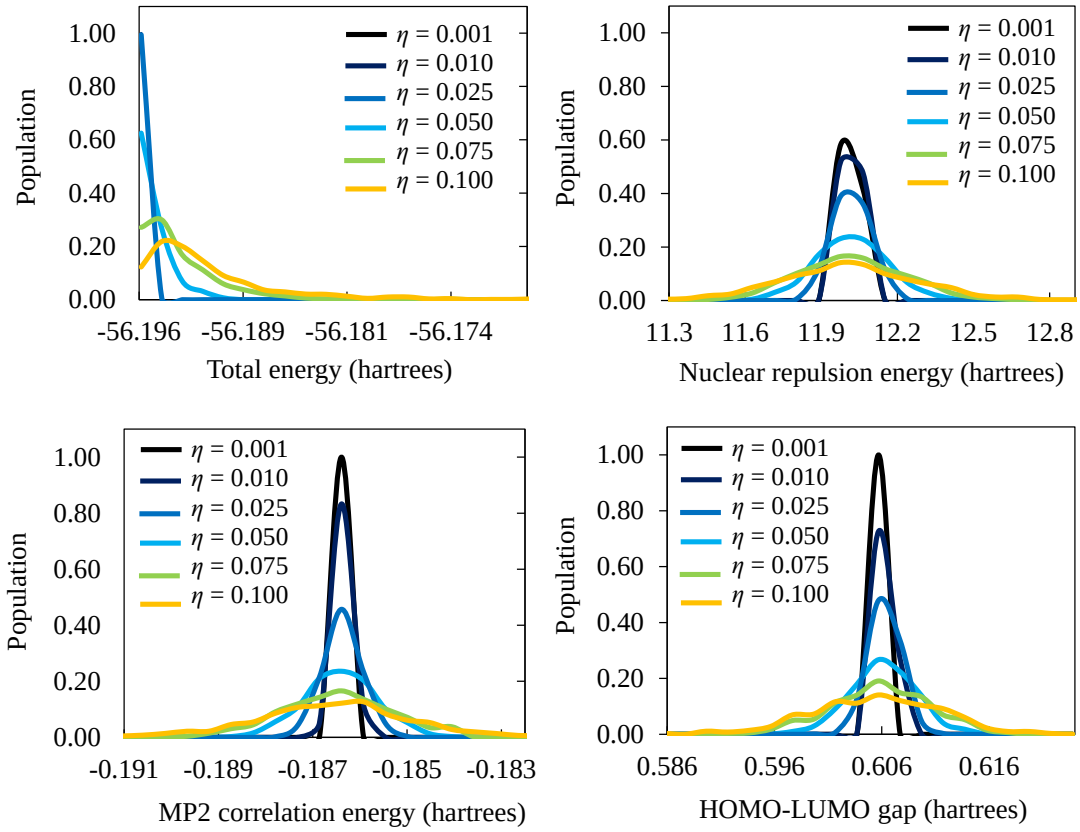

Figure 3.3: NH_3 population distributions at difference noise levels for **Top Left**: Total ground-state energy, **Top Right**: Nuclear repulsion energy, **Bottom Left**: MP2 correlation energy, and **Bottom Right**: HOMO-LUMO gap energy. All energies in hartrees.

the mathematical description for oscillator strength can be calculated as (Equation 3.8)

$$f_{12} = \frac{2}{3}(E_2 - E_1) \sum_{\alpha=x,y,z} |\langle 1|R_\alpha|2\rangle|^2, \tag{3.8}$$

Where f_{12} is the oscillator strength corresponding to an electronic transition from state $|1\rangle$ to state $|2\rangle$, E_1 and E_2 are the energies of $|1\rangle$ and $|2\rangle$, and the summation over R_α goes over all three spatial coordinates x,y and z [32]. In **??**, population distributions of the first ten CIS oscillator strengths (in a.u.) have been calculated for 1,000 deformed H_2O structures at $\eta = 0.1$ bohr. The numbered arrows indicate which CIS root each distribution corresponds to. It is immediately apparent that random noise in the nuclear coordinates in this system has a very different effect on each of the CIS root distributions. For some CIS roots, such as the 4^{th} root, the oscillator strength changes very little with respect to the noise, while other roots (especially the 6^{th}) are incredibly sensitive to deformations to the minimum energy structure. There are also big differences in the higher-order moments of these distributions as well. Many

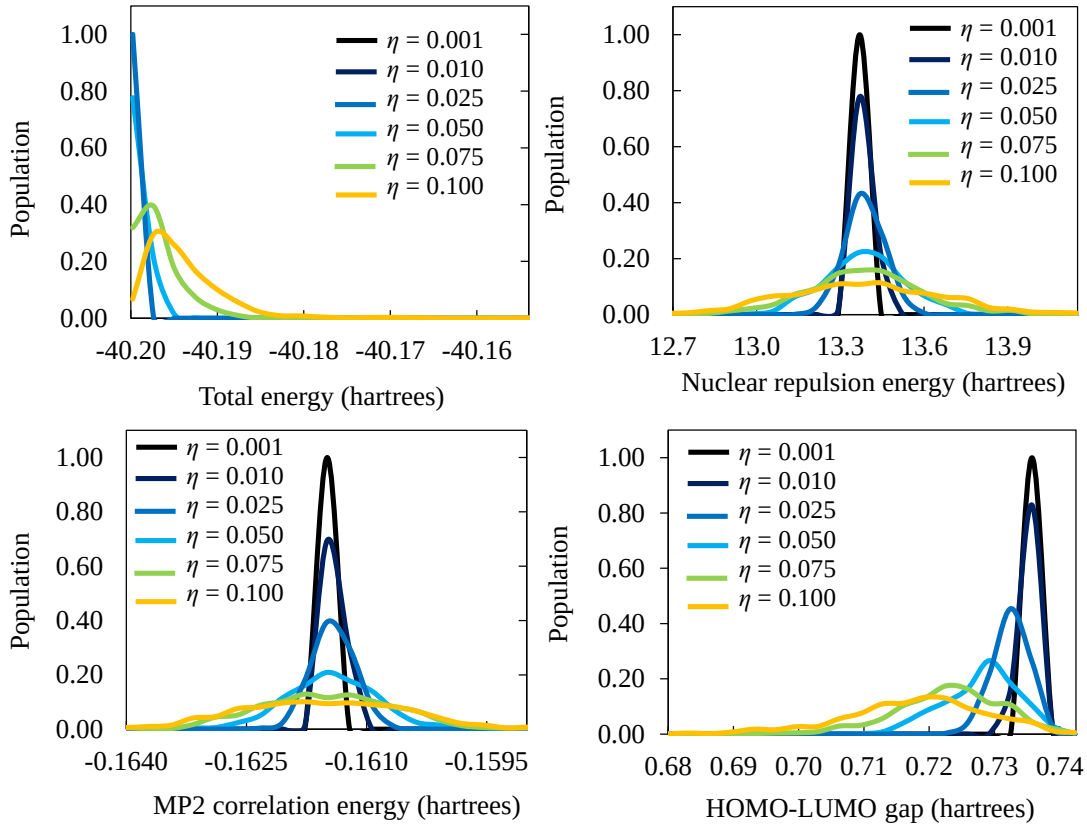

Figure 3.4: CH_4 population distributions at difference noise levels for **Top Left**: Total ground-state energy, **Top Right**: Nuclear repulsion energy, **Bottom Left**: MP2 correlation energy, and **Bottom Right**: HOMO-LUMO gap energy. All energies in hartrees.

of the distributions skew to the right, with an increase to the average oscillator strength with respect to the noise (as seen in the 1st root). Conversely, a number of other distributions skew to the left, with a decreasing average oscillator strength (as seen in the 9th root). The key point here is that even more so than these other electronic properties, the effect of noise in the nuclear repulsion energy on oscillator strengths is especially difficult to predict.

Determining Effective Temperature of Noise from Distribution of Ground State Energy

We see that most of the PDFs we have calculated broaden in both directions along the axis of the random variable in question. The exceptions are the PDFs of total electronic energy. Because the random variable of total electronic energy cannot take values less than the energy corresponding to the minimum energy structure of the system, these PDFs tend to follow a Boltzmann-like distribution. This is particularly true for $\eta = 0.001$ and $\eta = 0.01$ bohr, in which the applied random noise to the molecular structure behaves as a small perturbation. While this behavior of the total electronic energy PDFs breaks down for benzene and C_{60} at larger η values, it holds reasonably true for the

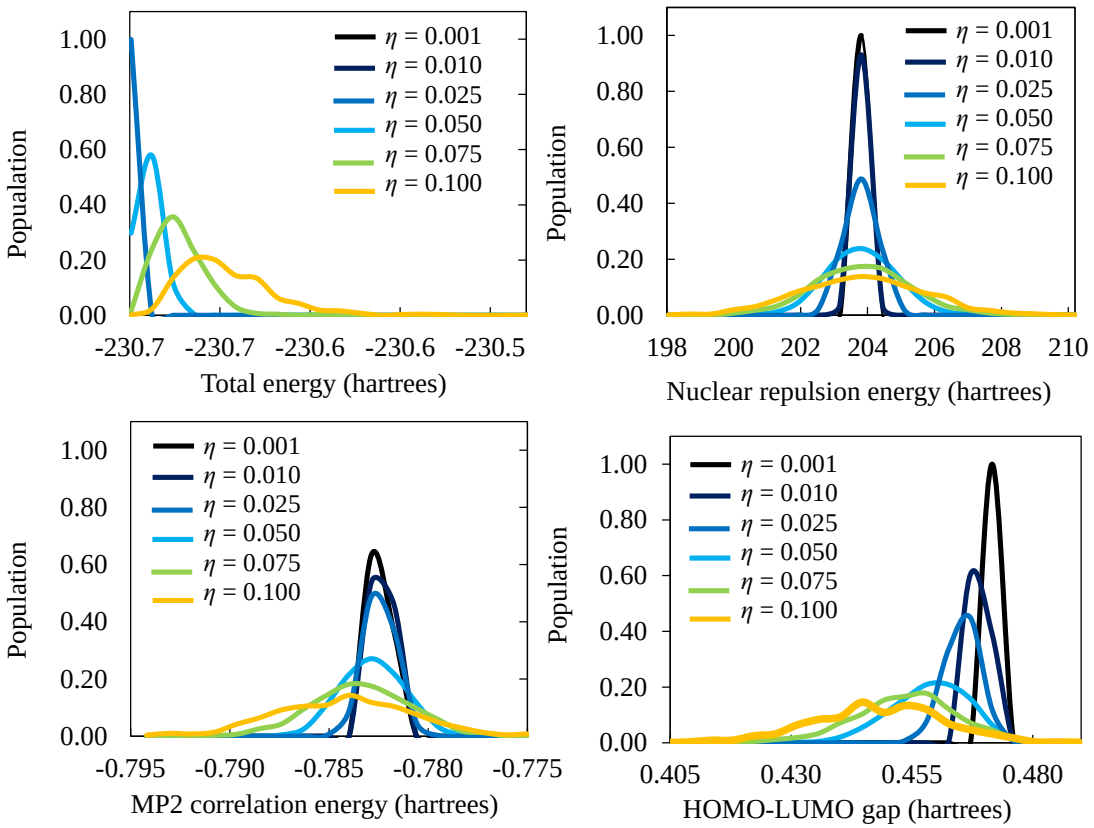

Figure 3.5: Benzene population distributions at difference noise levels for **Top Left**: Total ground-state energy, **Top Right**: Nuclear repulsion energy, **Bottom Left**: MP2 correlation energy, and **Bottom Right**: HOMO-LUMO gap energy. All energies in hartrees.

10-electron systems, even at larger values of η.

This characteristic of these PDFs enables us to relate this random noise in the structure to an effective temperature. We can search for a temperature that corresponds to a Boltzmann distribution which minimizes the error with respect to the calculated total electronic energy PDFs. The form of these Boltzmann distributions is (Equation 3.9)

$$f_{\mathrm{B}}(E) = e^{E/k_{\mathrm{B}}T_{\mathrm{eff}}}, \tag{3.9}$$

where E is the total ground state energy, k_{B} is the Boltzmann constant, and T_{eff} is the effective temperature, which is treated as an optimizable parameter in this instance. T_{eff} is then determined by minimizing the sum of the square differences between the true PDF and f_{B}, as in Equation 3.10:

$$\min_{T}\left[\sum_{i=1}^{N_{\mathrm{bin}}}\left[f_{\mathrm{i}}^{\mathrm{PDF}} - f_{i}^{\mathrm{B}}\right]^{2}\right] \rightarrow T_{\mathrm{eff}}. \tag{3.10}$$

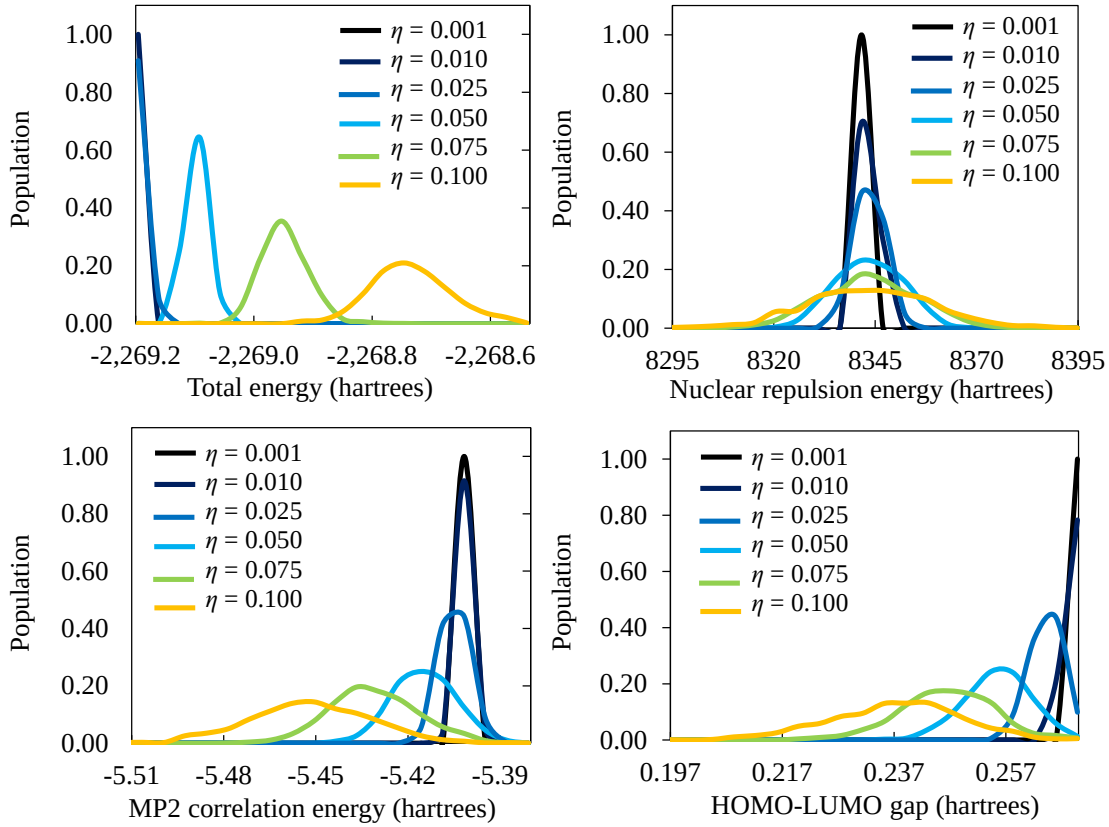

Figure 3.6: C_{60} population distributions at difference noise levels for **Top Left**: Total ground-state energy, **Top Right**: Nuclear repulsion energy, **Bottom Left**: MP2 correlation energy, and **Bottom Right**: HOMO-LUMO gap energy. All energies in hartrees.

Figure 3.8 shows what these effective-temperature Boltzmann distributions look like for H_2O at η values of 0.01, 0.05, 0.075 and 0.1 bohr. In all four cases the correlation coefficient $R^2 \geq 0.98$, so the effective temperature match quite well with the total ground state energy distributions. As expected, increasing the amount of random noise to the chemical structure corresponds to a higher effective temperature of the system. While this approach may not be viable for certain molecules at certain η values, there should always be some η which corresponds to a small enough perturbation of the minimum energy structure that this procedure may be applied.

Connection of Fluctuation in Nuclear Repulsion Energy to Electronic Properties

Now that we have a notion of how temperature relates to this random noise, and how the random noise we have applied to the structure effects the distributions of properties we have calculated, we return to the original motivation: Is it possible to find a functional relationship between the random variable of classical nuclear repulsion energy that exists at some temperature, and a random variable that corresponds to a QM property of interest?

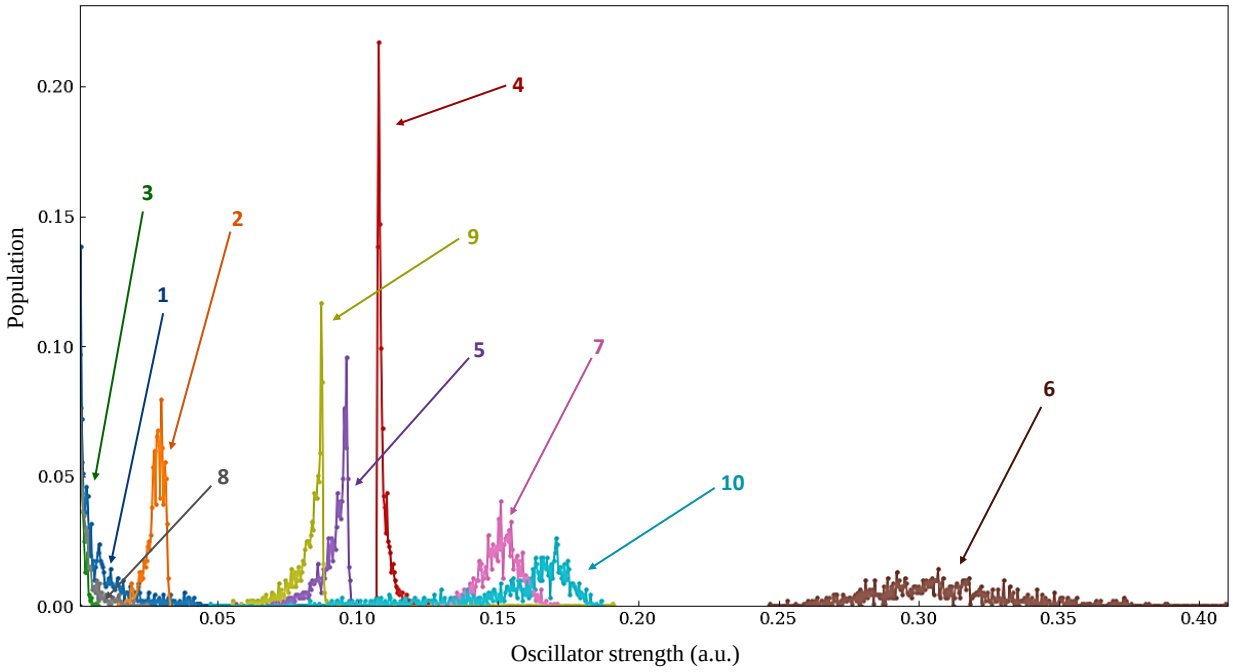

Figure 3.7: Population distribution of the first ten CIS oscillator strengths (a.u.) for 1,000 deformed H_2O structures at $\eta = 0.1$ bohr. Numbered arrows indicate which CIS root the distribution correspond to.

We have preliminary results which show that the answer is very likely yes, which are presented in Figure 3.9. In these scatter plots, we have taken the σ values of the total electronic energies, correlation energies, and HOMO-LUMO gap PDFs, and normalized them against the corresponding σ value of the nuclear-nuclear repulsion PDF for the same system. These plots then show how the spread in PDFs of the QM properties are changing relative to the spread in the nuclear repulsion PDF as a function of η. What we find is that for both correlation energy and HOMO-LUMO gap PDFs, these relative σ values are mostly invariant to increasing noise in the chemical structure. This implies that the σ in the nuclear-nuclear repulsion PDF is directly proportional to the σ in these two QM property PDFs.

Similarly, we find that the relative σ value for the total electronic energy increases *linearly* with increasing values of η, implying that σ of the total electronic energy PDF increases quadratically as σ in the nuclear-nuclear repulsion PDF increases. There does not appear to be an obvious trend with what these scaling factors look like with respect to system size, either in number of electrons or in number of degrees of nuclear freedom. However, this relationship between σ of the nuclear-nuclear repulsion PDF and σ of the QM property PDFs implies that there should be a function than can approximately transform from one random variable to the other in this small-perturbative regime.

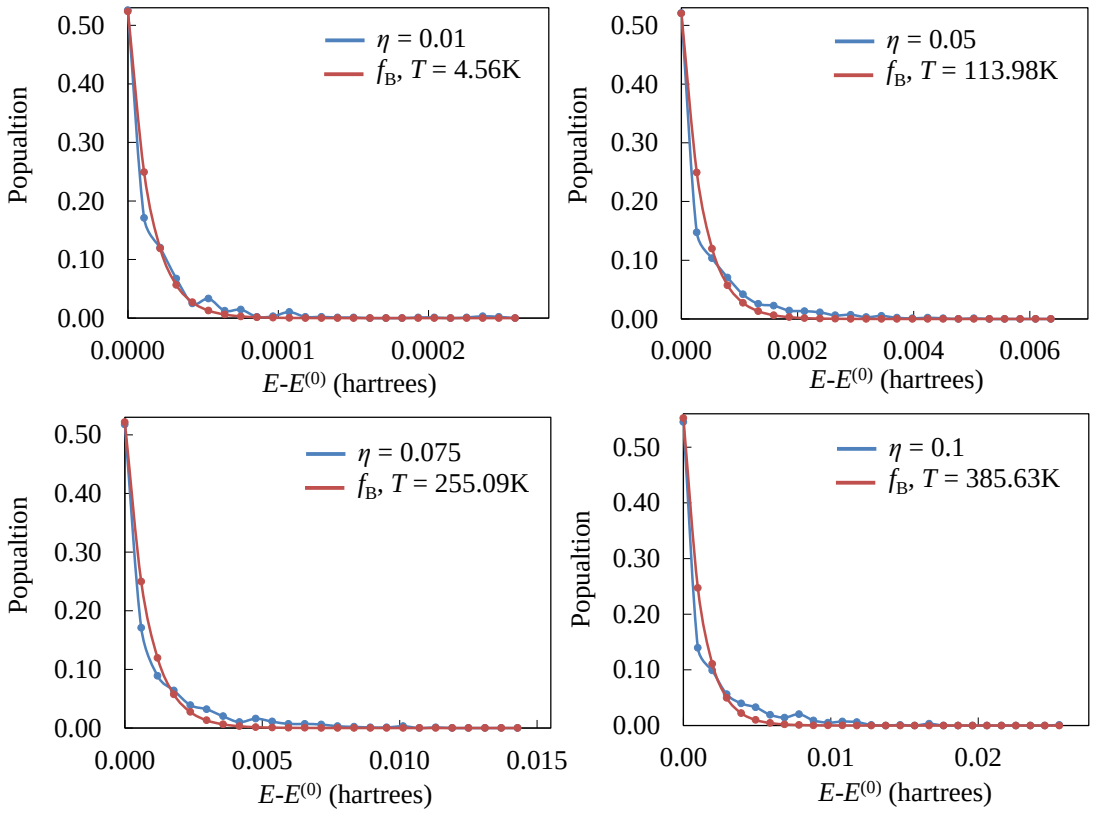

Figure 3.8: Effective temperatures for H_2O at $\eta = 0.1, 0.05, 0.075$, and 0.1 bohr calculated by fitting total energy population distributions to Boltzmann distributions.

Conclusions

The effect of systematic random normal noise in nuclear coordinates on electronic properties has been demonstrated. Noise can be related to an effective temperature, indicating it may be possible to predict the effect of temperature on distributions of quantum mechanical properties without doing electronic structure calculations. Even across different chemical systems, the standard deviations of correlation energy, HOMO-LUMO gaps, and total electronic energy tends to increase either linearly or quadratically with increasing standard deviations in the nuclear repulsion PDFs. This may be a useful avenue toward predicting temperature-dependent distributions of electronic properties. A suitable function relating distributions of nuclear repulsion energies to QM properties still needs to be determined.

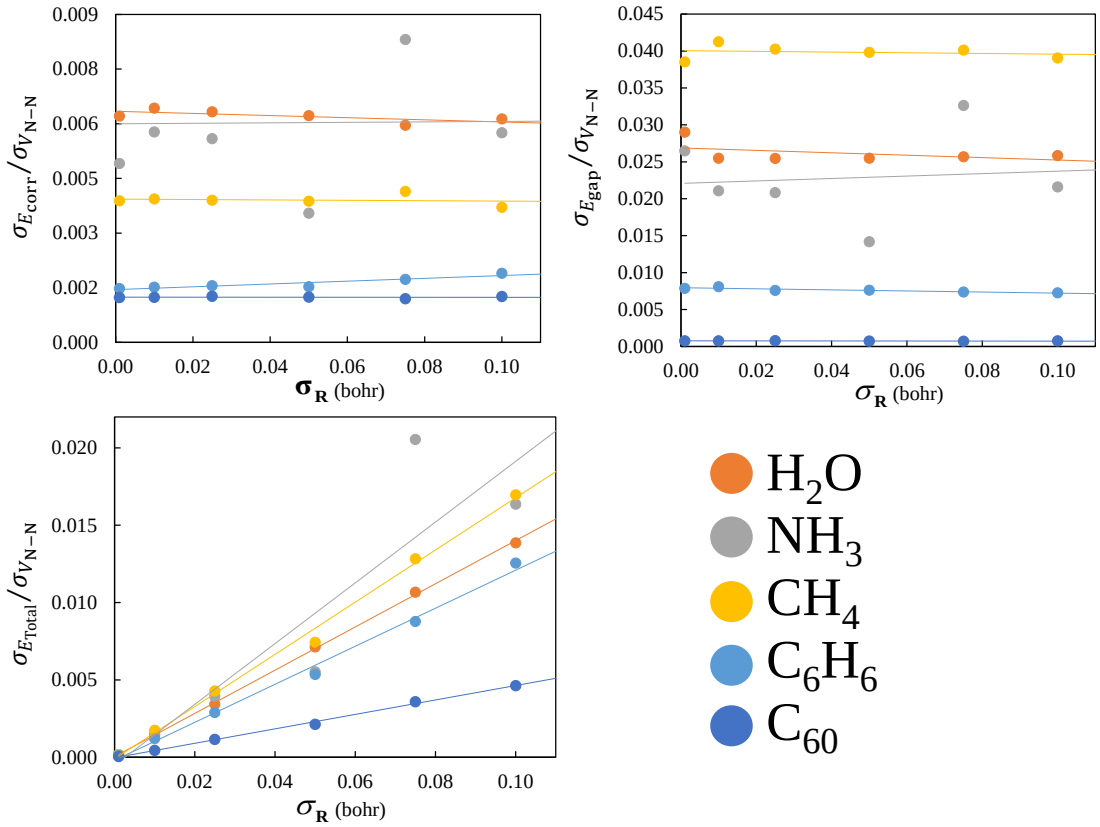

Figure 3.9: Scatter plots of how the standard deviations (relative to the standard deviation of the nuclear repulsion energies for the same noise level) of each calculated distribution change with increasing noise. Data shown for H_2O, NH_3, CH_4, benzene, and C_{60}.

Chapter 4

The Effective Stochastic Potential Method

Introduction

The Effect of Temperature and Solvent on Semiconductor Nanoparticles

The goal of this published work [24] was to develop efficient theoretical and computational method for performing ensemble-averaged properties of semiconductor nanoparticles (NPS). Semiconductor NPs such as quantum dots and rods, have important technological applications. Because of quantum confinement effect [33], their optoelectronic properties can be tuned by adjusting parameters such as the size, shape, material composition, and ligands of the NP. Consequently, NPs have promising applications in photovoltaics, [34, 35, 36, 37, 38] light emitting devices, [39, 40, 41] charge and energy transfer processes [42, 43, 44, 45], and biological labeling. [46, 47]

One of the important environmental factors that influence their optical and electronic property is the temperature and has been the focus of numerous theoretical and experimental studies. Early experimental investigation performed by Joshi and co-workers in 2006 looked at this temperature dependence of band gap energies for colloidal CdSe/ZnS core/shell nanocrystals of different diameters. They found that over a temperature range of 10K to 300K, the band gap energies decreased with increasing temperature for all nanocrystal sizes [48]. Recent experimental results on the temperature-effect on quantum dot optical properties have also been obtained by Savchenko and co-workers in 2017. They studied the first exciton peak shift as a function of temperature in InP/ZnS core/shell NPs in the range of 6.5K to 296K. Similarly to Joshi et. al. they found that the peak both broadens and shifts toward larger wavelengths with increasing temperature [49]. In 2011, Chen and co-workers performed non adiabatic molecular dynamics simulations on both spherical and elongated CdSe quantum dots using time-domain Kohn-Sham theory. Their results confirm the inverse temperature dependence on band gap energy in quantum dots. They also calculated that the temperature dependence on the relaxation rate of excited electrons was higher stronger in elongated quantum dots [50]. In the same year, Fischer et. al. performed time-dependent density functional theory (TD-DFT) calculations on a $Si_{29}H_{24}$ quantum dot trajectory. They found that the band gap energy of the NP shifted significantly throughout the dynamics

simulation [51]. More recent quantum dynamics simulations utilizing TD-DFT and the tight-binding approximation performed by High and co-workers looked at the excited state energy transfer in a porphyrin light-harvesting device. Their simulation showed that it is extremely important to couple the nuclear and electronic degrees of freedom in order to accurately simulate excited state energy transfer [52]. Liu and Jakubikova have also investigated the electron transfer rate in a pyridine-TiO_2 light harvesting assembly, and found that the transfer rate is faster when sampling from thermally accessible structures at room temperature compared to a single 0K optimized structure [53].

In colloidal systems, the NPs are surrounded by solvent molecules which provide a constant-temperature heat-bath for NPs. Constant-temperature ensembles such as NVT or NPT are used extensively for calculation and analysis of equilibrium properties. In molecular dynamics simulations, various methods are used to implement thermostat such as Anderson, velocity-scaling, and Nose-Hoover. Investigation of temperature dependence is complicated and computationally expensive because it requires electronic structure calculations on a large number of structures. This imposes serious limitations on the size of the systems that is being investigated.

Using Random Matrix Theory to Solve Chemical Problems

In this work, we present the effective stochastic potential (ESP) method to address the computational bottleneck associated with performing electronic structure calculations on a large number of molecular structures needed for obtaining ensemble-averaged quantities. The central idea of the ESP method is to approximate the explicit interactions between the system and the bath degrees of freedoms by statistically equivalent effective potential. In the ESP method, the construction of the effective potential is performed using the random-matrix theory (RMT) method. Before we describe this new method, a brief background in the history and usage of random matrix theory will be provided for context. Originally, RMT was designed by Wigner in 1951 to deal with the statistics of eigenvalues and eigenfunctions of complex many-body quantum nuclear systems [54]. Wigner later used RMT to investigate the statistical fluctuations of scattering processes. [55] After Wigner, RMT was successfully applied to the description of spectral fluctuations of atomic nuclei [56], complex atoms [57], and complex molecules [58]. The nature of the general theory greatly lends itself to the investigation of highly complex and chaotic systems. Other, more recent examples of how RMT has been applied to physical systems include equilibrium and transport properties of disordered and classically chaotic quantum systems [59], transitions between classical and quantum distributions of hydrogen energy levels [60], and spectral resonances in quartz [61]. Much work has also been done using RMT to investigate the quantum mechanical phenomenon of so-called "persistent current," the perpetual flow of interacting electrons in a static magnetic field [62, 63, 64, 65, 66].

There are many forms of RMT that have been used, but in general, RMT is the process of replacing the Hamiltonian of a system with an ensemble of Hamiltonians containing random matrix elements. Most popularly used in RMT is the Gaussian orthogonal ensemble (GOE), where the Hamiltonian is partitioned into two parts: a reference component

and a stochastic component where the matrix elements are uncorrelated, normally distributed random numbers. These two components are then coupled to form the total Hamiltonian. Using the GOE approach in this way can be useful for accurately reproducing the correct fluctuations of system properties, but fails dramatically at modeling average properties of the system. For example, the density of states that is produced by GOE are (non-physically) semicircular in shape [55]. Due to their highly complex nature, NPs are a natural candidate for investigation using RMT. One of the earliest investigations of NPs using RMT was done by Jalabert, Stone, and Alhassid in 1992. They developed a statistical theory of the effect of Coulomb blockade in NPs represented as a particle in a finite potential well using random matrices to determine the Coulomb blockade amplitudes. They were able to obtain good agreement with experiment. [67] In 1996, Šeba et. al. used a random matrix model to describe the conductance of a model NP connected to an ideal lead. To accurately match experimental results of NPs attached to two leads, they introduced a coupling constant to their RMT Hamiltonian. [68] In that same year, Sivan and co-workers performed an experimental investigation into the disorder of ground state energies of populations of GaAs NPs. They compared their experimental results to those produced by traditional RMT methods, and found that RMT produced fluctuations in energy larger than experimentally observed, and the overall distribution of energies was less symmetric. They concluded that RMT in general would only produce accurate results in electronic systems with weak Coulomb interactions. [69] More recently, in 2008 Kaplan et. al. investigated the fluctuation of two-body screen Coulomb interaction in ballistic NPs using the random wave model (a model related to RMT). They were able to derive analytical expressions for these fluctuations in terms of the linear size of the NP. Despite the Gaussian random single electron basis used in their theory, they found that both two-body and one-body matrix elements followed non-Gaussian distributions. [70] Shankar in 2006, and later in 2008, has discussed a technique for studying NPs using the renormalization group method in conjunction with RMT. [71, 72] Disorder arising from temperature or solvent effects can also impact the observed properties of organic molecules and systems as well. Much theoretical and computational work has been performed in this area. In 2001, Kwasniewski and coworkers have calculated UV-vis absorption spectra on various frames throughout molecular dynamics simulations of trans-stilbene using the ZINDO-CIS method. They found that thermal motion had a very strong impact on the the HOMO to LUMO transition energy. At temperatures less than 400K, the energy levels displayed pronounced Gaussian thermal broadening of the related band, up to 30 nm [73]. In 2003, Lewis and coworkers performed MD simulations combined with tight-binding density functional theory to calculation the electronic states of a model DNA double helix as the molecule underwent room temperature thermal fluctuations. They found that the population density of the HOMO state over time changed dramatically due to these thermal fluctiations [74]. In 2006, Morth and Autschbach investigated the temperature dependence of the optical rotation of fenchone using TDDFT. They found that optical rotation in this system increases linearly with temperature over the range of 273K-373K, and concluded that the temperature-dependent vibrational effects were largely responsible for the temperature-dependent rotational effects in rigid organic molecules [75].

Many researchers have also investigated the effects of solvent and temperature on organic chemical systems experimentally as well. In 2002, Ariu et. al. studied the temperature dependence on photoluminescence quantum yields (PLQYs) of poly(9, 9-dioctylfluorene) films in morphologies including spin-coated glass, quenched nematic glass, crystalline, and vapor-treated glass. They found that the PLQYs increased as the temperature of the crystalline, spin-coated glass, and quenched nematic glass systems was reduced. In 2005, Dauphas and co-workers investigated β-casein protein aggregation and properties as a function of concentration, temperature, and calcium content, characterized by dynamic light scattering, confocal microscopy, and fluorescence spectroscopy. Over a temperature range of 283K to 323K, they saw that the fluorescence absorption profiles of the protein were vary different when the concentration and temperature were changed. In 2014, Mani et. al. looked at the fluorescent properties of the salt of 2,6-diaminopyridinium with dihydrogen phosphate. They found that as a result of proton transfer from phosphoric acid in solution to the pyradine nitrogen, the band gap between the HOMO and LUMO states is smaller than compared to 2,6-diaminopyridine. This finding was confirmed by a red shift that was observed in its absorption spectrum [76].

Conceptual Picture of the Effective Stochastic Potential

The Effective Stochastic Potential (ESP) method was inspired by the idea of capturing the statistical effects of noisy chemical enviornments and using that information to predict what the ensemble should look like at a certain temperature. Figure 4.1 gives a conceptual idea of how the ESP method works.

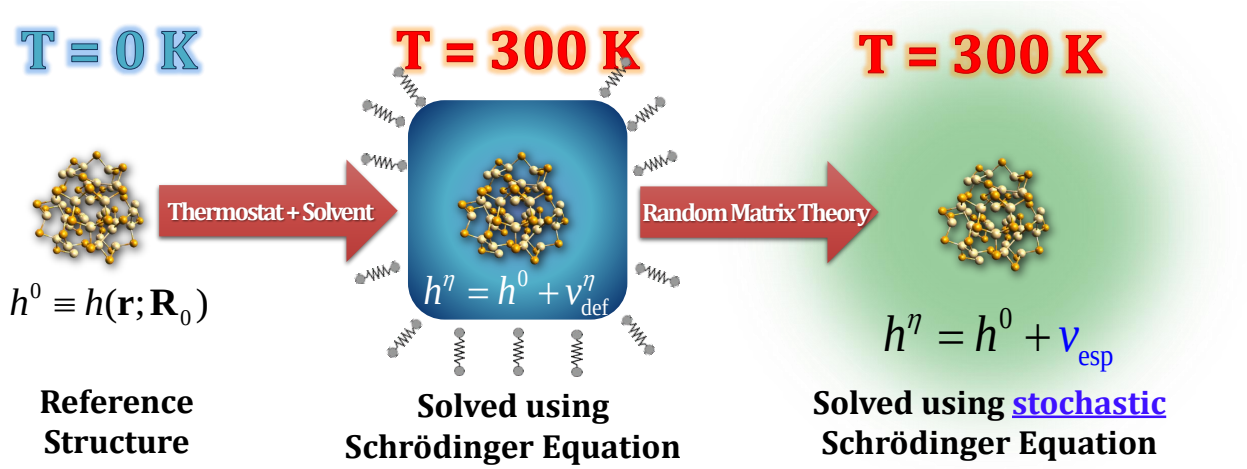

Figure 4.1: Conceptual diagram of how the Effective Stochastic Potential method corresponds to the chemical environment of a system at a given temperature.

We start by determining an energy-minimum reference structure, corresponding to the 0K ensemble. This can be done from a geometry optimization at the desired level of theory. The energy-minimum reference structure has a corresponding reference one-electron Hamiltonian h_0. By equilibrating this reference structure to a certain temperature in a certain solvent, we obtain an ensemble of structures corresponding to that chemical environment. Each of these

structures has its own one electron Hamiltonian h_0, and a corresponding deformation potential v^0_{def} which relates the deformed Hamiltonian to the reference Hamiltonian.

From here, we can sample from these deformation potentials, compute the statistical properties of the potentials, and construct a probability distribution function (PDF) that has the same statistical properties as the set of deformation potentials. This PDF is the effective stochastic potential (v_{ESP}) for the system in this chemical environment. We can apply RMT on this ESP to generate a stochastic Hamiltonian which we can sample from orders of magnitude more efficiently than by directly performing quantum mechanical calculations on each structure.

The remaining part of this chapter is organized as follows. The main theoretical development of the ESP method is described in section 4.2 The derivation includes definition of the quantum mechanical Hamiltonian under investigation, definition of the deformation potential, and conceptual construction of the effective stochastic potential. The computational details for implementation of the ESP method is presented in section 4.3. Issues such as choice of sampling schemes, choice of 1-particle basis functions, and stochastic sampling using Gaussian random matrices are presented. The developed ESP method was used to perform proof-of-concept calculations of ensemble-averaged HOMO-LUMO gap in chemical systems, and results for H_2O and $Cd_{20}Se_{19}$ are discussed in section 4.4.

Theory

System Setup and Definitions

We start by introducing key concepts and definitions that will be used repeatedly in this work. We will start by defining the effective one-particle Hamiltonian as

$$h(\mathbf{r};\mathbf{R}) = \frac{-\hbar^2}{2m}\nabla^2 + v_{\text{ext}}(\mathbf{r};\mathbf{R}) + v_{\text{eff}}(\mathbf{r}) \tag{4.1}$$

The one-particle Hamiltonian is the starting point for treating electron-electron correlation in many-electron systems. In the above expression, v_{eff} is the effective one-particle operator for treating electron-electron interaction which can be approximated using HF, DFT, pseudopotential, many-body perturbation theory (MBPT), or a model potential

$$v_{\text{eff}} = \{v_{\text{HF}}, v_{\text{KS}}, v_{\text{ps}}, v_{\text{model}}, \dots\} \tag{4.2}$$

For wave function based methods, the eigenfunctions of the one-particle Hamiltonian provide the one-particle basis for performing, MP2, CI, and, CCSD calculations [3].

$$h\chi_p = \varepsilon_p \chi_p \tag{4.3}$$

In case of DFT, these one-particle basis functions are used to construct the one-particle density. The derivation presented here is very general and does not make any *a priori* assumption about the form of the effective potential. Typically, v_{eff} is not known in advance and has to constructed iteratively using a self-consistently procedure. However, because of the SCF procedure, the final SCF-converged v_{eff} has a functional dependence on the nuclear geometry $\mathbf{R}$

$$h\chi_p = \varepsilon_p \chi_p \xrightarrow[\text{convergence}]{\text{SCF}} v_{\text{eff,SCF}}(\mathbf{r})[\mathbf{R}] \tag{4.4}$$

Using the SCF converged effective potential for any nuclear geometry $\mathbf{R}^\eta$, we define the following one-particle Hamiltonian

$$f^\eta(\mathbf{r};\mathbf{R}^\eta) = \frac{-\hbar^2}{2m}\nabla^2 + v_{\text{ext}}(\mathbf{r};\mathbf{R}^\eta) + v_{\text{eff,SCF}}(\mathbf{r})[\mathbf{R}^\eta] \tag{4.5}$$

We also define a reference structure $\mathbf{R}^0$ and the effective Hamiltonian corresponding to the reference structure is given by f^0.

$$f^0(\mathbf{r};\mathbf{R}^0) = \frac{-\hbar^2}{2m}\nabla^2 + v_{\text{ext}}(\mathbf{r};\mathbf{R}^0) + v_{\text{eff,SCF}}(\mathbf{r})[\mathbf{R}^0] \tag{4.6}$$

Typically, the reference structure is selected to the minimum energy structure, however, the derivation does not impose this as a requirement.

Definition of Deformation Potential

We define a structure $\mathbf{R}^\eta$ to be deformed if is different from the reference structure $\mathbf{R}^0$ and cannot be generated from the reference structure by simple rotational and translational transformation on $\mathbf{R}^0$. The difference between $\mathbf{R}^\eta$ and $\mathbf{R}^0$ is a consequence of deformation in the internal coordinates of the molecular system. Associated with each deformed structure, we define the deformation potential which is defined as

$$v^\eta_{\text{def}} = f^\eta - f^0 \tag{4.7}$$

Using the above definition, the deformation potential can be interpreted as the potential which must be added to the reference Hamiltonian to generate the deformed Hamiltonian. The existence of the deformation potential is an exact condition and can be proved using the following argument. Because f^η and f^0 exist, therefore, using Eq. (4.7) v^η_{def} must also exist.

Up until this point, we have used abstract Dirac representation for representing the reference and deformed Hamiltonians. However, now we seek a to represent the deformed potential as a matrix in a single-particle basis. The matrix

representation of the above equation is given as

$$\mathbf{F}^{\eta} = \mathbf{F}^{0} + \mathbf{V}^{\eta}_{\text{def}} \tag{4.8}$$

where, the matrix elements are defined using as set of single-particle basis functions $\{\phi_{\mu}^{[\eta]}\}$

$$F^{\eta}_{\mu\nu} = \langle \phi_{\mu}^{[\eta]} | \mathrm{f}^{\eta} | \phi_{\nu}^{[\eta]} \rangle \tag{4.9}$$

The choice of the single-particle basis functions is an important one and in principle, can or cannot depend on the nuclear geometry $\mathbf{R}^{\eta}$. The choice of the single-particle basis in which the deformed potential is represented is an important topic and will be discussed in section 4.3.

Conceptual Construction of Effective Stochastic Potential

Calculation of the deformation potential becomes computationally expensive for a large set of structures. The effective stochastic potential method is designed to address this computational bottleneck, by replacing the exact deformation potential by the effective potential that shares common identical statistical metric with the deformation potential for a set of structures. Conceptually, the ESP potential can be defined by the following three steps. First, we define a set of all possible unique structures that a chemical systems can exist in by $\{\mathbf{R}^{\eta}\}_{0}^{\infty}$. Second, for each of the structures, the deformation potential is determined, the set of all deformed potential is defined as

$$\mathscr{S}^{V}_{\text{def}} = \{\mathbf{V}^{\eta}_{\text{def}}\}_{0}^{\infty} \tag{4.10}$$

For each deformed structure $\mathbf{R}^{\eta}$, we associate a corresponding probability of p^{η} for existence of that structure in a physical system. As the definition of probability implies, p^{η} should satisfy the following two mathematical relationships.

$$p^{\eta} \geq 0 \tag{4.11}$$

and

$$\sum_{\eta \in \mathscr{S}_{\text{def}}} p^{\eta} = 1 \tag{4.12}$$

For the remainder of the derivation we will use the compact notation of v^{η}_{ij} to refer to the individual matrix elements

of the deformation potential

$$v_{ij}^{\eta} \equiv \left[\mathbf{V}_{\text{def}}^{\eta}\right]_{ij} \tag{4.13}$$

For each matrix element of $\mathbf{V}_{\text{def}}^{\eta}$ the mean μ or the expectation value of the distribution is defined as

$$s_{ij}^{(1)} \equiv \mu_{ij} = \sum_{\eta \in \mathscr{S}_{\text{def}}} p^{\eta} v_{ij}^{\eta} \tag{4.14}$$

Here, we have used both $s_{ij}^{(1)}$ and μ_{ij} to refer to the mean for convenience. Analogously, the variance σ of the distribution is defined as

$$s_{ij}^{(2)} \equiv \sigma_{ij} = \sum_{\eta \in \mathscr{S}_{\text{def}}} p^{\eta} [v_{ij}^{\eta} - \mu_{ij}]^2 \tag{4.15}$$

Using the mean μ_{ij}, we define the mth central moment of the distribution by s_m which is evaluated using the following expression

$$s_{ij}^{(m)} = \sum_{\eta \in \mathscr{S}_{\text{def}}} p^{\eta} [v_{ij}^{\eta} - \mu_{ij}]^m \qquad \text{with} \quad (m > 1) \tag{4.16}$$

Evaluation of the all the moments for each matrix elements of the set of deformation potential implies by the following relationship

$$\{\mathbf{V}_{\text{def}}^{\eta}\}_0^{\infty} \rightarrow \{\mathbf{s}^{(1,\text{def})}, \mathbf{s}^{(2,\text{def})}, \ldots, \mathbf{s}^{(\infty,\text{def})}\} \tag{4.17}$$

Using these statistical metrics, we are now in the position to define the effective stochastic potential in matrix representation. We start by defining a stochastic matrix whose matrix elements are random numbers Z drawn from a probability-distribution function $f_{ij}^{\text{pdf}}(z)$.

$$v_{ij}^{\text{sto}} = Z \tag{4.18}$$

The probability distribution function must satisfy the following two conditions.

$$f_{ij}^{\text{pdf}}(z) \geq 0 \tag{4.19}$$

$$\int_{-\infty}^{+\infty} dz \quad f_{ij}^{\text{pdf}}(z) = 1 \tag{4.20}$$

The probability of finding Z in the interval $[a,b]$ is given by

$$P[a \leq Z \leq b] = \int_a^b dz \quad f_{ij}^{\text{pdf}}(z) \tag{4.21}$$

We define the effective stochastic potential as the stochastic potential whose central-moments are closest to the central-moments of the deformed potential. Mathematical, the ESP potential is defined using the following constrained functional minimization.

$$\min_{f_{ij}^{\text{pdf}}} \left[\sum_{m=1}^{\infty} \left[s_{ij}^{(m,\text{def})} - s_{ij}^{(m,\text{sto})} \right]^2 \right] \rightarrow f_{ij}^{\text{pdf,min}} \rightarrow v_{ij}^{\text{esp}}[f_{ij}^{\text{pdf,min}}] \tag{4.22}$$

where the constraints on f_{ij}^{pdf} are given in Equation 4.20.

Computational Details

In this section, we present the implementation details of the ESP method by introducing additional approximations needed for the practical implementation of the method. Practical implementation of the ESP method require us to work with finite sets of data. As a consequence, only a finite sets of structures $\{\mathbf{R}^{\eta}\}_0^M$ are used for evaluation of the deformation potential and set of deformation potential is also finite. Computational implementation also requires us to limit the set of moments $(\mathbf{s}^{(1)},\ldots,\mathbf{s}^{(N)})$ on the set of deformation potential to a finite number. The various methods of sampling, choice of single-particle basis functions, and determination of the probability distribution function for ESP are presented below.

Canonical Ensemble Sampling Using Monte Carlo and Molecular Dynamics

The probability p^{η} associated with the structure $\mathbf{R}^{\eta}$ depends on the thermodynamical conditions of the physical system and can be chosen to described to both equilibrium and non-equilibrium conditions. In this work, we are interested in systems at thermal equilibrium which are well-described using the constraints of canonical ensemble with constant composition, temperature, and volume (N,V,T) For canonical ensemble, the probability is the well-known Boltzmann expression as shown below

$$p^{\eta} = \frac{e^{-\beta(E^{\eta}-E^0)}}{\sum_{\lambda \in \mathscr{S}_{\text{def}}} e^{-\beta(E^{\lambda}-E^0)}} \tag{4.23}$$

where, E^{η} is the energy and E^0 is the energy associated with the minimum-energy structure.

The first step in the determination of the deformation potential is the generation of the set of structures $\mathbf{R}^{\eta}$. In principle, the set of structures can be achieved using either Monte Carlo (MC) by molecular dynamics simulations. The

key point in both of these approaches is to generate a statistically meaningful sample of thermally accessible structures. In the MC procedure this is achieved by randomly distorting the optimized structure, calculating its energy and and calculating the mean and central moments using the Boltzmann-weighted procedure described in Equation 8.8. In the MD procedure, equilibrium molecular dynamics calculations are performed at fixed N,V,T and the structures are randomly selection from the equilibrium distribution. It is important to note that Boltzmann weights are only needed for MC sampling and should not be included in case of MD sampling. The relevant equations for MD sampling are presented in Equation 8.9

$$\boldsymbol{\mu} = \sum_{\eta \in \mathscr{S}_{\text{def}}^{\text{MD}}} \mathbf{V}_{\text{def}}^{\eta} \tag{4.24}$$

In the above equation, the superscript (MD) implies that the set of structures were obtained from the MD simulation.

1-Particle Basis for Representing the Deformation Potential

An important feature of the ESP method is the choice of the 1-particle basis that is used for representing the deformation potential. In this work, we will use the eigenvectors of the reference Hamiltonian for representing both the deformed and the ESP potential. We start by defining the AO-basis representation of the reference Hamiltonian matrix

$$\mathbf{F}^{\eta}\mathbf{C}^{\eta} = \mathbf{S}^{\eta}\mathbf{C}^{\eta}\boldsymbol{\epsilon}^{\eta} \tag{4.25}$$

In the first step, we perform canonical orthogonalization

$$\mathbf{X}^{\eta\dagger}\mathbf{F}^{\eta}\mathbf{X}^{\eta} = \tilde{\mathbf{F}}^{\eta} \tag{4.26}$$

$$\mathbf{X}^{\eta\dagger}\mathbf{S}^{\eta}\mathbf{X}^{\eta} = \boldsymbol{I} \tag{4.27}$$

In the next step, we obtain the unitary matrix that diagonalizes the reference transformed Fock matrix $\tilde{\mathbf{F}}^{0}$

$$\mathbf{U}^{0\dagger}\tilde{\mathbf{F}}^{0}\mathbf{U}^{0} = \tilde{\tilde{\mathbf{F}}}^{0} \equiv \boldsymbol{\epsilon}^{0} \tag{4.28}$$

Using $\mathbf{U}^{0}$, we transformed all the deformed Fock matrices $\tilde{\mathbf{F}}^{\eta}$ into the eigenbasis of the reference Fock matrix $\tilde{\mathbf{F}}^{0}$

$$\mathbf{U}^{0\dagger}\tilde{\mathbf{F}}^{\eta}\mathbf{U}^{0} = \tilde{\tilde{\mathbf{F}}}^{\eta} \tag{4.29}$$

It is important to note that we are transforming using $\mathbf{U}^{0}$ instead of $\mathbf{U}^{\eta}$. Finally, we obtain the matrix representation

of the deformed potential in the eigenbasis of the reference Fock matrix using the following expression

$$\mathbf{V}_{\text{def}} = \tilde{\tilde{\mathbf{F}}}^{\eta} - \tilde{\tilde{\mathbf{F}}}^{0} \tag{4.30}$$

which is equivalent to subtracting the eigenvalues of the reference Fock matrix from the deformed Fock matrix.

$$\mathbf{V}^{\eta}_{\text{def}} = \tilde{\tilde{\mathbf{F}}}^{\eta} - \boldsymbol{\epsilon}^{0} \tag{4.31}$$

Stochastic Sampling Using Gaussian Random Matrices

In practical implementation of the ESP method, require us to work with finite sets of data. As a consequence, only a finite sets of structures $\mathbf{R}^{\eta}$ are used for evaluation of the deformation potential. In addition to that.

not all moments $\{\mathbf{s}_n\}$ are included in the sampling and only a subset of moments are used for construction of the ESP. In this work, we have restricted the sampling to only the mean and the variance

$$\{\mathbf{V}^{\eta}_{\text{def}}\} \rightarrow \{\boldsymbol{\mu}^{\text{def}}, \boldsymbol{\sigma}^{\text{def}}\} \tag{4.32}$$

The above sampling condition is computationally implemented using Gaussian random matrices. Each element of the ESP matrix is is a Gaussian random number Z as shown in Equation 4.33

$$\left[\mathbf{V}_{\text{esp}}\right]_{ij} \equiv v^{\text{esp}}_{ij} = Z \quad \text{where} \quad Z \in \{f^{\text{Gauss}}_{ij}(z)\}. \tag{4.33}$$

The function f^{Gauss}_{ij} is the Gaussian or normal probability distribution function with mean μ and variance σ and has the following form

$$f^{\text{Gauss}}_{ij}(z) = \frac{1}{\sqrt{2\pi\sigma^{\text{def}^2}_{ij}}} \exp[-\frac{(z-\mu^{\text{def}}_{ij})^2}{2\sigma^{\text{def}^2}_{ij}}] \tag{4.34}$$

The corresponding Fock matrix associated with ESP is given by

$$\tilde{\tilde{\mathbf{F}}}_{\text{esp}} = \tilde{\tilde{\mathbf{F}}}^{0} + \mathbf{V}_{\text{esp}}(Z) \tag{4.35}$$

Results and Discussion

Statistical Distribution of HOMO-LUMO Gap of H_2O at 300 K

We begin with a proof of concept for the ESP method, with the goal of demonstrating that the properties of a distribution of thermally-accessible configurations of a chemical system can be accurately reproduced with a stochastic potential derived from that system. We use a single isolated water molecule as our test case. This serves as a useful example as a simple, well-studied polyatomic system. Starting with NVT ensemble, our goal is to calculate the frequency distribution of the HOMO-LUMO gap of water molecule at 300K.

System Setup and Electronic Structure Calculations

The calculations were performed using the canonical ensemble with constant N, V, and T at 300 K. The sampling of the structures for this ensemble was performed using the Monte Carlo procedure. A set of the 1000 structures of water molecules were generated by introducing random distortions to the bond-distances and bond-angles of the optimized structure of water. For each of the 1000 structures, Hartree-Fock (HF) calculations were performed using 6-31G* basis functions, using the GAMESS software package. [77] The probability associated with each of the 1000 structures were calculated using the Boltzmann expression as shown below.

$$p_i = \frac{e^{-\frac{E_i - E_0}{k_B T}}}{\sum e^{-\frac{E_i - E_0}{k_B T}}}, \tag{4.36}$$

where E_0 is the energy of the minimum-energy structure. The eigenvalues of the Fock matrix from the converged HF calculations, were used to calculate the HOMO-LUMO gap for the 1000 structures.

$$E^{\text{gap,HF}} = \varepsilon^{\text{HF}}_{\text{LUMO}} - \varepsilon^{\text{HF}}_{\text{HOMO}} \tag{4.37}$$

Using the thermal probabilities p_i, the thermally-weighted, frequency distribution of the HOMO-LUMO gaps for 1000 structures obtained from the HF/cc-pVDZ calculation at 300K is presented in Figure 5.1. The mean and variance of the distribution is presented in Table 4.1.

Construction of the Effective Stochastic Potential

The ESP for water at 300K was constructed from the set of 1000 Fock matrices obtained from the electronic structure calculations. Using Equation 4.25,Equation 4.25, Equation 4.27, Equation 4.28, and Equation 4.29 all the Fock matrices were first transformed into the eigenbasis of Fock matrix associated with the minimum-energy structure $\mathbf{F}^0$. Then, using the Equation 4.31, the set of 1000 deformation potentials matrices were obtained. The mean and the variance

associated with each matrix elements of the deformation potential matrices were calculated using Equation 4.14 and Equation 4.15. The means and the variances were used in the next step to calculated the matrix elements of the ESP using Gaussian random number as show in Equation 5.5. The ESP Fock matrix was constructed from the ESP matrix using Equation 5.3. A set of 1000 ESP Fock matrices were generated by stochastic sampling, and the eigenvalues of the ESP Fock matrices were used to calculate the ESP HOMO-LUMO gap

$$E^{\text{gap,ESP}} = \varepsilon^{\text{ESP}}_{\text{LUMO}} - \varepsilon^{\text{ESP}}_{\text{HOMO}} \tag{4.38}$$

Comparison of the ESP and Electronic Structure Results

Figure 5.1 compares the frequency distribution of HOMO-LUMO gap obtained using both Hartree Fock and ESP methods. The comparison of the mean and variance of the frequency distributions are presented in Table 4.1.

In order to compare the statistics of the Hartree Fock and ESP method distributions, we used Z-score (also called standard score) [78]. Z-score is defined mathematically as

$$\text{Z} - \text{score} = \frac{x - \mu}{\sigma}, \tag{4.39}$$

where x is a measured value, μ is the mean of the value over a distribution, and σ is the corresponding standard deviation. Z-score is a unit-less quantity that is relative to the distribution's standard deviation. A positive Z-score reflects a value greater than the mean, and negative Z-score reflects a value smaller than the mean. A Z-score of 1 corresponds to a value that is exactly one standard deviation greater than the mean of the distribution. The mean Z-score and standard deviation for the two methods coincided very well. We obtained excellent reproduction of not only the fluctuation of system properties, but also the average system properties.

Comparing the computational cost of the electronic structure calculations and the ESP method calculations, we found that even for a system this simple, our method was at least one full order of magnitude faster computationally. Each single-point energy calculation took approximately 5 seconds to perform, or a total of about 80 minutes to perform all 1000 calculations. The ESP method calculations took about 0.1 seconds per calculation, less than 2 minutes for 1000 calculations. This performance advantage becomes much greater as the size and complexity of the system of interest grows, as the ESP method scales much more favorably with system size versus electronic structure calculations.

Effect of Sample Size on Construction of ESP

As mentioned above, the distribution of ESP method properties for this system were generated by constructing the ESP from 1000 Hamiltonians of randomized configurations. We next wanted to look at how much the statistics of

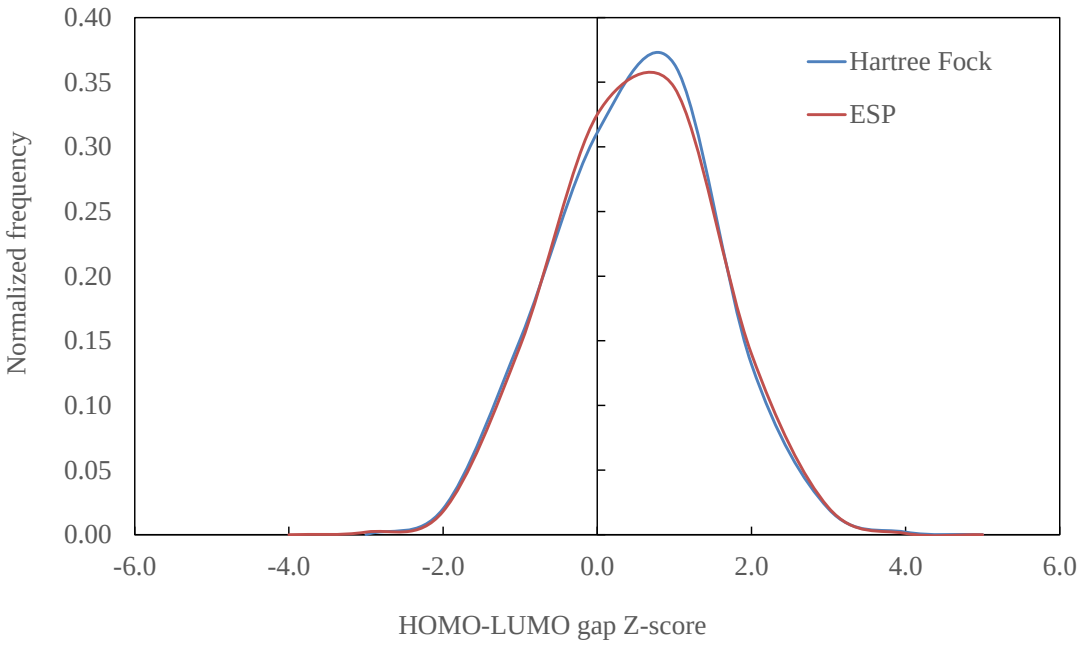

Figure 4.2: Comparison of HOMO-LUMO gap energy Z-scores of a single gas-phase water molecule between Hartree Fock (cc-pVDZ basis) and ESP method.

Method	μ (hartrees)	σ (hartrees)
Hartree Fock	0.5456664	0.0000725
ESP	0.5456658	0.0003847

Table 4.1: Absolute means (μ) and standard deviations (σ) of HOMO-LUMO gap energy in atomic units, and ratios of μ and σ HOMO-LUMO gap energy distributions between Hartree Fock (cc-pVDZ basis) and ESP method for 10,000 sampling points. Calculated Hartree-Fock values for μ and σ were 0.545523 hartrees and 0.004557 hartrees, respectively. Water geometries were generated from a Monte Carlo procedure.

the ESP method distribution would change by generating a smaller number of random Hamiltonians from the ESP. While generating these random matrices from the ESP is computationally cheap, it would be optimal to generate only as many matrices as are needed to reproduce the proper statistics of the system, especially as the system's complexity grows.

We approached this problem by sampling the ESP a different number of times, and comparing the mean HOMO-LUMO gap energy calculated awith the ESP method. Table 4.2 displays these mean values calculated using N_{def} = 10-1000 sampling points. The main observation from these results is that across the different number of sample points used, the mean fluctuates by only about 5 meV. Therefore, a small number of sample points from the ESP method distribution seems to be sufficient to reproduce the same statistics that using many sample points would.

Table 4.2: Mean HOMO-LUMO gap energy (in eV) of gas-phase water molecules calculated using the ESP method for an increasingly larger set of deformation potentials, N_{def}.

N_{def}	Mean HOMO-LUMO gap (eV)
100	14.8520
200	14.8477
300	14.8477
400	14.8488
500	14.8498
600	14.8508
700	14.8498
800	14.8507
900	14.8510
1000	14.8511

HOMO-LUMO Gap of $Cd_{20}Se_{19}$ in water at 300K

We now turn the discussion to the application of the ESP method to a small CdSe NP (1.2 nm in diameter) in aqueous media at 300K . These systems are excellent candidates on which to apply the ESP method, due to the potentially useful applications of NPs, the complexity of their electronic states, and the chaotic behavior of their nuclei at room temperature.

System Setup and Construction of the Effective Stochastic Potential

Equilibrium molecular dynamics simulations with constant N,V,T were performed for the $Cd_{20}Se_{19}$ cluster with explicit water molecules at 300K. The force-field developed by Rabani et al. [79] was used for the CdSe cluster, and the explicit water molecules were treated using TIP3 force. The MD calculations and analysis of the simulations were performed by the GROMACS molecular dynamics program. The initial structure for the MD calculations was obtained from the minimum-energy structure obtained from electronic structure theory at HF/LANL2Z ECP [80] level. The initial structure was then re-optimized using the CdSe force-field in the MD program in vacuum. The simulation cell was constructed by solvating the CdSe cluster in a water bath consisting of 11,763 water molecules. The entire system was equilibrated at 300K by performing MD simulation for 500 ns. The equilibration conditions were verified by monitoring the total energy, total potential energy, and the temperature of the system.

After equilibration, a set of 50 structures were randomly selected from the MD trajectories for construction of the ESP matrix. As a first step, HF calculation using LANL2DZ ECP basis functions were performed for the set of structures and the deformation potential matrices were calculated. The mean and variance of each matrix element were calculated and the ESP matrix and the ESP Fock matrix were constructed using the procedure described in section 4.3.

Table 4.3: Comparison of $Cd_{20}Se_{19}$ HOMO-LUMO gap energies (eV) calculated by ESP and Hartree Fock method (LANL2DZ basis).

	HOMO-LUMO gap (eV)		Number
	μ	σ	of structures
ESP	5.876	0.083	1000
Hartree Fock	5.756	0.073	45

Predictions from the ESP calculations

The results for this $Cd_{20}Se_{19}$ NP are shown below. Important to note about these results is the computation cost involved in obtaining them relative to the cost of doing the equivalent electronic structure calculations. The distribution of CdSe NP systems presented in this work here represents 10000 different thermally-accessible geometries of the NP. Each of these geometries would take us approximately 30 minutes to perform one Hartree-Fock level calculation, or about 5000 hours for the entire distribution. Instead we have spent fewer than 24 hours generating the ESP, and then used the ESP to determine each of the single-electron states in about 0.5 seconds, or 90 minutes for the entire distribution. This represents a calculation speed-up by more than a factor of 200 times.

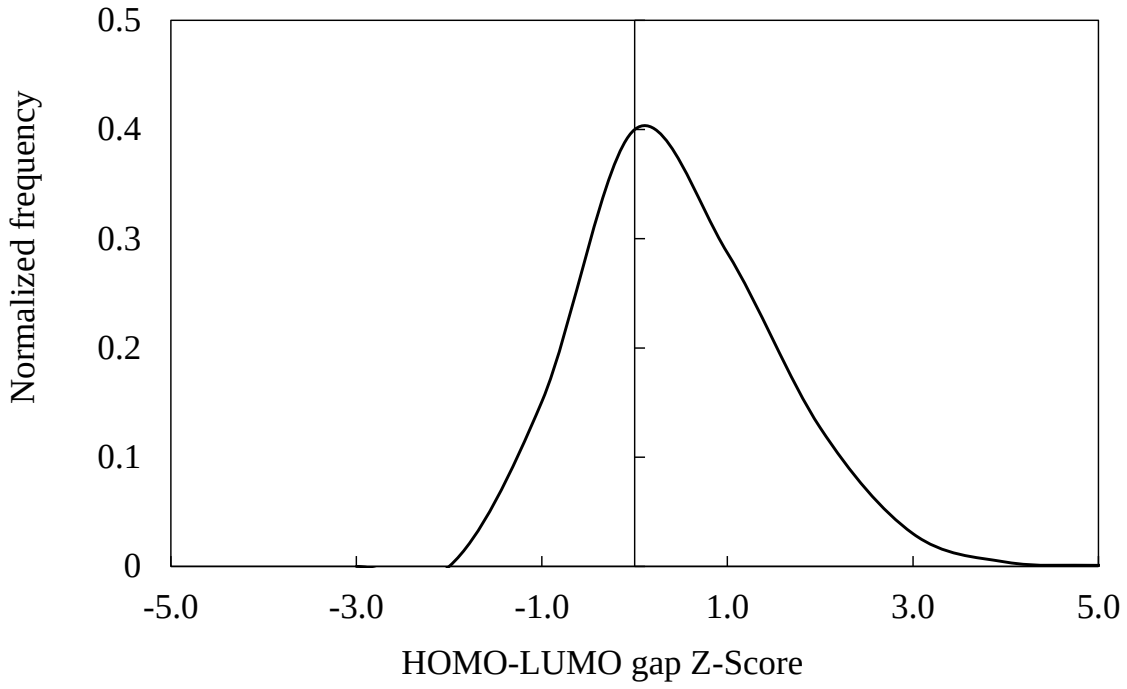

Figure 4.3: HOMO-LUMO gap Z-scores for a $Cd_{20}Se_{19}$ quantum dot at $T = 300$K.

Figure 8.3 show the Z-score frequencies for $Cd_{20}Se_{19}$ HOMO-LUMO gap energies calculated using the ESP method at 300K, compared to those calculated using Hartree Fock. The purpose of looking at Z-scores for these

properties is to compare the characteristics of the different distributions. In comparing the two HOMO-LUMO gap Z-score distributions, it can be seen that the two distributions share similar spreads and peak maxima.

Conclusions

We have developed the ESP method for calculating thermally averaged optical properties of quantum systems. The ESP method has been benchmarked using a single water molecule, and the usefulness of the method has been demonstrated by applying it to two CdSe quantum dots systems. Using the ESP method, we have been able to obtain chemically accurate results that would otherwise have been been computationally infeasible using standard electronic structure methods. The thermally averaged HOMO-LUMO gap energies and exciton binding energies of $Cd_{20}Se_{19}$ and $Cd_{33}Se_{33}$ quantum dots at both 300K and 350K were calculated, and our results compare well with experiment and similar theoretical findings.

Chapter 5

Using Effective Stochastic Potentials to Calculate Temperature-dependent Distributions of Excited-state Properties

Introduction

As I have discussed in previous chapters, the connection between temperature and chemical conformations is one of the central concepts in chemical thermodynamics. Specifically, for the canonical ensemble, the temperature dependent population of various conformations ($\mathbf{R}$) is given by the Boltzmann statistics. [4]

$$\mathscr{P}(\mathbf{R}) \propto \exp[-E(\mathbf{R})/k_{\mathrm{B}}T] \tag{5.1}$$

Consequently, the collective ground and excited state quantum mechanical properties (X) of chemical systems at thermal equilibrium are determined not by the single minimum-energy structure but by an ensemble of conformations.

$$\{\mathbf{R}\} \rightarrow \boxed{H(\mathbf{R})\Psi = E\Psi} \rightarrow \{X(\mathbf{R})\} \tag{5.2}$$

Generation, evaluation, and analysis of the the statistical distribution of the quantum mechanical (QM) properties is crucial for the describing and predicting temperature-dependent phenomena and continues to be an active field of research.

One of the principle metrics governing the reliability of statistical distributions is the sample size of the distribution. For example, the error in the sample-mean of a distribution approach zero with respect to increasing sample size as $1/\sqrt{N_{\mathrm{sample}}}$. [81] Generation of distribution of QM properties from first-principles calculations is especially challenging because of the high computational cost associated with performing calculations on large sample sizes to obtain reliable statistics. In recent studies, it has been estimated that that a sample size in the order of $10^5 - 10^6$ is needed to obtaining ensemble-averaged properties to within chemical accuracy. [23, 24] The problem is further exacerbated for excited state properties which have traditionally been more computationally demanding that ground state

calculations.

The focus of this work is to investigate the excited state properties of PbS quantum dots. Specifically, we investigate the $S_0 \rightarrow S_1$ excitation energies of three differently-sized PbS NPs, at temperatures of 200 K-400 K, respectively. PbS NPs have a great deal of promise in energy-related applications due to their tunable optoelectronic properties, and have been utilized in the areas of photovoltaics, [82, 83, 84, 85, 86, 87, 88, 89, 90, 91] solid state lighting, [92, 93] photodetectors, [94, 95, 96, 97] hydrogen generation, [98, 99] and energy transfer. [100, 101] In particular, PbS NPs have been shown to be highly capable in the area of near-IR light harvesting. [102, 103] Traditionally, the population of structures required to generate ensemble-averaged excited state properties is obtained from the trajectory of a chemical dynamics simulation. Following this prescription, excited state properties of nanomaterials have been investigated using both ab initio molecular dynamics (AIMD) [104, 105, 106, 107, 108, 109, 110, 111] and mixed quantum classical dynamics (MCQD). [112, 113, 25, 114, 115, 116, 117, 118, 119, 120, 121, 122]

In this work, we have obtained temperature-dependent statistical distributions of one million excitation energies by developing the effective stochastic potential configuration interaction singles (ESP-CIS) method. We have developed this approach by combining random matrix theory (RMT) with linear-response theory. We show the theoretical details of integrating linear response theory into the ESP method, and how the computational cost of performing costly excited state calculations on a large ensemble can be dramatically reduced via this approach. The results obtained also provide new insights into the effect of temperature on these distributions.

Theory

Construction of the Stochastic Fock Matrix

: The complete mathematical derivation and the implementation details of the ground-state ESP method has been presented earlier Chapter 4 , and summary of the key concepts are presented here to avoid repetition. The Fock matrix associated with the Effective Stochastic Potential (ESP) method [24] is given by

$$\mathbf{F}^{\mathrm{ESP}} = \mathbf{F}^{0} + \mathbf{V}^{\mathrm{ESP}} \tag{5.3}$$

where $\mathbf{F}^{0}$ is the Fock matrix of the energy-minimized reference structure and $\mathbf{V}^{\mathrm{ESP}}$ is the effective stochastic potential. Starting from a set of structures $\{\mathbf{R}\}$, the corresponding set of Fock operators associated with each structure is calculated. The ESP is obtained from the set of Fock operators using a Boltzmann-weighted moments expansion method. [24]

$$\{\mathbf{R}\} \rightarrow \{\mathbf{F}\} \rightarrow \mathbf{V}^{\mathrm{ESP}} \tag{5.4}$$

In the present work, 1,000 PbS QD structures were used to construct the ESP for each corresponding QD size. The ESP matrix is represented using a multivariate Gaussian random matrix shown in Equation 5.5,

$$\left[\mathbf{V}^{\mathrm{ESP}}\right]_{\mu\nu} = \frac{1}{\sqrt{2\pi{\sigma_{\mu\nu}}^2}} \exp[-\frac{(z-\mu_{\mu\nu})^2}{2{\sigma_{\mu\nu}}^2}] \tag{5.5}$$

where z is a random variate, and $\mu_{\mu\nu}$ and $\sigma_{\mu\nu}$ are obtained from Equation 5.4 using the method derived in Chapter 4. After the construction of the ESP Fock matrix, the ESP eigenvalues and eigenfunctions are obtained from the solution of the following equation. [24]

$$\mathbf{F}^{\mathrm{ESP}}\mathbf{C}^{\mathrm{ESP}} = \varepsilon^{\mathrm{ESP}}\mathbf{C}^{\mathrm{ESP}} \tag{5.6}$$

Derivation of the ESP-CIS Method

: The set of ESP molecular orbitals and energies $\left\{\varepsilon_p^{\mathrm{ESP}}, \chi_p^{\mathrm{ESP}}\right\}$ can be used for performing excited state energy calculations. The CIS eigenvalue equation for a system sampled with the ESP method can be written as,

$$\mathbf{A}^{\mathrm{ESP}}\mathbf{X}^{\mathrm{ESP}} = \omega^{\mathrm{ESP}}\mathbf{X}^{\mathrm{ESP}} \tag{5.7}$$

and was used to calculate electronic excitation energies ω and the corresponding amplitudes $\mathbf{X}$. The matrix elements of $\mathbf{A}^{\mathrm{ESP}}$ have the form, [123, 124]

$$A_{ia,jb}^{\mathrm{ESP}} = \delta_{ij}\delta_{ab}\left(\varepsilon_a^{\mathrm{ESP}} - \varepsilon_i^{\mathrm{ESP}}\right) + K_{ia,jb}^{\mathrm{ESP}} \tag{5.8}$$

and the ESP electron-hole interaction kernel, K^{ESP} has matrix elements of the form as in Equation 5.9

$$K_{pq,rs}^{\mathrm{ESP}} = \left(p^{\mathrm{ESP}}q^{\mathrm{ESP}}|r_{12}^{-1}|s^{\mathrm{ESP}}r^{\mathrm{ESP}}\right)_A, \tag{5.9}$$

where the subscript A denotes that the integral is antisymmetrized.

The terms of the ESP-CIS eigenvalue equation can be obtained from the ESP molecular orbital energies, coefficients, and two-electron integrals.

Connection to Linear Response Time Dependent Hartree Fock and Density Functional Theory

: Extended the previous derivation of the ESP-CIS equation to linear response time-dependent density functional theory is rather straightforward. The complete form of the linear response (or Casida) matrix equations is given by

Equation 5.2.3

$$\begin{bmatrix} \mathbf{A} & \mathbf{B} \\ \mathbf{B}^* & \mathbf{A}^* \end{bmatrix} \begin{bmatrix} \mathbf{X} \\ \mathbf{Y} \end{bmatrix} = \omega \begin{bmatrix} \mathbf{1} & \mathbf{0} \\ \mathbf{0} & -\mathbf{1} \end{bmatrix} \begin{bmatrix} \mathbf{X} \\ \mathbf{Y} \end{bmatrix}, \tag{5.10}$$

where $\mathbf{X}$ and $\mathbf{Y}$ are excitation amplitude vectors, and ω are the excitation energies. The $\mathbf{A}$ and $\mathbf{B}$ matrix elements have the form (Equation 5.12)

$$A_{ia,jb} = \delta_{ij}\delta_{ab}(\varepsilon_a - \varepsilon_i) + \langle ia|r_{12}^{-1}|bj\rangle - \langle ij|r_{12}^{-1}|ba\rangle \tag{5.11}$$

$$B_{ia,jb} = \langle ia|r_{12}^{-1}|jb\rangle - \langle ib|r_{12}^{-1}|ja\rangle, \tag{5.12}$$

where i, j are indexing occupied states, a, b are indexing unoccupied states, and ε are the molecular orbital energies. The electron-hole interaction kernel in this case, given in Equation 5.13

$$K_{\text{eh}} = \langle ia|r_{12}^{-1}|bj\rangle - \langle ij|r_{12}^{-1}|ba\rangle \tag{5.13}$$

corresponds to the time dependent Hartree-Fock (TDHF) equations. The time dependent density functional theory (TDDFT) equations can be arrived at by simply replacing the Hartree-Fock molecular orbital energies with Kohn Sham orbital energies, and the electron-hole interaction kernel with one that corresponds to the exchange correlation functional as shown in Equation 5.15 :

$$A^{\text{ESP}}_{ia,jb} = \delta_{ij}\delta_{ab}(\varepsilon_a - \varepsilon_i) + \langle ia|r_{12}^{-1}|bj\rangle - \langle ij|f_{\text{xc}}|ba\rangle \tag{5.14}$$

$$B^{\text{ESP}}_{ia,jb} = \langle ia|r_{12}^{-1}|jb\rangle - \langle ib|f_{\text{xc}}|ja\rangle. \tag{5.15}$$

As the effect of the $\mathbf{B}$ matrix elements often has little impact on the final excited-state properties calculated, and including them doubles the computational cost of the method, they are often assumed to be equal to 0. The approximation is called the Tamm-Dancoff Approximation (TDA) [123, 124]. The final ESP TDA-TDDFT equations can then be written using only $\mathbf{A}$ matrix elements in terms of the ESP Kohn Sham orbitals and ESP electron-hole interaction kernel shown in Equation 5.16:

$$A^{\text{ESP}}_{ia,jb} = \delta_{ij}\delta_{ab}(\varepsilon^{\text{ESP}}_a - \varepsilon^{\text{ESP}}_i) + \langle ia|r_{12}^{-1}|bj\rangle - \langle ij|f^{\text{ESP}}_{\text{xc}}|ba\rangle. \tag{5.16}$$

Computational Details

Generation of a Boltzmann-like Sample Population

In order to generate an accurate sample population of 1,000 structures that corresponds to a temperature of interest, we enforce a condition that population closely resemble the canonical ensemble at that temperature. This Boltzmann-conditioning is performed in the following way:

1. Systematically deform the coordinate of a minimum-energy reference structure to obtain 1,000 randomly deformed structures.
2. Perform a Hartree-Fock calculation on each deformed structure
3. Histogram the total energies from the set of 1,000 structures to obtain a PDF of the total energies.
4. Select a representative structure from each energy bin, and deform it only slightly a number of times to ensure that the new sample population will have a similar energy population to the Boltzmann population at the temperature of interest.
5. Perform Hartree-Fock calculations on the new population and confirm that the distribution of total energies conforms to the desired Boltzmann population.

It is important to note that for all deformed structures in the investigations that follow, the ensembles correspond to a system in vacuum. While studying most of these in vacuum is not a one-to-one comparison of what the the ensemble looks like in solvent, these calculations are an important first step towards incorporating solvent effect. It is also very straightforward to include the effect of solvent for these systems. By performing a molecular dynamics simulation on the molecule in the solvent of interest, the population of equilibrium structures will shift, as seen in **??**. Conformation from the corresponding trajectory can be sampled with ESP, incorporating the effect of solvent into the calculation.

Computational Setails of the ESP-CIS Method

We make an approximation to the ESP-CIS $\mathbf{A}$ matrix with respect to fluctuations with respect to the reference system $\mathbf{A}^0$,

$$A^{\mathrm{ESP}}_{ia,jb} \approx A^{0}_{ia,jb} + \delta_{ij}\delta_{ab}(\Delta\varepsilon_{ia}) + (\Delta c^{a}_{i} c^{b}_{j})(\Delta K_{ia,jb}) \tag{5.17}$$

where $\Delta\varepsilon_{ia}$ is the fluctuation in the difference between the ESP orbital energy gap the reference gap, $\Delta c^{a}_{i} c^{b}_{j}$ is the fluctuation in the difference between the molecular orbital coefficients of the deformation and the reference, and

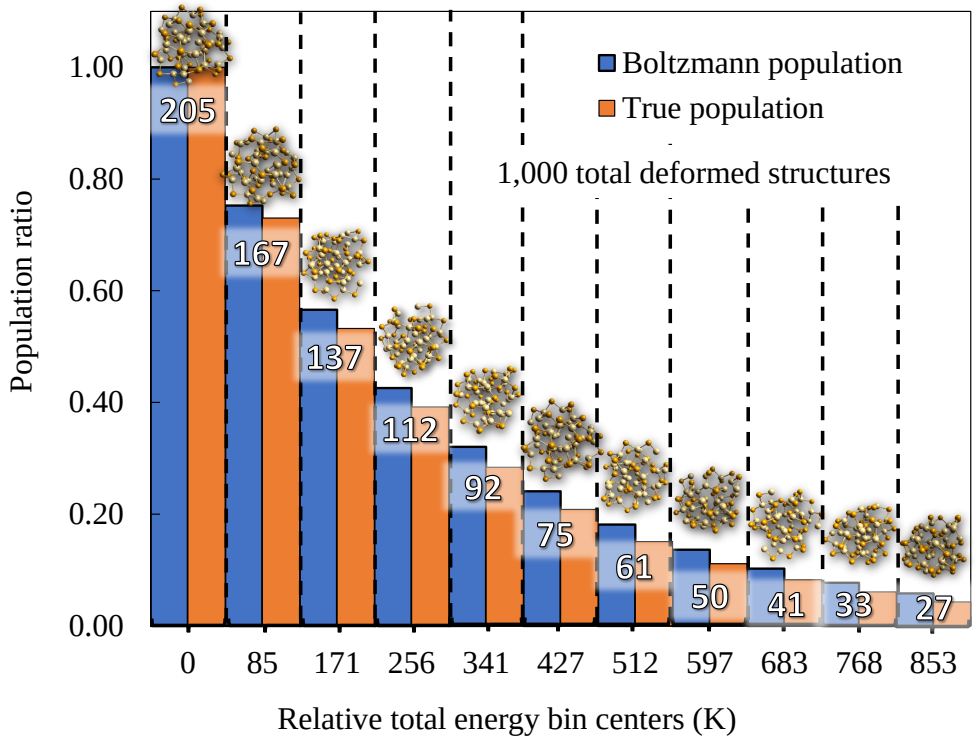

Figure 5.1: Example of histogrammed total ground state energies (in units of K) relative to the minimum energy structure for a sample population of 1,000 structures of H_2O at 300K.

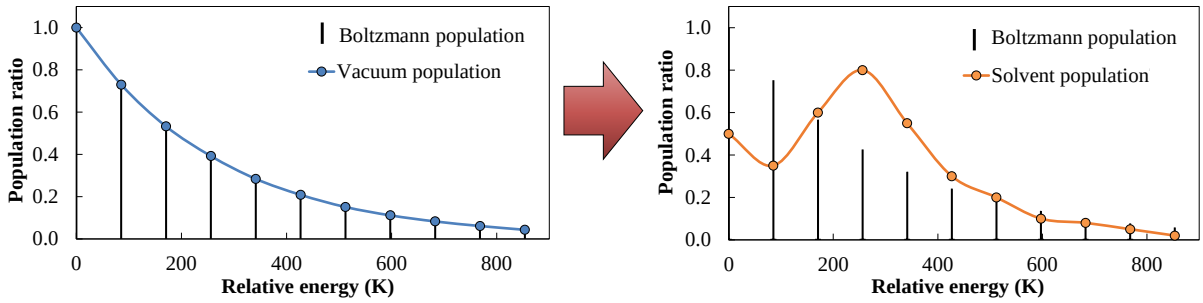

Figure 5.2: Example of how solvent can effect the ensemble of thermally-accessible structures at a given temperature.

$\Delta K_{ia,jb}$ is the fluctuation in difference between the e-h interaction kernel of the deformation and the reference. We also approximate the fluctuation the eh-kernel $\Delta K_{ia,jb}$ as the fluctuation in the average pair-wise Coulomb integral obtained from the deformed ground-state population,

$$\Delta K_{ia,jb} \approx \sum_{ij}^{N_{\text{elec}}} \frac{(ii|jj)_{\text{def}} - (ii|jj)_0}{N_{\text{elec}}(N_{\text{elec}}-1)/2} \tag{5.18}$$

The problem of finding ESP-CIS excitation energies and amplitudes is reduced to solving the eigenvalue equation for $\mathbf{A}_{\text{esp}}$ (**??**) and sampling over the random variate z (Equation 5.5). The method was implemented in the locally modified version of NWChem [125].

The ESP-CIS formulation and its computational implementation was benchmarked against 10^4 CIS calculations on water at 300K and results are presented in the supporting information.

System-specific Computational Details

All electronic structure calculations were performed using the NWChem ([125]) software package.

The 10,000 deformed structures of the H_2O benchmark system was treated with 6-31G basis sets at Hartree-Fock level of theory.

The 1,000 deformed structures of the three PbS NP systems were treated with the LANL2DZ-ECP basis sets and effective core potentials [80] at Hartree-Fock level of theory.

The 1,000 deformed structures of the TKX-50, TADF (**R**)-**1**, PROTAC MD-224, and CDN1162 systems were treated with cc-pVDZ basis sets at DFT level using B3LYP functionals [126].

Results

ESP-CIS Benchmark Calculations on H_2O at 300K

The ESP-CIS method was benchmarked against traditional CIS using H_2O, at 6-31g basis level. The ESP-CIS distribution of lowest excitation energies at 300K is compared to the CIS distribution of energies at the same temperature in Figure 5.3. Both the CIS and ESP-CIS distribution were generated from a population size of 10,000 samples. The mean and standard deviations of these distributions are tabulated in Table 5.1. From these statistical metrics, it can be seen that there is very good agreement between the ESP-CIS and CIS distributions.

	CIS	ESP-CIS
μ (eV)	9.441	9.463
σ (eV)	0.097	0.092

Table 5.1: Mean (μ) and standard deviation (σ) of the $S_0 \rightarrow S_1$ vertical excitation energies (in eV) of H_2O (6-31G basis) calculated using CIS and ESP-CIS ($N_{\text{sample}} = 10^4$) at 300K.

Excited-state Properties of PbS Nanoparticles

Effect of temperature: The probability distribution functions (PDF) and the cumulative distribution functions (CDF) of Pb_4S_4, $Pb_{28}S_{28}$, and $Pb_{43}S_{43}$ ESP-CIS excitation energies in the range of 200 K to 400 K are shown in Figure 5.4. The vertical dashed lines indicate the position of the lowest excitation energy of the minimum-energy reference structure

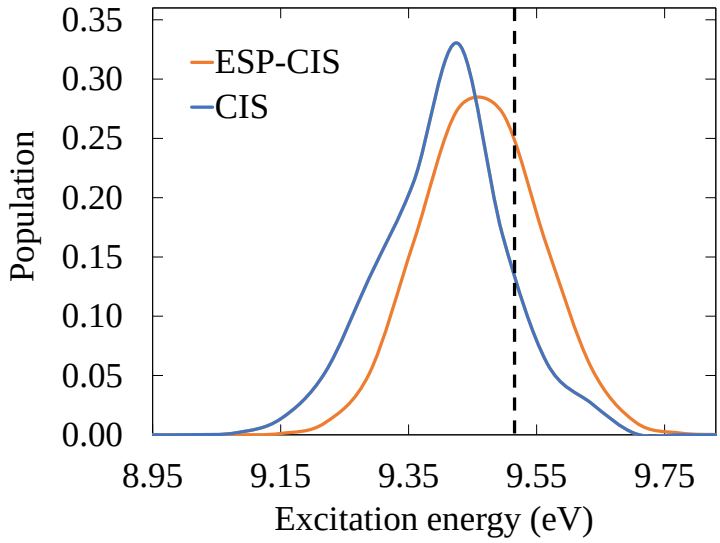

Figure 5.3: Benchmark comparisons of probability distributions of the $S_0 \rightarrow S_1$ vertical excitation energies of H_2O (6-31G basis) calculated using CIS and ESP-CIS ($N_{\text{sample}} = 10^4$), at 300K. Dashed line correspond to the excitation energy of the energy-minimum H_2O structure.

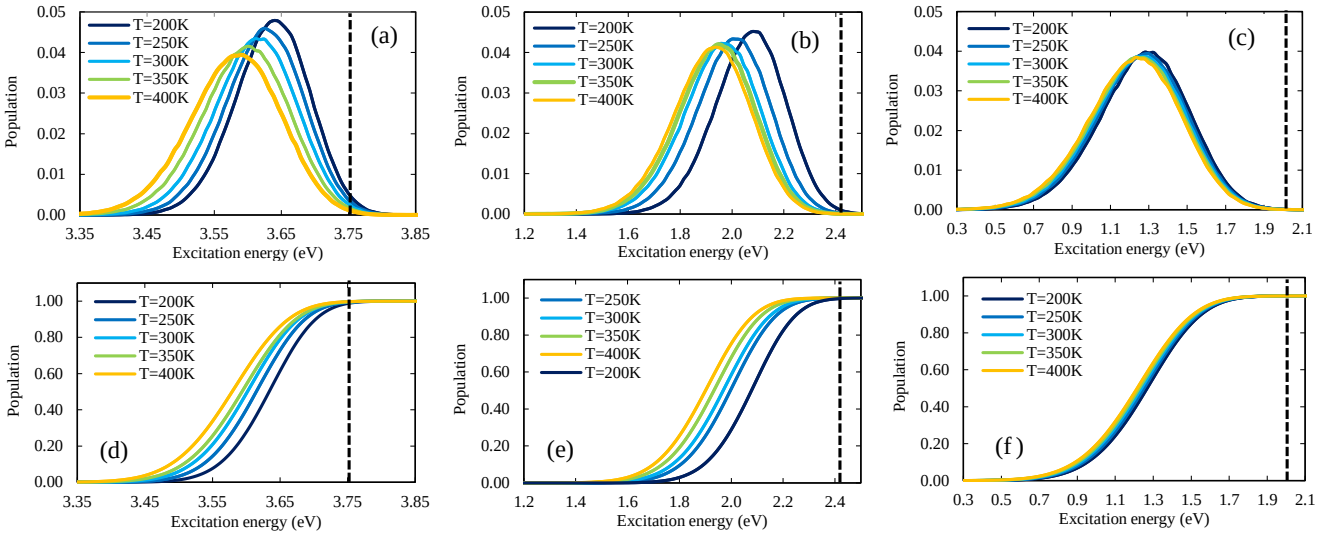

Figure 5.4: Probability distributions and cumulative distributions for the lowest ESP-CIS excitation energies (in eV) of Pb_4S_4, $Pb_{28}S_{28}$, and $Pb_{43}S_{43}$ at 200 K, 250 K, 300 K, 350 K, and 400 K (N_{sample} = 10^6). Vertical dashed lines indicate the respective lowest CIS excitation energies of the energy-minimized reference systems.

corresponding to each PbS NP and corresponds to the 0 K distribution. For all the NPs, the PDFs (Fig. 1 a-c) were found to be red-shifted with respect to the 0 K distribution for higher temperatures. This red-shift in excitation energy with respect to temperature is consistent with previous studies on PbS NPs. [127, 128, 129, 130, 131, 132, 133, 134, 135, 136] Looking at the excitation energy CDFs (Fig. 1 d-f), it can be seen than in nearly all cases, $>$ 90% of the calculated ESP-CIS excitation energies are red-shifted with respect to the 0 K distribution. This fact demonstrates

that the reference structure is pathological and is not an adequate metric for representing the global distribution of excitation energies at non-zero temperatures. Figure 5.5 presents a breakdown of some of the key statistical metrics of these distributions of ESP-CIS excitation energies as a function of temperature: the mean, mode, standard deviation, and range. All the four metrics were found to scale linearly with respect to temperature. The mean and the mode were found to decrease with increasing temperature, while the standard deviation and range were found to exhibit the opposite trend and increased with temperature.

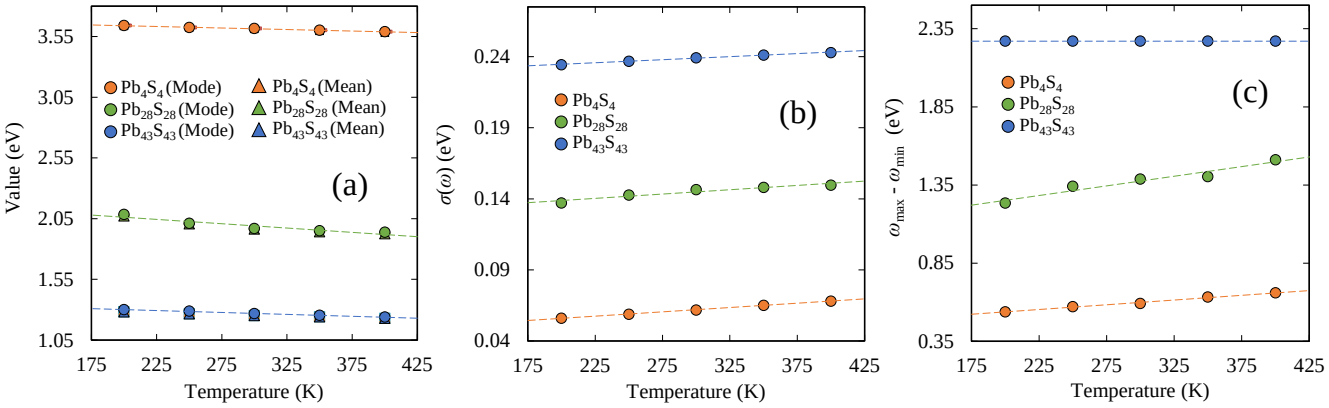

Figure 5.5: Effect of temperature on (a) mean and modes, (b) standard deviations (σ), and (c) ranges (all in eV) of excitation energies for Pb_4S_4, $Pb_{28}S_{28}$, and $Pb_{43}S_{43}$ NPs from 200 K to 400 K using 10^6 ESP-CIS samples using the LANL2DZ-ECP basis set and effective core potentials.

Skewness and sub-Gaussian character: The central moments of a distribution give important information about the distributions spread and symmetry. [81] The skewness $s = \mu_3/\sigma^3$ and kurtosis $\kappa = \mu_4/\sigma^4$ are obtained from the third (μ_3) and fourth (μ_4) central moments and are presented in Figure 5.6. The skewness of the data (Fig. 3a) shows that unlike a Gaussian distribution, the present distribution is both non-symmetric and is skewed negatively. For each NP, the skewness was found to increase monotonically with temperature, indicating that the distribution is significantly non-Gaussian at higher temperatures. The analysis from the kurtosis also exhibit similar trends. The kurtosis of a Gaussian distribution is exactly three, and distributions with kurtosis lower than that value are classified as sub-Gaussian. [81] The kurtosis of the present distributions (Fig. 3b) all exhibit values much lower than three, indicating the distributions are sub-Gaussian in nature. The analysis from both the PDFs (Figure 5.4) and skewness (Figure 5.6) indicates than any random distortion from the reference structure is most likely to result in lowering the excitation energy of these NPs.

Effect of size: From Figure 5.4 and Figure 5.5, it can be seen that larger NPs have a broader range of possible excitation energies. This trend is expected, owing to the increase in the number of low-frequency vibrational degrees of freedom in these bigger NPs. For all NP sizes, the distributions also broaden with increasing temperature as the

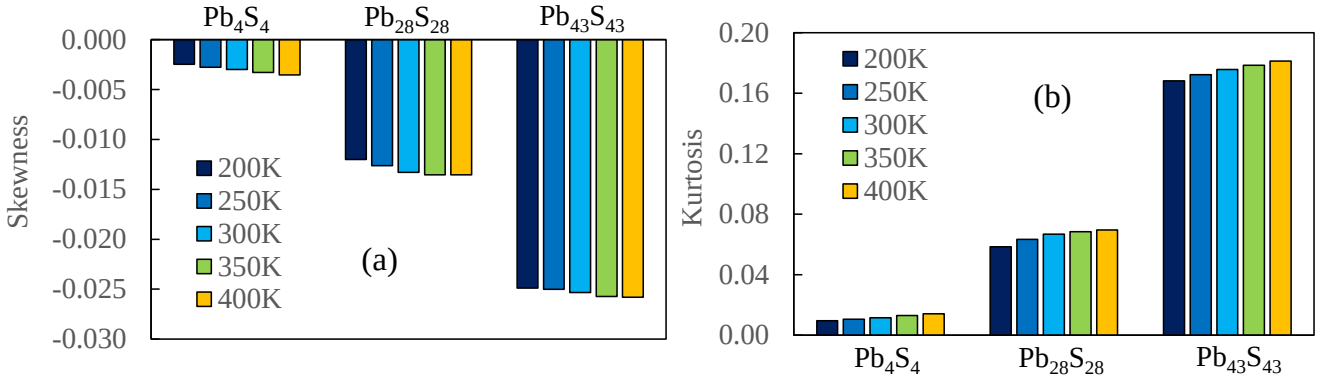

Figure 5.6: (a) Skewness and (b) Kurtosis of ESP-CIS excitation energies (in eV) of Pb_4S_4, $Pb_{28}S_{28}$, and $Pb_{43}S_{43}$ at 200 K, 250 K, 300 K, 350 K, and 400 K calculated with ESP-CIS ($N_{\text{sample}} = 10^6$) using the LANL2DZ-ECP basis set and effective core potentials.

higher-energy conformations become thermally accessible. The extent of broadening in the ensemble with respect to size and temperature has been quantified by the standard deviation and the range of these distributions. For example, while Pb_4S_4 spans a range of only 0.59 eV at 300 K, $Pb_{43}S_{43}$ has a range nearly four times as large, by comparison. From Figure 5.6, it is also seen that both the skewness and kurtosis of the distribution increases with size of the NP.

Efficiency of the ESP-CIS method: Figure 5.7 shows the timing results from performing 10^6 ESP-CIS samples for the three PbS NPs at 300 K, compared to the estimated timing for 10^6 conventional CIS samples based on the computational time of the single CIS calculation performed. Across the three PbS NPs, the ESP-CIS method was between 9,000 and 200,000 times more efficient than sampling using an equivalent number of CIS calculations. In general, we expect this ratio to increase even more as both the size of the system and the number of samples further increase. The timing analysis illustrates the power of the ESP-CIS method for performing efficient sampling.

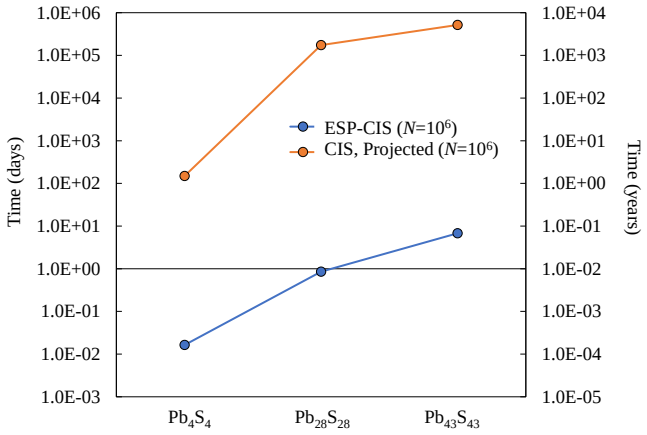

Figure 5.7: Comparison of timing data in days (left y-axis, log-scale) and seconds (right y-axis, log scale) for Pb_4S_4, $Pb_{28}S_{28}$, and $Pb_{43}S_{43}$ NPs using CIS vs. ESP-CIS. Timing shown is for ($N_{\text{sample}} = 10^6$) ESP-CIS calculations, and an approximate projection of the timing for ($N_{\text{sample}} = 10^6$) CIS calculations using the LANL2DZ-ECP basis set and effective core potentials.

Importance of large sample size: In order to demonstrate the need for large sample size for obtaining accurate statistics, a series of excitation energy distributions for $Pb_{43}S_{43}$ NP at 300 K were calculated using ESP-CIS with a number of sampling points (N_{sample}) equal to 10^2, 10^3, 10^4, and 10^6. These distributions are shown in Figure 5.8. The effect of increasing the number of sampling points is apparent: until N_{sample} is in the range of $10^5 - 10^6$, the

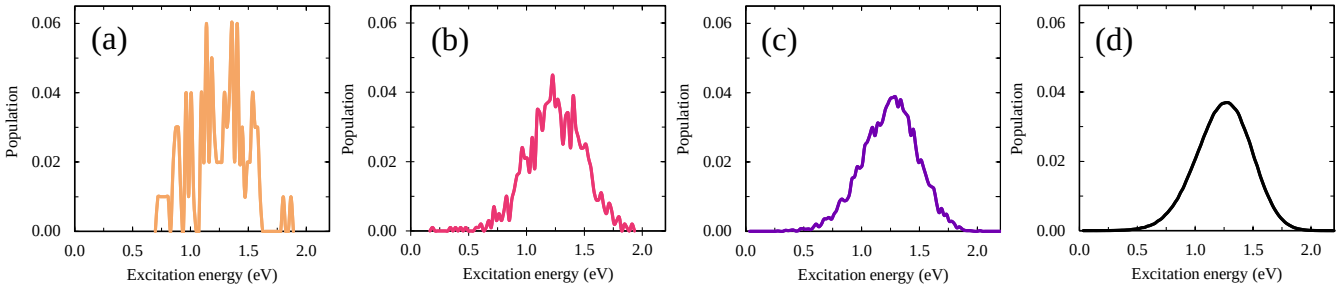

Figure 5.8: A comparison of excitation energy (eV) distributions obtained for $Pb_{43}S_{43}$ at 300 K using ESP-CIS with (a) $N_{sample} = 10^2$, (b) $N_{sample} = 10^3$, (c) $N_{sample} = 10^4$, and (d) $N_{sample} = 10^6$.

distributions exhibit significant noise and are not well-converged. Furthermore, large portions of the distribution, particularly at the tails, have no population where it can be seen that there ought to be from using a larger number of sampling points. This result highlights the importance of large sample sizes in order to obtain a reliably accurate distribution and statistics of properties.

Excited-state Properties of Energetic Material TKX-50

Energetic materials (EMs) are a class of compounds which can store large amounts of chemical energy that can be released through combustion or detonation. EMs have many important modern applications, including mining, construction, welding, and defense [137].

Two of the largest goals of developing better EMs for these applications are optimizing their detonation properties, and improving their safety characteristics.

In 2012, Fischer and coworkers were able to synthesize a new EM, dihydroxylammonium 5,5′-bitetrazole-1,1′-diolate (TKX-50) which satisfied these goals [138]. They found that TKX-50 had superior thermal and mechanical insensitivity compared to EMs with widespread industrial use such as RDX [139] and PETN [139]. Additionally, it was able to maintain those insensitivities without compromising its energy density, detonation pressure, and detonation velocity relative to those other EMs. Preliminary toxicity testing showed that TKX-50 also seems to have relatively low cytotoxicity, which is an important green characteristic for EMs which can often end up having residual presence in the environment.

Temperature-dependent stability of EMs is very important for their safe use, and HOMO-LUMO gap can been used as a first-order indicator of kinetic stability [140]. Molecules with larger HOMO-LUMO gaps tends to have have

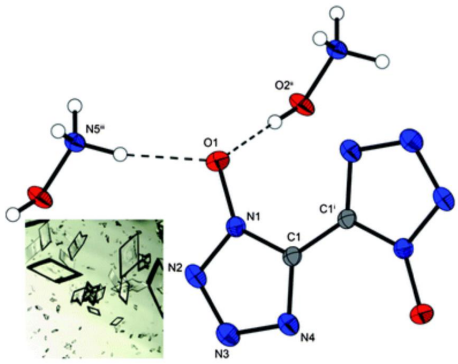

Figure 5.9: Solid-state structure of TKX-50 at 100K.

kinetic stability and lower chemical reactivity. For this reason, HOMO-LUMO gap can be a good indicator for toxicity and bioavailability of organic molecules [141].

For these reasons, we wanted to use the ESP-CIS method to investigate how increasing temperature changes the electronic energy gaps in TKX-50.

Figure 5.10 shows the PDFs and CDFs of TKX-50 HOMO-LUMO gap energies in the range of 250K-450K.

Both the mean and the mode of the PDF are red-shifted with respect to the energy-minimized reference structure. The range of thermally-accessible HOMO-LUMO gaps does not change significantly with increasing temperature. However, in this temperature region, the calculated gap energies span a range of about 4 eV, indicating that the HOMO-LUMO gap of TKX-50 appears to be very sensitive to deformations to its chemical structure.

From the CDF of HOMO-LUMO gap energies, it can be seen that for all temperatures, approximately 95% of the sampled ESP HOMO-LUMO gap energies were below the reference HOMO-LUMO gap. This indicates that the 0K reference structure poorly represents what the frontier orbital energy levels look like at finite temperature.

Figure 5.11 shows how the mean HOMO-LUMO gap energy in TKX-50 changes with increasing temperature. Error bars indicate one σ standard deviation from the mean. The mean HOMO-LUMO gap decreases linearly by only about 100 meV from 250K-450K. While standard deviation increases with increasing temperature, the systematic shifting of the PDF is relatively small.

Table 5.2 is a table of the first eight statistical moments of the HOMO-LUMO gap distribution for each temperature of interest. As indicated by the relatively high magnitude of odd central moments, these PDFs exhibit strongly non-Gaussian behavior.

Figure 5.12 shows the distribution corresponding to the first 15 ESP-CIS excitation energies in TKX-50 from 250K to 450K. It can be seen that there is an abrupt broadening of the distribution from 250K-300K, followed by more gradual broadening with further increasing temperature.

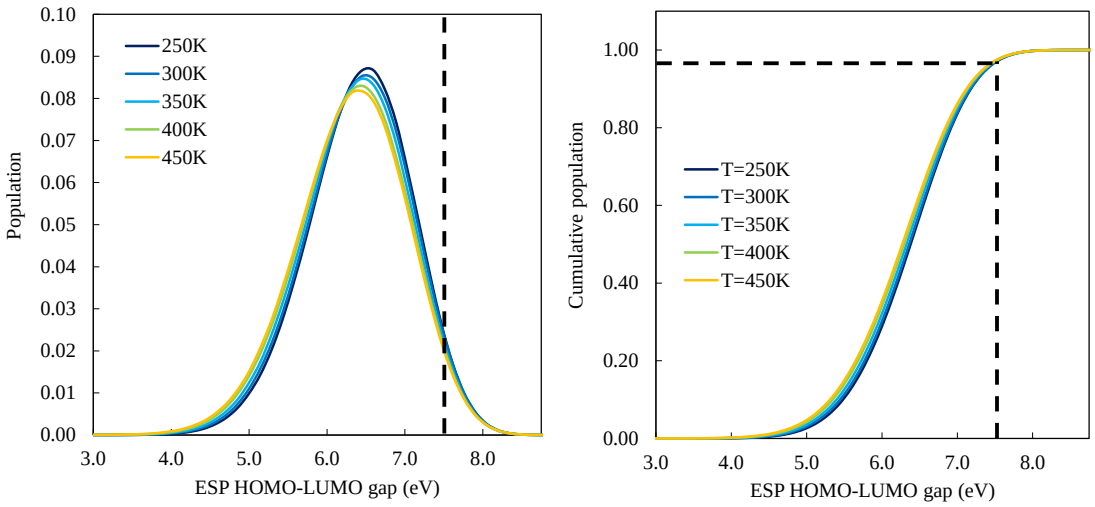

Figure 5.10: Probability distributions and cumulative distributions for the ESP HOMO-LUMO gaps (in eV) of TKX-50 at 250 K, 300 K, 350 K, 400 K, and 450 K ($N_{\text{sample}} = 10^6$). Vertical dashed lines indicate the respective HOMO-LUMO gap of the energy-minimized reference system.

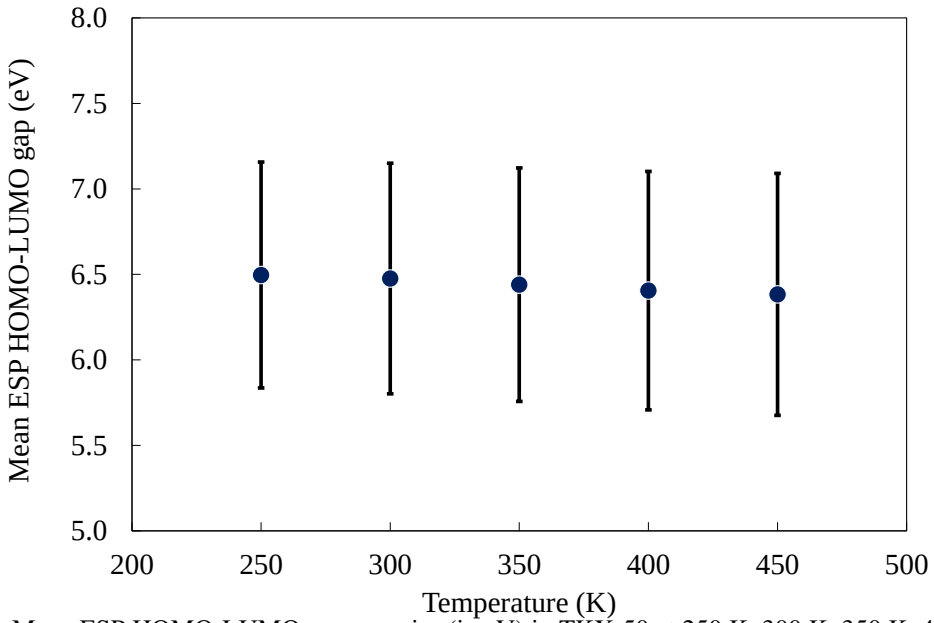

Figure 5.11: Mean ESP HOMO-LUMO gap energies (in eV) in TKX-50 at 250 K, 300 K, 350 K, 400 K, and 450 K. Error bars correspond to one standard deviation from the mean.

Excited-state Properties of (R)-1 TADF Organic Molecule

Thermally activated delayed fluorescence (TADF) is a type of photo-emission in which an electronic system absorbs thermal energy from its surroundings while in the triplet state, and then undergoes reverse intersystem crossing (RISC)

Table 5.2: First eight central moments (in eV) of the HOMO-LUMO gap distributions in TKX-50 at 250 K, 300 K, 350 K, 400 K, and 450 K ($N_{\text{sample}} = 10^6$).

Moment (eV)	250K	300K	350K	400K	450K
1	6.496	6.476	6.440	6.405	6.383
2	0.661	0.674	0.683	0.697	0.708
3	-0.418	-0.429	-0.438	-0.451	-0.462
4	0.870	0.889	0.902	0.923	0.938
5	-0.790	-0.810	-0.827	-0.853	-0.872
6	1.046	1.070	1.089	1.118	1.138
7	-1.046	-1.073	-1.099	-1.135	-1.160
8	1.206	1.235	1.262	1.300	1.326

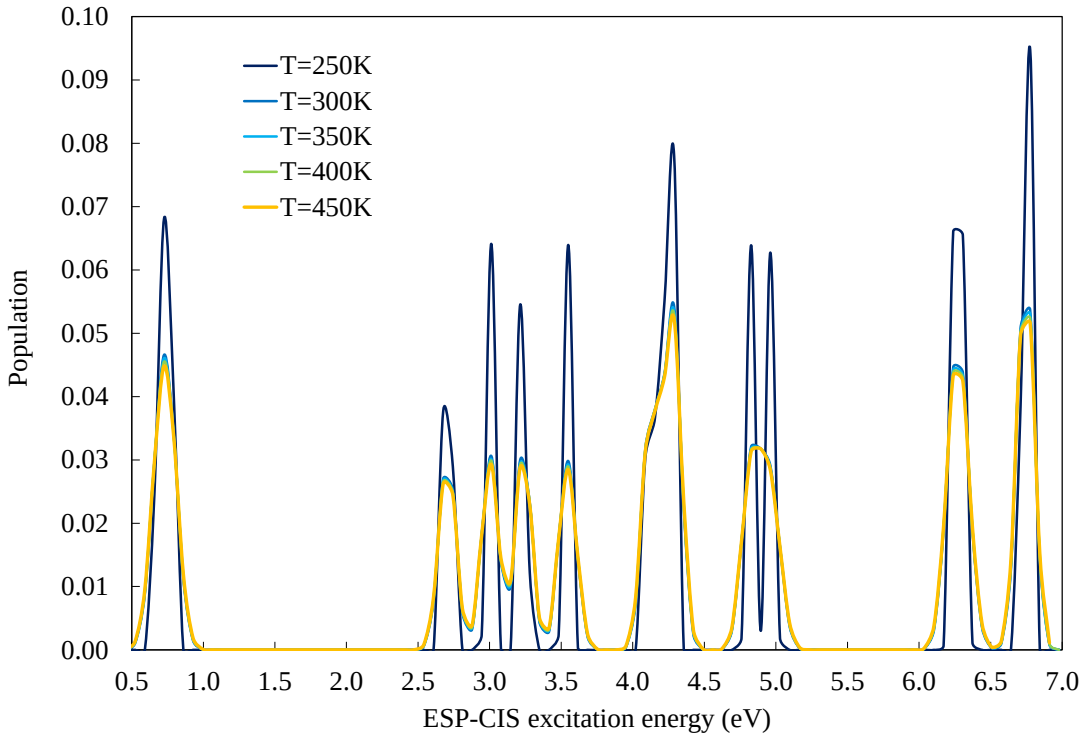

Figure 5.12: Probability distributions for the first 15 ESP-CIS excitation energies (in eV) of TKX-50 at 250 K, 300 K, 350 K, 400 K, and 450 K ($N_{\text{sample}} = 10^6$).

to transition to a singlet excited state [142]. From the singlet state, the excited electron then de-excites and the system fluoresces.

TADF emitters have unique optical and electronic properties due to the small energy gap between their singlet and triplet excited states [143]. This class of photoemitters can be very advantageous, as RISC increases fluorescence lifetimes, which makes harvesting their excitons much more efficient as compared to other emitters.

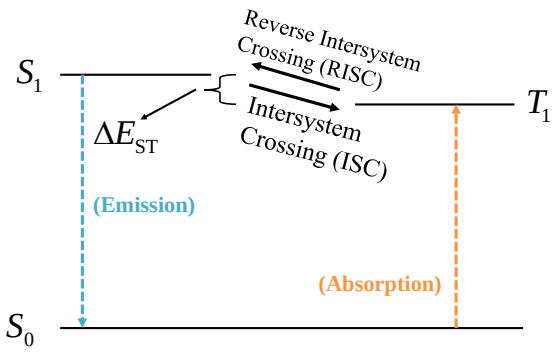

Figure 5.13: Schematic depiction of a general reverse-intersystem crossing process.

Due to their unique properties, TADF materials show great promise for use in optoelectronic devices such as organic light emitting diodes (OLEDs) and as biological labels [144], owing to their typically low cytotoxicity [145]. More recently, there has been a growing interest in small organic molecule emitters featuring circularly polarized luminescence emission (CPL-SOMs) [143]. CPL-SOMs would allow for development of even more advanced optoelectronic devices, such as 3D digital displays [146], data storage [147], and in circular dichroism spectroscopy [148].

In 2016, Feuillastre et. al. were able to develop the first purely organic TADF molecule where CPL is enabled on a single acting achiral chromophore through chiral perturbation [149]. They were able to synthesize the TADF emitter in question (named simply (**R**)-**1**) using a one-pot synthesis, and found it has high quantum efficiency (up to 74%) and fluorescence lifetimes on the order of μs time scales.

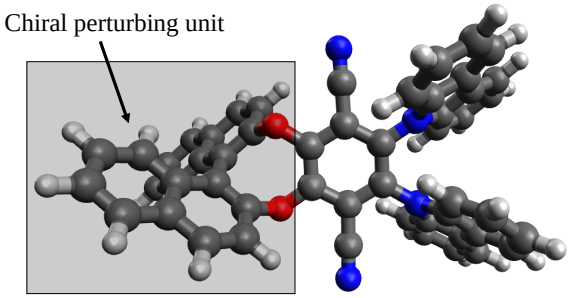

Figure 5.14: Structure of the (**R**)-**1** CPL-TADF emitter. The chiral perturbing unit is in the highlighted box. Molecule modeled in Avogadro [150].

When it comes to determining good potential TADF material candidates, one of the difficulties is in predicting where the HOMO and LUMO energy levels should be. In general though, it has been observed that spatially separated HOMO and LUMO orbitals is desirable for efficient RISC processes [143]. For this reason, we are interested in investing the HOMO-LUMO gap and low-lying electronic energy gaps in (**R**)-**1**, and see how fluctuations in temperature

Table 5.3: First eight central moments (in eV) of the HOMO-LUMO gap distributions in TADF (**R**)-**1** at 275 K, 300 K, 325 K, 350 K, and 375 K ($N_{\text{sample}} = 10^6$).

Moment (eV)	275K	300K	325K	350K	375K
1	3.090	3.086	3.082	3.078	3.071
2	0.125	0.132	0.137	0.143	0.149
3	-0.191	-0.198	-0.205	-0.211	-0.215
4	0.268	0.277	0.286	0.293	0.299
5	-0.339	-0.349	-0.360	-0.367	-0.374
6	0.406	0.417	0.430	0.437	0.445
7	-0.469	-0.481	-0.496	-0.503	-0.511
8	0.528	0.541	0.558	0.566	0.575

effect them.

Figure 5.15 shows the PDFs and CDFs of **R**)-**1** HOMO-LUMO gap energies in the range of 275K to 375K.

While the mean HOMO-LUMO gap decreases by 20 meV from 275K-375K (Figure 5.16), the modes of the distribution at these temperatures are blue-shifted with respect to the energy-minimized reference structure. Thermally-accessible HOMO-LUMO gaps at these temperatures span a range of around 1 eV.

From the CDFs, it can be seen that for all temperatures, just under 50% of the sampled HOMO-LUMO gaps were below the reference HOMO-LUMO gap.

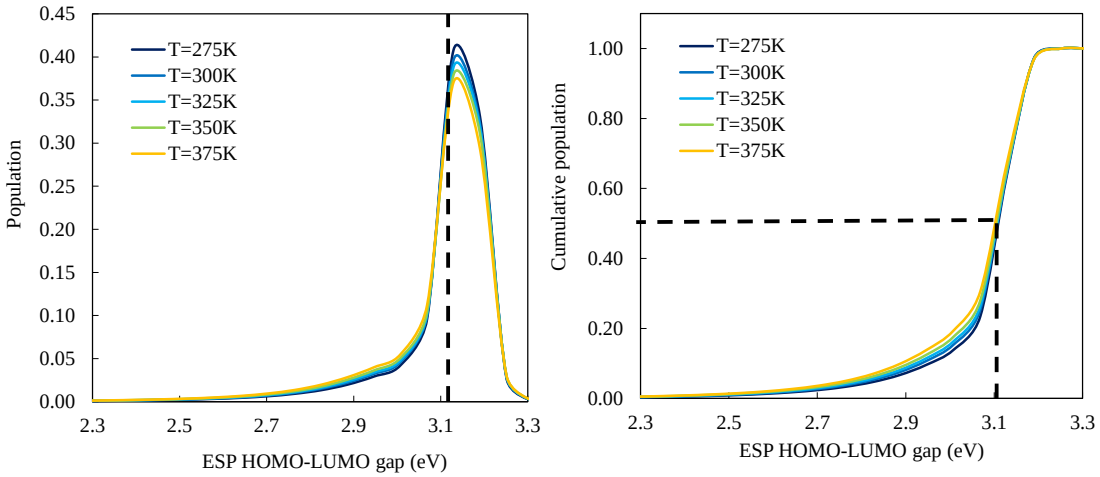

Figure 5.15: Probability distributions and cumulative distributions for the ESP HOMO-LUMO gaps (in eV) of TADF (**R**)-**1** at 275 K, 300 K, 325 K, 350 K, and 375 K ($N_{\text{sample}} = 10^6$). Vertical dashed lines indicate the respective HOMO-LUMO gap of the energy-minimized reference system.

Figure 5.17 shows the distribution corresponding to the first 15 singlet and triplet ESP-CIS excitation energies in **R**)-**1** from 275K to 375K. There is small, gradual broadening of ESP-CIS excitation energies over this temperature

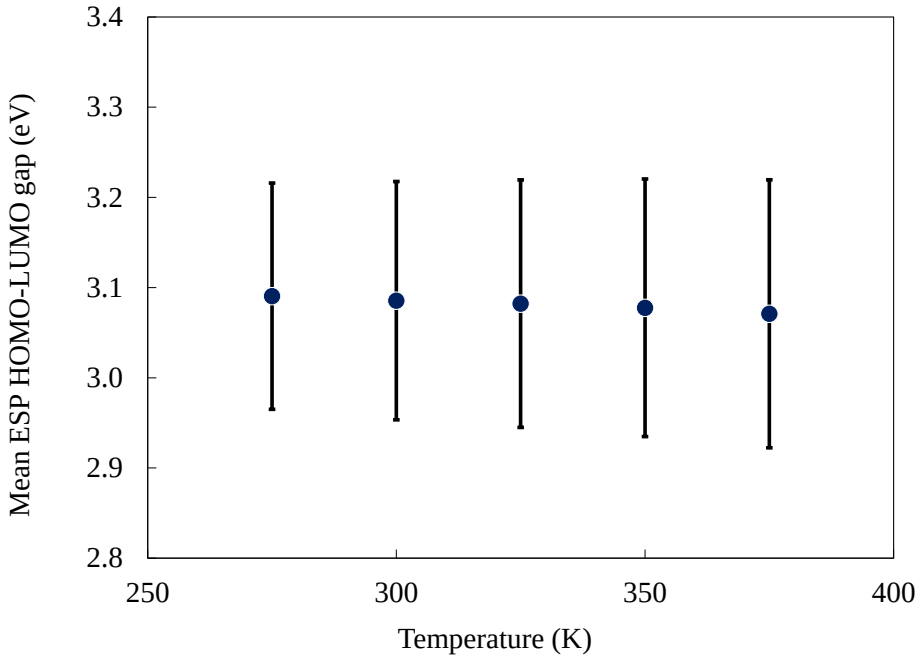

Figure 5.16: Mean ESP HOMO-LUMO gap energies (in eV) in TADF (**R**)-**1** at 275 K, 300 K, 325 K, 350 K, and 375 K. Error bars correspond to one standard deviation from the mean.

range. In the bottom figure, the excitation axis is focused in on the region of the first few singlet and triplet ESP-CIS excitations.

Important to note is how the line spectrum of the reference structure (indicated by the dashed lines) fails to illustrate all the features of the thermally-broadened spectra. There is a large singlet-triplet overlap in S_1-T_1 energy space around the first ESP-CIS roots, and weak singlet-triplet overlap around 3.0 eV.

Excited-state Properties of PROTAC MD-224

Human murine double minute 2 (MDM2) protein is a primary inhibitor of tumor suppressor p53 and has been a recent target for cancer therapy [151]. By functioning as an E3 ligase, MDM2 binds to and ubiquitinates p53, causing degradation of p53. The binding of MDM2 to p53 blocks interaction of p53 with targeted DNA molecules, transports p53 from the nucleus to the cytoplasm which decreases transcriptional activity of p53.

Since MDM2 inhibits the tumor suppressor function of p53 through direct proteinprotein interaction, there is a high level of interest in developing small-molecule inhibitors of the MDM2-p53 proteinprotein interaction. One avenue is through PROteolysis TArgeting Chimera molecules (PROTACs). The first PROTAC-like molecule was developed in 2012 my Molle and coworkers [152], though they did name it as such at the time. PROTACs are two-headed molecules

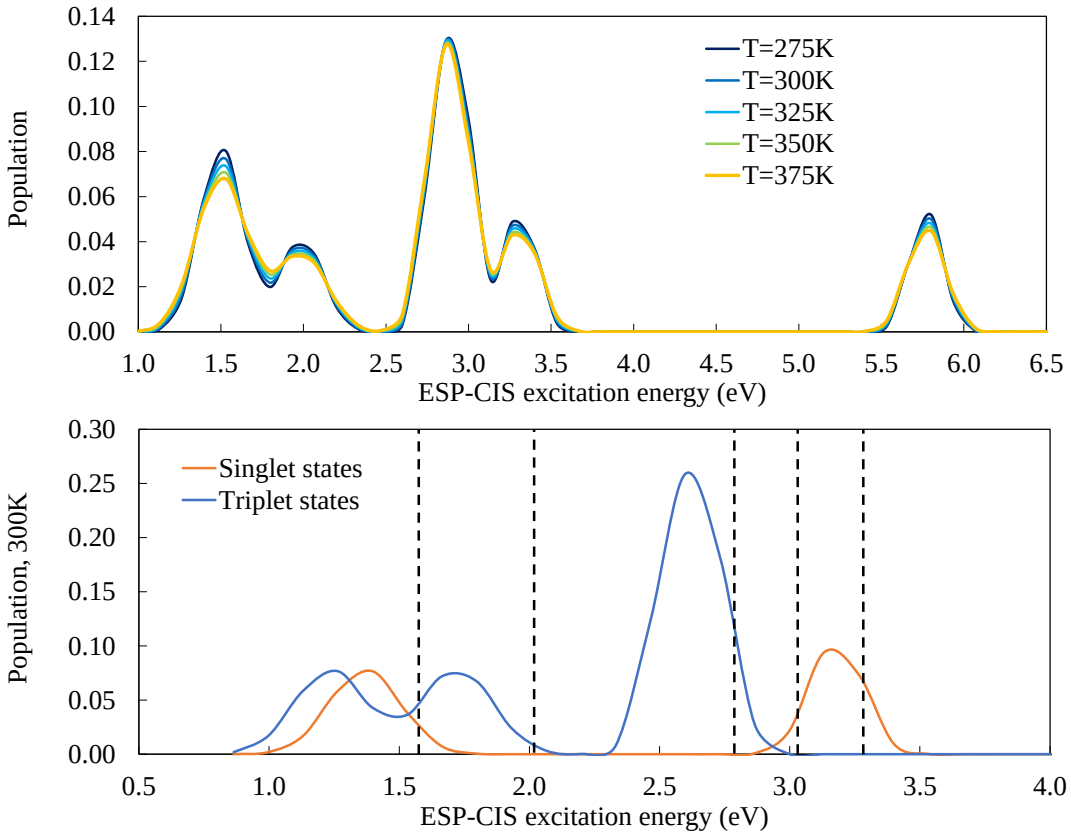

Figure 5.17: Probability distributions for the first 15 ESP-CIS excitation energies (in eV) of TADF **R**)-**1** at 275 K, 300 K, 325 K, 350 K, and 375 K ($N_{\text{sample}} = 10^6$).

capable of removing specific unwanted proteins. They consist of two covalently linked protein-binding molecules. The first binds to an E3 ubiquitin ligase, and the second binds to a target protein meant for degradation.

Recruitment of E3 ligase to the target protein results in ubiquitination and subsequent degradation of the target protein by the proteasome. This property allows PROTACS to be used as effective cancer therapy drugs as they can allow for the targeting of a broader range of proteins with fewer off-target effects compared to therapies which continuously expose the target proteins with small molecule inhibitors [153].

A PROTAC molecule by the name MD-224 was developed in 2018 by Li and coworkers [151] which has been shown to induce degradation of MDM2, inhibiting cell growth, and results in the apoptosis of leukemia cells. Li et. al. was able to demonstrate that MD-224 could regress tumors in vivo in mice models at well-tolerated doses.

In vivo, PROTAC MD-224 will exist in a distribution of thermally accessible structures due to interaction with temperature and solvent. It is important to understand what the distribution of corresponding energy gaps will be to predict its ability to interact with other chemical species in vivo. We have used the ESP-CIS method to calculation

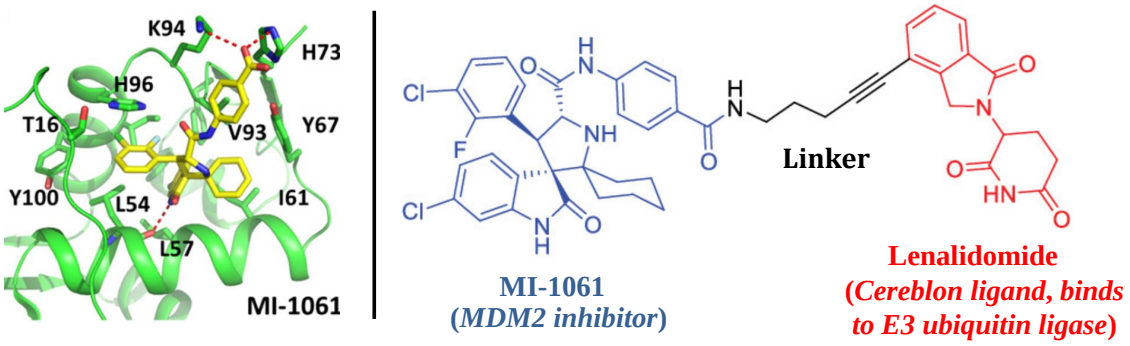

Figure 5.18: **Left**: MI-1061 molecule bound to MDM2 protein. **Right**: PROTAC MD-224 molecule.

these distributions.

Figure 5.19 shows the PDFs and CDFs of MD-224 HOMO-LUMO gap energies in the range of 280K-320K.

The mean and mode of the PDFs are blue-shifted with respect to energy-minimized reference structure at these temperatures. Interestingly, the HOMO-LUMO gap PDFs appear to be highly-invariant to temperature change over the range of 280K-320K.

Thermally-accessible HOMO-LUMO gaps span a range of only around 0.3 eV and only about 40% of the sampled HOMO-LUMO gaps were below the reference HOMO-LUMO gap. This is evidence that MD-224 is likely to be very stable in-vivo.

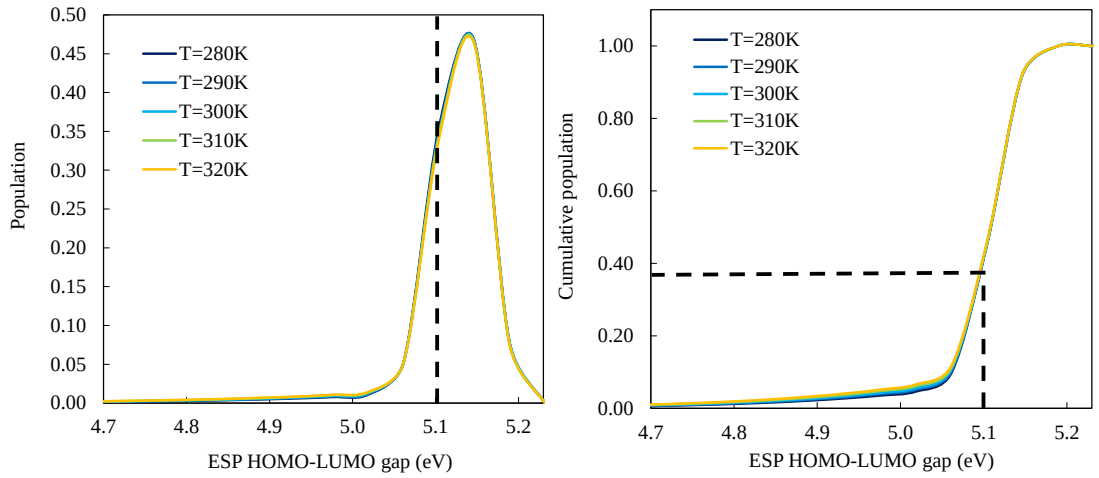

Figure 5.19: Probability distributions and cumulative distributions for the ESP HOMO-LUMO gaps (in eV) of MD-224 at 280 K, 290 K, 300 K, 310 K, and 320 K ($N_{\text{sample}} = 10^6$). Vertical dashed lines indicate the respective HOMO-LUMO gap of the energy-minimized reference system.

Figure 5.20 shows the distribution corresponding to the first three ESP-CIS excitation energies in MD-224 from

280K-320K.

There is gradual broadening of the ESP-CIS excitation energies with increasing temperature. Additionally the line spectrum of the reference structure fails to illustrate all the features of the thermally-broadened spectra. In particular, the first ESP-CIS excitation energy distribution is roughly twice as broad as the third ESP-CIS excitation energy distribution.

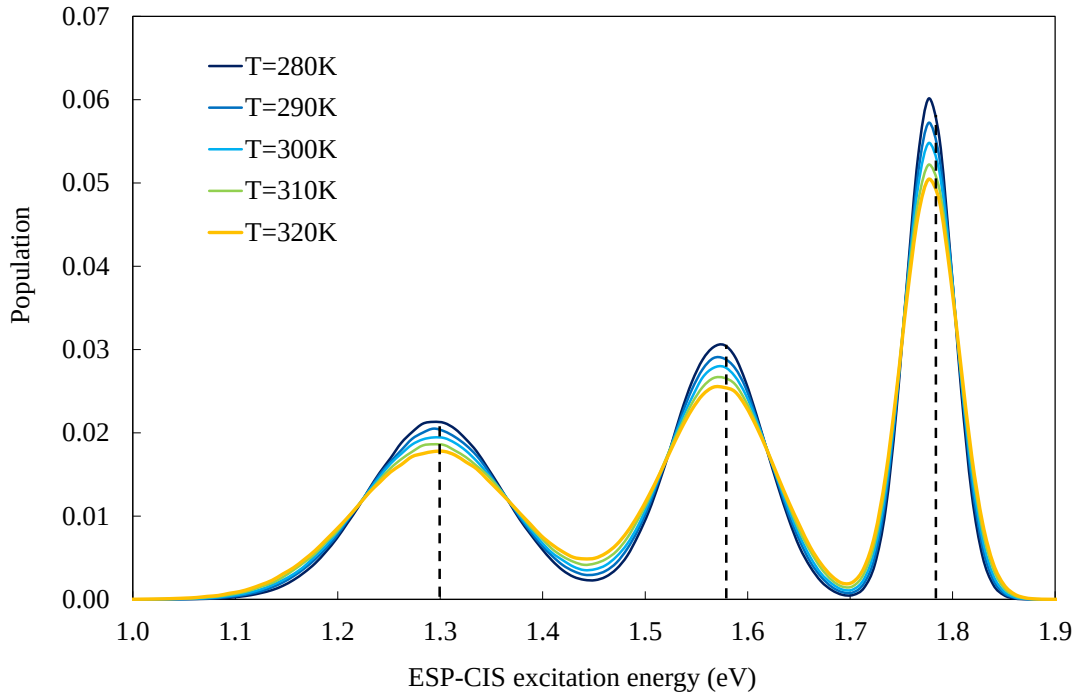

Figure 5.20: Probability distributions for the first three ESP-CIS excitation energies (in eV) of MD-224 at 280 K, 290 K, 300 K, 310 K, and 320 K ($N_{\text{sample}} = 10^6$). Vertical lines correspond to theline spectra of the minimum energy reference structure.

Excited-state Properties of SERCA Activator CDN1163

Alzheimers Disease (AD) and Parkinsons Disease (PD) both lead to loss of cognitive function, and effect millions of people around the world [154]. while treatments which relieve symptoms do exist, there are none that halt the progression of the disease, and a cure for either disease does not currently exist.

Endoplasmic reticulum (ER) stress is strongly linked to both AD and PD. ER stess is caused by dyshomeostasis of Ca^{2+} ions, and extreme ER stress coincides with Unfolded Protein Response (UPR), and eventually neuron death [155].

Repairing the Ca2+ homeostasis of the damaged neurons presents a good pathway to alleviating the ER stress and treating AD or PD. Compromised sarco/endoplasmic reticulum Ca^{2+}-ATPase (SERCA) has been identified as a major cause of ER stress and neuron loss in AD and PD.

Sarco/endoplasmic reticulum Ca^{2+}-ATPase (SERCA) protein is responsible for Ca^{2+} ion transport in muscular tissue. Low ER calcium caused by dysfunctional SERCA is a major cause of the UPR signaling cascade and subsequent ER stress. [156] The key point is that repairing SERCA activity seems like a good pathway towards restoring Ca^{2+} homeostasis and treating AD and PD symptoms.

CDN1163 is a quinoline derivative discovered through medicinal chemistry optimization in 2017 by Dahl [155]. CDN1163 is a small molecule SERCA activator, which binds allosterically to SERCA protein.

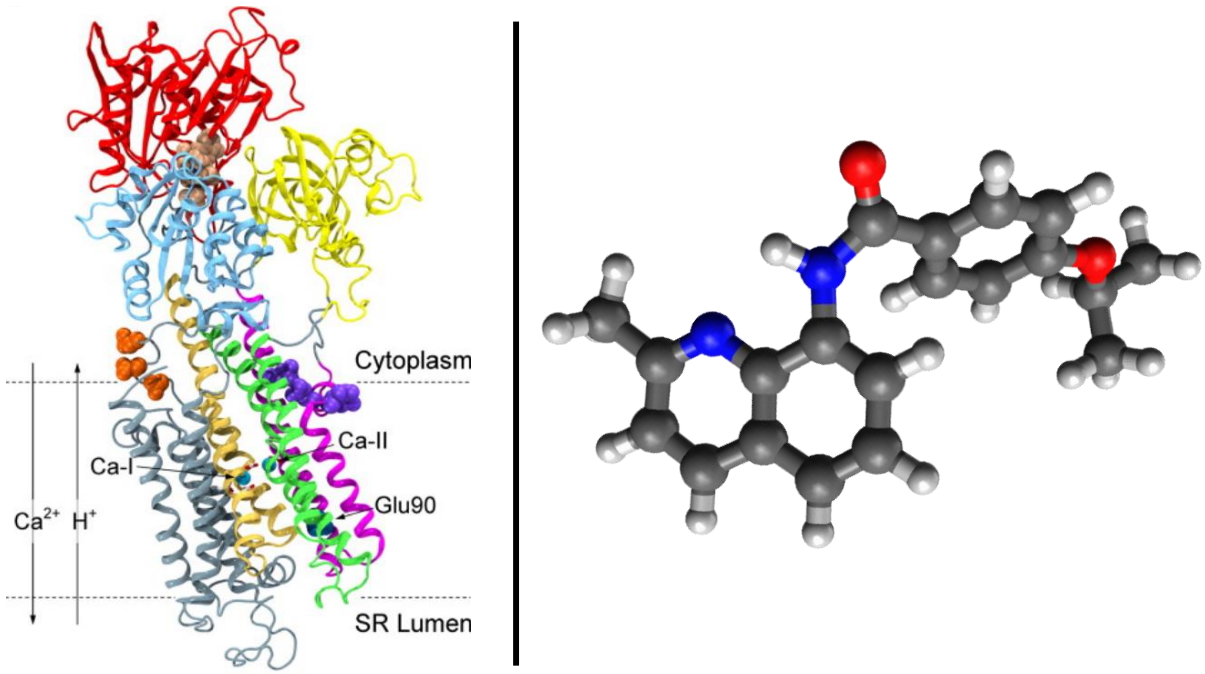

Figure 5.21: **Left**: SERCA protein in the Ca^{2+}/ATP bound state. **Right**: CDN1163 molecule.

Dahl showed that CDN1163 can raise ER Ca^{2+} concentration in-vitro. which has was developed for treating AD and PD. It has been shown to be efficacious in mouse and rat models of AD and PD [155].

As with the previous investigation of a drug molecule, CDN1163 will exist in a distribution of thermally accessible structures due to interaction with in-vivo temperature and solvent. We again have used the ESP-CIS method in order to calculation ensemble distributions of energy gaps for CDN1163.

Figure 5.22 shows the PDFs and CDFs of CDN1163 HOMO-LUMO gap energies in the range of 280K-320K.

While the mode of the distribution aligns with the energy-minimized reference structure, the means are broad and dramatically red-shifted. The HOMO-LUMO gap energy PDFs for this system at these temperatures have a particularly interesting shape, with a sharp peak near the energy minimum reference HOMO-LUMO gap, followed

Table 5.4: First eight central moments (in eV) of the HOMO-LUMO gap distributions in CDN1163 at 280 K, 290 K, 300 K, 310 K, and 320 K ($N_{\text{sample}} = 10^6$).

Moment (eV)	280K	290K	300K	310K	320K
1	3.932	3.863	3.848	3.758	3.736
2	0.479	0.565	0.614	0.636	0.645
3	-0.596	-0.712	-0.785	-0.772	-0.775
4	0.807	0.956	1.044	1.039	1.045
5	-0.976	-1.146	-1.244	-1.232	-1.237
6	1.136	1.320	1.423	1.411	1.415
7	-1.282	-1.474	-1.580	-1.565	-1.569
8	1.416	1.612	1.718	1.701	1.704

by a very long tail. Thermally-accessible HOMO-LUMO gaps span a range of around 4 eV for these PDFs. From the CDFs, it can be seen that for all temperatures, nearly 90% of the sampled HOMO-LUMO gaps were below the reference HOMO-LUMO gap.

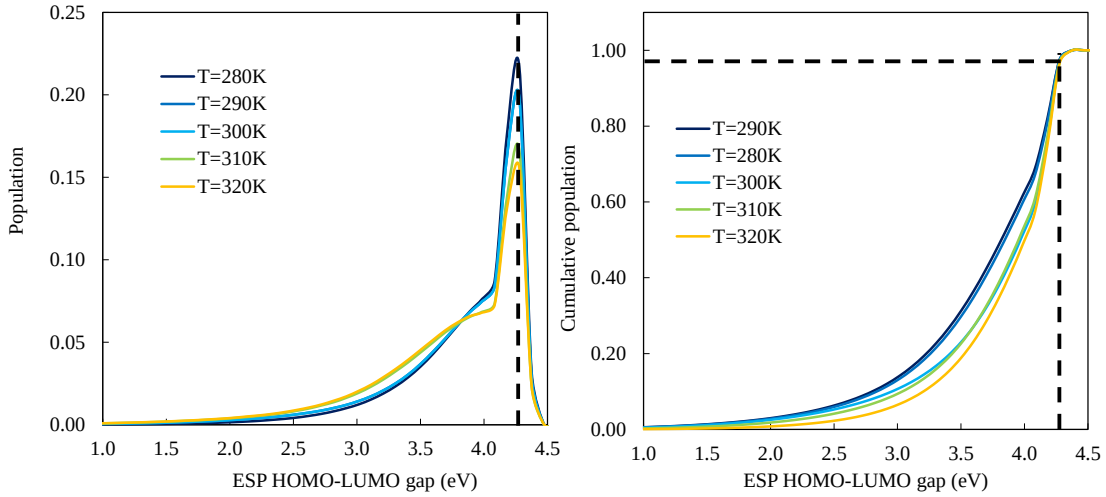

Figure 5.22: Probability distributions and cumulative distributions for the ESP HOMO-LUMO gaps (in eV) of CDN1163 at 280 K, 290 K, 300 K, 310 K, and 320 K ($N_{\text{sample}} = 10^6$). Vertical dashed lines indicate the respective HOMO-LUMO gap of the energy-minimized reference system.

Figure 5.23 shows how the mean HOMO-LUMO gap energy in CDN1163 changes with increasing temperature.=, and Table 5.4 is a table of the first eight statistical moments of the HOMO-LUMO gap distribution for each temperature of interest.

While the standard deviation does increase with increasing temp, the mean HOMO-LUMO gap decreases only by 200 meV from 280K-320K. These PDFs exhibit odd central moments that are both negative and of appreciable magnitude, indicating strongly non-Gaussian behavior, apparent from how the PDFs themselves appear.

Figure 5.24 shows the distribution corresponding to the first ten ESP-CIS excitation energies in CDN1163 from

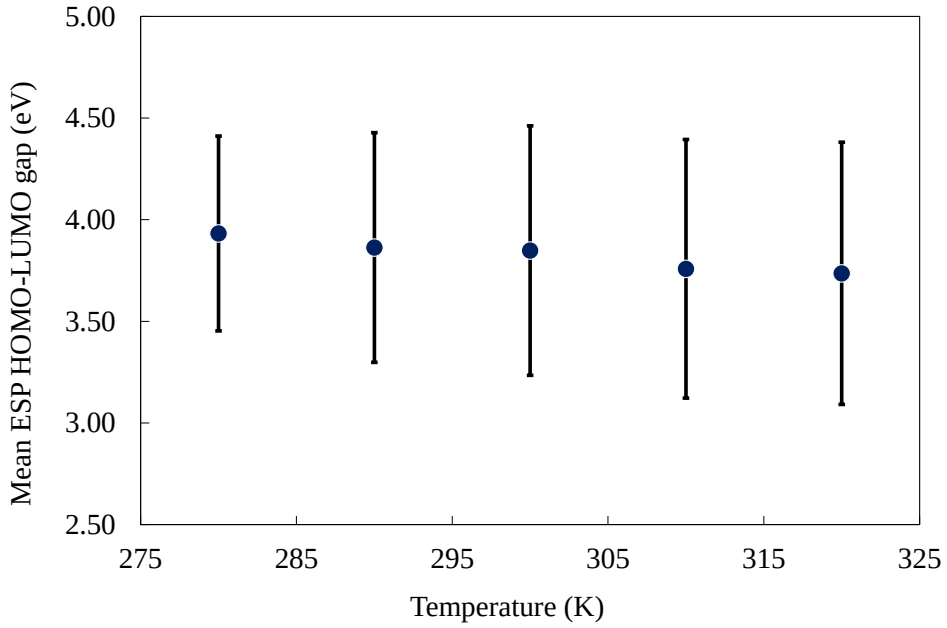

Figure 5.23: Mean ESP HOMO-LUMO gap energies (in eV) in CDN1163 at 280 K, 290 K, 300 K, 310 K, and 320 K. Error bars correspond to one standard deviation from the mean.

280K-320K. The ESP-CIS excitation energies smoothly broaden over this temperature range. The line spectrum of the reference structure, indicated again by vertical dashed lines, fails to capture the effect of some excitations merging together, forming a convolution of distributions.

Conclusions

In conclusion, this work presented the effect of both temperature and particle size on the distribution of excitation energies in PbS quantum dots. The distributions at non-zero temperatures were found to be significantly red-shifted with respect to the 0 K distribution, and were sub-Gaussian in nature with a negative skewness. This effect was found to be more pronounced in bigger dots. The mean and mode of the distributions were found to linearly decrease with temperature. In contrast, the range and the standard deviations were found to increase linearly with temperature. All the calculations were performed using the newly-developed effective stochastic potential-configuration interaction singles (ESP-CIS) method, and a total of 15 million excitation energy calculations were performed (1 million samples for each of the three QDs at five different temperatures). The results from this work highlight the ability of the ESP-CIS method to overcome the steep computational barrier of generating chemically accurate distributions of QM properties at non-zero temperatures from first-principles excited state methods.

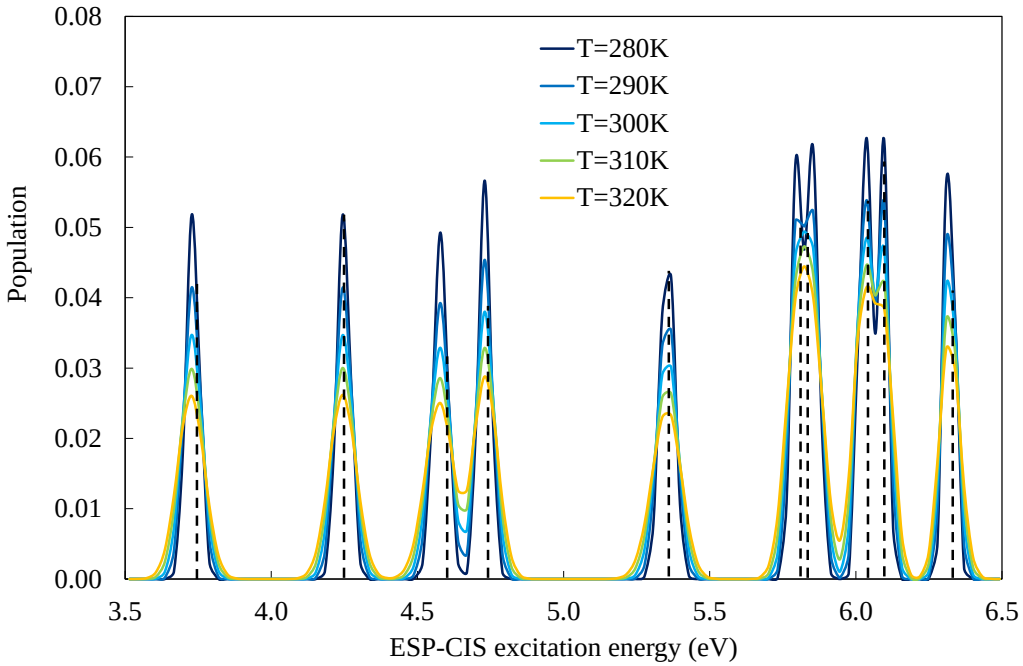

Figure 5.24: Probability distributions for the first 10 ESP-CIS excitation energies (in eV) of CDN1163 at 280 K, 290 K, 300 K, 310 K, and 320 K ($N_{\text{sample}} = 10^6$). Vertical lines correspond to theline spectra of the minimum energy reference structure.

Chapter 6

The Effect of Isovolumetric Transformation on the Optoelectronic Properties of Semiconducting Nanoparticles

Introduction

The Computational Challenge of Investigating Optoelectronic Properties of Semiconductor Nanoparticles

Semiconductor nanoparticles (NPs) have tunable optical and electronic properties that make them attractive in applications such as photovoltaics, [34, 35, 36, 37, 38] light emitting devices, [39, 40, 41] charge and energy transfer processes [42, 43, 44, 45], and biological labeling. [46, 47]

One of the principle challenges of investigating the optoelectronic properties of NPs computationally is the large number of electrons in the system. Most NPs reside in a system-size regime that makes them particularly difficult to perform calculations on: they are finite systems, so treating them with periodic boundary conditions is inappropriate, but they are still much bigger than most traditional electronic structure methods can handle.

Because NPs are semiconductors, they are amenable to approximations made after electron-hole quasiparticle transformation. A diagram of this transformation is shown in Figure 6.1.

In the many-electron picture, there are many electrons in the ground energy state occupying so called "occupied" molecular orbitals. In this representation, electronic representations looks like one of the electrons in an occupied molecular orbital exciting up to one of the unoccupied (or "virtual") molecular orbitals.

The electron-hole representation is mathematically equivalent to the many electron picture. In the e-h representation, the ground state looks like an empty vacuum state, and electronic excitation looks like an electron being created in the unoccupied space, and a positively-charged *hole* get created in the occupied space. Both the electron and hole are treated as quasi-particles, as the two particles mathematically represent all of the electrons in the system [157, 158]. A graphical representation of this property is shown in Figure 6.2. On the left, two electrons interact with one another through a bare Coulomb potential (r_{12}^{-1}). In the many-electron picture, there is one of these interaction for every pair of electrons in the system. On the right, there is only one pairing of electron and hole quasiparticles, which interact

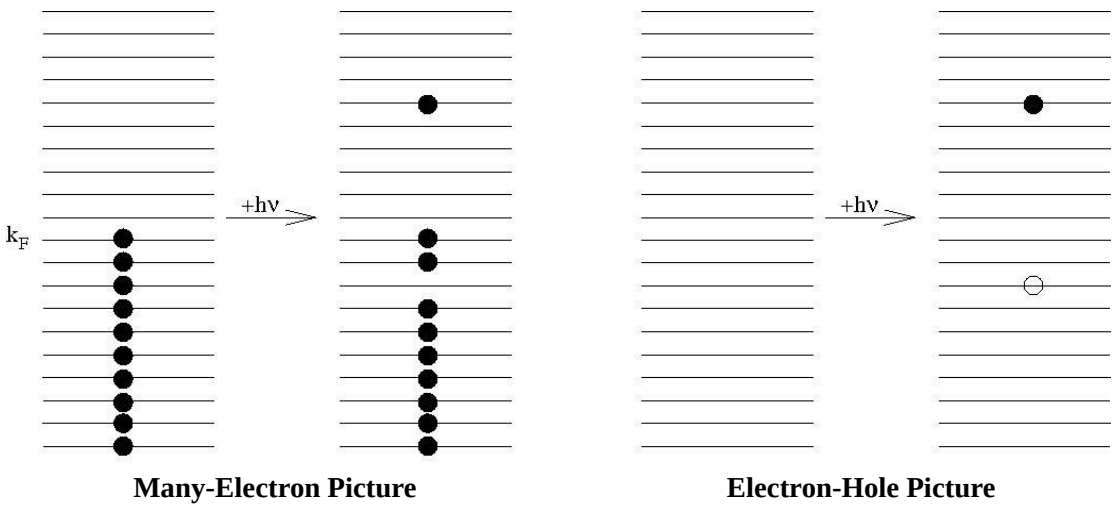

Figure 6.1: Pictorial diagram of the difference between how electronic excitation is represented in the many-electron picture and in the electron-hole picture.

with one another through a ”dressed” Coulomb potential (K_{eh}). In this representation, the interaction is effectively screened due to the presence of all other electrons in the system.

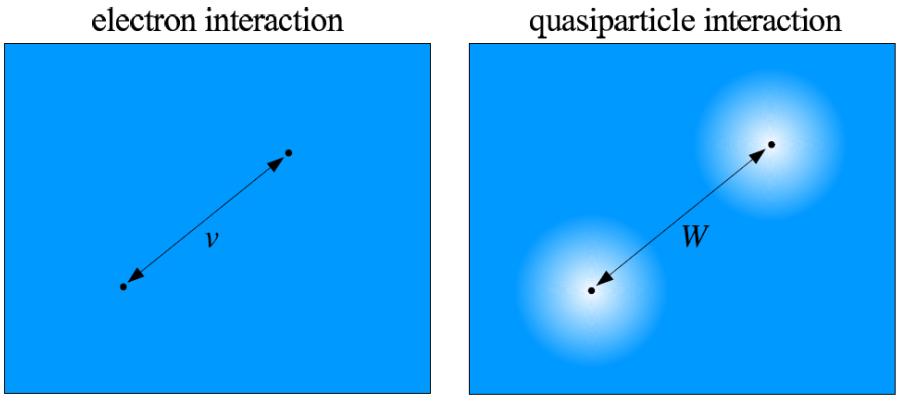

Figure 6.2: Graphical representation of the difference between two real electrons interacting and a quasi-electron interaction with a quasi-hole.

The bound electron-hole pair is called an exciton. An exciton is a unit of electronic excitation, and can be created in a NP when it absorbs light, exciting an electron from the valence band to the conduction band of the NP. The electron-hole representation allows for prediction of chemical properties through study of exciton, rather than the set of all electrons in the system [158].

Size-tunability of Semiconductor Nanoparticles

This tunability is a consequence of differences in the quantum confinement effect with variations in the size and shape of the NPs. The size of the NP not only determines its density of states, but also restricts the spatial localization of excitons when the NP is electronically excited.

Adjusting the NP's size has been used extensively to manipulate excitonic interactions. [159, 160, 161, 162, 163] For example, one well-studied phenomenon is the change in photoluminescence spectra of quantum dots (QDs) as function of dot size. [164, 165, 166, 167, 168, 169, 170, 162, 171, 172] The effect of dot size on Auger recombination rates [173, 164, 174, 164, 165, 175, 176], electron-transfer processes [35, 42, 177, 178, 179, 180, 181, 182], energy transfer processes [183, 184, 185, 165, 186, 187, 188, 189, 190, 191, 192, 193], carrier multiplicity [194, 195, 196, 197, 198, 199, 200, 201, 202, 203, 204, 205, 176, 206], and dissociation of excitons [170, 207, 208] has been and continues to be extensively studied using both experimental and theoretical methods.

Shape-tunability of Semiconductor Nanoparticles

In contrast to size, NP shape controls the spatial asymmetry of the confinement volume, which leads to shape-dependent effects on exciton behavior. The shape of a NP is associated with a number of different electron-hole (eh-) confinement regimes. [209, 210, 211, 208, 212, 213, 214, 215, 216, 217, 218, 219, 220, 221, 222, 223] Specifically, spherical NPs such as quantum dots exhibit 3D quantum confinement, nanoplatelets and nanodisks exhibit 2D confinement, [224, 225, 226, 227] and nanorods and wires exhibit 1D confinement. [34, 228, 208] For 1D quantum confined materials, theoretical and experimental studies have shown that modifying the aspect ratio in quantum rods can substantially change their optical properties. [216, 210, 220, 229, 221, 230, 231, 232] Nanorods have been used to enhance carrier multiplicity, [208] optimize resonance energy transfer, [183] and generate linear polarized light. [233] The properties and shape effects of 2D quantum confined materials such as disks and plate-like nanoparticles have also been investigated. [203, 234, 235] Song et al. have studied excitons confined to quantum disks, and calculated the geometrical effects on exciton binding energy, eh-separation, and the resulting linear optical properties observed. [171] Bialda et al. investigated eh-recombination behavior in CdSe nanoplates, and observed that the behavior of this 2D material was different than that of their corresponding 3D spherical CdSe NPs. [236, 237]

Isovolumetric Transformation on Semiconductor Nanoparticles

In this chapter, I present my published computational approach to investigate the effect of quantum confinement in a series of semiconductor NPs [238]. To differentiate the effect of shape from size on the NP excitonic properties, we performed calculations on semiconductor nanorods, nanodisks, and nanospheres under isovolumetric conditions. This constraint ensures that the overall amount of material in the NPs is equivalent, while allowing the spatial distribution

of the material to differ with shape. This isovolumetric condition is very difficult to reproduce experimentally, and the control over NP structure in this way provides us with unprecedented theoretical insight into the structure-property relationship of these materials.

For each NP shape, three representative particle sizes were selected (Figure 6.3), and each volume/shape combination was investigated for four different materials: CdSe, CdS, CdTe, and PbS. These compositions were chosen because many of these NPs have been successfully synthesized [239, 240], which allowed us to benchmark and validate the computational procedures used.

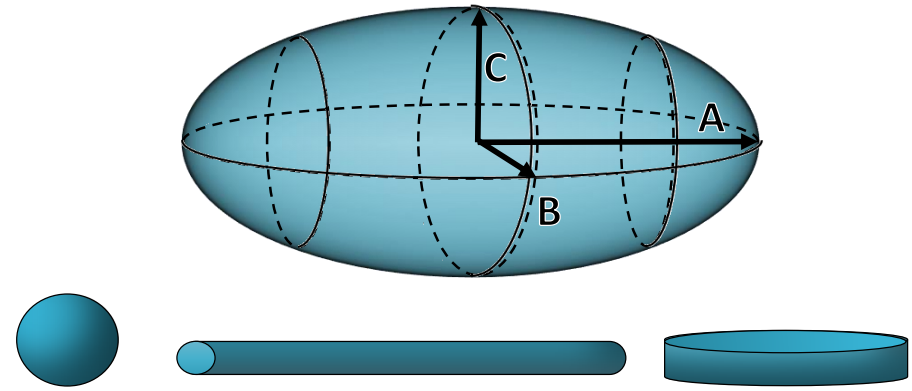

Sphere (*A* = *B* = *C*) **Rod** (*8A* = *8B* = *C*) **Disk** (*A* = *B* = *8C*)

Size	Chemical Formula	Shape	A semi-axis (nm)	B semi-axis (nm)	C semi-axis (nm)
V = 524 nm^3	$Cd_{9338}Se_{9363}$	Sphere	5.00	5.00	5.00
		Disk	10.0	10.0	1.25
		Rod	2.50	2.50	20.0
V = 1437 nm^3	$Cd_{25631}Se_{25629}$	Sphere	7.00	7.00	7.00
		Disk	14.0	14.0	1.75
		Rod	3.50	3.50	28.0
V = 4189 nm^3	$Cd_{74608}Se_{74837}$	Sphere	10.0	10.0	10.0
		Disk	20.0	20.0	2.50
		Rod	5.00	5.00	40.0

Figure 6.3: A representative ellipsoid showing the *A*, *B*, and *C* semi-axes. The nanoparticles in this investigation are ellipsoids with semi-axis lengths constructed so that there are three sets of differently shaped NPs of equal volume. Nanorods are constructed to have length equal to eight times their diameter, and nanodisks are constructed to have diameter equal to eight times their thickness.

The nanoscale dimensions (3D, 2D, and 1D) combined with the isovolumetric constraint of these systems led to a number of significant questions about the excitonic interactions in the NPs. To elucidate the relationship between shape and the excitonic properties of select material compositions, we conducted investigations on (1) the binding

energy of the eh-interaction, (2) the spatial separation between the eh-pair, and (3) the eh-recombination probability.

Theory

Treatment of Electron-hole Correlation

The NPs in this study were modeled using the electron-hole explicitly correlated Hartree-Fock method. While the complete details of this method are outlined in the work by Elward et al. [241], a brief overview of the method is discussed here. To solve the electron-hole Schrödinger equation for these systems, the effective electron-hole Hamiltonian [242, 243, 244, 245, 246] was used

$$\hat{H} = \sum_{ij} \langle i| \frac{-\hbar^2}{2m_{\mathrm{e}}} + v^{\mathrm{e}}_{\mathrm{ext}} |j\rangle e^{\dagger}_i e_j \tag{6.1}$$

$$+ \sum_{ij} \langle i| \frac{-\hbar^2}{2m_{\mathrm{h}}} + v^{\mathrm{h}}_{\mathrm{ext}} |j\rangle h^{\dagger}_i h_j \tag{6.2}$$

$$+ \sum_{ijj'j'} \langle iji'j'|\varepsilon^{-1} r^{-1}_{\mathrm{eh}} |iji'j'\rangle e^{\dagger}_i e_j h^{\dagger}_{i'} h_{j'} \tag{6.3}$$

$$+ \sum_{ijkl} w^{\mathrm{ee}}_{ijkl} e^{\dagger}_i e^{\dagger}_j e_l e_k + \sum_{ijkl} w^{\mathrm{hh}}_{ijkl} h^{\dagger}_i h^{\dagger}_j h_l h_k. \tag{6.4}$$

The effective electron-hole Hamiltonian provides a computationally efficient means of calculating the optical properties of interest in these NPs.

The external potential used in this investigation is a parabolic potential for both the electron and hole. Parabolic potentials have been used extensively to approximate the confinement potential of semiconductor NPs [247, 248, 249, 250].

$$v^{\alpha}_{\mathrm{ext}} = \frac{1}{2} k_{\alpha} |\mathbf{r}_{\alpha}|^2 \quad \alpha = \mathrm{e}, \mathrm{h}, \tag{6.5}$$

The magnitude of the force constants in this external confining potential is important for the accurate calculation of exciton binding energy in these NPs. The force constants are calculated such that the electron and hole are confined to the physical dimensions of the NP [250]

$$\min_{k^{min}_{\alpha}} = \left(N_{\alpha} - \int_0^{\frac{D_{dot}}{2}} dr r^2 \int d\Omega \rho_{\alpha}(\mathbf{r}) [v^{\alpha}_{ext}] \right)^2, \tag{6.6}$$

where $\alpha = \mathrm{e}, \mathrm{h}$, $d\Omega = \sin d\theta d\varphi$, D_{dot} is the diameter of the corresponding spherical quantum dot, and k_{α} is the smallest force constant that satisfies the above minimization conditions. An appropriate force constant for the spherical CdSe NP was obtained using this approach, and then the force constants corresponding to all other semi axis lengths were

scaled using this quantity

$$k_{\alpha a} = \frac{k_{\alpha_{\text{sphere}}} r_{\text{sphere}}^2}{a^2}, \tag{6.7}$$

where a is the length of the semi axis, and r_{sphere} is the radius of a spherical NP with a corresponding force constant $k_{\alpha_{\text{sphere}}}$.

The ansatz of the eh-XCHF wave function is a product of electron and hole reference wave functions and a correlation function [241]. The electron and hole reference wave functions are Slater determinants and the correlation function is a Gaussian type geminal operator

$$\Psi_{\text{eh-XCHF}} = \hat{G}\Phi^{\text{e}}\Phi^{\text{h}}. \tag{6.8}$$

The geminal operator $\hat{G}$ is a two body operator, and introduces an explicit dependence on the electron-hole separation distance to the wave function, as well as variational parameters b_k and γ_k. This geminal operator has the form of a linear combination of Gaussian functions [241]

$$\hat{G} = \sum_{i=1}^{N_e} \sum_{j=1}^{N_h} \sum_{k=1}^{N_g} b_{\text{k}} e^{-\gamma_{\text{k}} {r_{\text{eh}}}^2}. \tag{6.9}$$

The eh-XCHF wave function is obtained variationally by minimizing the total energy with respect to the parameters of the electron and hole reference wave functions, as well as the geminal parameters b_k and γ_k

$$\text{E} = \min_{\hat{G},\Phi^{\text{e}},\Phi^{\text{h}}} \frac{\langle \Psi_{\text{eh-XCHF}} | \hat{H} | \Psi_{\text{eh-XCHF}} \rangle}{\langle \Psi_{\text{eh-XCHF}} | \Psi_{\text{eh-XCHF}} \rangle}. \tag{6.10}$$

To improve the efficiency of the calculation in Equation 6.10, the effect of the geminal operator is moved from the wave function to the Hamiltonian. This congruent transformation of the Hamiltonian has the form seen in Equation 6.11

$$\tilde{H} = \hat{G}^{\dagger} \hat{H} \hat{G} \tag{6.11}$$

$$\tilde{1} = \hat{G}^{\dagger} 1 \hat{G}. \tag{6.12}$$

This transformation changes the form of the eh-XCHF energy, such that the wave function used is composed only of Slater determinants for the electron and hole

$$\text{E} = \frac{\langle \Phi^{\text{e}}\Phi^{\text{h}} | \tilde{H} | \Phi^{\text{e}}\Phi^{\text{h}} \rangle}{\langle \Phi^{\text{e}}\Phi^{\text{h}} | \tilde{1} | \Phi^{\text{e}}\Phi^{\text{h}} \rangle}. \tag{6.13}$$

Table 6.1: **Approximate chemical formula of CdSe, CdS, CdTe, and PbS nanoparticle systems in this study**. All volumes are in nm^3.

Volume	CdSe	CdS	CdTe	PbS
524	$Cd_{875}Se_{875}$	$Cd_{997}S_{997}$	$Cd_{746}Te_{746}$	$Pb_{925}S_{925}$
1437	$Cd_{2401}Se_{2401}$	$Cd_{2736}S_{2736}$	$Cd_{2046}Te_{2046}$	$Pb_{2537}S_{2537}$
4189	$Cd_{7000}Se_{7000}$	$Cd_{7976}S_{7976}$	$Cd_{5964}Te_{5964}$	$Pb_{7397}S_{7397}$

Table 6.2: **System parameters used to calculate properties of nanoparticles. [250, 251]** ε is the dielectric screening constant of the material, m_e is the effective mass of the electron, m_h is the effective mass of the hole, and m_0 is the mass of a free electron. η is the composite material parameter that depends on ε and the reduced mass of the electron-hole pair.

	CdSe	CdS	CdTe	PbS
ε	6.2	5.4	7.1	17.2
m_e	0.13 m_0	0.19 m_0	0.12 m_0	0.08 m_0
m_h	0.38 m_0	0.22 m_0	0.13 m_0	0.075 m_0
η	0.0156	0.0189	0.0088	0.0023

Computational Details

The three optical properties of interest in this study are the exciton binding energy, the electron-hole recombination probability, and the electron-hole separation distance. The exciton binding energy is defined as the total energy of a fully interacting electron-hole system, less the fully non-interacting system.

$$E_{\mathrm{EB}} = \langle E_{\mathrm{non-interacting}} \rangle - \langle E_{\mathrm{exciton}} \rangle. \tag{6.14}$$

The electron-hole separation distance is calculated as the expectation value of the absolute difference between the electron and hole coordinates

$$\langle r_{\mathrm{eh}} \rangle = \langle \Psi_{\mathrm{eh-XCHF}} || \mathbf{r}_e - \mathbf{r}_h || \Psi_{\mathrm{eh-XCHF}} \rangle. \tag{6.15}$$

The electron-hole recombination probability is calculated as the probability of finding a hole within a small finite region around the electron coordinate

$$P_{\mathrm{eh}} = \frac{1}{N_e N_h} \int d\mathbf{r}_e \int_{\mathbf{r}_e - \frac{\boldsymbol{\Delta}}{2}}^{\mathbf{r}_e + \frac{\boldsymbol{\Delta}}{2}} d\mathbf{r}_h \, \rho_{\mathrm{eh}}(\mathbf{r}_e, \mathbf{r}_h). \tag{6.16}$$

Results

Spheres, disks, and rods were selected to represent the 3D, 2D, and 1D, quantum confinement effect, respectively. We calculated three excitonic properties of each NP: exciton binding energy (E_{EB}), eh-recombination probability (P_{eh}), and eh-separation distance ($\langle r_{\mathrm{eh}} \rangle$). We performed these calculations using the eh-explicitly correlated Hartree-Fock (eh-XCHF) method [241]. The effect of size, shape and NP material (i.e., chemical composition) on the calculated excitonic properties was analyzed, and is presented here.

Effect of Shape and Size on Exciton Binding Energy

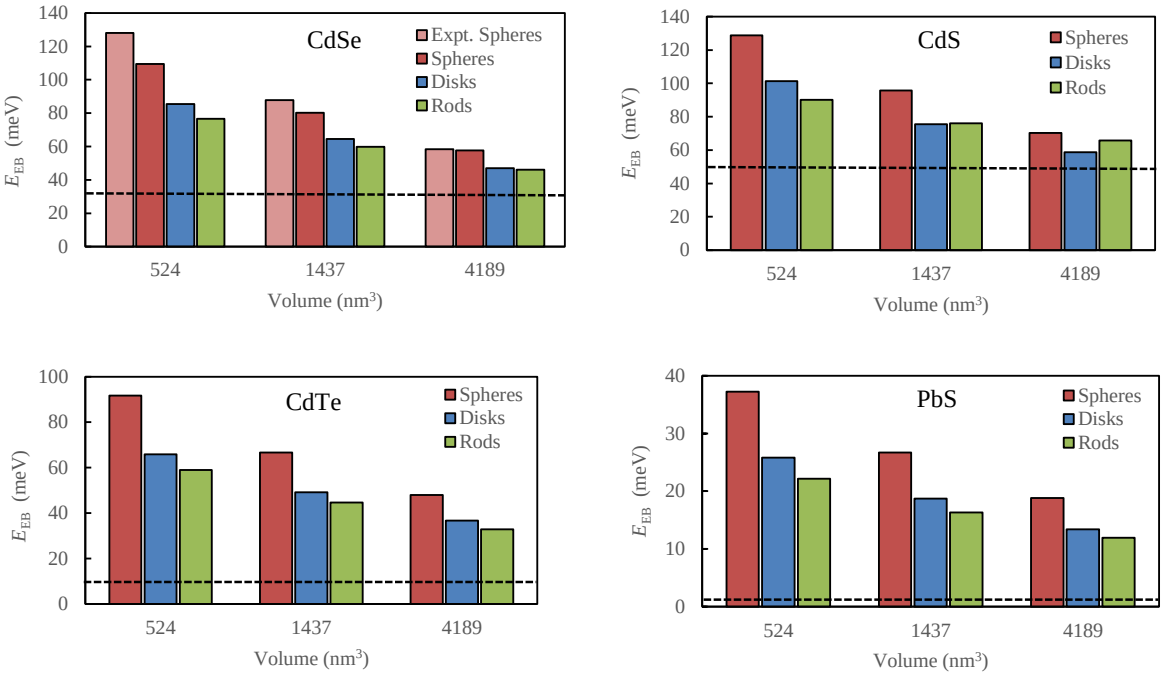

Figure 6.4: Exciton binding energies (in meV) of CdSe, CdS, CdTe, and PbS nanoparticle spheres, disks, and rods. Experimental results for CdSe nanospheres provided for comparison. Dashed lines correspond to the exciton Rydberg energy (in meV) for each material.

An important first step for the evaluation of excitonic properties is to benchmark and validate the computational procedure. In this work, we benchmarked the eh-XCHF method by comparing the calculated E_{EB} values with experimental data [252] for spherical CdSe NPs, and the results are presented in Figure 6.4. The calculated eh-XCHF E_{EB} values were found to recover between 86-99% of the experimental binding energies.

The effect of isovolumetric deformation on E_{EB} for all other NPs are also presented in Figure 6.4. For CdSe NPs, we found that the nanorods exhibited lower E_{EB} than isovolumetric nanodisks and nanospheres. This trend is observed at all three representative volumes. The E_{EB} values showed significant variation with change in material

type. Specifically, E_{EB} was found to follow the trend of $E_{\mathrm{EB}}(\mathrm{PbS}) < E_{\mathrm{EB}}(\mathrm{CdTe}) < E_{\mathrm{EB}}(\mathrm{CdSe}) < E_{\mathrm{EB}}(\mathrm{CdS})$, which was consistently observed across all NP shapes.

In addition to the eh-XCHF method, an approximate description of eh-interaction can also be obtained by modeling the exciton as a hydrogenic system. [253] The advantage of this approach is that one can obtain an analytical expression for the exciton binding energy (called the exciton Rydberg energy [253]) in terms of the material parameters. A comparison between the hydrogenic and eh-XCHF exciton binding energies are presented in Figure 6.4. In all cases, it was found that the hydrogenic model underestimated the exciton binding energies. Although the hydrogenic model fails to capture the size-dependence of the exciton binding energies, it was able to capture the general trend with respect to material types $E_{\mathrm{EB}}(\mathrm{PbS}) < E_{\mathrm{EB}}(\mathrm{CdTe}) < E_{\mathrm{EB}}(\mathrm{CdSe}) < E_{\mathrm{EB}}(\mathrm{CdS})$. The variation in observed E_{EB} across the different NP morphologies, as compared to the static exciton Rydberg energies, highlights the differences in the quantum confinement effect in these systems.

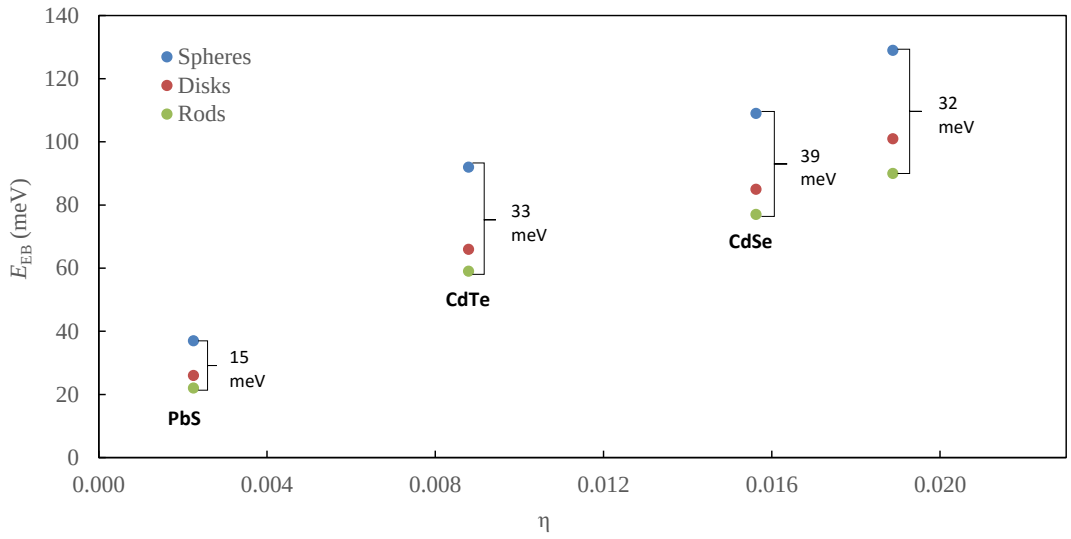

Figure 6.5: Material parameter η vs. exciton binding energy. Data points are grouped into four sets, each corresponding to the labeled material type with volumes of $V = 524$ nm^3.

The E_{EB} values depend on the fundamental interactions between eh-pairs in these NPs, and are strongly influenced by material parameters such as effective masses and dielectric screening parameters. To understand the roles of these material parameters on E_{EB}, we investigated how the excitonic wave function depends on them. Specifically, analysis of the excitonic wave function in the vicinity of the eh-coalescence point ($r_{\mathrm{eh}} \to 0$) shows that up to first order, the exciton wave function can be expressed as [254]

$$\left(\frac{\partial \Psi_{\mathrm{eh}}}{\partial r_{\mathrm{eh}}}\right)_{r_{\mathrm{eh}}=0} \propto \eta \Psi_{\mathrm{eh}}(r_{\mathrm{eh}} = 0) \qquad \text{(in atomic units)} \tag{6.17}$$

where the unit-less parameter η is defined as (Equation 6.18)

$$\eta = \frac{m_e m_h}{\varepsilon(m_e + m_h)} \times \frac{1}{m_0}, \tag{6.18}$$

where m_e and m_e are effective electron and hole masses, and ε is the dielectric constant. The dependence of E_{EB} as a function of η is presented in Figure 6.5 for NPs with volumes $V = 524$ nm^3. For the present set of materials, each material type has a unique value of η that is independent of NP size or shape. In general, we found that E_{EB} increased with increasing η. Figure 6.5 also shows the variation in binding energies of differently shaped NPs made of the same material. The results showed that PbS, which had a total range of only 15 meV, is least sensitive to changing E_{EB} with respect to shape deformation. In contrast, CdSe was the material most sensitive to changing shape, with a total range in E_{EB} values of 39 meV.

Effect of Shape on Electron-hole Recombination Probability

Figure 6.6 presents results for the calculated eh-recombination probability (P_{eh}) for the NPs investigated at the three volumes and three morphologies of interest. As expected, smaller NPs had higher P_{eh} values than larger NPs, since

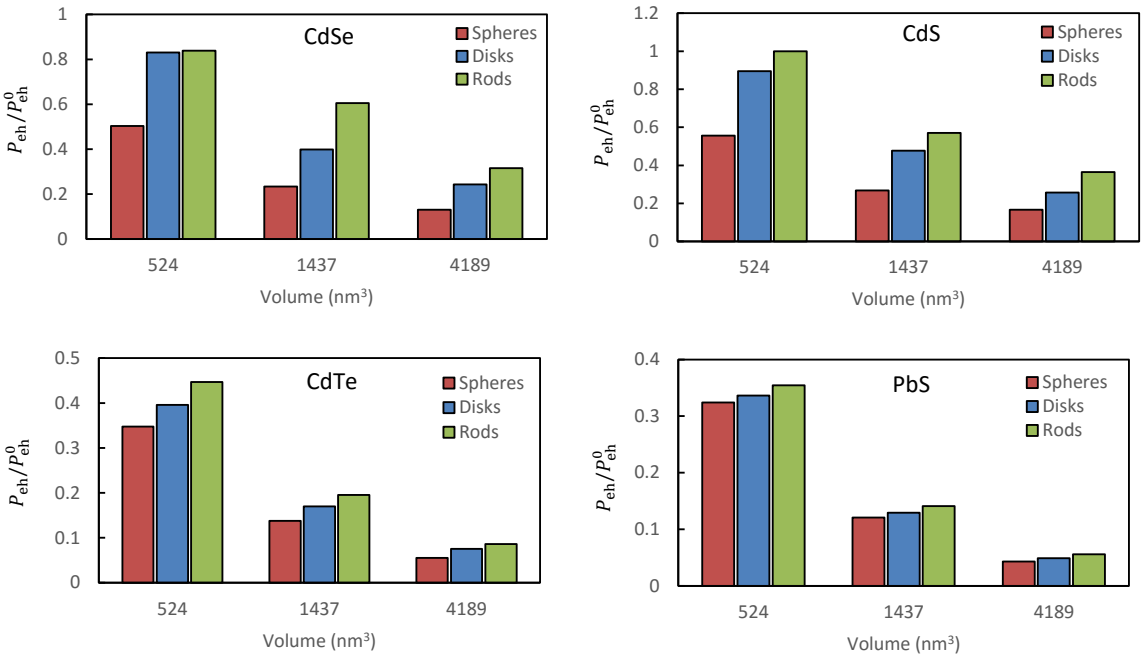

Figure 6.6: Electron hole recombination probabilities of CdSe, CdS, CdTe, and PbS nanoparticle spheres, disks, and rods. P_{eh} is presented relative to a referenced P^0_{eh} with $P^0_{eh} = 2.9945 \times 10^{-18}$).

smaller NPs confine the electron and hole to a smaller total volume, and the electron and hole are more likely to

recombine when they are close to one another.

Focusing on the efect of shape, we found that nanospheres exhibited the smallest P_{eh} values, followed by disks, and then rods, which had the largest recombination probabilities. The CdS nanorods had the largest P_{eh}, and the PbS nanospheres had the smallest P_{eh}. While P_{eh} did become larger the smaller the NP volume became, unlike E_{EB} it also increased as the anisotropy of the NP increased. This result suggests that P_{eh} is dominated not by the average eh-separation distance in the NP, but rather by the smallest confining dimension of the system. Since the isovolumetric nanorods have a comparatively small radial axis relative to their length, this small confining dimension forces the electron and hole close together. Although on average the electron and hole can be further apart than in other NP morphologies, they still have more opportunities to recombine than they do in nanospheres. Therefore, for NPs of identical volume, nanospheres exhibit the least amount of recombination. Increasing the NP volume will still further decrease the recombination probability of all morphologies.

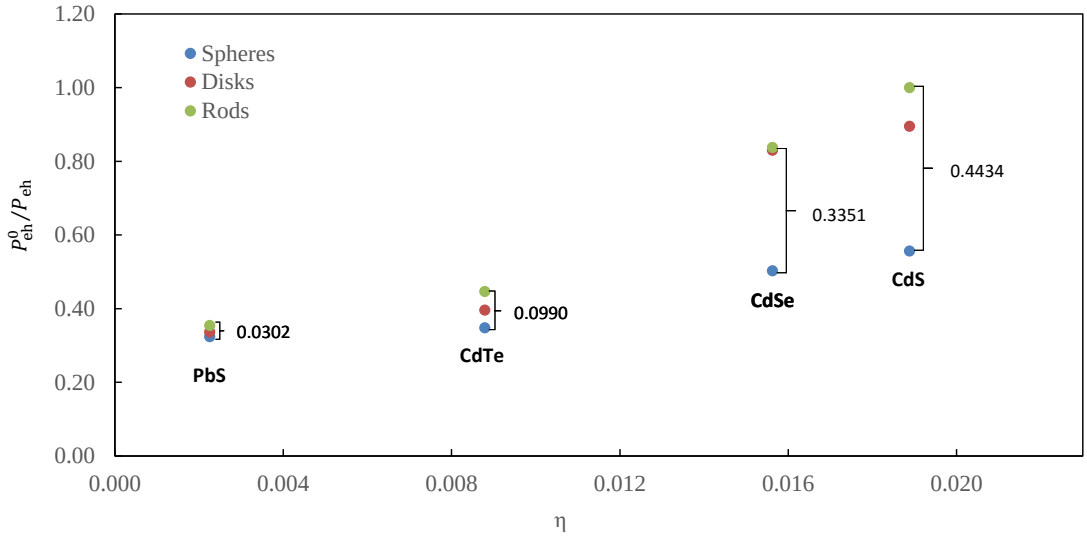

Figure 6.7: Material parameter η vs. electron-hole recombination probability. Data points are grouped into four sets, each corresponding to the labelled material type with volumes of $V = 524$ nm^3. P_{eh} is presented relative to a referenced P^0_{eh} with $P^0_{\text{eh}} = 2.9945 \times 10^{-18}$).

Figure 6.7 shows the relationship between P_{eh} vs. η. As observed with E_{EB}, increases in η resulted in increased P_{eh}. The range of P_{eh} values across spheres, disks and rods was again smallest for PbS, but largest for CdS, rather than CdSe as it was with E_{EB}. PbS was again the least sensitive to changing P_{eh} with respect to changing NP shape. The total range of P_{eh} values was only 0.0302 relative units. CdS was most sensitive to changing P_{eh} with respect to changing shape, with a total range of 0.4434 relative units. This property of PbS to be highly resistant to changing optical properties with respect to shape deformation is likely a result of its large dielectric screening of the eh-interaction.[253]

Effect of Shape on Electron-hole Separation Distance

The eh-separation distance was obtained from the expectation value of the eh-distance $\langle \rho_{eh} r_{eh} \rangle$. Figure 6.8 presents the calculated values of $\langle r_{eh} \rangle$ for the investigated NPs. For comparison to the bulk material, the dashed lines on each plot indicate the exciton Bohr radius [253] of these materials (in nm). As expected, $\langle r_{eh} \rangle$ increased with increasing volume. The $\langle r_{eh} \rangle$ distance was inversely correlated with E_{EB}, and thus NPs with large $\langle r_{eh} \rangle$ distances exhibited smaller E_{EB}. This phenomenon was true for all materials investigated, and suggests that unlike P_{eh}, the largest structural dimension of the system controls $\langle r_{eh} \rangle$.

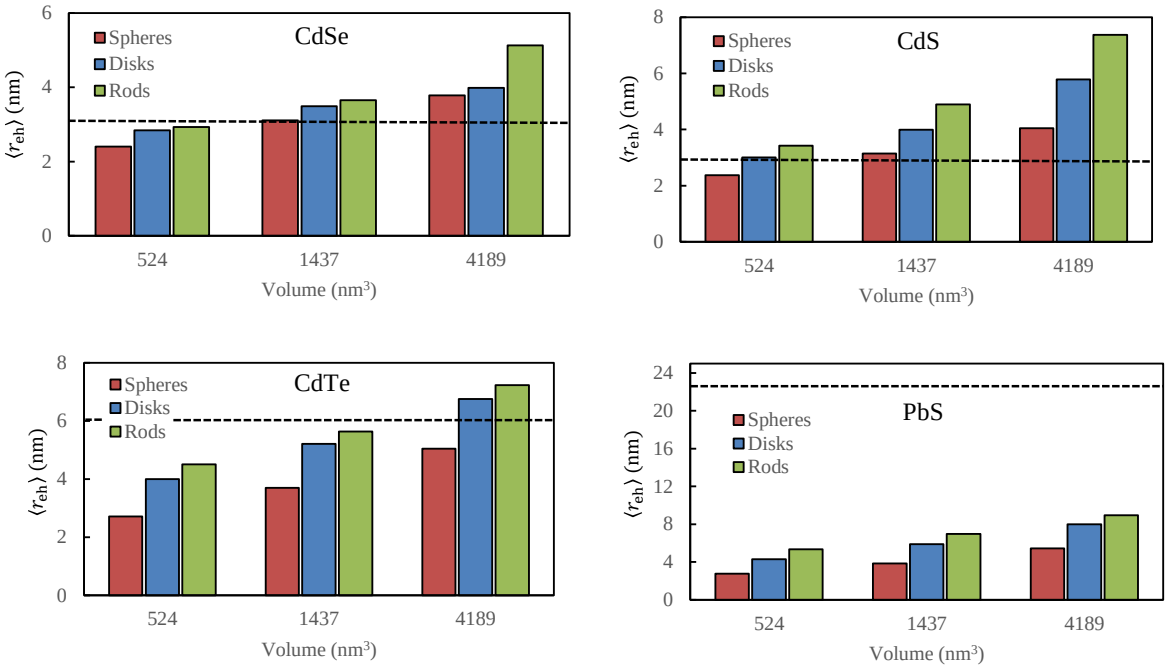

Figure 6.8: Electron-hole separation distance of CdSe, CdS, CdTe, and PbS nanoparticle spheres, disks, and rods. The separation distance increases as both nanoparticle size and anisotropy increases. Dashed lines correspond to the exciton Bohr radius (in nm) for each material.

We see that as with exciton Rydberg energies, our $\langle r_{eh} \rangle$ results followed a similar trend to the exciton Bohr radii of these materials. However, $\langle r_{eh} \rangle$ is a much better description of the spatial separation of the bound eh-pair, because unlike the exciton Bohr radius which treats the exciton approximately as a hydrogenic atom, $\langle r_{eh} \rangle$ is a system-dependant property that will changed based on the NP size, shape, and composition.

Upon obtaining all of these calculated optical properties of each NP, we were interested in determining the structural parameters that make a particular NP more or less sensitive to changes in its observed optical properties. To do

CdSe				
	V (nm^3)	E_{EB} (meV)	r_{eh} (nm)	$P_{\mathrm{eh}}/P^0_{\mathrm{eh}}$
Sphere	524	109	2.41	0.503
	1437	80	3.10	0.234
	4189	58	3.78	0.131
Disk	524	85	2.84	0.830
	1437	65	3.49	0.398
	4189	47	3.98	0.244
Rod	524	77	2.93	0.838
	1437	60	3.65	0.605
	4189	46	5.13	0.316

CdS				
	V (nm^3)	E_{EB} (meV)	r_{eh} (nm)	$P_{\mathrm{eh}}/P^0_{\mathrm{eh}}$
Sphere	524	129	2.37	0.557
	1437	96	3.15	0.269
	4189	70	4.04	0.166
Disk	524	101	3.01	0.895
	1437	76	3.99	0.476
	4189	59	5.79	0.257
Rod	524	90	3.42	1.000
	1437	76	4.90	0.571
	4189	66	7.38	0.365

CdTe				
	V (nm^3)	E_{EB} (meV)	r_{eh} (nm)	$P_{\mathrm{eh}}/P^0_{\mathrm{eh}}$
Sphere	524	92	2.71	0.348
	1437	67	3.70	0.137
	4189	48	5.05	0.055
Disk	524	66	3.99	0.396
	1437	49	5.22	0.170
	4189	37	6.75	0.075
Rod	524	59	4.50	0.447
	1437	45	5.63	0.196
	4189	33	7.23	0.086

PbS				
	V (nm^3)	E_{EB} (meV)	r_{eh} (nm)	$P_{\mathrm{eh}}/P^0_{\mathrm{eh}}$
Sphere	524	37	2.78	0.324
	1437	27	3.86	0.121
	4189	19	5.43	0.043
Disk	524	26	4.30	0.337
	1437	19	5.87	0.129
	4189	13	8.00	0.049
Rod	524	22	5.35	0.355
	1437	16	6.98	0.141
	4189	12	8.94	0.056

Figure 6.9: The entire set of calculated results for each nanoparticle studied. Spheres, disks, and rods were studied at volumes of 524, 1437, and 4189 nm^3. CdSe, CdS, CdTe, and PbS nanoparticles were investigated at these morphologies, and exciton binding energy (E_{EB}), electron hole recombination probability (P_{eh}), and electron hole separation distance ($\langle r_{\mathrm{eh}} \rangle$) were all calculated using eh-XCHF. P_{eh} is presented relative to probabilty $P^0_{\mathrm{eh}} = 2.9945 \times 10^{-18}$.

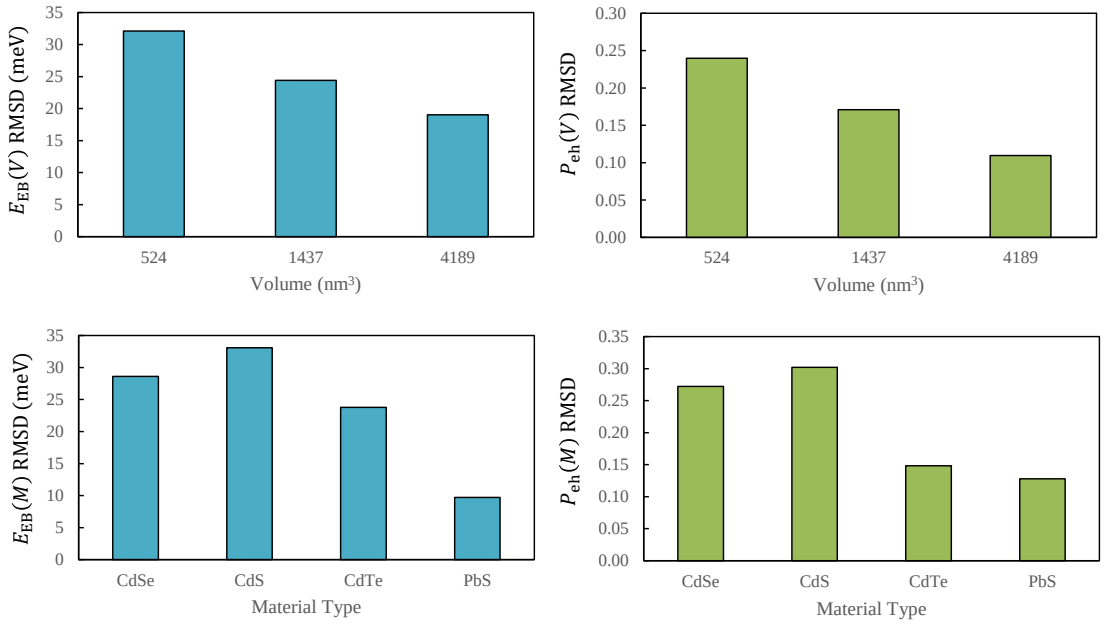

Figure 6.10: **Top**: Nanoparticle volume V vs. $A(V)_{\mathrm{RMSD}}$ for both $A = E_{\mathrm{EB}}$ (left) and $A = P_{\mathrm{eh}}$ (right). **Bottom**: Nanoparticle material type M vs. $A(M)_{\mathrm{RMSD}}$ for both $A = E_{\mathrm{EB}}$ (left) and $A = P_{\mathrm{eh}}$ (right).

this, we define the root-mean-squared deviation $A(\alpha)_{\text{RMSD}}$ below in Equation 6.19 as:

$$A(\alpha)_{\text{RMSD}} = \sqrt{\frac{\sum_{i=1}^{n} \left(A_i(\alpha) - \langle A(\alpha) \rangle\right)^2}{n}}, \tag{6.19}$$

where α is a structural property of the NP being fixed, $A_i(\alpha)$ is the optical property of a particular NP satisfying α, $\langle A(\alpha) \rangle$ is the average of that optical property across all NPs satisfying α, and n is the total number of NPs that satisfy α. $A(\alpha)_{\text{RMSD}}$ was calculated for both E_{EB} and P_{eh} at fixed NP volume and fixed material composition. These results are plotted in Figure 6.10. For a given NP size, we see that $A(\alpha)_{\text{RMSD}}$ for both E_{EB} and P_{eh} were smaller for larger NPs. Therefore, larger NPs are, on average, less susceptible to changing E_{EB} and P_{eh} with respect to changing shape or material type. Compared to E_{EB}, $A(\alpha)_{\text{RMSD}}$ for P_{eh} is smaller across all corresponding NP sizes. We conclude that in general, NPs are more resistant to changes in P_{eh} than they are to E_{EB} when the particle shape or composition is changed. With respect to material type, PbS NPs were, on average, more resistant to changing E_{EB} and P_{eh} with respect to changing NP size and shape. CdS nanoparticles were more sensitive to changing E_{EB} and P_{eh} with respect to changing NP size and shape.

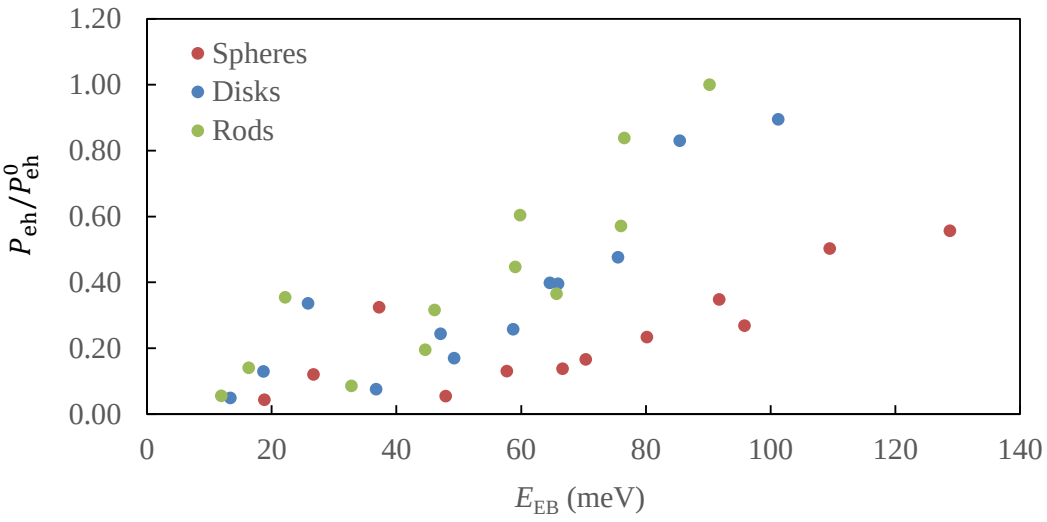

Figure 6.11: Exciton binding energy vs. recombination probability in CdSe, CdS, CdTe, and PbS nanoparticles. Data includes nanoparticles of all shapes, sizes, and compositions investigated.

Understanding the relationship between E_{EB} and P_{eh} can help make informed decisions about what types of NP systems to use when designing semiconductor devices. Figure 6.11 shows this relationship for the set of all CdSe, CdS, CdTe, and PbS NPs studied. In general, as E_{EB} increased, P_{eh} also increased, but this trend was not strictly

adhered to by all NPs. The actual relationship between these quantities is impacted largely by material type. Overall, P_{eh} scaled fastest with E_{EB} in spheres, and slowest in rods. This scaling again varies based on NP material type. The conclusion from this analysis is that in general, NP spheres may be the best candidates for semiconductor applications where large binding energies and low P_{eh} values are desired.

Effect of Shape on Exciton Binding Energy in Isovolumetric CdSe Nanoparticles

The calculated optical properties for the spheres, disks and rods were insightful, but limited our scope to only three rigidly defined morphologies. We additionally wanted to investigate the effect on observed optical properties of incremental deformation of the NP. In an effort to obtain a more detailed description of the shape-property relationship in semiconductor NPs, we performed calculations on a set of 900 isovolumetric ($V = 4189$ nm^3) ellipsoidal CdSe NPs.

Each ellipsoid's shape in this investigation can be fully defined by the A and B semi-axes, since the C semi-axis is defined by the other two as a result of the isovolumetric condition ($A \times B \times C = 1000$ nm^3). In constructing these systems in this way, we obtain a very large set of NPs with small, continuous shape deformation. Here we can see the optical properties not only of spheres, disks, and rods, but also of the transitional morphologies as well.

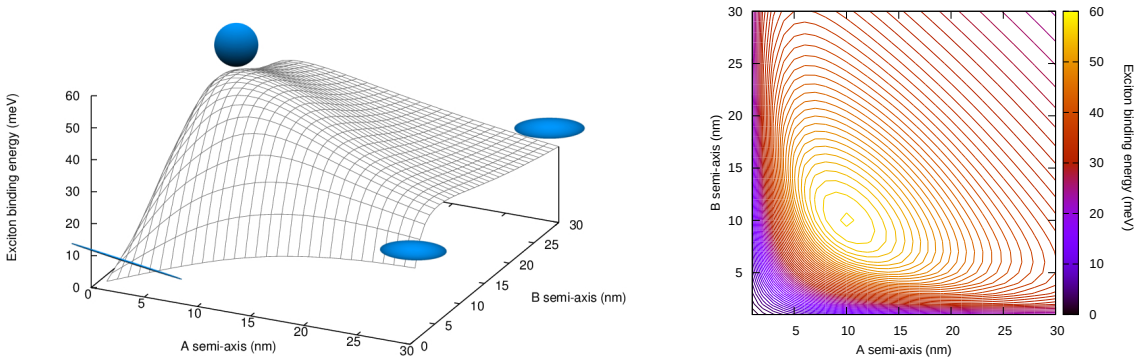

(a) (b)

Figure 6.12: Surface plot (a) and contour plot (b) of CdSe nanoparticle A and B semi axis lengths vs. exciton binding energy. Representative ellipsoids are placed over the surface plot for reference.

The E_{EB} values of the entire set of 900 CdSe NPs are presented in Figure 6.12. Representative ellipsoids are placed above the surface to indicate what the NP morphology looks like within selected regions. The local maximum and minimum can be seen more precisely in the corresponding contour plot in Figure 6.12b. A number of interesting conclusions can be drawn from this data. The spherical CdSe NP exhibited the largest E_{EB} (57.0 meV), whereas the binding energy for the wire-like CdSe NP was much smaller (1.3 meV). The disk and "surfboard" morphologies were in between the sphere and the wire, with moderate decreases in binding energy relative to the sphere (23.8 meV and 22.6 meV respectively).

Effect of Shape on Electron-hole Separation Distance in Isovolumetric CdSe Nanoparticles

In addition to E_{EB}, the effect of shape on $\langle r_{eh} \rangle$ in these CdSe systems was also investigated. As seen in our previous results, the observed trend from the effect of shape on $\langle r_{eh} \rangle$ was essentially the opposite of the trend for E_{EB}. The wire-like ellipsoid exhibited an $\langle r_{eh} \rangle$ distance of 284 nm, while the spherical ellipsoid exhibited an $\langle r_{eh} \rangle$ distance of only 5.6 nm. The $\langle r_{eh} \rangle$ distance of the disk and surfboard shapes increased moderately relative to the sphere (13.21 nm and 14 nm respectively). This data can be seen in Figure 6.13.

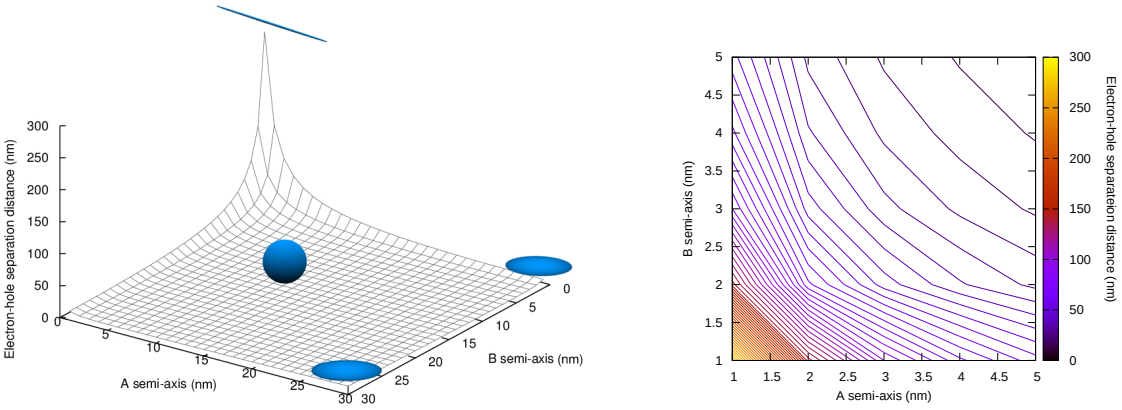

(a) (b)

Figure 6.13: Surface plot (a) and contour plot (b) of nanoparticle A and B semi-axis lengths vs. electron-hole separation distance.

Interestingly, once a semi-axis of one of these isovolumetric NPs becomes sufficiently large, $\langle r_{eh} \rangle$ becomes very insensitive to further changes in morphology. The contour plot in Figure 6.13b corresponds to this surface plot, and focuses only on the region where the A and B semi-axis lengths are ≤ 5 nm, and therefore is centered where the C semi-axis is very large. The sudden decrease in $\langle r_{eh} \rangle$ with increasing A and B semi-axis length is apparent. It can be seen from these plots that E_{EB} and $\langle r_{eh} \rangle$ distance had an inverse relationship with one another.

Effect of Shape on Electron-hole Recombination Probability in Isovolumetric CdSe Nanoparticles

Lastly we investigate the P_{eh} exhibited by these CdSe NP systems. As seen in Figure 6.14, when the NP was deformed stepwise in this manner, there is no simple trend observed for P_{eh} as a function of NP shape as was seen with E_{EB} and $\langle r_{eh} \rangle$.

The P_{eh} values in this study were calculated relative to the recombination probability for the spherical ($A = B = C = 10$nm) CdSe ellipsoid. In this way, the relative P_{eh} calculated for the sphere is 1.000, for the wire ($A = B = 1\text{nm}, C = 1000\text{nm}$) is 0.620, and for a disk ($A = B = 30\text{nm}, C = 1\text{nm}$) is 1.814. The general trends of A and B axis length on relative P_{eh} are more easily distinguished in the contour plot corresponding to this data in Figure 6.14b.

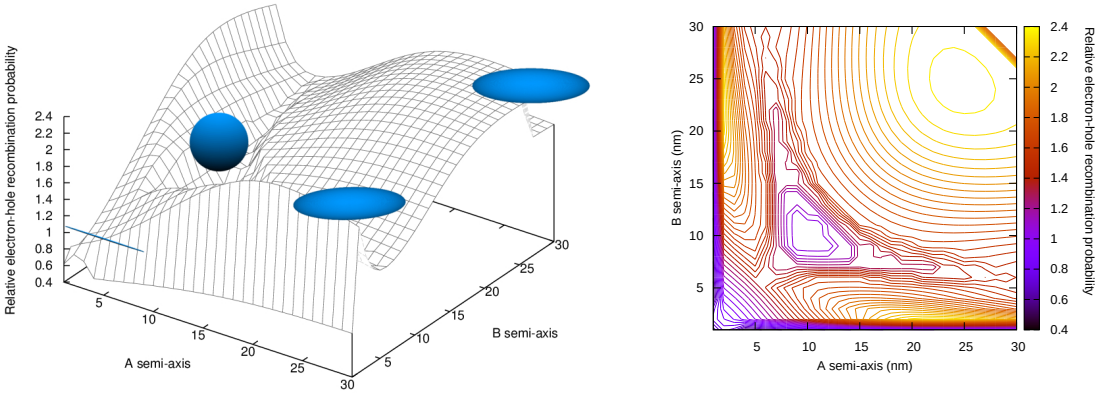

(a) (b)

Figure 6.14: Surface plot (a) and contour plot (b) of nanoparticle A and B semi axis lengths vs. relative electron-hole recombination probability.

The recombination behavior with respect to ellipsoid semi-axis length is non-uniform and complicated. However, there are certain interesting characteristics in the data. Two local maxima exist in the plot of P_{eh}, one where both A and B semi-axes are large (as in disk-like ellipsoids), and one when a single semi-axis is very small. There are local minima when both semi-axes are very small as in wire-like ellipsoids, and when both semi-axes are equal as in the sphere. The surface plot forms a saddle point through the diagonal of the plot, where the A and B semi axis lengths are equal.

The motivation for determining a relationship between NP geometry and optical properties is to be able to define an intrinsic length scale that relates the shape of these NPs to their optical properties. Figure 6.15 shows E_{EB} plotted

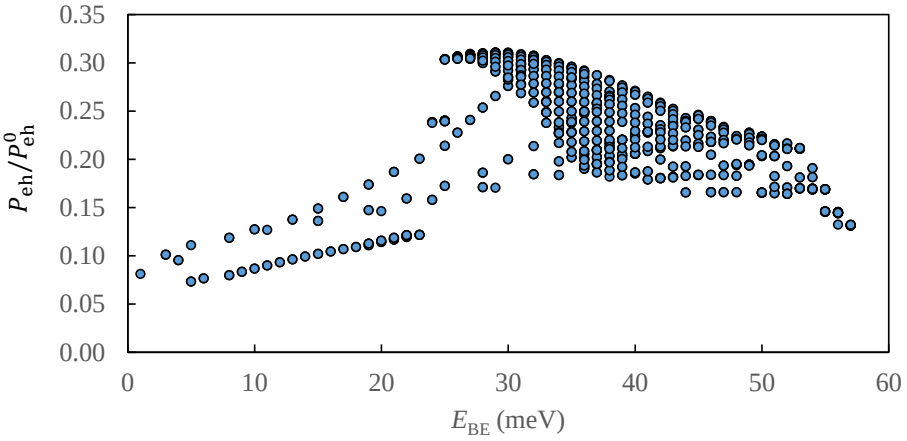

Figure 6.15: Exciton binding energy vs. recombination probability for 900 ellipsoidal isovolumetric CdSe nanoparticles.

vs. P_{eh} for the set of 900 isovolumetric CdSe NPs. The lack of a distinct trend demonstrates that for a system of fixed size and material type, there is no clear relationship between E_{EB} and P_{eh} for a given NP. The data that corresponds to the range of smaller E_{EB} values belongs to the extremely anisotropic NPs. It can be seen that the ratio between P_{eh} and E_{EB} did not change very much until extreme deformation of the NP shape from nanosphere to nanowire occurred.

E_{EB} was additionally plotted against $\langle r_{\text{eh}} \rangle^{-1}$, since an inverse relationship between the two was observed. A well-behaved linear dependence was found from a plot of these two properties. Rather intuitively, the negatively charged electron and positively charged hole bind more strongly the closer they are to one another, and less strongly the further apart they are. It is for this reason that semiconducting nanowires (which exhibit large $\langle r_{\text{eh}} \rangle$) experience smaller values of E_{EB}, while spheres (which exhibit smaller r_{eh}) have larger E_{EB}. This plot can be seen in Figure 6.16, and provides evidence that the eh-separation distance is a characteristic length scale that relates to E_{EB} in semiconducting NPs.

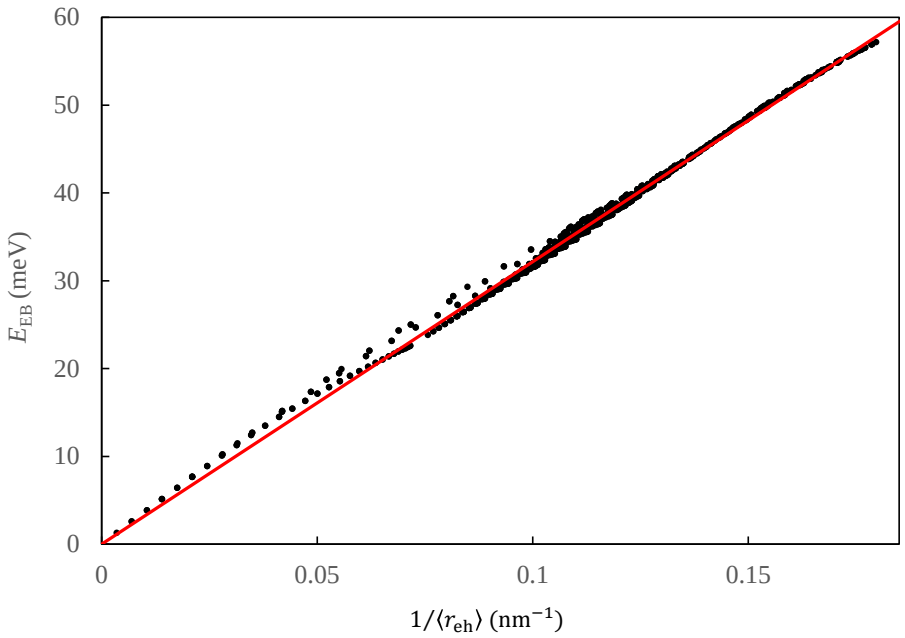

Figure 6.16: Exciton binding energy vs. $\langle r_{\text{eh}} \rangle^{-1}$ in CdSe ellipsoids. The linear relationship between exciton binding energy and $\langle r_{\text{eh}} \rangle^{-1}$ is readily apparent. The red line is a linear fit with the form $f(x) = 321$ meV(x), and has a correlation coefficient [255] $R^2 = 0.9997$, max deviation = 2.140, average signed deviation = 0.03909, average unsigned deviation = 0.4510.

Conclusions

The eh-XCHF method was used to study optoelectronic properties of CdSe, CdS, CdTe, and PbS NP ellipsoids by performing isovolumetric transformations. This general method can be used to study a large variety of electron-

hole systems. In work presented here, the electron and hole were treated as an interacting pair confined to a three-dimensional parabolic potential. The eh-XCHF wave function was used to calculate the ground state exciton binding energy, electron-hole separation distance, and electron-hole recombination probability of the NPs. We found that all three properties were found to have a strong dependence on ellipsoid shape, even at constant volumes. We also found that exciton binding energy was maximum in the case of a sphere and minimum in rods, which had the largest aspect ratio. The electron-hole separation distance exhibited the opposite trend. These trends were observed consistently across all semiconductor NPs, regardless of size. The exciton binding energies exhibited a strong linear dependence with respect to the inverse of the electron-hole separation distance, making this inverse distance a useful intrinsic length scale for predicting optical properties in these materials.

Chapter 7

Investigating Optoelectronic Properties of Perovskite Nanoparticles

Introduction

Cesium Lead Halide Nanoparticles

In 2015, Protesescu et al. were the first to synthesize all-inorganic $CsPbX_3$ (X=Cl,Br,I) perovskite nanoparticles (NPs) [256]. While these materials are not as soluble as their hybrid organic-inorganic $MAPbX_3$ counterparts, they have been observed to possess very advantageous and promising optical properties. They found that these NPs exhibited narrow emission line widths of 12-42 nm, high quantum yields of 50-90%, and short radiative lifetimes of 1-29 ns. The NPs also possess band gap tunability though modification of the halide ion, as well as size-tunability of their band gap energies through the entire visible spectral region. These NPs are able to exhibit these properties without the need for an epitaxial shell material [256].

Optoelectronic Properties of $CsPbX_3$ Nanoparticles

Since $CsPbX_3$ were first synthesized, there has been a large amount of investigation done in order to better characterize the electronic structure and optoelectronic properties of these NPs. In 2015, Nedelcu et al. showed that by adjusting the halide ratios in $CsPbX_3$ NPs with anion-exchange reactions, the photoluminescence they exhibit can be tuned over the entire visible spectral region while maintaining high quantum yields and narrow emission line widths [257]. In 2015, Akkerman et al. were able to tune the chemical composition and the optical properties of pre-synthesized colloidal cesium lead halide perovskte NPs. Again using controlled anion-exchange reactions, they were able to change a green-emitting $CsPbBr_3$ NP to any other region of the visible spectrum by displacing the Br^- ions and inserting Cl^- or I^- ions [258].

In 2015, Park et al. investigated the properties of a single-photon emission from an isolated $CsPbX_3$ NP at room temperature. They calculated very fast nonradiative Auger recombination times, which they found rendered multiexciton states virtually non-emissive [259]. A year later in 2016, Makarov and coworkers investigated the properties of

excitons and biexcitons in $CsPbX_3$ NPs. They found that the spectroscopic properties of these NPs are very similar to those of CdSe and PbSe NPs. However, two of the key differences they noted were that there is a strong effect of the halide ion on the radiative lifetimes of the NP, and that there is a deviation in the size-dependent properties from the so-called "universal volume scaling" observed for CdSe and PbSe NPs. [260]

Applications of $CsPbX_3$ Nanoparticles

Because of their excellent spectroscopic qualities and the convenient tunability of their properties through halide ion exchange, much work has already been done to study the potential applications of $CsPbX_3$ NPs in optoelectronic devices.

Song and coworkers were able to develop $CsPbX_3$ NP-based LEDS in 2015, where they were able to tune the luminescence wavelength by changing both the size and halide composition o the NPs [261].

In 2016, Li et al. coated green-emissive $CsPbBr_3$ NPs with red phosphors onto an InGaN chip, which produced warm white light emission with a high rendering index of 93.2 [262]. The following year, Zhang et al. were able to optimize $CsPbBr_3$ NP-based LEDS by incorporating a small amount of methylammonium organic cation into the lattice. They found that this improved the previously low efficiency resulting from high leakage current caused by poor perovskte morphology [263].

In 2015, Yakunin and coworkers demonstrated that $CsPbX_3$ (X=Cl, Br or I) colloidal NPs were capable of exhibiting low-threshold amplified spontaneous emission and lasing over the entire visible spectrum [264]. Wang et al. were also able to produce $CsPbX_3$ NP lasers in 2016, where they were able to obtain a large two-photon absorption cross-section of 1.2×10^5 GM for the 9 nm $CsPbBr_3$ NPs [265].

Ramsay et al. were able to develop $CsPbI_3$ NP photodetectors in 2016, which exhibited good on/off photocurrent ratios of around 105 [266].

In 2015, Kulbak, Kahen, and Hodes showed that the organic cation in methylammonium lead halide perovskte NPs was unnessecary to obtain high quality perovskte NP-based solar cells [267]. A year later, Sutton et al. developed an efficient, all-inorganic, band-gap tunable $CsPbX_3$ NP-based solar cell with high thermal stability [268].

Calculation of $CsPbX_3$ Nanoparticle Optoelectronic Properties

In this work, we present theoretical calculations on $CsPbX_3$ NPs similar in nature to Protesescu NP systems [256]. Here, we investigate the optical properties of spherical NPs (rather than cubic), which have radii equal to the edge length of the cubic NP counterparts. Using the electron-hole explicitly correlated Hartree-Fock method (eh-XCHF), we calculate the effect of NP size and composition on the exciton binding energy (E_{EB}), the electron hole recombination probability (P_{eh}), and the electron hole separation distance ($\langle r_{\mathrm{eh}} \rangle$).

Table 7.1: **System parameters used to calculate properties of NPs. ε is the dielectric constant of the material, m_e is the effective mass of the electron, m_h is the effective mass of the hole, and m_0 is the mass of a free electron.**

	$CsPbCl_3$	$CsPbBr_3$	$CsPbI_3$
ε	6.2	5.4	7.1
m_e	0.13 m_0	0.19 m_0	0.12 m_0
m_h	0.38 m_0	0.22 m_0	0.13 m_0

Computational Details

System Setup and Parameters

The NPs in this study were modeled using the electron-hole explicitly correlated Hartree-Fock (eh-XCHF) method, under the effective mass approximation regime. The complete details of the eh-XCHF method are outlined in the work by Elward et. al. [241]. Only a brief overview of the method is discussed here. In order to solve the electron-hole Schrödinger equation for these systems, the effective electron-hole Hamiltonian [242, 243, 244, 245, 246] was used, shown in Equation 7.4:

$$\hat{H} = \sum_{ij} \langle i| \frac{-\hbar^2}{2m_e} + v^e_{ext} |j\rangle e^\dagger_i e_j \tag{7.1}$$

$$+ \sum_{ij} \langle i| \frac{-\hbar^2}{2m_h} + v^h_{ext} |j\rangle h^\dagger_i h_j \tag{7.2}$$

$$+ \sum_{iji'j'} \langle iji'j'| \varepsilon^{-1} r^{-1}_{eh} |iji'j'\rangle e^\dagger_i e_j h^\dagger_{i'} h_{j'} \tag{7.3}$$

$$+ \sum_{ijkl} w^{ee}_{ijkl} e^\dagger_i e^\dagger_j e_l e_k + \sum_{ijkl} w^{hh}_{ijkl} h^\dagger_i h^\dagger_j h_l h_k. \tag{7.4}$$

The effective electron-hole Hamiltonian provides a computationally efficient means of calculating the optical properties of interest in these NPs. A table of the effective mass parameters used for each system is tabulated in Table 7.2.

The external potential used in this investigation is a parabolic potential for both the electron and hole. Parabolic potentials have been used extensively to approximate the confinement potential of semiconductor NPs [247, 248, 249, 250].

$$v^\alpha_{ext} = \frac{1}{2} k_\alpha |\mathbf{r}_\alpha|^2 \quad \alpha = e, h, \tag{7.5}$$

The magnitude of the force constants in the external confining potential are important for accurately calculating exciton binding energy in these NPs. The force constants are calculated such that the electron and hole are confined to the

physical dimensions of the NP [250] shown in Equation 7.6

$$\min_{k_\alpha^{min}} = \left(N_\alpha - \int_0^{\frac{D_{dot}}{2}} dr r^2 \int d\Omega \rho_\alpha(\mathbf{r})[v_{ext}^\alpha] \right)^2, \tag{7.6}$$

where $\alpha = \mathrm{e,h}$, $d\Omega = \sin d\theta d\varphi$, D_{dot} is the diameter of the NP, and k_α is the smallest force constant that satisfies the above minimization conditions.

Mathematical Description of Optoelectronic Properties of Interest

The three optical properties of interest in this study are the exciton binding energy, the electron hole recombination probability, and the electron hole separation distance. The exciton binding energy is defined as the total energy of a fully interacting electron hole system, less the fully non-interacting system (Equation 8.12)

$$E_{\mathrm{EB}} = \langle E_{\mathrm{non-interacting}} \rangle - \langle E_{\mathrm{exciton}} \rangle. \tag{7.7}$$

The electron-hole separation distance is calculated as the expectation value of the absolute difference between the electron and hole coordinates (Equation 7.8)

$$\langle r_{\mathrm{eh}} \rangle = \langle \Psi_{\mathrm{eh-XCHF}} || \mathbf{r}_\mathrm{e} - \mathbf{r}_\mathrm{h} || \Psi_{\mathrm{eh-XCHF}} \rangle. \tag{7.8}$$

The electron hole recombination probability is calculated as the probability of finding a hole within a small finite region around the electron coordinate (Equation 7.9)

$$P_{\mathrm{eh}} = \frac{1}{N_\mathrm{e} N_\mathrm{h}} \int d\mathbf{r}_\mathrm{e} \int_{\mathbf{r}_\mathrm{e} - \frac{\mathbf{\Delta}}{2}}^{\mathbf{r}_\mathrm{e} + \frac{\mathbf{\Delta}}{2}} d\mathbf{r}_\mathrm{h} \, \rho_{\mathrm{eh}}(\mathbf{r}_\mathrm{e}, \mathbf{r}_\mathrm{h}). \tag{7.9}$$

Results and Discussion

Effect of Dot Size on Electron-hole Separation Distance

In Figure 7.1, the electron hole separation distance ($\langle r_{\mathrm{eh}} \rangle$) is plotted vs. r_{dot}. Defined in Equation 7.8, $\langle r_{\mathrm{eh}} \rangle$ is the average distance between the electron and hole in the NP. It can be seen that the $\langle r_{\mathrm{eh}} \rangle$ was essentially independent of halide ion in the crystal structure. $\langle r_{\mathrm{eh}} \rangle$ increased linearly as the size of the NPs increased, and scaled nearly the same

independent of halide type. This property of $\langle r_{eh} \rangle$ to increase linearly with increasing spherical NP radius has been observed previously in other systems studied with eh-XCHF [250].

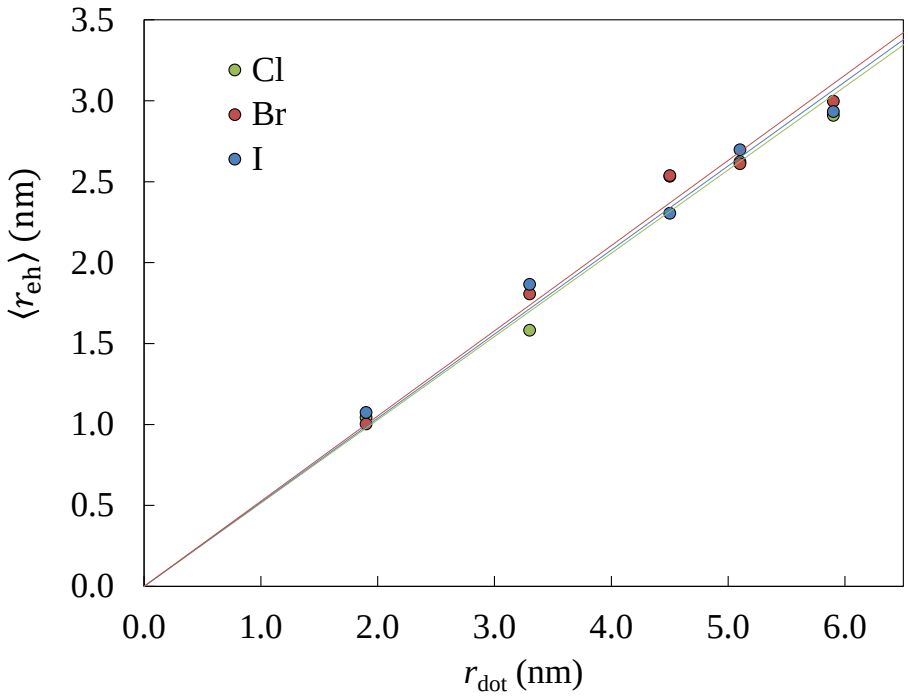

Figure 7.1: Electron hole separation distance vs. NP radius for $CsPbCl_3$ ($y = 0.5145x, R^2 = 0.9675$), $CsPbBr_3$ ($y = 0.5263x, R^2 = 0.9797$), and $CsPbI_3$ NPs ($y = 0.5195x, R^2 = 0.9763$).

Effect of Dot Size on Exciton Binding Energy

In Figure 7.2, exciton binding energy (E_{EB}) of each NP is plotted vs. the radius of the NP (r_{dot}). E_{EB} is defined as the differences between the interacting and non-interacting electron-hole system, as seen in Equation 8.12. It can be seen that E_{EB} follows a power-scaling with respect to increasing NP radius. Additionally, the values were largest in $CsPbCl_3$ NPs at all corresponding NP sizes, and smallest in $CsPbI_3$ NPs. This trend is additionally followed by the exciton Rydberg energies of these materials.

Also observed is that E_{EB} in smaller NPs were larger than the binding energies in larger NPs. As NP size increases, the binding energies appear to decrease exponentially. This same property of $CsPbX_3$ spherical NPs has been observed in the past both experimentally and theoretically [269].

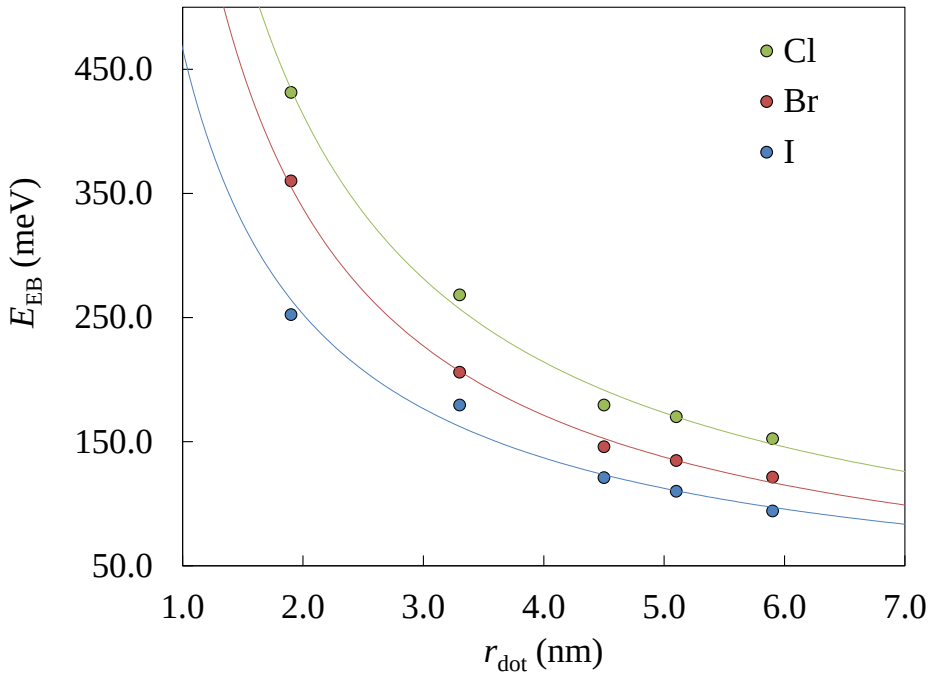

Figure 7.2: Exciton binding energy vs. NP radius for $CsPbCl_3$ ($y = 12.284x^{-5.713}, R^2 = 0.993$), $CsPbBr_3$ ($y = 14.522x^{-6.004}, R^2 = 0.9973$), and $CsPbI_3$ ($y = 97.187x^{-6.938}, R^2 = 0.992$) NPs.

Effect of Dot Size on Electron Hole Recombination

In Figure 7.3, the electron hole recombination probability (P_{eh}) is plotted vs. r_{dot}. Defined in Equation 7.9, P_{eh} is the on-top probability that an electron and hole will recombine . It can be seen that P_{eh} follows a power-scaling law with respect to NP radius, as it does with E_{EB}. P_{eh} was greatest in $CsPbI_3$ NPs, and smallest in $CsPbCl_3$ NPs. Perovskite NPs with bromide ions are in-between the two. Interestingly, this relationship with halide type exhibited for P_{eh} is the opposite of the observed trend for exciton binding energy.

Also seen is that P_{eh} in smaller NPs was larger than the recombination probabilities in larger NPs. Recombination probability dropped off rapidly as the NP size increased. This is a trend that has been observed previously in other systems studied with eh-XCHF [238, 241, 250].

Effect of Electron-hole Separation Distance on Exciton Binding Energy and Electron-hole Recombination

In Figure 7.4, exciton binding energy is plotted vs. inverse electron hole separation distance ($\langle r_{eh} \rangle^{-1}$). Here again, the chloride-containing NPs exhibited larger E_{EB} values than bromide NPs, which exhibited larger E_{EB} values than iodide NPs. E_{EB} increased linearly with increasing $\langle r_{eh} \rangle^{-1}$ for all NPs, but scaled differently for different NPs. It is the

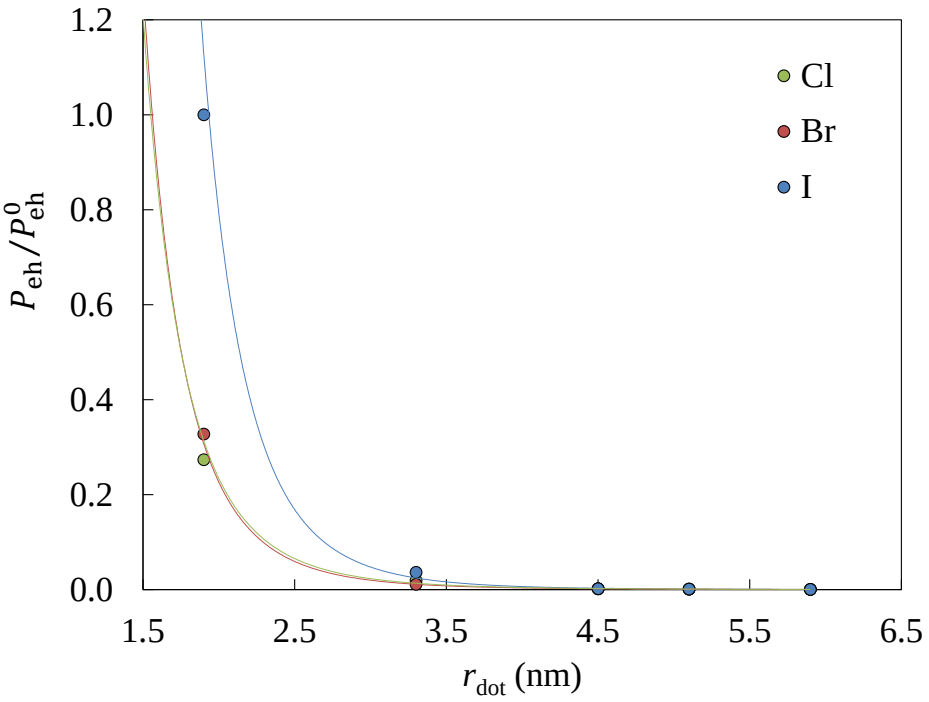

Figure 7.3: Electron hole recombination probability vs. NP radius for $CsPbCl_3$ ($y = 798.48x^{-0.949}, R^2 = 0.9907$), $CsPbBr_3$ ($y = 666.89x^{-0.98}, R^2 = 0.9955$), and $CsPbI_3$ ($y = 466.33x^{-0.884}, R^2 = 0.9786$) NPs.

halide ion in the perovskite structure that appears to determine this scaling relationship. This material-dependent linear scaling of EEB with respect to r_{eh}^{-1} has been observed in previous investigations of NPs using eh-XCHF. [238, 250]

In Figure 7.5, P_{eh} is plotted vs. $\langle r_{eh} \rangle^{-1}$. The trend for this data closely fits a power relationship. Here again, the chloride-containing NPs exhibited larger E_{EB} values than bromide NPs, which exhibited larger E_{EB} values than iodide NPs. E_{EB} increased linearly with increasing $\langle r_{eh} \rangle^{-1}$ for all NPs, but scaled differently for different NPs. It is the halide ion in the perovskite structure that appears to determine this scaling relationship. This material-dependent linear scaling of E_{EB} with respect to $\langle r_{eh} \rangle^{-1}$ has been observed in previous investigations on NPs using eh-XCHF. [238, 250]

Comparison of Trends to Bulk $CsPbX_3$ Exciton Properties

In order to demonstrate the size-tunability of the electron and hole confinement in these systems, Protesescu et. al. calculated exciton Bohr radius and exciton Rydberg energy using effective electron and hole masses. They determined that their calculations produced the same trend in exciton binding energies that we calculated using eh-XCHF, where $CsPbI_3$ NPs have smaller binding energies than the other perovskite NPs. This result is further confirmed by DFT analysis done by Murtaza and coworkers [270], and experimental work by Diroll and cowrokers [271].

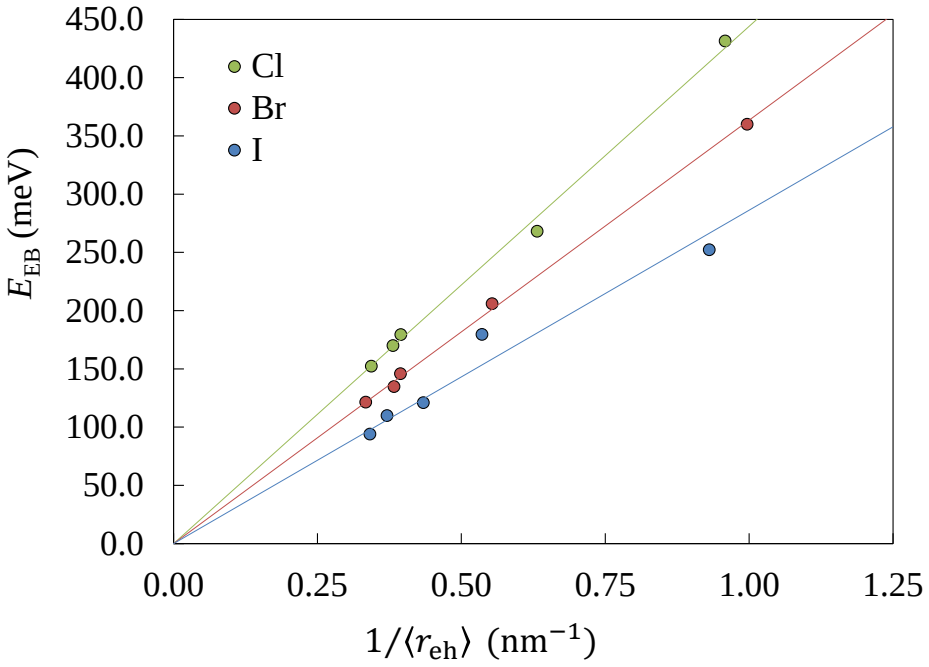

Figure 7.4: Exciton binding energy vs. inverse electron hole separation distance for $CsPbCl_3$ ($y = 444.1x, R^2 = 0.9962$), $CsPbBr_3$ ($y = 363.53x, R^2 = 0.9985$), and $CsPbI_3$ ($y = 286.26x, R^2 = 0.9454$) NPs.

Table 7.2: **Exciton Bohr radii of the three different perovskite systems, and their respective exciton Rydberg energies. Calculated exciton binding energies for $D = 5$ nm spherical NPs are included for comparison.**

	Exciton Bohr radius	Exciton Rydberg energy	eh-XCHF E_{EB}
$CsPbCl_3$	5 nm	75 meV	152 meV
$CsPbBr_3$	7 nm	40 meV	121 meV
$CsPbI_3$	12 nm	20 meV	94 meV

Conclusions

In conclusion, we have been able to determine the effect of size and material composition on spherical $CsPbX_3$ perovskite NPs. We have demonstrated that these perovskite NPs exhibit size tunability similar to other semiconductor NP systems. Additionally, modification of the halide ion in the perovskite structure has an equally important effect on the calculated exciton binding energies and electron-hole recombination probabilities. In the future, fully atomistic calculations performed on cubic perovskite $CsPbX_3$ NPs can be done in order to more fully characterize and benchmark the exciton behavior in these perovskite systems,

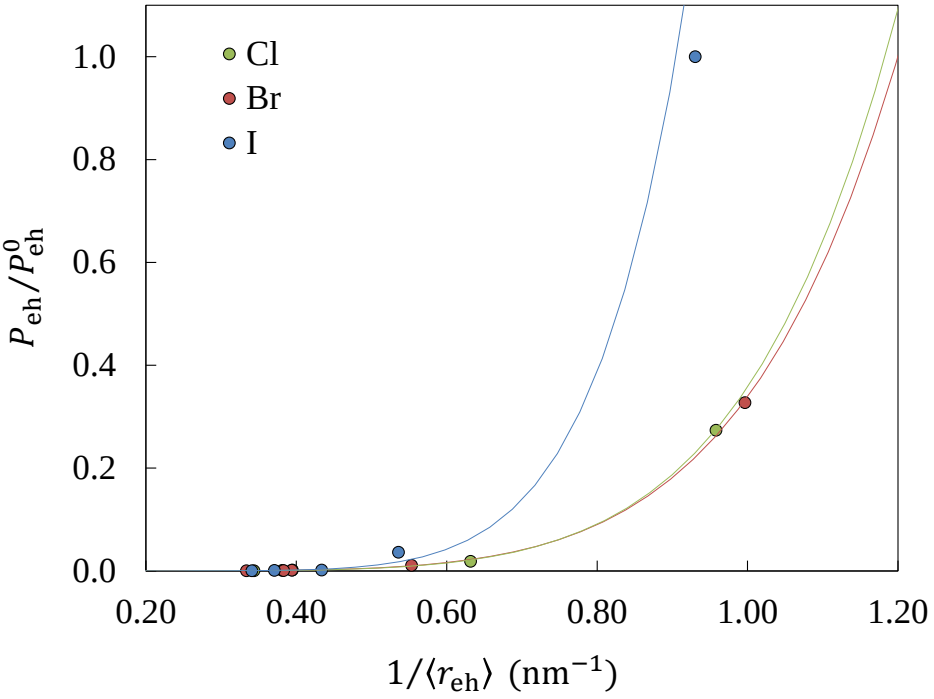

Figure 7.5: Electron hole recombination probability vs. inverse electron hole separation distance for $CsPbCl_3$ ($y = 0.3388x^{5.9377}, R^2 = 0.9926$), $CsPbBr_3$ ($y = 0.3575x^{6.128}, R^2 = 0.9957$), and $CsPbI_3$ ($y = 2.16x^{7.710}, R^2 = 0.9752$) NPs.

Chapter 8

Temperature-dependent Exciton Binding Energies of CdSe Nanoparticles

Introduction

In the previous chapters, I have presented the utility of both the Effective Stochastic Potential (ESP) [24] and electron-hole explicitly correlated Hartree-Fock (eh-XCHF) [241] methods. Within the chapters on ESP and ESP-CIS, I demonstrated the importance of obtaining very large sample sizes of thermally-accessible structures in order to accurately calculate distributions of quantum mechanical properties. The previous two chapters on eh-XCHF covered answers to a very different type of chemical challenge, namely the efficient treatment of calculating electron-hole correlation and exciton properties in large NP systems.

Ideally, we would like be able to address both of these challenges simultaneously, since temperature and solvent play a very important role in the distribution of exciton properties in semiconductor NPs.

Thermal and Solvent Effects on Optical Properties of Semiconductor Nanoparticles

The effect of temperature on calculated and experimentally observed exciton properties has been studied extensively. In 2006, Kamisaka and co-workers performed quantum dynamics simulations on $Pb_{16}Se_{16}$ and $Pb_{68}Se_{68}$ QDs using density functional theory (DFT). They found that at ambient temperatures the vibrationally-induced dephasing of electronically excited states was extremely rapid, and was only weakly depended on the magnitude of the excitation energy. They also found that multiexciton states dephased more quickly than single exciton states [112]. In 2007, Morello and co-workers used photoluminescence spectroscopy to showed that the optical gap of CdTe NPs decreased with increasing temperature. They found that while the coupling constant with acoustic phonons was strongly enhanced in NPs with respect bulk CdTe, the exciton-LO phonons coupling constant decreases as the NP size decreases [272]. In 2009, Madrid et al studied multi-exciton generation (MEG) and fission (MEF) in hydrogen-passivated Si NPs using AIMD. They found that the dynamics of the lower-frequency modes were more significantly affected by temperature variations, and the MEF dephasing time showed stronger temperature dependence than MEG in these systems. [273]. Chon and co-workers found in 2011 that the band gaps of CdTe/CdSe core-shell NPs decreased with increasing temperature,

and their PL peaks broadend. They also found that band gap shift was less temperature sensitive in NPs with thicker shells, but the broadening was more sensitive. [274]. In 2013, Dey et al investigated the temperature dependence of band gap of PbS and PbSe semiconductor nanocrystals of different diameter, which they measured using FTIR spectroscopy. They found that while in general the PbSe NPs showed increasing optical gap with increasing temperature, at some critical size between $D = 3.2$ nm and $D = 2.3$ nm, the trend between gap and temperature flipped [275].

Early theoretical work performed on NPs in the area of solvent effect where Rabani et al. investigated the electronic properties of CdSe nanocrystals, both in absence and presence of dielectric medium, using an empirical pseudopotential method. They found that the band gaps for CdSe NPs decreased for all NP sizes investigated as dielectric constant of the surroundings increased, but that the NPs with larger dipole moments were much more sensitive to this effect than those with smaller dipoles. [276] In 2001, Leatherdale et al reported on solvatochromatic shifts in the absorption spectra of colloidal CdSe NPs. Their results agreed well with expected change in polarization energy of the confined exciton from theory when accounting from the screening effect on the exciton due to the ligand shell. [277] In 2012, Lee and co-workers developed a method they call nanoscale solvothermal reaction in order to induce the quantum confinement effect of CdSe on nanostructured TiO_2. CdSE NP growth on the oxide surface only occured in the presence of solvent, and increasing temperature of the synthetic conditions systematically decreased the band gap of the NPs [278]. In 2014, Kuznetslv et al performed DFT (B3LYP/Lanl2dz) studies of the structural and electronic properties of both bare and NH_3-, SCH_3-, and OPH_3-capped $Cd_{33}Se_{33}$ and $Cd_{33}Te_{33}$ NPs in the presence of solvent. Specifically, they were able to calculate HOMO-LUMO gap stabilization effects, and found that inclusion of implicit solvent tended to destabilize HOMO and LUMO energies in bare NPs, while it tended to stabilize them in ligand-capped NPs. [279]

In 2011, Long et. al. reported on their NAMD simulation of electron transfer from PbSe NP to a TiO_2 surface, serving as a model NP-sensitized solar cell. Their simulation supported the observation that electron transfer successfully competes with energy loss due to electron-phonon interaction. They described this difference between NPs and molecules as arising from from increased rigidity of NPs compared to molecular systems. In molecular systems, optical phonons are not thermally accessible in ambient conditions, while in the NPs, electron transfer can be promoted by low-frequency optical phonons [181]. That same year, Chen et al also performed NAMD simulations to study phono-assisted hot electron relaxation dynamics in both spherical and rod-like CdSe NPs. They found that the band gap showed a stronger negative dependence in the rod-like NPs, and that electron-phonon coupling was generally stronger in the rod-like NP compared to the spherical one. They also saw that the relaxation of hot electrons in the rod-like NP proceeded faster and had stronger temperature dependence than the spherical NP [221]. In 2012, Hyeon-Duek et al investigated MEG and multiexciton recombination (MER) dynamics semidoncudtor NPs using time-dependent density functional theory (TDDFT) combined with NAMD. They observed MEG at energies below the purely electronic threshold in the presence of high-frequency ligand vibrations, and found that exciton-phonon

coupling was essential for MER due to the fact that higher-energy biexcitons must relax to recombine into single excitons, and the single excitons must further relax to avoid recreating the biexcitons. [280] In 2016, Pal and co-workers, investigated excited state dynamics by developing an approach that combines NAMD with the self-consistent charge density functional tight binding method. They tested their method against ab initio DFT and experimental data with good agreement. They found their method was able to accurately and effciently treat excitation dynamics in large, realistic nanomaterials. [281]

Integration of the ESP and eh-XCHF Methods

Our approach for calculating temperature-dependent electron-hole properties of NPs is to combine the ESP and eh-XCHF methods. In this way, we are able to both capture the effect of the chemical environment on the NP ensemble and sample exciton properties much more efficiently than with traditional ab-initio techniques. In this work, we have used an effective stochastic potential in conjunction with the eh-XCHF method in order to calculate ensemble-averaged exciton binding energies at room temperature in CdSe NPs. We call the combination of these two methods the ESP-XCHF method.

An overview of the theoretical details of the ESP-XCHF is described in section 8.2. The computational details for implementation of the ESP method with the eh-XCHF method, including sampling schemes, choice of basis, and form of the ESP, and definitions of the properties of interest are presented in section 8.3. The developed ESP-XCHF method was used to perform calculations of ensemble-averaged HOMO-LUMO gap energies and exciton binding energies in chemical systems, and results for $Cd_{20}Se_{19}$ are presented in section 8.4.

Theory

Generation of Stochastic Electron-hole States

As in the previous chapters on the eh-XCHF method, the ansatz of the electron-hole wave function is a product of electron an hole states, correlated by a two-body Gaussian-type geminal operator [241] shown in Equation 8.1

$$\Psi_{\mathrm{eh}} = \hat{G}|\Phi_{\mathrm{e}}\Phi_{\mathrm{h}}\rangle, \tag{8.1}$$

where Ψ_{eh} is the exact wave function of the system, $\hat{G}$ is the geminal operator, and Φ_{e} and Φ_{h} are the electron and hole wave functions, respectively. If we make the approximation that the singly-excited state of the system is entirely dominated by the HOMO-to-LUMO transition, we can then write Ψ_{eh} in terms of the HOMO and LUMO eigenvectors

of the Fock operator as in Equation 8.2:

$$\Psi_{\text{eh}} = \hat{G}|\chi_{\text{LUMO}}\chi_{\text{HOMO}}\rangle. \tag{8.2}$$

With a suitable effective stochastic potential (ESP), the orbitals of the system are themselves stochastic eigenvectors of the ESP Hamiltonian (Equation 8.3):

$$F^{\text{ESP}}\chi^{\text{ESP}} = \varepsilon^{\text{ESP}}\chi^{\text{ESP}}. \tag{8.3}$$

From here we are in position to define the ESP-XCHF electron-hole wave function Equation 8.4:

$$\Psi^{\text{ESP}}_{\text{eh}} = \hat{G}|\chi^{\text{ESP}}_{\text{LUMO}}\chi^{\text{ESP}}_{\text{HOMO}}\rangle. \tag{8.4}$$

In this way, $\Psi^{\text{ESP}}_{\text{eh}}$ is a stochastic electron-hole wave function that depends explicitly on the electron-hole separation distance and whose orbitals randomly fluctuate according to the ground-state ensemble at a given temperature.

Calculation of Temperature-Dependent Exciton Binding Energies

All CdSe NPs in this study were modeled using the ESP-XCHF method. We have defined the exciton binding energy, as in previous chapters, as the total energy of a fully interacting electron-hole system, less the fully non-interacting system, shown in Equation 8.5:

$$E_{\text{EB}} = \langle E_{\text{non-interacting}}\rangle - \langle E_{\text{exciton}}\rangle. \tag{8.5}$$

The energy of the electron-hole ESP-XCHF interaction can be calculated by taking the expectation value given in Equation 8.6

$$E_{\text{EB}} = \frac{\langle \chi_{\text{e}}\chi_{\text{h}}|r_{12}^{-1}|\chi_{\text{e}}\chi_{\text{h}}\rangle}{\langle \chi_{\text{e}}\chi_{\text{h}}|\chi_{\text{e}}\chi_{\text{h}}\rangle} - \frac{\langle \chi_{\text{e}}\chi_{\text{h}}|Gr_{12}^{-1}G|\chi_{\text{e}}\chi_{\text{h}}\rangle}{\langle \chi_{\text{e}}\chi_{\text{h}}|GG|\chi_{\text{e}}\chi_{\text{h}}\rangle}, \tag{8.6}$$

where χ_{e} and χ_{h} are the electron and hole states, G is the geminal operator, and r_{12}^{-1} is the inverse electron-hole separation distance. The numerator bust be divided by the denominator to ensure the value is properly normalized for the chosen geminal operator.

In the present work, where the electron and hole states are chosen to be the ESP LUMO and HOMO eigenvectors, the expression for the electron-hole interaction energy can be expanded in terms of ESP molecular orbital coefficients

of the HOMO and LUMO orbitals as shown in Equation 8.7

$$\sum_{\mu'\nu'}\sum_{\mu\nu} c^e_\mu c^e_\nu c^h_{\mu'} c^h_{\nu'} [\mu\nu|g r_{12}^{-1} g|\mu'\nu']. \tag{8.7}$$

Computational Details

System Details

The geometry of the reference system was generated by cutting out a spherical section from a CdSe wurtzite crystal structure, and then optimizing the resulting cluster using the Universal Force Field [282]. The 1-particle states of the minimum energy reference structure were obtained by performing single point energy calculation on the resulting UFF optimized structure at restricted Hartree Fock (RHF) level of theory using LANL2DZ ECP basis [80] using the GAMESS software package [283].

The ESP for this NP system is generated from 45 ground state Hartree-Fock calculations.

Canonical Ensemble Sampling Using Monte Carlo and Molecular Dynamics

The probability p^η associated with the structure $\mathbf{R}^\eta$ depends on the thermodynamic conditions of the physical system, and can be chosen to describe both equilibrium and non-equilibrium conditions. In this work, we are interested in systems at thermal equilibrium, which are well-described using the constraints of canonical ensemble with constant composition, temperature, and volume (N,V,T). For canonical ensemble, the probability is the well-known Boltzmann expression as shown below:

$$p^\eta = \frac{e^{-\beta(E^\eta - E^0)}}{\sum_{\lambda\in\mathscr{S}_{\text{def}}} e^{-\beta(E^\lambda - E^0)}}, \tag{8.8}$$

where, $\beta = (k_B T)^{-1}$ and E^η is the energy of the deformed structure and E^0 is the energy associated with the minimum-energy structure. The first step in the determination of the deformation potential is the generation of the set of structures $\mathbf{R}^\eta$. In principle, the set of structures can be achieved using either Monte Carlo (MC) by molecular dynamics (MD) simulations. The key point in both of these approaches is to generate a statistically meaningful sample of thermally accessible structures. In the MC procedure, this is achieved by randomly distorting the optimized structure, calculating its energy, and and calculating the mean and central moments using the Boltzmann-weighted procedure described in Equation 8.8. In the MD procedure, equilibrium molecular dynamics calculations are performed at fixed N,V,T and the structures are then randomly selected from the equilibrium distribution. It is important to note that Boltzmann weights are only needed for MC sampling, and should not be included in the case of MD sampling. The relevant

equations for MD sampling are presented in Equation 8.9

$$\boldsymbol{\mu} = \sum_{\eta \in \mathscr{D}_{\text{def}}^{\text{MD}}} \mathbf{V}_{\text{def}}^{\eta}. \tag{8.9}$$

In the above equation, the superscript (MD) implies that the set of structures were obtained from the MD simulation. In order to generate a set of realistic deformed geometries, molecular dynamics calculations were performed at 300K. The deformation potential was generated by sampling 45 random geometries on the resulting MD trajectory and performing RHF calculations on those sampled configurations.

As detailed in our previous work with ESP [24], each deformed potential was transformed into the 1-particle basis of the reference structure. For practical generation of the ESP, only the mean and variance of each deformation potential matrix element were used to construct the ESP. Higher order central moments were discarded, as it has been shown that this Gaussian approximation to the ESP matrix elements is a good one [24].

To properly weight the deformed potentials by statistical significance, we used Boltzmann weighting of each of the ESP matrix element terms, such that lower-energy conformations of the QD contribute proportionately more than high-energy ones.

eh-XCHF Geminal Parameters and Exciton Binding Energy Approximations

In order to calculate e-h interaction in these stochastic systems, the eh-XCHF method was used on the resulting ESP states. For the purposes of calculating E_{EB}, we treat the ESP HOMO and LUMO states as the e-h reference states in our eh-XCHF equation.

Approximate b and γ eh-XCHF parameters are obtained analytically in terms of the r_{eh} distance using the expressions

$$b = \langle r_{\text{eh}} \rangle \tag{8.10}$$

$$\gamma = \frac{1}{2\langle r_{\text{eh}}^2 \rangle}. \tag{8.11}$$

The derivation for these analytical forms of the geminal parameters can be found in the work done by Bayne and co-workers [284].

Exciton binding energy is calculated (as seen in Equation 8.12) as the the total energy of the non-interacting exciton less the energy of the fully-interacting exciton:

$$E_{\text{EB}} = \langle E_{\text{non-interacting}} \rangle - \langle E_{\text{exciton}} \rangle. \tag{8.12}$$

We have used an in-house stratified sampling integration technique developed by Bayne et al. [285] to calculate the necessary two-body integrals for determination of E_{EB}. To expedite these calculations, we have only used the top three most dominant AO contributions from HOMO and LUMO states to calculate these integrals.

Flowchart: Calculation of Exciton Binding Energy

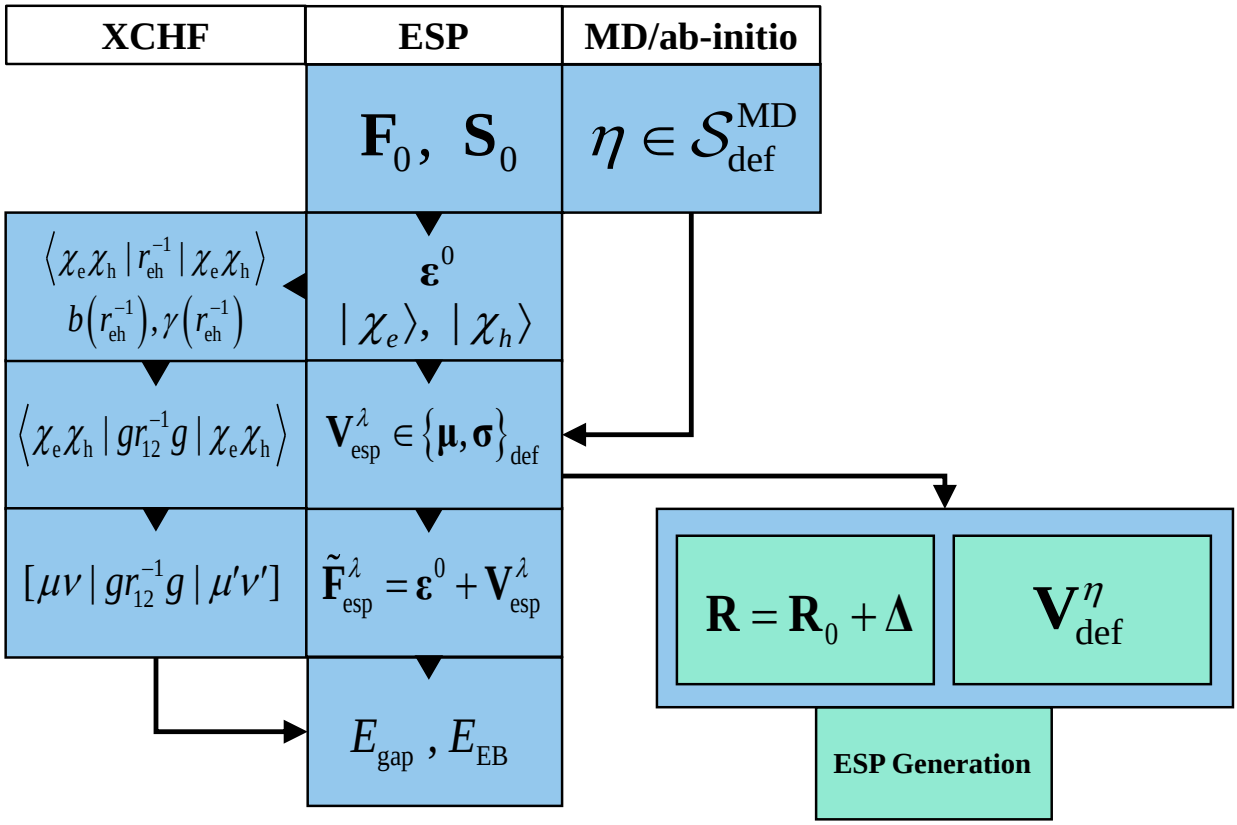

Figure 8.1: Flowchart of exciton binding energy calculation.

Figure 8.1 outlines the overall procedure used to combined ESP with eh-XCHF to calculate the distribution of E_{EB}. The steps from start to finish for running a set of ESP-XCHF calculations using the the current implementation are as follows:

1. Obtain the 1-particle electronic states of the energy minimum reference structure from a geometry optimization calculation at Hartree-Fock level.

2. Obtain the molecular dynamics (MD) trajectory of the equilibrated CdSe NP reference structure solvated in explicit water at 300K.

3. Perform Hartree-Fock calculations over 45 conformations of the MD trajectory using Monte Carlo sampling, and calculate those structures' corresponding deformation potentials (v_{def}) and total ground state energies (E_{total}).

4. Construct the ESP for the system from the set of obtained v_{def} and E_{total} using Boltzmann weighting at 300K and 350K.

5. Using stratified sampling integration developed by Bayne [285], and treating the ESP-HOMO$_{\text{ESP}}$ and ESP-LUMO$_{\text{ESP}}$ states as ESP-hole and ESP-electron states, respectively, calculate the bare r_{eh}^{-1} interaction. Use the resulting analytical terms [284] of b and γ to calculate the screened e-h interaction, $\frac{Gr_{\text{eh}}^{-1}G}{GG}$.

6. Continue sampling the stochastic ESP-HOMO and ESP-LUMO molecular orbitals to obtain 10,000 samples of ESP-XCHF exciton binding energies.

Results and Discussion

Temperature-Dependent Mean HOMO-LUMO Gaps for $Cd_{20}Se_{19}$

These systems are excellent candidates on which to apply the ESP method, due to the potentially useful applications of QDs, the complexity of their electronic states, and the chaotic behavior of their nuclei at room temperature. In order to observe the effect of temperature and how the HOMO-LUMO gap energy of this system scales with temperature, we generated ESPs at 49K, 100K, 140K, 197K, 248K, 296K, 342K, and 511K. These temperatures were selected in order to compare to the temperature scaling results for $Cd_{33}Se_{33}$ obtained by Prezdo and coworkers [286]. These results are shown in Figure 8.2. As expected there is a significant shift in the HOMO-LUMO gap energies, do to the difference in QD sizes of the two systems being investigated. However, we do find that $Cd_{20}Se_{19}$ band gaps do decrease with increasing temperature, as do the $Cd_{33}Se_{33}$ band gaps. This is good confirmation that the ESP method successfully captures and reproduces the thermal effects of a chemical system.

Distribution of Exciton Binding Energies of $Cd_{20}Se_{19}$ at 300K and 350K

The results for this $Cd_{20}Se_{19}$ QD are shown below.

Important to note about these results is the computation cost involved in obtaining them relative to the cost of doing the equivalent electronic structure calculations. The distribution of CdSe QD systems presented in this work here represents 10^5 different thermally-accessible geometries of the QD. Each of these geometries would take us approximately 30 minutes to perform one Hartree-Fock level calculation, or about 50,000 hours for the entire distribution. Instead, we have spent fewer than 24 hours generating the ESP, and then used the ESP to determine each of the single-

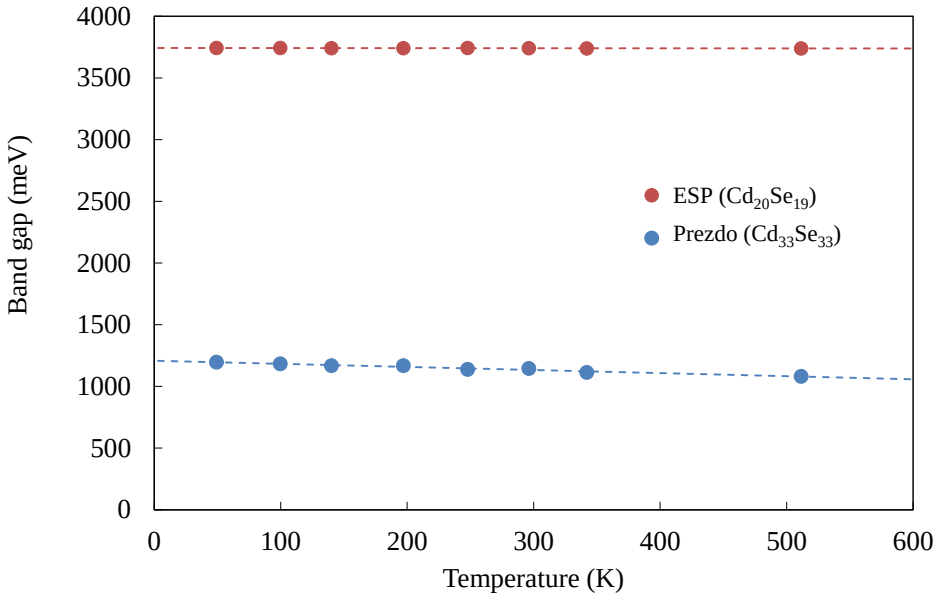

Figure 8.2: HOMO-LUMO gap energy scaling of $Cd_{20}Se_{19}$ quantum dot ($m = -0.0068, R^2 = 0.745$) with respect to temperature. Temperature scaling results of $Cd_{33}Se_{33}$ as calculated by Prezdo and coworkers for comparison ($m = -0.25$, $R^2 = 0.966$).

	HOMO-LUMO gap (eV)		E_{EB} (eV)	
	μ	σ	μ	σ
ESP	5.876	0.083	0.704	0.010
Hartree Fock	5.756	0.073	0.680	0.037

Table 8.1: Comparison of $Cd_{20}Se_{19}$ optical properties calculated by ESP and Hartree Fock method (cc-pVDZ basis).

electron states in about 0.5 seconds, or 90 minutes for the entire distribution. This represents a calculation speed-up by more than a factor of 2000 times.

Figure 8.3 and Figure 8.4 show the Z-score frequencies for $Cd_{20}Se_{19}$ HOMO-LUMO gap and exciton binding (E_{EB}) energies calculated using the ESP method at 300K, compared to those calculated using Hartree-Fock.

The purpose of looking at Z-scores for these properties is to compare the characteristics of the different distributions. In comparing the two HOMO-LUMO gap Z-score distributions, it can be seen that the two distributions share similar spreads and peak maxima.

Figure 8.5 shows the frequency of thermalized E_{EB} energies for a $Cd_{20}Se_{19}$ QD at 300K. The mean E_{EB} energy we calculated is 0.704 eV ($\sigma = 0.0100$ eV). Elward et. al performed theoretical calculations on this system and obtained an E_{EB} energy of 0.855 eV. Zunger and coworkers pseudopotential method produces an E_{EB} for this system of 1.003 eV. Meulenberg et. al. have calculated E_{EB} energies for CdSe QDs experimentally, and found that $Cd_{20}Se_{19}$ QDs had E_{EB} energies of 0.990 eV.

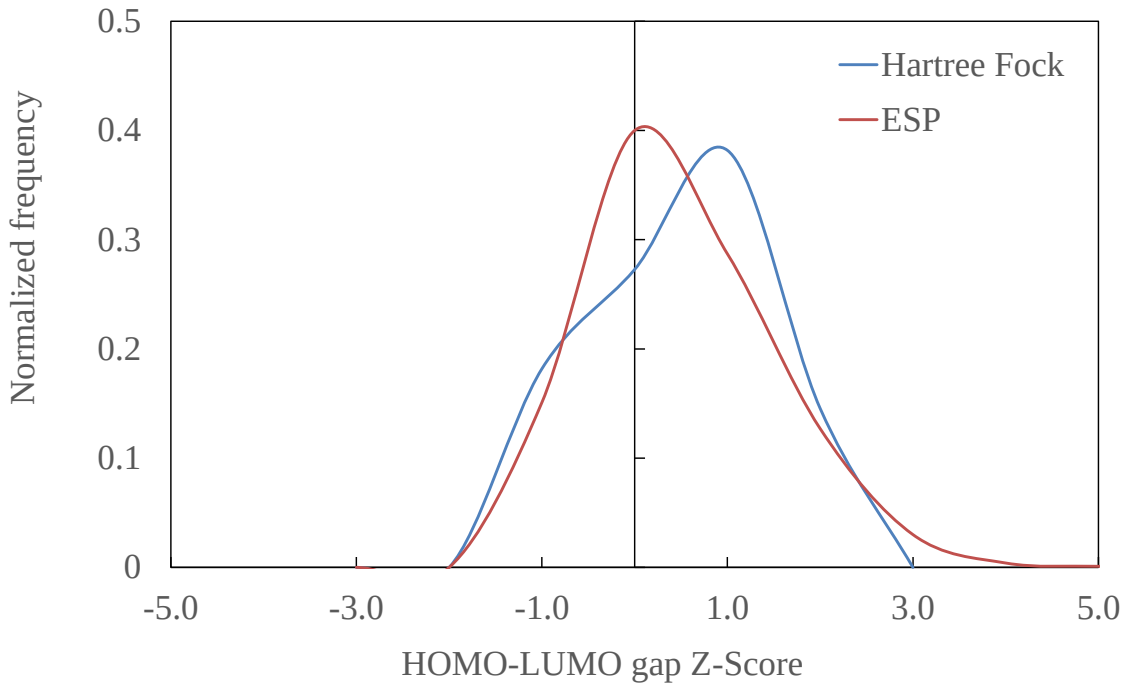

Figure 8.3: HOMO-LUMO gap Z-scores for a $Cd_{20}Se_{19}$ quantum dot at $T = 300$K.

Conclusions

In conclusion, the ESP method was successfully combined with the eh-XCHF method to perform conformational sampling on water-solvated CdSe NPs and to obtain the distribution of corresponding HOMO-LUMP gaps and exciton binding energies at 300K and 350K. It was shown that only looking at the optical properties of the minimum-energy 0K structure of the NP will fail to reproduce physically relevant results. Using a sufficiently large sample size of deformed NP geometries was found to be very important in obtaining accurate HOMO-LUMO gaps and exciton binding energies. It was shown that despite using a Gaussian approximation of the ESP matrix elements, non-Gaussian distributions of properties can still be calculated. This technique is general and can be applied to any electron-hole system.

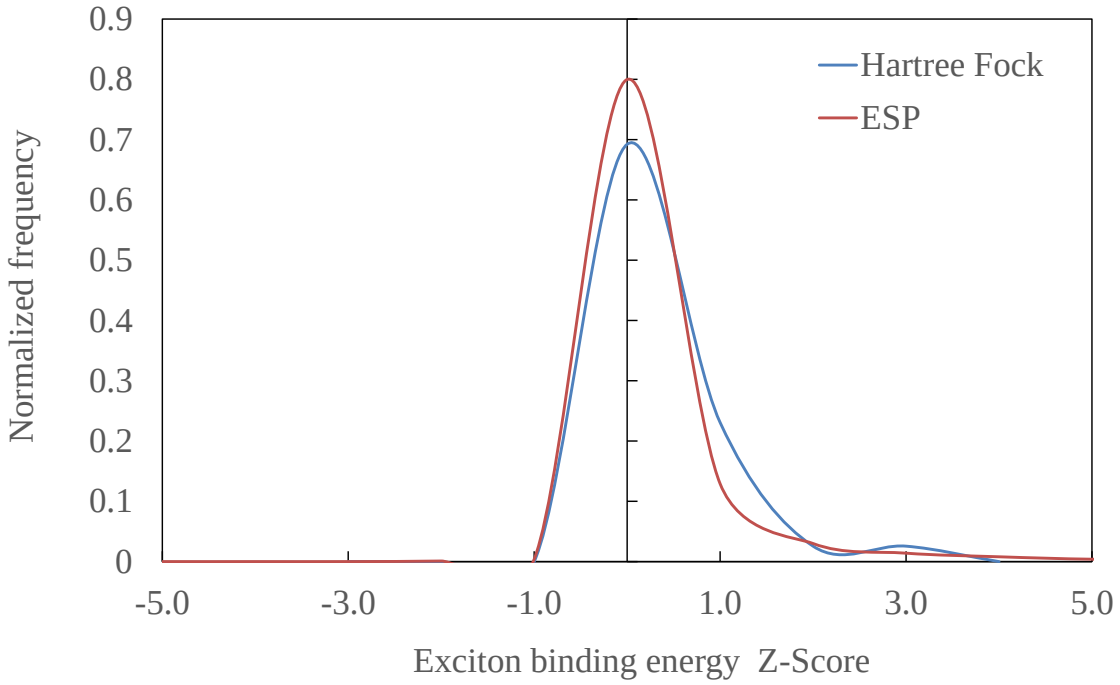

Figure 8.4: Exciton binding energy Z-scores for a $Cd_{20}Se_{19}$ quantum dot at $T = 300$K.

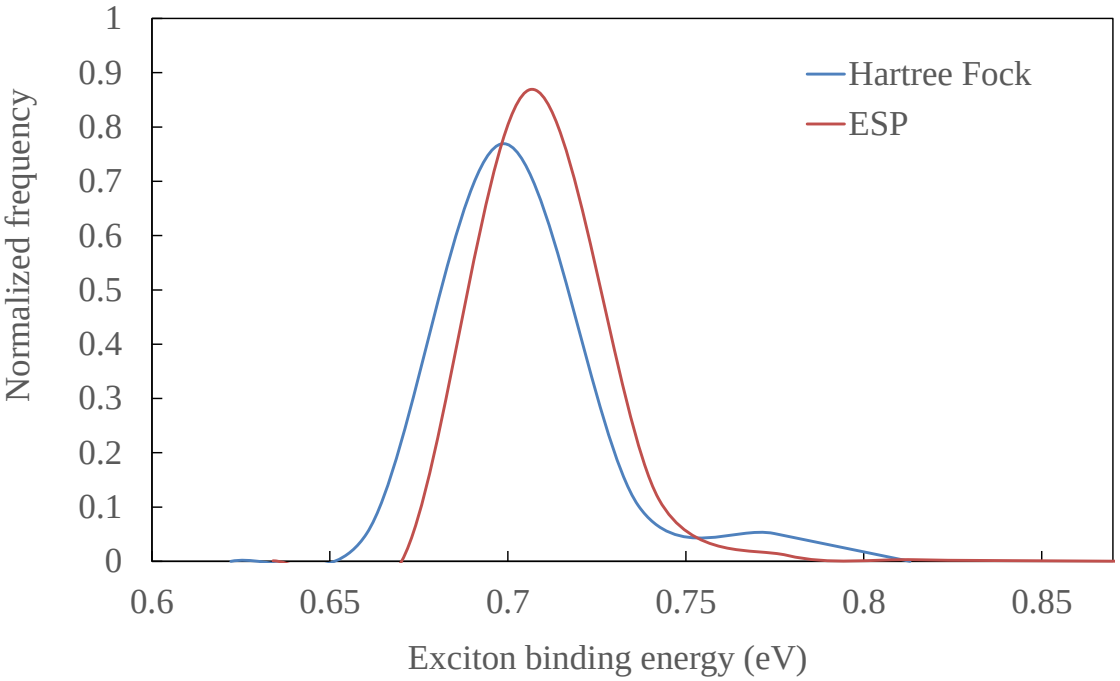

Figure 8.5: Exciton binding energy (in eV) distributions of a thermalized $Cd_{20}Se_{19}$ QD calculated using ESP method at T=300K.

Chapter 9

Conclusions and Future Work

In conclusion, the capabilities and usefulness of the Effective Stochastic Potential (ESP) method has been demonstrated. The method developed here is general, versatile technique for studying the effect of temperature and solvent on distributions of electronic properties. The ESP method has been applied to study the excited-state properties of variety of chemical systems including H_2O, PbS nanoparticles, CdSe nanoparticles, cesium lead halide nanoparticles, an anti-cancer therapy molecule (MD-224), a drug molecule for treating neurodegenerative disease (CDN1163), an energetic material, and an organic fluorophore (TADF (**R**)-**1**). In addition to these systems, the ESP method has been successfully combined with eh-XCHF to calculate exciton binding energies of CdSe nanoparticles.

The accuracy of the ESP method has been demonstrated through benchmarking calculations on H_2O. These calculations have highlighted the importance of using the necessary number of sampling points in order to capture the effect of chemical environment accurately.

Using the ESP method, I have been able to make a number of significant findings regarding the effect of temperature on excited-state properties. Substantial red-shifting of excitation energies in both PbS and CdSe nanoparticles were calculated using ESP-CIS and ESP-XCHF, respectively. Sub-Gaussian behavior of the excitation energy probability distribution of PbS nanoparticles was observed in the temperature range of 200K to 400K. The temperature trends of HOMO-LUMO gaps of various molcules were calculated using ESP, and a general trend of pathological behavior of energy minimum reference has been observed. In almost all cases, the HOMO-LUMO gap of the energy mininum reference structure does not correspond to the most probable HOMO-LUMO gap energy.

These investigations have shown and confirmed the finding of others that an insufficient number of sampling points leads to poor reproduction of probability distributions of quantum mechanical properties of interest. Specifically, we have found from using the ESP method that on the order of 10^5 to 10^6 structures from a given ensemble need to be sampled in order to calculate a property of that ensemble accurately. While most chemical systems are too large to sample their quantum mechanical properties a million times, the ESP method is able to reproduce results for systems for which many first-principles calculations can be performed. For the majority of systems which cannot be sampled

such a large number of times using traditional methods, ESP can be used do to being so much more efficient.

One major advantage to the ESP method is that it is complementary to existing methods for treating molecular dynamics. Once an equilibrium trajectory for the system is obtained, it becomes a simple matter to sample conformations along that trajectory using ESP.

While many advantages of the ESP method have been demonstrated, there are still multiple avenues for future improvements to the method. Two major areas of possible future development include avoiding the computational bottleneck of calculating a sample of deformation potentials, and including correlation in the ESP between matrix elements. For the former, it may be possible to analytically derive an approximate ESP from a distribution of easier-to-calculate classical properties, such as the nuclear repulsion energy. For the latter, machine learning presents exciting possibilities with respect to generating more sophisticated potential that include the effects of cross-correlation between the matrix elements of the ESP.

Bibliography

[1] Andel. Eight allotropes of carbon, June 2019.

[2] Keministi. Butane conformations and relative energies, September 2018.

[3] Attila Szabo and Neil S. Ostlund. *Modern Quantum Chemistry: Introduction to Advanced Electronic Structure Theory*. Dover Publications, Inc., first edition, 1996.

[4] D.A. McQuarrie. *Statistical Mechanics*. University Science Books, 2000.

[5] Henry Margenau. Theory of pressure effects of foreign gases on spectral lines. *Phys. Rev.*, 48:755–765, November 1935.

[6] Earl W. Smith and C. F. Hooper. Relaxation theory of spectral line broadening in plasmas. *Phys. Rev.*, 157:126–137, May 1967.

[7] G. Peach. Theory of the pressure broadening and shift of spectral lines. *Adv. Phys.*, 30:367–474, 1981.

[8] Leonidas Petrakis. Spectral line shapes: Gaussian and Lorentzian functions in magnetic resonance. *J. Chem. Educ.*, 44(8):432, 1967.

[9] Antoine Royer. Shift, width, and asymmetry of pressure-broadened spectral lines at intermediate densities. *Phys. Rev. A*, 22:1625–1654, October 1980.

[10] J. Szudy and W.E. Baylis. Asymmetry in pressure-broadened spectral lines. *J. Quant. Spectrosc. Ra.*, 17(5):681–684, 1977.

[11] W. F. Maddams. The scope and limitations of curve fitting. *Appl. Spectrosc.*, 34(3):245–267, 1980.

[12] G.J.O. Beran. Modeling polymorphic molecular crystals with electronic structure theory. *Chemical Reviews*, 116(9):5567–5613, 2016.

[13] G.M. Day. Current approaches to predicting molecular organic crystal structures. *Crystallography Reviews*, 17(1):3–52, 2011.

[14] S.L. Price. From crystal structure prediction to polymorph prediction: Interpreting the crystal energy landscape. *Physical Chemistry Chemical Physics*, 10(15):1996–2009, 2008.

[15] S.L. Price and J.G. Brandenburg. *Molecular Crystal Structure Prediction*. 2017.

[16] S.L. Price. Control and prediction of the organic solid state: A challenge to theory and experiment. *Proceedings of the Royal Society A: Mathematical, Physical and Engineering Sciences*, 474(2217), 2018.

[17] J.G. Brandenburg, J. Potticary, H.A. Sparkes, S.L. Price, and S.R. Hall. Thermal expansion of carbamazepine: Systematic crystallographic measurements challenge quantum chemical calculations. *Journal of Physical Chemistry Letters*, 8(17):4319–4324, 2017.

[18] E.C. Dybeck, D.P. McMahon, G.M. Day, and M.R. Shirts. Exploring the multi-minima behavior of small molecule crystal polymorphs at finite temperature. *Crystal Growth and Design*, 19(10):5568–5580, 2019.

[19] J. Nyman, O.S. Pundyke, and G.M. Day. Accurate force fields and methods for modelling organic molecular crystals at finite temperatures. *Physical Chemistry Chemical Physics*, 18(23):15828–15837, 2016.

[20] Y.N. Heit and G.J.O. Beran. How important is thermal expansion for predicting molecular crystal structures and thermochemistry at finite temperatures? *Acta Crystallographica Section B: Structural Science, Crystal Engineering and Materials*, 72(4):514–529, 2016.

[21] M.E. Tuckerman. Ab initio molecular dynamics: Basic concepts, current trends and novel applications. *Journal of Physics Condensed Matter*, 14(50):R1297–R1355, 2002. cited By 152.

[22] R. Kapral. Mixed quantum-classical dynamics. *J. Chem. Phys.*, 110(18):8919–8929, 1999. cited By 447.

[23] Ulf Ryde. How many conformations need to be sampled to obtain converged QM/MM energies? the curse of exponential averaging. *J. Chem. Theory Comput.*, 13(11):5745–5752, 2017.

[24] Jeremy A. Scher, Michael G. Bayne, Amogh Srihari, Shikha Nangia, and Arindam Chakraborty. Development of effective stochastic potential method using random matrix theory for efficient conformational sampling of semiconductor nanoparticles at non-zero temperatures. *J. Chem. Phys.*, 149(1):014103, 2018.

[25] F. Trani, G. Scalmani, G. Zheng, I. Carnimeo, M.J. Frisch, and V. Barone. Time-dependent density functional tight binding: New formulation and benchmark of excited states. *J. Chem. Theory Comput.*, 7(10):3304–3313, 2011. cited By 54.

[26] L.B. Castañeda, V. Arunachalam, and S. Dharmaraja. *Introduction to Probability and Stochastic Processes with Applications*. Wiley, 2012.

[27] Uxe Richter. Nist standard reference database number 101, Aug 2019.

[28] Chr. Møller and M. S. Plesset. Note on an approximation treatment for many-electron systems. *Phys. Rev.*, 46:618–622, October 1934.

[29] Martin Feyereisen, George Fitzgerald, and Andrew Komornicki. Use of approximate integrals in ab initio theory. an application in mp2 energy calculations. *Chem. Phys. Lett.*, 208(5):359–363, 1993.

[30] R. Palangsuntikul, R. Polly, and B. Hartke. Global and local optimization of auxiliary basis sets for ri-mp2 calculations. *Phys. Chem. Chem. Phys.*, 6(24):5456–5462, 2004. cited By 12.

[31] Yihan Shao, Zhengting Gan, Evgeny Epifanovsky, Andrew T.B. Gilbert, Michael Wormit, Joerg Kussmann, Adrian W. Lange, Andrew Behn, Jia Deng, Xintian Feng, Debashree Ghosh, Matthew Goldey, Paul R. Horn, Leif D. Jacobson, Ilya Kaliman, Rustam Z. Khaliullin, Tomasz Ku, Arie Landau, Jie Liu, Emil I. Proynov, Young Min Rhee, Ryan M. Richard, Mary A. Rohrdanz, Ryan P. Steele, Eric J. Sundstrom, H. Lee Woodcock III, Paul M. Zimmerman, Dmitry Zuev, Ben Albrecht, Ethan Alguire, Brian Austin, Gregory J. O. Beran, Yves A. Bernard, Eric Berquist, Kai Brandhorst, Ksenia B. Bravaya, Shawn T. Brown, David Casanova, Chun-Min Chang, Yunqing Chen, Siu Hung Chien, Kristina D. Closser, Deborah L. Crittenden, Michael Diedenhofen, Robert A. DiStasio Jr., Hainam Do, Anthony D. Dutoi, Richard G. Edgar, Shervin Fatehi, Laszlo Fusti-Molnar, An Ghysels, Anna Golubeva-Zadorozhnaya, Joseph Gomes, Magnus W.D. Hanson-Heine, Philipp H.P. Harbach, Andreas W. Hauser, Edward G. Hohenstein, Zachary C. Holden, Thomas-C. Jagau, Hyunjun Ji, Benjamin Kaduk, Kirill Khistyaev, Jaehoon Kim, Jihan Kim, Rollin A. King, Phil Klunzinger, Dmytro Kosenkov, Tim Kowalczyk, Caroline M. Krauter, Ka Un Lao, Adèle D. Laurent, Keith V. Lawler, Sergey V. Levchenko, Ching Yeh Lin, Fenglai Liu, Ester Livshits, Rohini C. Lochan, Arne Luenser, Prashant Manohar, Samuel F. Manzer, Shan-Ping Mao, Narbe Mardirossian, Aleksandr V. Marenich, Simon A. Maurer, Nicholas J. Mayhall, Eric Neuscamman, C. Melania Oana, Roberto Olivares-Amaya, Darragh P. O'Neill, John A. Parkhill, Trilisa M. Perrine, Roberto Peverati, Alexander Prociuk, Dirk R. Rehn, Edina Rosta, Nicholas J. Russ, Shaama M. Sharada, Sandeep Sharma, David W. Small, Alexander Sodt, Tamar Stein, David Stück, Yu-Chuan Su, Alex J.W. Thom, Takashi Tsuchimochi, Vitalii Vanovschi, Leslie Vogt, Oleg Vydrov, Tao Wang, Mark A. Watson, Jan Wenzel, Alec White, Christopher F. Williams, Jun Yang, Sina Yeganeh, Shane R. Yost, Zhi-Qiang You, Igor Ying Zhang, Xing Zhang, Yan Zhao, Bernard R. Brooks, Garnet K.L. Chan, Daniel M. Chipman, Christopher J. Cramer, William A. Goddard III, Mark S. Gordon, Warren J. Hehre, Andreas Klamt, Henry F. Schaefer III, Michael W. Schmidt, C. David Sherrill, Donald G. Truhlar, Arieh Warshel, Xin Xu, Alán Aspuru-Guzik, Roi Baer, Alexis T. Bell, Nicholas A. Besley, Jeng-Da Chai, Andreas Dreuw, Barry D. Dunietz, Thomas R. Furlani, Steven R. Gwaltney, Chao-Ping Hsu, Yousung Jung, Jing Kong, Daniel S. Lam-

brecht, WanZhen Liang, Christian Ochsenfeld, Vitaly A. Rassolov, Lyudmila V. Slipchenko, Joseph E. Subotnik, Troy Van Voorhis, John M. Herbert, Anna I. Krylov, Peter M.W. Gill, and Martin Head-Gordon. Advances in molecular quantum chemistry contained in the q-chem 4 program package. *Mol. Phys.*, 113(2):184–215, 2015.

[32] T.M. Atkins, A. Thibert, D.S. Larsen, S. Dey, N.D. Browning, and S.M. Kauzlarich. Femtosecond ligand/core dynamics of microwave-assisted synthesized silicon quantum dots in aqueous solution. *J. Am. Chem. Soc.*, 133(51):20664–20667, 2011.

[33] Y. Wang and N. Herron. Nanometer-sized semiconductor clusters: Materials synthesis, quantum size effects, and photophysical properties. *J. Phys. Chem.*, 95(2):525–532, 1991.

[34] A.P. Alivisatos. Perspectives on the physical chemistry of semiconductor nanocrystals. *J. Phys. Chem.*, 100(31):13226–13239, 1996.

[35] K. Žídek, K. Zheng, M. Abdellah, N. Lenngren, P. Chábera, and T. Pullerits. Ultrafast dynamics of multiple exciton harvesting in the cdse-zno system: Electron injection versus auger recombination. *Nano Lett.*, 12(12):6393–6399, 2012.

[36] P.K. Santra and P.V. Kamat. Mn-doped quantum dot sensitized solar cells: A strategy to boost efficiency over 5%. *J. Am. Chem. Soc.*, 134(5):2508–2511, 2012.

[37] J. Tang, H. Liu, D. Zhitomirsky, S. Hoogland, X. Wang, M. Furukawa, L. Levina, and E.H. Sargent. Quantum junction solar cells. *Nano Lett.*, 12(9):4889–4894, 2012.

[38] A. Salant, M. Shalom, Z. Tachan, S. Buhbut, A. Zaban, and U. Banin. Quantum rod-sensitized solar cell: Nanocrystal shape effect on the photovoltaic properties. *Nano Lett.*, 12(4):2095–2100, 2012.

[39] S.C. Boehme, H. Wang, L.D.A. Siebbeles, D. Vanmaekelbergh, and A.J. Houtepen. Electrochemical charging of cdse quantum dot films: Dependence on void size and counterion proximity. *ACS Nano*, 7(3):2500–2508, 2013.

[40] S. Jun, J. Lee, and E. Jang. Highly luminescent and photostable quantum dot-silica monolith and its application to light-emitting diodes. *ACS Nano*, 7(2):1472–1477, 2013.

[41] I.-K. Park, M.-K. Kwon, C.-Y. Cho, J.-Y. Kim, C.-H. Cho, and S.-J. Park. Effect of InGaN quantum dot size on the recombination process in light-emitting diodes. *Appl. Phys. Lett.*, 92(25):253105, 2008.

[42] J. Huang, K.L. Mulfort, P. Du, and L.X. Chen. Photodriven charge separation dynamics in cdse/zns core/shell quantum dot/cobaloxime hybrid for efficient hydrogen production. *J. Am. Chem. Soc.*, 134(40):16472–16475, 2012.

[43] X. Ji, G. Palui, T. Avellini, H.B. Na, C. Yi, K.L. Knappenberger Jr., and H. Mattoussi. On the ph-dependent quenching of quantum dot photoluminescence by redox active dopamine. *J. Am. Chem. Soc.*, 134(13):6006–6017, 2012.

[44] X. Peng, J.A. Misewich, S.S. Wong, and M.Y. Sfeir. Efficient charge separation in multidimensional nanohybrids. *Nano Lett.*, 11(11):4562–4568, 2011.

[45] K. Žídek, K. Zheng, C.S. Ponseca, M.E. Messing, L.R. Wallenberg, P. Chábera, M. Abdellah, V. Sundström, and T. Pullerits. Electron transfer in quantum-dot-sensitized zno nanowires: Ultrafast time-resolved absorption and terahertz study. *J. Am. Chem. Soc.*, 134(29):12110–12117, 2012.

[46] Y. Zhang, X. Ke, Z. Zheng, C. Zhang, Z. Zhang, F. Zhang, Q. Hu, Z. He, and H. Wang. Encapsulating quantum dots into enveloped virus in living cells for tracking virus infection. *ACS Nano*, 7(5):3896–3904, 2013.

[47] M. Bruchez Jr., M. Moronne, P. Gin, S. Weiss, and A.P. Alivisatos. Semiconductor nanocrystals as fluorescent biological labels. *Science*, 281(5385):2013–2016, 1998.

[48] Abhishek Joshi, K. Y. Narsingi, M. O. Manasreh, E. A. Davis, and B. D. Weaver. Temperature dependence of the band gap of colloidal cdsezns core/shell nanocrystals embedded into an ultraviolet curable resin. *Appl. Phys. Lett.*, 89(13):131907, 2006.

[49] S. S. Savchenko, A. S. Vokhmintsev, and I. A. Weinstein. Temperature-induced shift of the exciton absorption band in InP/zns quantum dots. *Opt. Mater. Express*, 7(2):354–359, February 2017.

[50] Liangliang Chen, Hua Bao, Taizhi Tan, Oleg V. Prezhdo, and Xiulin Ruan. Shape and temperature dependence of hot carrier relaxation dynamics in spherical and elongated cdse quantum dots. *J. Phys. Chem. C*, 115(23):11400–11406, 2011.

[51] Sean A. Fischer, Bradley F. Habenicht, Angeline B. Madrid, Walter R. Duncan, and Oleg V. Prezhdo. Regarding the validity of the time-dependent kohn–sham approach for electron-nuclear dynamics via trajectory surface hopping. *J. Chem. Phys.*, 134(2):024102, 2011.

[52] Judah S. High, Luis G. C. Rego, and Elena Jakubikova. Quantum dynamics simulations of excited state energy transfer in a zinc–free-base porphyrin dyad. *J. Phys. Chem. A*, 120(41):8075–8084, 2016.

[53] Chang Liu and Elena Jakubikova. Two-step model for ultrafast interfacial electron transfer: limitations of fermi's golden rule revealed by quantum dynamics simulations. *Chem. Sci.*, 8:5979–5991, 2017.

[54] Eugene P. Wigner. Characteristic vectors of bordered matrices with infinite dimensions. *Annals of Mathematics*, 62(3):548–564, 1955.

[55] T. Guhr, A. Müller-Groeling, and H.A. Weidenmüller. Random-matrix theories in quantum physics: Common concepts. *Physics Report*, 299(4-5):189–425, 1998.

[56] A. Pandey O. Bohigas, R.U. Haq. *Nuclear Data for Science and Technology*. Number 1 in Research Reports in Physics. Springer Berlin Heidelberg, 1992.

[57] J.B. Garg, J. Rainwater, J.S. Petersen, and W.W. Havens. Neutron resonance spectroscopy. iii. th232 and u238. *Phys. Rev.*, 134(5B):B985–B1009, 1964.

[58] O. Häusser, A. Richter, W. Von Witsch, and W.J. Thompson. Direct and compound nuclear reaction mechanisms in 26mg(p, p)26mg. *Nucl. Phys. A*, 109(2):329–346, 1968.

[59] T Ericson and Theo Mayer-Kuckuk. Fluctuations in nuclear reactions. *Annu. Rev. Nucl. Sci.*, 16(1):183–206, 1966.

[60] D. Wintgen and H. Friedrich. Classical and quantum-mechanical transition between regularity and irregularity in a hamiltonian system. *Phys. Rev. A*, 35:1464–1466, February 1987.

[61] C. Ellegaard, T. Guhr, K. Lindemann, J. Nygård, and M. Oxborrow. Symmetry breaking and spectral statistics of acoustic resonances in quartz blocks. *Phys. Rev. Lett.*, 77:4918–4921, December 1996.

[62] G. Montambaux. Persistent current of interacting electrons: a simple hartree-fock picture. *J. Phys. I France*, 6(1):1–4, 1996.

[63] H. Kato and D. Yoshioka. Suppression of persistent currents in one-dimensional disordered rings by the coulomb interaction. *Phys. Rev. B*, 50:4943–4946, August 1994.

[64] Georges Bouzerar and Didier Poilblanc. Persistent currents in multichannel interacting systems. *Phys. Rev. B*, 52:10772–10775, October 1995.

[65] M. Pascaud and G. Montambaux. Magnetization of mesoscopic disordered networks. *EPL (Europhysics Letters)*, 37(5):347, 1997.

[66] R. Berkovits and Y. Avishai. Significant interaction-induced enhancement of persistent currents in 2D disordered cylinders. *EPL (Europhysics Letters)*, 29(6):475, 1995.

[67] R.A. Jalabert, A.D. Stone, and Y. Alhassid. Statistical theory of coulomb blockade oscillations: Quantum chaos in quantum dots. *Phys. Rev. Lett.*, 68(23):3468–3471, 1992.

[68] P. Šeba. Random matrix theory and mesoscopic fluctuations. *Phys. Rev. B*, 53(19):13024–13028, 1996.

[69] U. Sivan, R. Berkovits, Y. Aloni, O. Prus, A. Auerbach, and G. Ben-Yoseph. Mesoscopic fluctuations in the ground state energy of disordered quantum dots. *Phys. Rev. Lett.*, 77(6):1123–1126, 1996.

[70] L. Kaplan and Y. Alhassid. Interaction matrix element fluctuations in ballistic quantum dots: Random wave model. *Phys. Rev. B*, 78(8), 2008.

[71] R. Shankar. Dots for dummies. *Journal of Statistical Physics*, 125(5-6):1173–1182, 2006.

[72] R. Shankar. Colloquium: Chaotic quantum dots with strongly correlated electrons. *Reviews of Modern Physics*, 80(2):379–394, 2008.

[73] S.P. Kwasniewski, J.P. François, and M.S. Deleuze. Temperature effects on the UV-vis electronic spectrum of trans-stilbene. *Int. J. Quantum Chem.*, 85(4-5):557–568, 2001.

[74] J.P. Lewis, T.E. Cheatham III, E.B. Starikov, H. Wang, and O.F. Sankey. Dynamically amorphous character of electronic states in poly(da)-poly(dt) DNA. *J. Phys. Chem. B*, 107(11):2581–2587, 2003.

[75] B.C. Mort and J. Autschbach. Temperature dependence of the optical rotation of fenchone calculated by vibrational averaging. *J. Phys. Chem. A*, 110(40):11381–11383, 2006.

[76] R. Mani, I.B. Rietveld, K. Varadharajan, M. Louhi-Kultanen, and S. Muthu. Fluorescence properties reinforced by proton transfer in the salt 2,6-diaminopyridinium dihydrogen phosphate. *J. Phys. Chem. A*, 118(34):6883–6892, 2014.

[77] Michael W. Schmidt, Kim K. Baldridge, Jerry A. Boatz, Steven T. Elbert, Mark S. Gordon, Jan H. Jensen, Shiro Koseki, Nikita Matsunaga, Kiet A. Nguyen, Shujun Su, Theresa L. Windus, Michel Dupuis, and John A. Montgomery. General atomic and molecular electronic structure system. *J. Comput. Chem.*, 14(11):1347–1363, 1993.

[78] T.C. Urdan. *Statistics in Plain English, Third Edition*. Taylor & Francis, 2011.

[79] Eran Rabani. An interatomic pair potential for cadmium selenide. *J. Chem. Phys.*, 116(1):258–262, 2002.

[80] P. Jeffrey Hay and Willard R. Wadt. Ab initio effective core potentials for molecular calculations. potentials for k to au including the outermost core orbitals. *J. Chem. Phys.*, 82(1):299–310, 1985.

[81] B.W. Pelham. *Intermediate Statistics: A Conceptual Course*. SAGE Publications, 2012.

[82] P.C.J. Clark, D.C.J. Neo, R. Ahumada-Lazo, A.I. Williamson, I. Pis, S. Nappini, A.A.R. Watt, and W.R. Flavell. Influence of multistep surface passivation on the performance of PbS colloidal quantum dot solar cells. *Langmuir*, 34(30):8887–8897, 2018.

[83] L. Hu, Z. Zhang, R.J. Patterson, Y. Hu, W. Chen, C. Chen, D. Li, C. Hu, C. Ge, Z. Chen, L. Yuan, C. Yan, N. Song, Z.L. Teh, G.J. Conibeer, J. Tang, and S. Huang. Achieving high-performance PbS quantum dot solar cells by improving hole extraction through Ag doping. *Nano Energy*, 46:212–219, 2018.

[84] D.M. Kroupa, D.H. Arias, J.L. Blackburn, G.M. Carroll, D.B. Granger, J.E. Anthony, M.C. Beard, and J.C. Johnson. Control of energy flow dynamics between tetracene ligands and PbS quantum dots by size tuning and ligand coverage. *Nano Lett.*, 18(2):865–873, 2018.

[85] Z. Zhang, C. Shi, J. Chen, G. Xiao, and L. Li. Combination of short-length TiO_2 nanorod arrays and compact PbS quantum-dot thin films for efficient solid-state quantum-dot-sensitized solar cells. *Appl. Surf. Sci.*, 410:8–13, 2017.

[86] G. Seo, J. Seo, S. Ryu, W. Yin, T.K. Ahn, and S.I. Seok. Enhancing the performance of sensitized solar cells with PbS/CH_3 NH_3 PbI_3 core/shell quantum dots. *J. Phys. Chem. Lett.*, 5(11):2015–2020, 2014.

[87] V. González-Pedro, C. Sima, G. Marzari, P.P. Boix, S. Giménez, Q. Shen, T. Dittrich, and I. Mora-Seró. High performance PbS quantum dot sensitized solar cells exceeding 4% efficiency: The role of metal precursors in the electron injection and charge separation. *Phys. Chem. Chem. Phys.*, 15(33):13835–13843, 2013.

[88] H. Wang, T. Kubo, J. Nakazaki, T. Kinoshita, and H. Segawa. PbS-quantum-dot-based heterojunction solar cells utilizing ZnO nanowires for high external quantum efficiency in the near-infrared region. *J. Phys. Chem. Lett.*, 4(15):2455–2460, 2013.

[89] L.-Y. Chang, R.R. Lunt, P.R. Brown, V. Bulović, and M.G. Bawendi. Low-temperature solution-processed solar cells based on Pbs colloidal quantum dot/cds heterojunctions. *Nano Lett.*, 13(3):994–999, 2013.

[90] A.E. Colbert, E.M. Janke, S.T. Hsieh, S. Subramaniyan, C.W. Schlenker, S.A. Jenekhe, and D.S. Ginger. Hole transfer from low band gap quantum dots to conjugated polymers in organic/inorganic hybrid photovoltaics. *J. Phys. Chem. Lett.*, 4(2):280–284, 2013.

[91] K.S. Jeong, J. Tang, H. Liu, J. Kim, A.W. Schaefer, K. Kemp, L. Levina, X. Wang, S. Hoogland, R. Debnath, L. Brzozowski, E.H. Sargent, and J.B. Asbury. Enhanced mobility-lifetime products in PbS colloidal quantum dot photovoltaics. *ACS Nano*, 6(1):89–99, 2012.

[92] B.N. Pal, I. Robel, A. Mohite, R. Laocharoensuk, D.J. Werder, and V.I. Klimov. High-sensitivity p-n junction photodiodes based on PbS nanocrystal quantum dots. *Adv. Funct. Mater.*, 22(8):1741–1748, 2012.

[93] L. Sun, J.J. Choi, D. Stachnik, A.C. Bartnik, B.-R. Hyun, G.G. Malliaras, T. Hanrath, and F.W. Wise. Bright infrared quantum-dot light-emitting diodes through inter-dot spacing control. *Nat. Nanotechnol.*, 7(6):369–373, 2012.

[94] D. Kufer, I. Nikitskiy, T. Lasanta, G. Navickaite, F.H.L. Koppens, and G. Konstantatos. Hybrid 2D-0D MoS_2-PbS quantum dot photodetectors. *Advanced Materials*, 27(1):176–180, 2015.

[95] J. He, K. Qiao, L. Gao, H. Song, L. Hu, S. Jiang, J. Zhong, and J. Tang. Synergetic effect of silver nanocrystals applied in PbS colloidal quantum dots for high-performance infrared photodetectors. *ACS Photonics*, 1(10):936–943, 2014.

[96] R. Dong, C. Bi, Q. Dong, F. Guo, Y. Yuan, Y. Fang, Z. Xiao, and J. Huang. An ultraviolet-to-NIR broad spectral nanocomposite photodetector with gain. *Adv. Opt. Mater.*, 2(6):549–554, 2014.

[97] Y. Tang, F. Wu, F. Chen, Y. Zhou, P. Wang, M. Long, W. Zhou, Z. Ning, J. He, F. Gong, Z. Zhu, S. Qin, and W. Hu. A colloidal-quantum-dot infrared photodiode with high photoconductive gain. *Small*, 14(48):1803158, 2018.

[98] R. Trevisan, P. Rodenas, V. González-Pedro, C. Sima, R.S. Sanchez, E.M. Barea, I. Mora-Seró, F. Fabregat-Santiago, and S. Giménez. Harnessing infrared photons for photoelectrochemical hydrogen generation. a PbS quantum dot based "quasi-artificial leaf". *J. Phys. Chem. Lett.*, 4(1):141–146, 2013.

[99] Y. Yan, R.W. Crisp, J. Gu, B.D. Chernomordik, G.F. Pach, A.R. Marshall, J.A. Turner, and M.C. Beard. Multiple exciton generation for photoelectrochemical hydrogen evolution reactions with quantum yields exceeding 100%. *Nat. Energy*, 2(5):17052, 2017.

[100] K.E. Knowles, M. Malicki, and E.A. Weiss. Dual-time scale photoinduced electron transfer from PbS quantum dots to a molecular acceptor. *J. Am. Chem. Soc.*, 134(30):12470–12473, 2012.

[101] Y. Yang, W. Rodríguez-Córdoba, and T. Lian. Ultrafast charge separation and recombination dynamics in lead sulfide quantum dot-methylene blue complexes probed by electron and hole intraband transitions. *J. Am. Chem. Soc.*, 133(24):9246–9249, 2011.

[102] Jesse R. Allardice, Arya Thampi, Simon Dowland, James Xiao, Victor Gray, Zhilong Zhang, Peter Budden, Anthony J. Petty, Nathaniel J. L. K. Davis, Neil C. Greenham, John E. Anthony, and Akshay Rao. Engineering

molecular ligand shells on quantum dots for quantitative harvesting of triplet excitons generated by singlet fission. *J. Am. Chem. Soc.*, 141(32):12907–12915, 2019.

[103] Antonio Braga, Sixto Giménez, Isabella Concina, Alberto Vomiero, and Iván Mora-Seró. Panchromatic sensitized solar cells based on metal sulfide quantum dots grown directly on nanostructured TiO_2 electrodes. *J. Phys. Chem. Lett.*, 2(5):454–460, 2011.

[104] N. Yazdani, D. Bozyigit, K. Vuttivorakulchai, M. Luisier, I. Infante, and V. Wood. Tuning electron-phonon interactions in nanocrystals through surface termination. *Nano Lett.*, 18(4):2233–2242, 2018.

[105] I.-Y. Chang, D. Kim, and K. Hyeon-Deuk. Control of electronic structures and phonon dynamics in quantum dot superlattices by manipulation of interior nanospace. *ACS Appl. Mater. Interfaces*, 8(28):18321–18327, 2016.

[106] F. Nattino, D. Migliorini, G.-J. Kroes, E. Dombrowski, E.A. High, D.R. Killelea, and A.L. Utz. Chemically accurate simulation of a polyatomic molecule-metal surface reaction. *J. Phys. Chem. Lett.*, 7(13):2402–2406, 2016.

[107] L. Zhang, M.-G. Ju, and W. Liang. The effect of moisture on the structures and properties of lead halide perovskites: A first-principles theoretical investigation. *Phys. Chem. Chem. Phys.*, 18(33):23174–23183, 2016.

[108] A.J. Neukirch, Z. Guo, and O.V. Prezhdo. Time-domain ab initio study of phonon-induced relaxation of plasmon excitations in a silver quantum dot. *J. Phys. Chem. C*, 116(28):15034–15040, 2012.

[109] Michael P. Esch, Yinan Shu, and Benjamin G. Levine. A conical intersection perspective on the low nonradiative recombination rate in lead halide perovskites. *J. Phys. Chem. A*, 123(13):2661–2673, 2019.

[110] Wei-Tao Peng and Benjamin G. Levine. Ab initio molecular dynamics study of the interaction between defects during nonradiative recombination. *J. Phys. Chem. C*, 123(27):16588–16595, 2019.

[111] Aaron Sisto, Clem Stross, Marc W. van der Kamp, Michael O'Connor, Simon McIntosh-Smith, Graham T. Johnson, Edward G. Hohenstein, Fred R. Manby, David R. Glowacki, and Todd J. Martinez. Atomistic nonadiabatic dynamics of the LH2 complex with a GPU-accelerated ab initio exciton model. *Phys. Chem. Chem. Phys.*, 19:14924–14936, 2017.

[112] H. Kamisaka, S.V. Kilina, K. Yamashita, and O.V. Prezhdo. Ultrafast vibrationally-induced dephasing of electronic excitations in PbSe quantum dots. *Nano Lett.*, 6(10):2295–2300, 2006.

[113] R. Mitrić, U. Werner, M. Wohlgemuth, G. Seifert, and V. Bonačić-Koutecký. Nonadiabatic dynamics within time-dependent density functional tight binding method. *J. Phys. Chem. A*, 113(45):12700–12705, 2009.

[114] S. Pal, P. Nijjar, T. Frauenheim, and O.V. Prezhdo. Atomistic analysis of room temperature quantum coherence in two-dimensional CdSe nanostructures. *Nano Lett.*, 17(4):2389–2396, 2017.

[115] E. Titov, A. Humeniuk, and R. Mitrić. Exciton localization in excited-state dynamics of a tetracene trimer: A surface hopping LC-TDDFTB study. *Phys. Chem. Chem. Phys.*, 20(40):25995–26007, 2018.

[116] F. Alkan and C.M. Aikens. TD-DFT and TD-DFTB investigation of the optical properties and electronic structure of silver nanorods and nanorod dimers. *J. Phys. Chem. C*, 122(41):23639–23650, 2018.

[117] Svetlana V. Kilina, Patrick K. Tamukong, and Dmitri S. Kilin. Surface chemistry of semiconducting quantum dots: Theoretical perspectives. *Acc. Chem. Res.*, 49(10):2127–2135, 2016.

[118] Svetlana Kilina, Kirill A. Velizhanin, Sergei Ivanov, Oleg V. Prezhdo, and Sergei Tretiak. Surface ligands increase photoexcitation relaxation rates in cdse quantum dots. *ACS Nano*, 6(7):6515–6524, 2012.

[119] Tammie Nelson, Sebastian Fernandez-Alberti, Adrian E. Roitberg, and Sergei Tretiak. Nonadiabatic excited-state molecular dynamics: Modeling photophysics in organic conjugated materials. *Acc. Chem. Res.*, 47(4):1155–1164, 2014.

[120] Ravithree D. Senanayake, Emilie B. Guidez, Amanda J. Neukirch, Oleg V. Prezhdo, and Christine M. Aikens. Theoretical investigation of relaxation dynamics in $au_{38}(sh)_{24}$ Thiolate-protected gold nanoclusters. *J. Phys. Chem. C*, 122(28):16380–16388, 2018.

[121] A. Nijamudheen and Alexey V. Akimov. Criticality of symmetry in rational design of chalcogenide perovskites. *J. Phys. Chem. Lett.*, 9(1):248–257, 2018.

[122] Wei Li, Liujiang Zhou, Oleg V. Prezhdo, and Alexey V. Akimov. Spin–orbit interactions greatly accelerate nonradiative dynamics in lead halide perovskites. *ACS Energy Lett.*, 3(9):2159–2166, 2018.

[123] M.E. Casida and M. Huix-Rotllant. Progress in time-dependent density-functional theory. *Annu. Rev. Phys. Chem.*, 63(1):287–323, 2012.

[124] A. Dreuw and M. Head-Gordon. Single-reference ab initio methods for the calculation of excited states of large molecules. *Chem. Rev.*, 105(11):4009–4037, 2005.

[125] M. Valiev, E.J. Bylaska, N. Govind, K. Kowalski, T.P. Straatsma, H.J.J. Van Dam, D. Wang, J. Nieplocha, E. Apra, T.L. Windus, and W.A. de Jong. NWChem: A comprehensive and scalable open-source solution for large scale molecular simulations. *Comput. Phys. Commun.*, 181(9):1477–1489, 2010.

[126] A. D. Becke. Density-functional exchange-energy approximation with correct asymptotic behavior. *Phys. Rev. A*, 38:3098–3100, September 1988.

[127] Wei Chen, Jialin Zhong, Junzi Li, Nitin Saxena, Lucas P. Kreuzer, Haochen Liu, Lin Song, Bo Su, Dan Yang, Kun Wang, Johannes Schlipf, Volker Körstgens, Tingchao He, Kai Wang, and Peter Müller-Buschbaum. Structure and charge carrier dynamics in colloidal PbS quantum dot solids. *J. Phys. Chem. Lett.*, 10(9):2058–2065, 2019.

[128] Nuri Yazdani, Deniz Bozyigit, Kantawong Vuttivorakulchai, Mathieu Luisier, Ivan Infante, and Vanessa Wood. Tuning electron–phonon interactions in nanocrystals through surface termination. *Nano Lett.*, 18(4):2233–2242, 2018.

[129] Haiguang Zhao, Hongyan Liang, François Vidal, Federico Rosei, Alberto Vomiero, and Dongling Ma. Size dependence of temperature-related optical properties of PbS and PbS/CdS core/shell quantum dots. *J. Phys. Chem. C*, 118(35):20585–20593, 2014.

[130] Rachelle Ihly, Jason Tolentino, Yao Liu, Markelle Gibbs, and Matt Law. The photothermal stability of PbS quantum dot solids. *ACS Nano*, 5(10):8175–8186, 2011.

[131] Ha-Sung Kong, Byoung-Ju Kim, and Kwang-Sun Kang. Room temperature photoluminescence of PbS quantum dots: Capping agent and thermal effect. *J. Lumin.*, 34(3):387–390, 2019.

[132] W. Heller and U. Bockelmann. Electric-field effects on excitons in quantum dots. *Phys. Rev. B*, 57(11):6270–6273, 1998.

[133] F. Gesuele, M.Y. Sfeir, W.-K. Koh, C.B. Murray, T.F. Heinz, and C.W. Wong. Ultrafast supercontinuum spectroscopy of carrier multiplication and biexcitonic effects in excited states of PbS quantum dots. *Nano Lett.*, 12(6):2658–2664, 2012.

[134] A. Markus, M. Rossetti, V. Calligari, J.X. Chen, and A. Fiore. Role of thermal hopping and homogeneous broadening on the spectral characteristics of quantum dot lasers. *J. Appl. Phys.*, 98(10):104506, 2005.

[135] J.M. Azpiroz and F. De Angelis. Ligand induced spectral changes in CdSe quantum dots. *ACS Appl. Mater. Interfaces*, 7(35):19736–19745, 2015.

[136] K. Kang and K. Daneshvar. Matrix and thermal effects on photoluminescence from PbS quantum dots. *J. Appl. Phys.*, 95(9):4747–4751, 2004.

[137] D.M. Badgujar, M.B. Talawar, S.N. Asthana, and P.P. Mahulikar. Advances in science and technology of modern energetic materials: An overview. *J. Hazard. Mater.*, 151(2-3):289–305, 2008. cited By 563.

[138] N. Fischer, D. Fischer, T.M. Klapötke, D.G. Piercey, and J. Stierstorfer. Pushing the limits of energetic materials - the synthesis and characterization of dihydroxylammonium 5,5′-bistetrazole-1,1′- diolate. *J. Mater. Chem.*, 22(38):20418–20422, 2012. cited By 370.

[139] P.W. Cooper. *Explosives Engineering*. Wiley, 2018.

[140] B.A. Hess and L.J. Schaad. Hückel molecular orbital ϕ resonance energies. a new approach. *J. Am. Chem. Soc.*, 93(2):305–310, 1971. cited By 384.

[141] M.M. Lynam, M. Kuty, J. Damborsky, J. Koca, and P. Adriaens. Molecular orbital calculations to describe microbial reductive dechlorination of polychlorinated dioxins. *Environ. Toxicol. Chem.*, 17(6):988–997, 1998. cited By 45.

[142] D.A. McQuarrie, J.D. Simon, H.A. Cox, and J. Choi. *Physical Chemistry: A Molecular Approach*. Physical Chemistry: A Molecular Approach. University Science Books, 1997.

[143] Zhiyong Yang, Zhu Mao, Zongliang Xie, Yi Zhang, Siwei Liu, Juan Zhao, Jiarui Xu, Zhenguo Chi, and Matthew P. Aldred. Recent advances in organic thermally activated delayed fluorescence materials. *Chem. Soc. Rev.*, 46:915–1016, 2017.

[144] Ayataka Endo, Keigo Sato, Kazuaki Yoshimura, Takahiro Kai, Atsushi Kawada, Hiroshi Miyazaki, and Chihaya Adachi. Efficient up-conversion of triplet excitons into a singlet state and its application for organic light emitting diodes. *Appl. Phys. Lett.*, 98(8):083302, 2011.

[145] A. Maciejewski, M. Szymanski, and R.P. Steer. Thermally activated delayed s1 fluorescence of aromatic thiones. *J. Phys. Chem.*, 90(23):6314–6318, 1986. cited By 59.

[146] H. Tanaka, M. Ikenosako, Y. Kato, M. Fujiki, Y. Inoue, and T. Mori. Symmetry-based rational design for boosting chiroptical responses. *Communications Chemistry*, 1(1), 2018. cited By 9.

[147] Jana Zaumseil. Electronic control of circularly polarized light emission. *Science*, 344(6185):702–703, 2014.

[148] Nina Berova, Lorenzo Di Bari, and Gennaro Pescitelli. Application of electronic circular dichroism in configurational and conformational analysis of organic compounds. *Chem. Soc. Rev.*, 36:914–931, 2007.

[149] S. Feuillastre, M. Pauton, L. Gao, A. Desmarchelier, A.J. Riives, D. Prim, D. Tondelier, B. Geffroy, G. Muller, G. Clavier, and G. Pieters. Design and synthesis of new circularly polarized thermally activated delayed fluorescence emitters. *J. Am. Chem. Soc.*, 138(12):3990–3993, 2016. cited By 80.

[150] M.D. Hanwell, D.E. Curtis, D.C. Lonie, T. Vandermeerschd, E. Zurek, and G.R. Hutchison. Avogadro: An advanced semantic chemical editor, visualization, and analysis platform. *Journal of Cheminformatics*, 4(8), 2012. cited By 1862.

[151] Y. Li, J. Yang, A. Aguilar, D. McEachern, S. Przybranowski, L. Liu, C.-Y. Yang, M. Wang, X. Han, and S. Wang. Discovery of md-224 as a first-in-class, highly potent, and efficacious proteolysis targeting chimera murine double minute 2 degrader capable of achieving complete and durable tumor regression. *J. Med. Chem.*, 62(2):448–466, 2019. cited By 24.

[152] Inge Van Molle, Andreas Thomann, Dennis L. Buckley, Ernest C. So, Steffen Lang, Craig M. Crews, and Alessio Ciulli. Dissecting fragment-based lead discovery at the von hippel-lindau protein:hypoxia inducible factor 1α protein-protein interface. *Chemistry & Biology*, 19(10):1300–1312, 2012.

[153] S. An and L. Fu. Small-molecule protacs: An emerging and promising approach for the development of targeted therapy drugs. *EBioMedicine*, 36:553–562, 2018. cited By 22.

[154] Joseph Gaugler, Bryan James, Tricia Johnson, Allison Marin, and Jennifer Weuve. 2019 Alzheimer's disease facts and figures. *Alzheimer's & Dementia*, 15(3):321–387, 2019.

[155] Russell Dahl. A new target for parkinson's disease: Small molecule serca activator CDn1163 ameliorates dyskinesia in 6-ohda-lesioned rats. *Bioorganic & Medicinal Chemistry*, 25(1):53–57, 2017.

[156] M. Musgaard, L. Thøgersen, B. Schiøtt, and E. Tajkhorshid. Tracing cytoplasmic ca 2+ ion and water access points in the ca 2+-ATPase. *Biophys. J.*, 102(2):268–277, 2012. cited By 22.

[157] A.L. Fetter and J.D. Walecka. *Quantum Theory of Many-particle Systems*. Dover Books on Physics. Dover Publications, 2003.

[158] R.D. Mattuck. *A Guide to Feynman Diagrams in the Many-body Problem*. Dover Books on Physics Series. Dover Publications, 1992.

[159] A.P. Alivisatos. Semiconductor clusters, nanocrystals, and quantum dots. *Science*, 271(5251):933–937, 1996.

[160] D.M. Sagar, R.R. Cooney, S.L. Sewall, E.A. Dias, M.M. Barsan, I.S. Butler, and P. Kambhampati. Size dependent, state-resolved studies of exciton-phonon couplings in strongly confined semiconductor quantum dots. *Phys. Rev. B*, 77(23):235321–235335, 2008.

[161] J.-W. Luo, A. Franceschetti, and A. Zunger. Quantum-size-induced electronic transitions in quantum dots: Indirect band-gap GaAs. *Phys. Rev. B*, 78(3):035306–035314, 2008.

[162] A. Narayanaswamy, L.F. Feiner, A. Meijerink, and P.J. Van Der Zaag. The effect of temperature and dot size on the spectral properties of colloidal InP/zns core-shell quantum dots. *ACS Nano*, 3(9):2539–2546, 2009.

[163] Z. Lin, H. Li, A. Franceschetti, and M.T. Lusk. Efficient exciton transport between strongly quantum-confined silicon quantum dots. *ACS Nano*, 6(5):4029–4038, 2012.

[164] W.K. Bae, L.A. Padilha, Y.-S. Park, H. McDaniel, I. Robel, J.M. Pietryga, and V.I. Klimov. Controlled alloying of the core-shell interface in cdse/cds quantum dots for suppression of auger recombination. *ACS Nano*, 7(4):3411–3419, 2013.

[165] A.W. Cohn, A.M. Schimpf, C.E. Gunthardt, and D.R. Gamelin. Size-dependent trap-assisted auger recombination in semiconductor nanocrystals. *Nano Lett.*, 13(4):1810–1815, 2013.

[166] C. De Mello Donegá, M. Bode, and A. Meijerink. Size- and temperature-dependence of exciton lifetimes in cdse quantum dots. *Phys. Rev. B*, 74(8), 2006.

[167] A.M. Dennis, B.D. Mangum, A. Piryatinski, Y.-S. Park, D.C. Hannah, J.L. Casson, D.J. Williams, R.D. Schaller, H. Htoon, and J.A. Hollingsworth. Suppressed blinking and auger recombination in near-infrared type-ii InP/cds nanocrystal quantum dots. *Nano Lett.*, 12(11):5545–5551, 2012.

[168] D. Katz, T. Wizansky, O. Millo, E. Rothenberg, T. Mokari, and U. Banin. Size-dependent tunneling and optical spectroscopy of cdse quantum rods. *Phys. Rev. Lett.*, 89(8):086801/1–086801/4, 2002.

[169] S. Kim, S.W. Hwang, M.-K. Kim, D.Y. Shin, D.H. Shin, C.O. Kim, S.B. Yang, J.H. Park, E. Hwang, S.-H. Choi, G. Ko, S. Sim, C. Sone, H.J. Choi, S. Bae, and B.H. Hong. Anomalous behaviors of visible luminescence from graphene quantum dots: Interplay between size and shape. *ACS Nano*, 6(9):8203–8208, 2012.

[170] I. Musa, F. Massuyeau, L. Cario, J.L. Duvail, S. Jobic, P. Deniard, and E. Faulques. Temperature and size dependence of time-resolved exciton recombination in zno quantum dots. *Appl. Phys. Lett.*, 99(24), 2011.

[171] J. Song and S.E. Ulloa. Geometrical-confinement effects on excitons in quantum disks. *Phys. Rev. B*, 52(12):9015–9022, 1995.

[172] E.V. Ushakova, A.P. Litvin, P.S. Parfenov, A.V. Fedorov, M. Artemyev, A.V. Prudnikau, I.D. Rukhlenko, and A.V. Baranov. Anomalous size-dependent decay of low-energy luminescence from Pbs quantum dots in colloidal solution. *ACS Nano*, 6(10):8913–8921, 2012.

[173] W.K. Bae, Y.-S. Park, J. Lim, D. Lee, L.A. Padilha, H. McDaniel, I. Robel, C. Lee, J.M. Pietryga, and V.I. Klimov. Controlling the influence of auger recombination on the performance of quantum-dot light-emitting diodes. *Nat. Comm.*, 4, 2013.

[174] K. Hyeon-Deuk and O.V. Prezhdo. Time-domain ab initio study of auger and phonon-assisted auger processes in a semiconductor quantum dot. *Nano Lett.*, 11(4):1845–1850, 2011.

[175] Y. Ghosh, B.D. Mangum, J.L. Casson, D.J. Williams, H. Htoon, and J.A. Hollingsworth. New insights into the complexities of shell growth and the strong influence of particle volume in nonblinking "giant" core/shell nanocrystal quantum dots. *J. Am. Chem. Soc.*, 134(23):9634–9643, 2012.

[176] L.A. Padilha, J.T. Stewart, R.L. Sandberg, W.K. Bae, W.-K. Koh, J.M. Pietryga, and V.I. Klimov. Aspect ratio dependence of auger recombination and carrier multiplication in Pbse nanorods. *Nano Lett.*, 13(3):1092–1099, 2013.

[177] I. Robel, M. Kuno, and P.V. Kamat. Size-dependent electron injection from excited cdse quantum dots into tio2 nanoparticles. *J. Am. Chem. Soc.*, 129(14):4136–4137, 2007.

[178] I.V. Lightcap and P.V. Kamat. Fortification of cdse quantum dots with graphene oxide. excited state interactions and light energy conversion. *J. Am. Chem. Soc.*, 134(16):7109–7116, 2012.

[179] D.M. Adams, L. Brus, C.E.D. Chidsey, S. Creager, C. Creutz, C.R. Kagan, P.V. Kamat, M. Lieberman, S. Lindsay, R.A. Marcus, R.M. Metzger, M.E. Michel-Beyerle, J.R. Miller, M.D. Newton, D.R. Rolison, O. Sankey, K.S. Schanze, J. Yardley, and X. Zhu. Charge transfer on the nanoscale: Current status. *J. Phys. Chem. B*, 107(28):6668–6697, 2003.

[180] R. Long and O.V. Prezhdo. Instantaneous generation of charge-separated state on tio2 surface sensitized with plasmonic nanoparticles. *J. Am. Chem. Soc.*, 136(11):4343–4354, 2014.

[181] R. Long and O.V. Prezhdo. Ab initio nonadiabatic molecular dynamics of the ultrafast electron injection from a Pbse quantum dot into the tio 2 surface. *J. Am. Chem. Soc.*, 133(47):19240–19249, 2011.

[182] I.L. Medintz, D. Farrell, K. Susumu, S.A. Trammell, J.R. Deschamps, F.M. Brunel, P.E. Dawson, and H. Mattoussi. Multiplex charge-transfer interactions between quantum dots and peptide-bridged ruthenium complexes. *Anal. Chem.*, 81(12):4831–4839, 2009.

[183] R. Alam, D.M. Fontaine, B.R. Branchini, and M.M. Maye. Designing quantum rods for optimized energy transfer with firefly luciferase enzymes. *Nano Lett.*, 12(6):3251–3256, 2012.

[184] W.R. Algar, M.G. Ancona, A.P. Malanoski, K. Susumu, and I.L. Medintz. Assembly of a concentric förster resonance energy transfer relay on a quantum dot scaffold: Characterization and application to multiplexed protease sensing. *ACS Nano*, 6(12):11044–11058, 2012.

[185] N.J. Borys, M.J. Walter, J. Huang, D.V. Talapin, and J.M. Lupton. The role of particle morphology in interfacial energy transfer in cdse/cds heterostructure nanocrystals. *Science*, 330(6009):1371–1374, 2010.

[186] S. Jin, H.-J. Son, O.K. Farha, G.P. Wiederrecht, and J.T. Hupp. Energy transfer from quantum dots to metal-organic frameworks for enhanced light harvesting. *J. Am. Chem. Soc.*, 135(3):955–958, 2013.

[187] Y. Fedutik, V.V. Temnov, O. Schöps, U. Woggon, and M.V. Artemyev. Exciton-plasmon-photon conversion in plasmonic nanostructures. *Phys. Rev. Lett.*, 99(13), 2007.

[188] I.L. Medintz and H. Mattoussi. Quantum dot-based resonance energy transfer and its growing application in biology. *Phys. Chem. Chem. Phys.*, 11(1):17–45, 2009.

[189] A.R. Clapp, T. Pons, I.L. Medintz, J.B. Delehanty, J.S. Melinger, T. Tiefenbrunn, P.E. Dawson, B.R. Fisher, B. O'Rourke, and H. Mattoussi. Two-photon excitation of quantum-dot-based fluorescence resonance energy transfer and its applications. *Advanced Materials*, 19(15):1921–1926, 2007.

[190] A.R. Clapp, I.L. Medintz, and H. Mattoussi. Förster resonance energy transfer investigations using quantum-dot fluorophores. *ChemPhysChem*, 7(1):47–57, 2006.

[191] S.A. Crooker, J.A. Hollingsworth, S. Tretiak, and V.I. Klimov. Spectrally resolved dynamics of energy transfer in quantum-dot assemblies: Towards engineered energy flows in artificial materials. *Phys. Rev. Lett.*, 89(18):186802/1–186802/4, 2002.

[192] C.R. Kagan, C.B. Murray, and M.G. Bawendi. Long-range resonance transfer of electronic excitations in close-packed cdse quantum-dot solids. *Phys. Rev. B*, 54(12):8633–8643, 1996.

[193] C.R. Kagan, C.B. Murray, M. Nirmal, and M.G. Bawendi. Electronic energy transfer in cdse quantum dot solids. *Phys. Rev. Lett.*, 76(9):1517–1520, 1996.

[194] L.A. Padilha, J.T. Stewart, R.L. Sandberg, W.K. Bae, W.-K. Koh, J.M. Pietryga, and V.I. Klimov. Carrier multiplication in semiconductor nanocrystals: Influence of size, shape, and composition. *Acc. Chem. Res.*, 46(6):1261–1269, 2013.

[195] K. Hyeon-Deuk and O.V. Prezhdo. Photoexcited electron and hole dynamics in semiconductor quantum dots: Phonon-induced relaxation, dephasing, multiple exciton generation and recombination. *Journal of Physics Condensed Matter*, 24(36), 2012.

[196] K. Hyeon-Deuk and O.V. Prezhdo. Multiple exciton generation and recombination dynamics in small si and cdse quantum dots: An ab initio time-domain study. *ACS Nano*, 6(2):1239–1250, 2012.

[197] J.T. Stewart, L.A. Padilha, M.M. Qazilbash, J.M. Pietryga, A.G. Midgett, J.M. Luther, M.C. Beard, A.J. Nozik, and V.I. Klimov. Comparison of carrier multiplication yields in Pbs and Pbse nanocrystals: The role of competing energy-loss processes. *Nano Lett.*, 12(2):622–628, 2012.

[198] J.A. McGuire, M. Sykora, J. Joo, J.M. Pietryga, and V.I. Klimov. Apparent versus true carrier multiplication yields in semiconductor nanocrystals. *Nano Lett.*, 10(6):2049–2057, 2010.

[199] J.A. Mcguire, J. Joo, J.M. Pietryga, R.D. Schaller, and V.I. Klimov. New aspects of carrier multiplication in semiconductor nanocrystals. *Acc. Chem. Res.*, 41(12):1810–1819, 2008.

[200] C.M. Isborn, S.V. Kilina, X. Li, and O.V. Prezhdo. Generation of multiple excitons in Pbse and cdse quantum dots by direct photoexcitation: First-principles calculations on small Pbse and cdse clusters. *J. Phys. Chem. C*, 112(47):18291–18294, 2008.

[201] R.D. Schaller, M. Sykora, J.M. Pietryga, and V.I. Klimov. Seven excitons at a cost of one: Redefining the limits for conversion efficiency of photons into charge carriers. *Nano Lett.*, 6(3):424–429, 2006.

[202] B. Patton, W. Langbein, and U. Woggon. Trion, biexciton, and exciton dynamics in single self-assembled cdse quantum dots. *Phys. Rev. B*, 68(12):1253161–1253169, 2003.

[203] M. Aerts, T. Bielewicz, C. Klinke, F.C. Grozema, A.J. Houtepen, J.M. Schins, and L.D.A. Siebbeles. Highly efficient carrier multiplication in PbS nanosheets. *Nat. Comm.*, 5, 2014.

[204] P.D. Cunningham, J.E. Boercker, E.E. Foos, M.P. Lumb, A.R. Smith, J.G. Tischler, and J.S. Melinger. Enhanced multiple exciton generation in quasi-one-dimensional semiconductors. *Nano Lett.*, 11(8):3476–3481, 2011.

[205] Z. Lin, A. Franceschetti, and M.T. Lusk. Size dependence of the multiple exciton generation rate in cdse quantum dots. *ACS Nano*, 5(4):2503–2511, 2011.

[206] D. Timmerman, J. Valenta, K. Dohnalová, W.D.A.M. De Boer, and T. Gregorkiewicz. Step-like enhancement of luminescence quantum yield of silicon nanocrystals. *Nat. Nanotechnol.*, 6(11):710–713, 2011.

[207] Y. Yang, W. Rodríguez-Córdoba, and T. Lian. Multiple exciton generation and dissociation in Pbs quantum dot-electron acceptor complexes. *Nano Lett.*, 12(8):4235–4241, 2012.

[208] H. Zhu and T. Lian. Enhanced multiple exciton dissociation from cdse quantum rods: The effect of nanocrystal shape. *J. Am. Chem. Soc.*, 134(27):11289–11297, 2012.

[209] C. Burda, X. Chen, R. Narayanan, and M.A. El-Sayed. Chemistry and properties of nanocrystals of different shapes. *Chem. Rev.*, 105(4):1025–1102, 2005.

[210] F. Wang and W.E. Buhro. Determination of the rod-wire transition length in colloidal indium phosphide quantum rods. *J. Am. Chem. Soc.*, 129(46):14381–14387, 2007.

[211] M.B. Mohamed, C. Burda, and M.A. El-Sayed. Shape dependent ultrafast relaxation dynamics of cdse nanocrystals: Nanorods vs nanodots. *Nano Lett.*, 1(11):589–593, 2001.

[212] H. Htoon, J.A. Hollingsworth, R. Dickerson, and V.I. Klimov. Effect of zero- to one-dimensional transformation on multiparticle auger recombination in semiconductor quantum rods. *Phys. Rev. Lett.*, 91(22):227401/1–227401/4, 2003.

[213] J.S. Son, K. Park, S.G. Kwon, J. Yang, M.K. Choi, J. Kim, J.H. Yu, J. Joo, and T. Hyeon. Dimension-controlled synthesis of cds nanocrystals: From 0d quantum dots to 2D nanoplates. *Small*, 8(15):2394–2402, 2012.

[214] Y. Li, O. Voskoboynikov, C.P. Lee, S.M. Sze, and O. Tretyak. Electron energy state dependence on the shape and size of semiconductor quantum dots. *J. Appl. Phys.*, 90(12):6416–6420, 2001.

[215] Y. Li, O. Voskoboynikov, C.P. Lee, and S.M. Sze. Computer simulation of electron energy levels for different shape inas/GaAs semiconductor quantum dots. *Comput. Phys. Commun.*, 141(1):66–72, 2001.

[216] L.-S. Li, J. Hu, W. Yang, and A.P. Alivisatos. Band gap variation of size- and shape-controlled colloidal cdse quantum rods. *Nano Lett.*, 1(7):349–351, 2001.

[217] E. Kadantsev and P. Hawrylak. Theory of exciton fine structure in semiconductor quantum dots: Quantum dot anisotropy and lateral electric field. *Phys. Rev. B*, 81(4), 2010.

[218] G.E. Cragg and A.L. Efros. Suppression of auger processes in confined structures. *Nano Lett.*, 10(1):313–317, 2010.

[219] L.M. Thu, W.T. Chiu, and O. Voskoboynikov. Effects of geometrical shape dispersion on inhomogeneous broadening of excitonic peaks of semiconductor nano-objects. *Phys. Rev. B*, 83(12), 2011.

[220] A.-M. Lepadatu, I. Stavarache, M.L. Ciurea, and V. Iancu. The influence of shape and potential barrier on confinement energy levels in quantum dots. *J. Appl. Phys.*, 107(3):033721, 2010.

[221] L. Chen, H. Bao, T. Tan, O.V. Prezhdo, and X. Ruan. Shape and temperature dependence of hot carrier relaxation dynamics in spherical and elongated cdse quantum dots. *J. Phys. Chem. C*, 115(23):11400–11406, 2011.

[222] B. Peng, J.W. May, D.R. Gamelin, and X. Li. Effects of crystallographic and shape anisotropies on dopant-carrier exchange interactions in magnetic semiconductor quantum dots. *J. Phys. Chem. C*, 118(14):7630–7636, 2014.

[223] J. Wang, F. Demangeot, R. Péchou, C. Bayon, A. Mlayah, and B. Daudin. Size and shape effects in the raman scattering by single GaN nanowires. *J. Appl. Phys.*, 114(22), 2013.

[224] C. Bouet, M.D. Tessier, S. Ithurria, B. Mahler, B. Nadal, and B. Dubertret. Flat colloidal semiconductor nanoplatelets. *Chem. Mater.*, 25(8):1262–1271, 2013.

[225] R. Bardoux, A. Kaneta, M. Funato, Y. Kawakami, A. Kikuchi, and K. Kishino. Positive binding energy of a biexciton confined in a localization center formed in a single inx ga1-x n/GaN quantum disk. *Phys. Rev. B*, 79(15):155307–155313, 2009.

[226] M.M. Glazov, E.L. Ivchenko, R.V. Baltz, and E.G. Tsitsishvili. Fine structure of excited excitonic states in quantum disks. *Int. J. Nanosci.*, 6(3-4):265–268, 2007.

[227] H. Gotoh, H. Kamada, H. Ando, and J. Temmyo. Lateral electric-field effects on excitonic photoemissions in InGaAs quantum disks. *Appl. Phys. Lett.*, 76(7):867–869, 2000.

[228] F. Qian, Y. Li, S. Gradečak, D. Wang, C.J. Barrelet, and C.M. Lieber. Gallium nitride-based nanowire radial heterostructures for nanophotonics. *Nano Lett.*, 4(10):1975–1979, 2004.

[229] D.N. Tafen, R. Long, and O.V. Prezhdo. Dimensionality of nanoscale tio2 determines the mechanism of photoinduced electron injection from a cdse nanoparticle. *Nano Lett.*, 14(4):1790–1796, 2014.

[230] H. Lange, M. Artemyev, U. Woggon, and C. Thomsen. Geometry dependence of the phonon modes in cdse nanorods. *Nanotechnology*, 20(4), 2009.

[231] N. Le Thomas, E. Herz, O. Schöps, U. Woggon, and M.V. Artemyev. Exciton fine structure in single cdse nanorods. *Phys. Rev. Lett.*, 94(1), 2005.

[232] M. Artemyev, B. Möller, and U. Woggon. Unidirectional alignment of cdse nanorods. *Nano Lett.*, 3(4):509–512, 2003.

[233] J. Hu, L.-S. Li, W. Yang, L. Manna, L.-W. Wang, and A.P. Alivisatos. Linearly polarized emission from colloidal semiconductor quantum rods. *Science*, 292(5524):2060–2063, 2001.

[234] A. Prudnikau, A. Chuvilin, and M. Artemyev. Cdse-cds nanoheteroplatelets with efficient photoexcitation of central cdse region through epitaxially grown cds wings. *J. Am. Chem. Soc.*, 135(39):14476–14479, 2013.

[235] S. Pedetti, B. Nadal, E. Lhuillier, B. Mahler, C. Bouet, B. Abécassis, X. Xu, and B. Dubertret. Optimized synthesis of cdte nanoplatelets and photoresponse of cdte nanoplatelets films. *Chem. Mater.*, 25(12):2455–2462, 2013.

[236] L. Biadala, F. Liu, M.D. Tessier, D.R. Yakovlev, B. Dubertret, and M. Bayer. Recombination dynamics of band edge excitons in quasi-two-dimensional cdse nanoplatelets. *Nano Lett.*, 14(3):1134–1139, 2014.

[237] M.D. Tessier, P. Spinicelli, D. Dupont, G. Patriarche, S. Ithurria, and B. Dubertret. Efficient exciton concentrators built from colloidal core/crown cdse/cds semiconductor nanoplatelets. *Nano Lett.*, 14(1):207–213, 2014.

[238] J.A. Scher, J.M. Elward, and A. Chakraborty. Shape matters: Effect of 1D, 2D, and 3D isovolumetric quantum confinement in semiconductor nanoparticles. *J. Phys. Chem. C*, 120(43):24999–25009, 2016. cited By 4.

[239] C.B. Murray, D.J. Norris, and M.G. Bawendi. Synthesis and characterization of nearly monodisperse cde (e = s, se, te) semiconductor nanocrystallites. *J. Am. Chem. Soc.*, 115(19):8706–8715, 1993.

[240] † Jin Joo, † Hyon Bin Na, † Taekyung Yu, † Jung Ho Yu, ‡ Young Woon Kim, § Fanxin Wu, § Jin Z. Zhang, , and † Taeghwan Hyeon*. Generalized and facile synthesis of semiconducting metal sulfide nanocrystals. *J. Am. Chem. Soc.*, 125(36):11100–11105, 2003. PMID: 12952492.

[241] J.M. Elward, B. Thallinger, and A. Chakraborty. Calculation of electron-hole recombination probability using explicitly correlated hartree-fock method. *J. Chem. Phys.*, 136(12):124105, 2012.

[242] Xuejun Zhu, Mark S. Hybertsen, and P. B. Littlewood. Electron-hole system revisited: A variational quantum Monte Carlo study. *Phys. Rev. B*, 54:13575–13580, November 1996.

[243] Y. Z. Hu, M. Lindberg, and S. W. Koch. Theory of optically excited intrinsic semiconductor quantum dots. *Phys. Rev. B*, 42:1713–1723, July 1990.

[244] E. A. Burovski, A. S. Mishchenko, N. V. Prokof'ev, and B. V. Svistunov. Diagrammatic quantum Monte Carlo for two-body problems: Applied to excitons. *Phys. Rev. Lett.*, 87:186402, October 2001.

[245] Michael Wimmer, S. V. Nair, and J. Shumway. Biexciton recombination rates in self-assembled quantum dots. *Phys. Rev. B*, 73:165305, April 2006.

[246] M. Braskén, M. Lindberg, D. Sundholm, and J. Olsen. Full configuration interaction calculations of electron-hole correlation effects in strain-induced quantum dots. *Phys. Rev. B*, 61:7652–7655, March 2000.

[247] V. Halonen, Tapash Chakraborty, and P. Pietiläinen. Excitons in a parabolic quantum dot in magnetic fields. *Phys. Rev. B*, 45:5980–5985, March 1992.

[248] M El-Said. The ground-state energy of an exciton in a parabolic quantum dot. *Semicond. Sci. Technol.*, 9(3):272, 1994.

[249] S Jaziri and R Bennaceur. Excitons in parabolic quantum dots in electric and magnetic fields. *Semicond. Sci. Technol.*, 9(10):1775, 1994.

[250] Jennifer M. Elward and Arindam Chakraborty. Effect of dot size on exciton binding energy and electron-hole recombination probability in cdse quantum dots. *J. Chem. Theory Comput.*, 9(10):4351–4359, 2013.

[251] M. Kuno. *Introductory Nanoscience*. Garland Science, 2011.

[252] Jacek Jasieniak, Marco Califano, and Scott E. Watkins. Size-dependent valence and conduction band-edge energies of semiconductor nanocrystals. *ACS Nano*, 5(7):5888–5902, 2011. PMID: 21662980.

[253] P. Yu and M. Cardona. *Fundamentals of Semiconductors: Physics and Materials Properties*. Number v. 3 in Advanced texts in physics. Springer Berlin Heidelberg, 2005.

[254] Christopher R. Myers, Cyrus J. Umrigar, James P. Sethna, and John D. Morgan. Fock's expansion, kato's cusp conditions, and the exponential ansatz. *Phys. Rev. A*, 44:5537–5546, November 1991.

[255] Joseph Lee Rodgers and W. Alan Nicewander. Thirteen ways to look at the correlation coefficient. *J. Am. Stat. Assoc.*, 42(1):pp.59–66, 1988.

[256] L. Protesescu, S. Yakunin, M.I. Bodnarchuk, F. Krieg, R. Caputo, C.H. Hendon, R.X. Yang, A. Walsh, and M.V. Kovalenko. Nanocrystals of cesium lead halide perovskites (cspbx¡inf¿3¡/inf¿, x = cl, br, and i): Novel optoelectronic materials showing bright emission with wide color gamut. *Nano Letters*, 15(6):3692–3696, 2015. cited By 2153.

[257] G. Nedelcu, L. Protesescu, S. Yakunin, M.I. Bodnarchuk, M.J. Grotevent, and M.V. Kovalenko. Fast anion-exchange in highly luminescent nanocrystals of cesium lead halide perovskites (cspbx3, x = cl, br, i). *Nano Lett.*, 15(8):5635–5640, 2015.

[258] Q.A. Akkerman, V. D'Innocenzo, S. Accornero, A. Scarpellini, A. Petrozza, M. Prato, and L. Manna. Tuning the optical properties of cesium lead halide perovskite nanocrystals by anion exchange reactions. *J. Am. Chem. Soc.*, 137(32):10276–10281, 2015.

[259] Y.-S. Park, S. Guo, N.S. Makarov, and V.I. Klimov. Room temperature single-photon emission from individual perovskite quantum dots. *ACS Nano*, 9(10):10386–10393, 2015. cited By 217.

[260] N.S. Makarov, S. Guo, O. Isaienko, W. Liu, I. Robel, and V.I. Klimov. Spectral and dynamical properties of single excitons, biexcitons, and trions in cesium-lead-halide perovskite quantum dots. *Nano Letters*, 16(4):2349–2362, 2016. cited By 230.

[261] J. Song, J. Li, X. Li, L. Xu, Y. Dong, and H. Zeng. Quantum dot light-emitting diodes based on inorganic perovskite cesium lead halides (cspbx3). *Advanced Materials*, 27(44):7162–7167, 2015. cited By 1021.

[262] G. Li, H. Wang, T. Zhang, L. Mi, Y. Zhang, Z. Zhang, W. Zhang, and Y. Jiang. Solvent-polarity-engineered controllable synthesis of highly fluorescent cesium lead halide perovskite quantum dots and their use in white light-emitting diodes. *Advanced Functional Materials*, 26(46):8478–8486, 2016. cited By 56.

[263] L. Zhang, X. Yang, Q. Jiang, P. Wang, Z. Yin, X. Zhang, H. Tan, Y.M. Yang, M. Wei, B.R. Sutherland, E.H. Sargent, and J. You. Ultra-bright and highly efficient inorganic based perovskite light-emitting diodes. *Nature Communications*, 8, 2017. cited By 252.

[264] S. Yakunin, L. Protesescu, F. Krieg, M.I. Bodnarchuk, G. Nedelcu, M. Humer, G. De Luca, M. Fiebig, W. Heiss, and M.V. Kovalenko. Low-threshold amplified spontaneous emission and lasing from colloidal nanocrystals of caesium lead halide perovskites. *Nature Communications*, 6, 2015.

[265] Y. Wang, X. Li, X. Zhao, L. Xiao, H. Zeng, and H. Sun. Nonlinear absorption and low-threshold multiphoton pumped stimulated emission from all-inorganic perovskite nanocrystals. *Nano Letters*, 16(1):448–453, 2016. cited By 252.

[266] P. Ramasamy, D.-H. Lim, B. Kim, S.-H. Lee, M.-S. Lee, and J.-S. Lee. All-inorganic cesium lead halide perovskite nanocrystals for photodetector applications. *Chemical Communications*, 52(10):2067–2070, 2016. cited By 355.

[267] M. Kulbak, D. Cahen, and G. Hodes. How important is the organic part of lead halide perovskite photovoltaic cells? efficient cspbbr3 cells. *Journal of Physical Chemistry Letters*, 6(13):2452–2456, 2015. cited By 436.

[268] R.J. Sutton, G.E. Eperon, L. Miranda, E.S. Parrott, B.A. Kamino, J.B. Patel, M.T. Hrantner, M.B. Johnston, A.A. Haghighirad, D.T. Moore, and H.J. Snaith. Bandgap-tunable cesium lead halide perovskites with high thermal stability for efficient solar cells. *Advanced Energy Materials*, 6(8), 2016. cited By 464.

[269] Xiaoming Li, Ye Wu, Shengli Zhang, Bo Cai, Yu Gu, Jizhong Song, and Haibo Zeng. Cspbx3 quantum dots for lighting and displays: Room-temperature synthesis, photoluminescence superiorities, underlying origins and white light-emitting diodes. *Adv. Funct. Mater.*, 26(15):2435–2445, 2016.

[270] G. Murtaza and I. Ahmad. First principle study of the structural and optoelectronic properties of cubic perovskites cspbm3 (m=cl, br, i). *Physica B: Condensed Matter*, 406(17):3222–3229, 2011.

[271] Benjamin T. Diroll, Hua Zhou, and Richard D. Schaller. Low-temperature absorption, photoluminescence, and lifetime of cspbx3 (x = cl, br, i) nanocrystals. *Adv. Funct. Mater.*, 28(30):1800945, 2018.

[272] G. Morello, M. De Giorgi, S. Kudera, L. Manna, R. Cingolani, and M. Anni. Temperature and size dependence of nonradiative relaxation and exciton-phonon coupling in colloidal cdte quantum dots. *J. Phys. Chem. C*, 111(16):5846–5849, 2007.

[273] A.B. Madrid, K. Hyeon-Deuk, B.F. Habenicht, and O.V. Prezhdo. Phonon-induced dephasing of excitons in semiconductor quantum dots: Multiple exciton generation, fission, and luminescence. *ACS Nano*, 3(9):2487–2494, 2009.

[274] B. Chon, J. Bang, J. Park, C. Jeong, J.H. Choi, J.-B. Lee, T. Joo, and S. Kim. Unique temperature dependence and blinking behavior of cdte/cdse (core/shell) type-ii quantum dots. *J. Phys. Chem. C*, 115(2):436–442, 2011.

[275] P. Dey, J. Paul, J. Byisma, D. Karaiskaj, J.M. Luther, M.C. Beard, and A.H. Romero. Origin of the temperature dependence of the band gap and Pbse quantum dots of Pbs. *Solid State Commun.*, 165:49–54, 2013.

[276] E. Rabani, B. Hetényi, B.J. Berne, and L.E. Brus. Electronic properties of cdse nanocrystals in the absence and presence of a dielectric medium. *J. Chem. Phys.*, 110(11):5355–5369, 1999.

[277] C.A. Leatherdale and M.G. Bawendi. Observation of solvatochromism in cdse colloidal quantum dots. *Phys. Rev. B*, 63(16), 2001.

[278] J.-W. Lee, J.-H. Im, and N.-G. Park. Quantum confinement effect of cdse induced by nanoscale solvothermal reaction. *Nanoscale*, 4(20):6642–6648, 2012.

[279] A.E. Kuznetsov and D.N. Beratan. Structural and electronic properties of bare and capped cd 33Se33 and cd33Te33 quantum dots. *J. Phys. Chem. C*, 118(13):7094–7109, 2014.

[280] K. Hyeon-Deuk and O.V. Prezhdo. Multiple exciton generation and recombination dynamics in small si and cdse quantum dots: An ab initio time-domain study. *ACS Nano*, 6(2):1239–1250, 2012.

[281] S. Pal, D.J. Trivedi, A.V. Akimov, B. Aradi, T. Frauenheim, and O.V. Prezhdo. Nonadiabatic molecular dynamics for thousand atom systems: A tight-binding approach toward pyxaid. *J. Chem. Theory Comput.*, 12(4):1436–1448, 2016.

[282] A.K. Rapp, C.J. Casewit, K.S. Colwell, W.A. Goddard, and W.M. Skiff. Uff, a full periodic table force field for molecular mechanics and molecular dynamics simulations. *Journal of the American Chemical Society*, 114(25):10024–10035, 1992. cited By 5636.

[283] Michael W. Schmidt, Kim K. Baldridge, Jerry A. Boatz, Steven T. Elbert, Mark S. Gordon, Jan H. Jensen, Shiro Koseki, Nikita Matsunaga, Kiet A. Nguyen, Shujun Su, Theresa L. Windus, Michel Dupuis, and John A.

Montgomery Jr. General atomic and molecular electronic structure system. *J. Comput. Chem.*, 14(11):1347–1363, 1993.

[284] M.G. Bayne, Y. Uchida, J. Eller, C. Daniels, and A. Chakraborty. Construction of explicitly correlated geminal-projected particle-hole creation operators for many-electron systems using the diagrammatic factorization approach. *Phys. Rev. A*, 94(5), 2016.

[285] Michael G. Bayne and Arindam Chakraborty. Development of composite control-variate stratified sampling approach for efficient stochastic calculation of molecular integrals, 2018.

[286] L. Chen, H. Bao, T. Tan, O.V. Prezhdo, and X. Ruan. Shape and temperature dependence of hot carrier relaxation dynamics in spherical and elongated cdse quantum dots. *J. Phys. Chem. C*, 115(23):11400–11406, 2011.

Jeremy Scher

103 Boise Dr.,
Syracuse, NY, 13210, United States

860-550-2383

03/26/1990

jeremyascher@gmail.com

linkedin.com/in/jeremy-scher

@ScherFire

Profile

I am a driven and resourceful researcher who is comfortable working in fast-paced environments and collaborating with others. My primary research interests lie in the area of developing new methods for treating excited-state properties of chemical systems. My experience in scientific writing and presenting highlights my ability to effectively communicate technical knowledge. My goal is to pursue a career at a national laboratory in order to utilize my strong analytical skills and satisfy my passion for solving challenging problems.

Education

08/2012 – 05/2020
Syracuse, NY

Syracuse University
PhD in Chemistry
Research Advisor: Prof. Arindam Chakraborty

08/2008 – 05/2012
Binghamton, NY

Binghamton University
B.S. in Chemistry
Research Advisor: Prof. Nikolay Dimitrov

Doctoral Thesis

12/2019

Development and Application of Effective Stochastic Potential Method for Investigating Temperature-dependent Electronic Properties of Nanomaterials

Professional Experience

08/2012 – 05/2020
Syracuse, NY

Syracuse University
Graduate Research Assistant
Developed new first-principles methods for calculating the effects of structure, temperature, and solvent on optoelectronic properties of materials. Implemented methods in Python, Fortran 90, and C++.

08/2013 – 12/2017
Syracuse, NY

Syracuse University
Graduate Teaching Assistant
Designed and instructed undergraduate computational chemistry labs. Graded in-lab performance and written lab reports. Held recitations and office hours for general chemistry classes. Guest-lectured classes on thermodynamics and statistical mechanics.

06/2010 – 08/2011
Simsbury, CT

Ensign Bickford Aerospace & Defense
Analytical Laboratory Summer Intern
Calibrated and tested analytical chemistry instruments. Wrote standard operating procedures for their use. Safely handled and characterized primary and secondary explosive compounds.

Skills

Programming
Developed codes (~16,000 total lines) in Python 2.7 and 3.x, Fortran 90, C++. Experience with cross-language coding

High-performance Computing
Performed calculations on massively parallel, grid-based computing environments

Project Management
Supervised and oversaw the workflow of small teams of undergraduate researchers

Technical Writing
Wrote three first-author manuscripts published in peer-reviewed journals using LaTeX

Linux
Proficient in vi and bash/tcsh shell scripting

Microsoft Office
Proficient in Word, Excel, and PowerPoint

Molecular Modeling
Proficient in running simulations in QChem, NWChem, Gaussian, TeraChem, GROMACS, VMD

Chemistry
Organic Chemistry, Solid-state chemistry, Quantum chemistry, Thermodynamics, Statistical mechanics, Electrochemistry, Crystallography

Oral Communication
Presented 13 times at chemical conferences around the United States.

Mentoring
Acted as the mentor to seven different undergraduates and high school students

Git
Managed version control of multiple source codes and research manuscripts

Awards

06/2019 **American Chemical Society Poster Award**
Journal of Physical Chemistry
Awarded at the 51st Midwest Theoretical Chemistry Conference (MWTCC). This conference has been held every year since 1968, and is described as *"the chemistry conference for theoreticians, by theoreticians."*

08/2012 **Syracuse University Graduate Teaching Fellowship Award**

Highlighted Research

Investigating the effect of isovolumetric change in semiconductor nanoparticles on their optical properties
- Wrote a C++ code to implement an explicitly correlated method for treating excitons in anisotropic CdSe, CdS, CdTe, and PbS nanoparticles
- Analyzed results to find a characteristic length feature corresponding to exciton binding energies and electron-hole recombination probabilities.
- Presented findings at the American Chemical Society Fall National Meeting in 2015

Development of an effective stochastic potential method for calculation of temperature and solvent dependent properties
- Developed and formalized the mathematical and theoretical details of the Effective Stochastic Potential (ESP) method and implemented the ESP method into Fortran 90 and Python 3.x codes
- Benchmarked the codes against traditional sampling methods by comparing distributions of HOMO-LUMO gap energies in water at 300K.
- Presented theoretical details at the ACS Fall National Meeting in 2018 and the Midwest Theoretical Chemistry Conference in 2019

Investigating the effect of temperature and solvent on the excited-state properties of PbS quantum dots

- Incorporated treatment of excited-state properties into the implementations of the ESP method
- Calculated temperature-dependent distributions of millions of excitation energies in PbS quantum dots for applications in near-IR light harvesting
- Presented findings at the American Chemical Society Northeast Regional Meeting and the American Chemical Society Fall National Meeting in 2019

Publications

All published work is featured exclusively in top-ranking peer-reviewed chemistry and physics journals.

01/2020 — **J.A. Scher,** N. Govind, A. Chakraborty. Evidence of Skewness and Sub-Gaussian Character in Temperature-Dependent Distributions of One Million Electronic Excitation Energies in PbS Quantum Dots. *The Journal of Physical Chemistry Letters* **2020** *11* (3), 986-992.

07/2018 — **J.A. Scher**, M.G. Bayne, A. Srihari, S. Nangia, A. Chakraborty. Development of effective stochastic potential method using random matrix theory for efficient conformational sampling of semiconductor nanoparticles at non-zero temperatures. *The Journal of Chemical Physics* **2018** *149*, 014103.

05/2018 — M.G. Bayne, **J.A. Scher**, B.H. Ellis, A. Chakraborty. Linked-Cluster Formulation of Electron-Hole Interaction Kernel in Real-Space Representation without Using Unoccupied States. *The Journal of Chemical Theory and Computation* **2018** *14* (7), 3656-3666.

10/2016 — **J.A. Scher**, J.M. Elward, A. Chakraborty. Shape Matters: Effect of 1D, 2D, and 3D Isovolumetric Quantum Confinement in Semiconductor Nanoparticles. *The Journal of Physical Chemistry C* **2016** *120* (43), 24999-25009.

Exhibitions

08/2019
San Diego, CA

Highly efficient conformational sampling of in vivo SERCA activator CDN1163 for determination of thermal and solvent effects on its excited state properties
American Chemical Society National Meeting and Exposition
Poster, Paper Number: COMP 389

08/2019
San Diego, CA

Computational investigation of the thermal stability and temperature-dependent electronic properties of highly energetic material TKX-50
American Chemical Society National Meeting and Exposition
Oral Presentation, Paper Number: ORGN 243

08/2019
Philadelphia, PA

Obtaining temperature-dependent statistical distributions of one million electronic excitation energies using the Effective Stochastic Potential method
Penn Conference in Theoretical Chemistry
Poster

08/2019
San Diego, CA

Investigating the effect of solvatochromism in thermally activated delayed fluorescence emitters exhibiting circularly polarized luminescence
American Chemical Society National Meeting and Exposition
Oral Presentation, Paper Number: ENFL 240

06/2019
South Bend, IN

Obtaining temperature-dependent statistical distributions of one million electronic excitation energies using the Effective Stochastic Potential method
The 51st Midwest Theoretical Chemistry Conference
Poster, received Journal of Physical Chemistry poster award

06/2019
Saratoga Springs, NY

Investigating the effect of solvatochromism in thermally activated delayed fluorescence emitters exhibiting circularly polarized luminescence
American Chemical Society Northeast Regional Meeting
Oral Presentation, Abstract ID: 3213806

06/2019
Saratoga Springs, NY

Determining the effect of hydration shell on the spectra of proteolysis targeting chimera MD-224 by efficiently sampling conformations using the Effective Stochastic Potential method
American Chemical Society Northeast Regional Meeting
Oral Presentation, Abstract ID: 3213798

06/2019
Saratoga Springs, NY

Highly efficient conformational sampling of in-vivo SERCA activator CDN1163 for determination of thermal and solvent effects on its excited state properties
American Chemical Society Northeast Regional Meeting
Oral Presentation, Abstract ID: 3213795

06/2019
Saratoga Springs, NY

Computational investigation of the thermal stability and temperature-dependent electronic properties of highly energetic material TKX-50
American Chemical Society Northeast Regional Meeting
Oral Presentation, Abstract ID: 3208164

08/2018
Boston, MA

Development of stochastic linear-response TDDFT method for obtaining distribution of excited state properties
American Chemical Society National Meeting and Exposition
Oral Presentation, Paper Number: COMP 172

08/2018
Boston, MA

Development of effective stochastic potential method using random matrix theory for efficient conformational sampling of molecular quantum mechanical properties at non-zero temperatures
American Chemical Society National Meeting and Exposition
Poster, Paper Number: PHYS 435

09/2015
Boston, MA

Shape matters: 1D, 2D, and 3D quantum confinement in semiconducting nanocrystals
American Chemical Society National Meeting and Exposition
Oral Presentation, Paper Number: COMP 398

09/2015
Boston, MA

Explicitly correlated electron-hole method for calculating optical properties of semiconductor nanocrystals
American Chemical Society National Meeting and Exposition
Poster, Paper Number: PHYS 499

References

Prof. Arindam Chakraborty, *Associate Professor*, Syracuse University
archakra@syr.edu, 315-443-5803

Prof. Mathew Maye, *Professor*, Syracuse University
mmmaye@syr.edu, 315-443-2146

Prof. Lisa Manning, *Professor*, Syracuse University
mmanning@syr.edu, 315-443-3920

Prof. Timothy Korter, *Professor*, Syracuse University
tmkorter@syr.edu, 315-443-0269

Dr. Jennifer Elward, *Investigator, Computational Chemistry*, GSK
jennifer.m.elward@gsk.com, 570-709-0089